NUREG/CR-6516
SAND96-2877

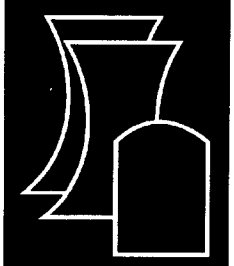

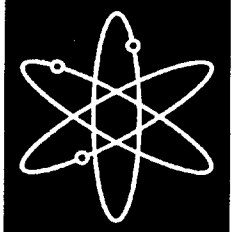

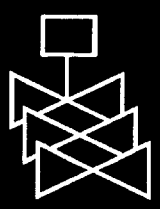

Pretest Analyses of the Steel Containment Vessel Model

Sandia National Laboratories

U.S. Nuclear Regulatory Commission
Office of Nuclear Regulatory Research
Washington, DC 20555-0001

AVAILABILITY NOTICE

Availability of Reference Materials Cited in NRC Publications

NRC publications in the NUREG series, NRC regulations, and *Title 10, Energy,* of the *Code of Federal Regulations,* may be purchased from one of the following sources:

1. The Superintendent of Documents
   U.S. Government Printing Office
   P.O. Box 37082
   Washington, DC 20402–9328
   <http://www.access.gpo.gov/su_docs>
   202–512–1800

2. The National Technical Information Service
   Springfield, VA 22161–0002
   <http://www.ntis.gov/ordernow>
   703–487–4650

The NUREG series comprises (1) technical and administrative reports, including those prepared for international agreements, (2) brochures, (3) proceedings of conferences and workshops, (4) adjudications and other issuances of the Commission and Atomic Safety and Licensing Boards, and (5) books.

A single copy of each NRC draft report is available free, to the extent of supply, upon written request as follows:

Address: Office of the Chief Information Officer
Reproduction and Distribution
Services Section
U.S. Nuclear Regulatory Commission
Washington, DC 20555–0001
E–mail: <GRW1@NRC.GOV>
Facsimile: 301–415–2289

A portion of NRC regulatory and technical information is available at NRC's World Wide Web site:

<http://www.nrc.gov>

All NRC documents released to the public are available for inspection or copying for a fee, in paper, microfiche, or, in some cases, diskette, from the Public Document Room (PDR):

NRC Public Document Room
2121 L Street, N.W., Lower Level
Washington, DC 20555–0001
<http://www.nrc.gov/NRC/PDR/pdr1.htm>
1–800–397–4209 or locally 202–634–3273

Microfiche of most NRC documents made publicly available since January 1981 may be found in the Local Public Document Rooms (LPDRs) located in the vicinity of nuclear power plants. The locations of the LPDRs may be obtained from the PDR (see previous paragraph) or through:

<http://www.nrc.gov/NRC/NUREGS/SR1350/V9/lpdr/html>

Publicly released documents include, to name a few, NUREG-series reports; *Federal Register* notices; applicant, licensee, and vendor documents and correspondence; NRC correspondence and internal memoranda; bulletins and information notices; inspection and investigation reports; licensee event reports; and Commission papers and their attachments.

Documents available from public and special technical libraries include all open literature items, such as books, journal articles, and transactions, *Federal Register* notices, Federal and State legislation, and congressional reports. Such documents as theses, dissertations, foreign reports and translations, and non-NRC conference proceedings may be purchased from their sponsoring organization.

Copies of industry codes and standards used in a substantive manner in the NRC regulatory process are maintained at the NRC Library, Two White Flint North, 11545 Rockville Pike, Rockville, MD 20852–2738. These standards are available in the library for reference use by the public. Codes and standards are usually copyrighted and may be purchased from the originating organization or, if they are American National Standards, from—

American National Standards Institute
11 West 42nd Street
New York, NY 10036–8002
<http://www.ansi.org>
212–642–4900

NUREG/CR-6516
SAND96-2877

Pretest Analyses of the Steel Containment Vessel Model

Manuscript Completed: December 1998
Date Published: January 1999

Prepared by
V.L. Porter, P.A. Carter, S.W. Key

Sandia National Laboratories
Albuquerque, NM 87185

J.F. Costello, NRC Project Manager

Prepared for
Division of Engineering Technology
Office of Nuclear Regulatory Research
U.S. Nuclear Regulatory Commission
Washington, DC 20555-0001
NRC Job Code L1299, A1401

Abstract

Development and validation of predictive methods for structural response of containment vessels in nuclear power plants to the overpressures that may be experienced during the unlikely occurrence of a severe accident continue to be of interest in the United States and the international community. As part of an international joint program sponsored by the Nuclear Power Engineering Corporation (NUPEC) of Japan and the U.S. Nuclear Regulatory Commission (NRC), Sandia National Laboratories (SNL) conducted a high pressure test of a steel containment vessel (SCV) model. The test model is nominally based on a Japanese Improved MK-II boiling water reactor containment. It is one-tenth in overall size but has wall thicknesses at one-fourth scale. In addition to the SCV model, the test includes an external contact structure (CS), a thick steel conical shell that covers most of the SCV with a nominal gap between the walls of the two structures. The nominal gap size was selected to allow the SCV model to deform as a stand-alone structure beyond the elastic range prior to its contact with the CS.

An objective of the test is to develop a set of validated methods that can be used to predict the response of containment buildings subjected to severe accident loads. Measures of structural response of the containment include displacement and strain during loading and characterization of the failure. Failure is characterized by the internal pressure at failure, the failure mechanism, and the location of failure. This test also allowed specific features of the SCV/CS interaction to be studied, including closure of gap, progression of contact, and load sharing.

This report describes finite element analyses conducted by Sandia in support of the overall design of the model and the development of the instrumentation plan, and for prediction of model behavior during the test. Preliminary scoping calculations were performed to answer design questions such as the effects of mixed scaling of the SCV model and the effects of including a contact structure in the test. These analyses were also used to answer modeling questions such as the best types of elements to use, the effects of friction between the SCV and the CS, and rational extrapolation of the materials tests for input to the finite element code. Global and local analyses were then conducted to examine the response of the final design using actual material test data. First the global response was predicted using both axisymmetric and three-dimensional shell models. Subsequent detailed local submodels were developed to refine features included in only a coarse fashion in the global analyses. These local analyses included an axisymmetric continuum analysis of the top head and a three-dimensional shell analysis of the equipment hatch region. Finally, one selected as-built feature, local wall thinning detected in the area of the equipment hatch, was incorporated into the local submodel of the equipment hatch.

Contents

Appendices

Figures

Figures (continued)

Figures (continued)

Figures (continued)

Figures (continued)

Tables

Executive Summary

Development and validation of methods for predicting structural response of containment vessels in nuclear power plants to the overpressures that may be experienced during the unlikely occurrence of a severe accident continue to be of interest in the United States and the international community. As part of the Cooperative Containment Program sponsored by the Nuclear Power Engineering Corporation (NUPEC) of Japan and the U.S. Nuclear Regulatory Commission (NRC), Sandia National Laboratories (SNL) will conduct a high pressure test of a steel containment vessel (SCV) model. This report describes finite element analyses conducted by SNL in support of the overall design of the model and the test and for prediction of model behavior during the test.

The SCV model is nominally based on a Japanese Improved MK-II boiling water reactor containment. A mixed-scale design was used for the SCV model. The overall geometry of the model was scaled at one-tenth to facilitate shipping of the model from Japan to the United States, but the shell thicknesses were scaled at one-fourth for manufacturability and material availability. The top head, knuckle region, and stiffeners were also scaled using this mixed-scale approach and were not designed to simulate buckling or bending behavior of the actual containment vessel. The SCV model includes an equipment hatch penetration with the reinforcement plate, the drywell head, and a material interface in the vessel wall where two different steels are welded together. The equipment hatch sleeve and the top head flanges are not to scale. The equipment hatch cover is welded shut, and the top head flanges are represented as a single thick ring rather than separate flanges bolted together. All other hatches, airlocks, and penetrations have been omitted from the model. In addition, the lower wetwell and wall-basemat junction have been replaced with a thick bottom head designed to remain essentially elastic throughout the test. Finally, all internal structures not integral to the vessel wall have been omitted. Detailed drawings of the SCV are included in Appendix A.

In typical Japanese Improved MK-II plants, the steel containment vessel is inside a reinforced concrete shield building. Axisymmetric finite element analyses of the actual containment inside an idealized rigid shield showed that the response of shielded and unshielded containments would be quite different. Notably, the analyses showed that the location of the highest strains in the high pressure regimes shifts from the middle conical sections of the unshielded containment to the top head region of the shielded containment. Therefore, the test has been designed to include a conical steel contact structure (CS) on the outside of the SCV model. While the CS in no way provides the same restraining effect on the SCV model as that of a reinforced concrete shield building on an actual containment vessel, it does force modeling of the contact and more closely represents an actual containment scenario than a test of an unshielded model. Appendix A includes drawings of the CS.

Preliminary finite element analyses were performed to evaluate the effects of the proposed mixed scaling on the model behavior and its relationship to the actual containment. While results showed that overall behavior was similar at the correctly scaled pressures, concern still exists over the effects on localized bending and the potential for top head buckling. In particular, since the critical pressure for buckling of the torispherical top head is approximately proportional to the ratio of wall thickness to radius, the mixed-scale SCV model (in which this ratio is 2.5 times that of the actual containment) is much less susceptible to this mode of failure. Therefore, the data from this test should be regarded as a validation of numerical modeling techniques that can then be applied for analysis of an actual containment, but the behavior of the actual containment cannot be directly inferred from the results of the test or the analyses of the mixed-scale model.

Finite element computations were also performed early in the program to answer numerical modeling questions such as the best type of elements, an appropriate value for the coefficient of friction between the SCV and the CS, and how to extend the provided material data to the range required for failure analyses. Axisymmetric analyses of the actual containment indicated that the two-node shell element represented the SCV wall quite well, except in the area of the top head where large thickness transitions occur. In this area, continuum elements are probably necessary for good local results. Axisymmetric shell analyses of the SCV model with a preliminary conceptual design of the CS indicated that

the two-node sliding interface element could be used to model contact between the structures and that model behavior was not significantly affected by coefficients of friction ranging from 0.1 to 0.5. In the final series of preliminary analyses, uniaxial test data provided by Hitachi were extrapolated beyond the point of maximum load in the tensile test using an axisymmetric continuum model of the test specimen.

The analyses used for pretest predictions of the behavior of the SCV/CS model were based on design information available at the time of the analyses and uniaxial test data of the actual material used to construct the model. Except for one analysis of the area around the equipment hatch, as-built geometric information was not used.

Global axisymmetric shell analyses were used to predict overall containment behavior. Two-node shell elements were used for the SCV wall and four-node continuum elements for the contact structure. Contact between the two structures was simulated using two-node interface elements that can accommodate large sliding. The coefficient of friction was assumed to be 0.20. These analyses indicated that the highest strain occurred in the top head.

A three-dimensional shell model of one-half of the structure was developed to incorporate the equipment hatch and reinforcement plate, the only non-axisymmetric feature in the model. Four-node shell elements were used in the vessel wall, along with four-node interface elements for the contact. However, in the three-dimensional analysis, the available contact simulation algorithm was limited to small relative sliding between the structures. As in the axisymmetric shell analyses, the coefficient of friction was assumed to be 0.20. This global three-dimensional model indicated locally high strains in the area around the equipment hatch insert plate near the material interface.

Output from the global three-dimensional model was then used to develop three different localized submodels, (1) an axisymmetric submodel of the top head using continuum elements due to the thickness variations near the knuckle and flange, (2) a three-dimensional shell submodel of the equipment hatch area based on design thicknesses, and (3) a three-dimensional shell submodel of the equipment hatch area incorporating an approximation of wall thinning discovered during examination of the actual SCV model.

Results of the global axisymmetric and three-dimensional analyses based on the final design indicate that the two regions with the highest strain are the top head and the area near the thickened insert plate at the equipment hatch. Based on the final design of the SCV model, failure is equally likely to occur in either of these areas. However, the actual SCV model includes a region of unknown extent near the equipment hatch insert plate where the material is thinner than specified in the design. Results of the local finite element analysis that included an approximation of wall thinning in this area indicate higher strains near the equipment hatch than in the top head. The computed plastic strain in the thinned region of the SPV490 steel near the equipment hatch insert plate and the material interface reaches a level that suggests local ductile failure at an internal pressure of 4.5 MPa. Therefore, based on the inclusion of this as-built feature, failure is considered to be more likely to occur near the equipment hatch than in the top head.

The pretest analysis efforts have demonstrated that the analysis results for failure prediction are very much dependent on the local details that have been included in the analysis model. Because several of the known as-built features of the SCV/CS assembly have not been included in the pretest analyses, the analysis results will best serve to provide predictions of the global deformation of the SCV model and will be less reliable for local failure predictions.

Acknowledgments

This pretest analyses project was sponsored by the U.S. Nuclear Regulatory Commission (NRC). Special thanks are due to Dr. James F. Costello of the NRC for his guidance throughout the program.

The SCV model test program is jointly sponsored by the Nuclear Power Engineering Corporation (NUPEC) of Japan and the U.S. NRC. We are indebted to Dr. Hideo Ogasawara and Mr. Tomoyuki Matsumoto for their support and guidance. We are also grateful to Mr. Kuniaki Komine and other members of NUPEC and Hitachi for many discussions regarding analysis methods and results.

The authors wish to acknowledge the work of Dr. Billy J. Thorne in performing many of the early analyses. Thanks are also due to members of the International Nuclear Safety Department at Sandia, specifically to Dr. Vincent Luk, the SCV Test Leader, and to Mr. Michael Hessheimer, the NRC/NUPEC Project Leader. Others whose assistance is greatly appreciated include Dr. Brad Parks, who was the program manager for the first four years, and Dr. Robert Watson who served as the SCV lead engineer for the first three years of the program.

Acronyms

BWR	boiling water reactor
CS	contact structure
LWR	light water reactor
NRC	Nuclear Regulatory Commission
NUPEC	Nuclear Power Engineering Corporation
PWR	pressurized water reactor
SCV	steel containment vessel
SNL	Sandia National Laboratories

1. Introduction

1.1 Program Background

The performance of containment systems in postulated severe accidents is a matter of continuing interest and concern in both the United States and the international community. Testing and analysis of numerous scale models of containment buildings that are pressurized to failure have been conducted for several years at Sandia National Laboratories (SNL) as part of the Containment Integrity Programs sponsored by the U.S. Nuclear Regulatory Commission (NRC). The overall objective of the programs has been to develop test-validated methods that can be used to predict the performance of light water reactor (LWR) containment buildings subject to loads beyond the design basis.

Previous test programs sponsored by the NRC and carried out at SNL focussed on scale models of steel containment geometries typical of pressurized water reactor (PWR) and boiling water reactor (BWR) Mark III containment designs. SNL's pretest analyses results are also included in a Round Robin analysis activity (Luk and Klamerus, 1996) that provided a forum for various international analysis groups to share pretest predictions of the steel containment vessel (SCV) model behavior. However, BWR Mark I and Mark II containment designs have geometries distinctly different from PWR and BWR Mark III containments. The most significant structural difference is the region of sharp curvature in the top head of the BWR Mark I and II reactor containments. Currently, no experimental data exist for the validation of finite element modeling techniques for these types of containments.

SNL is now involved in a Cooperative Containment Integrity Program under the joint sponsorship of the NUPEC of Tokyo, Japan and the NRC. This program grew out of the realization that there was sufficient similarity in goals in containment integrity research to warrant a cooperative effort between the United States and Japan. The focus of this new program remains LWR containments, but the current test is of a scale model of an SCV that represents some features of an Improved Mark II BWR containment vessel in Japan.

1.2 Objectives

One objective of the SCV test is to evaluate the validity of current methods for prediction of the performance of containment buildings subjected to severe accident loads and to identify areas needing improvement. Important measures of containment performance include the strain response during the loading history, the pressure capacity, the failure mechanism, and the location of failure. The test includes a thick steel shell contact structure (CS) that sits over the SCV model with a nominally uniform gap between the walls of the two structures. The nominal gap size was selected to allow the SCV model to experience deformation well beyond the elastic range prior to its contact with the CS. This test allowed specific features of the SCV/CS interaction to be studied including closure of gap, progression of contact, and load sharing between the SCV and the CS.

The pretest finite element analyses can be categorized based on their objectives. Early scoping calculations were performed to support the design efforts, mainly to answer questions regarding the effects of the mixed scaling of the SCV model and the effects of including the CS in the test. These analyses also answered modeling questions such as the best types of elements to use and the effects of friction between the SCV and the CS. Because these analyses were conducted before the material test data were available, nominal material properties were used. When uniaxial test data became available, finite element analyses of the test specimens were used to extrapolate the data for later input to the finite element analyses used for pretest predictions of the SCV model behavior.

Global and local analyses based on the final design geometry and actual material properties were conducted to examine the response the SCV/CS assembly. Except for one local analysis of the area around the equipment hatch, as-built geometric information was not used. The finite element models used for pretest predictions of SCV/CS behavior are described below and summarized in Table 1-1. All analyses of the SCV model were performed using current versions of the ABAQUS general purpose finite element code (ABAQUS, 1993a; 1993b; 1994; 1995).

Table 1-1. Summary of Pretest Prediction Analyses

Model	Purpose	Analysis/Type Elements
GAX18	Global behavior	Axisymmetric/1500 shell and continuum elements
GAX34	Global behavior with worst case gap dimension of 34 mm	Axisymmetric/1500 shell and continuum elements
G3DS	Global behavior with equipment hatch	3-dimensional/4800 shell elements
LTHAXC	Local behavior at top head and knuckle; include latest contact structure design	Axisymmetric/7200 continuum elements
LEHS	Local behavior near equipment hatch insert plate and material change interface	3-dimensional/4800 shell elements
LEHSTh	Effect of thinned area near equipment hatch insert plate and material change interface	3-dimensional/4800 shell elements

Global response throughout the loading history was predicted using both axisymmetric and three-dimensional shell models. Two axisymmetric shell analyses were performed to predict overall SCV model/CS response given two different sizes for the gap between the exterior surface of the SCV model and the interior surface of the CS. Both of these models incorporated the extrapolated uniaxial test data of the materials used in construction of the SCV model. However, properties of the CS were based on design properties for A36 steel because the CS design was in a preliminary phase at the time of the analyses. The first axisymmetric analysis (designated GAX18) included an 18 mm gap, the nominal gap size used for design of the CS. Because a worst case scenario based on fabrication tolerancing information postulated that the gap could be as much as 34 mm, a second axisymmetric analysis using a 34 mm gap (GAX34) was used as a bounding calculation. Results for stress and strain distribution histories from both axisymmetric models were evaluated and used to guide development of the mesh for the subsequent three-dimensional shell model.

Much of the SCV/CS assembly behaves as an axisymmetric structure. However, the design does include one non-axisymmetric feature—the equipment hatch with its surrounding reinforcement plate. Therefore, a global three-dimensional shell model (G3DS) based on the final design dimensions of the SCV model and the CS was developed to determine the effects of this non-axisymmetric feature. Like the axisymmetric models, the three-dimensional shell model used the uniaxial test data for the SCV model and A36 steel for the CS. The only difference between this model and the axisymmetric model with the 18 mm gap is the explicit inclusion of the equipment hatch and reinforcement plate. This model indicated that the two areas of highest strain were the top head and the area around the equipment hatch. Although the global model could provide acceptable results for most areas of the SCV model, mesh refinement was required in areas of high strain gradients, especially in order to model response at internal pressures near failure. Therefore, two submodels with more refined meshes were developed for local analyses of the critical areas identified by the global analyses, the top head and the area near the equipment hatch.

The first local submodel was an axisymmetric model of the top head (LTAXC). This model was developed with continuum elements rather than shell elements to capture the stress and strain concentrations at the drastic changes in wall thickness near the knuckle and the top head flange. Boundary conditions from the global three-dimensional shell analysis were averaged over the circumference so they could be applied to the axisymmetric model. At the time this model was developed, the design of the CS had changed in the area near the top head. Therefore, the top head submodel used representations of the top head of the SCV model and the top of the CS that were both based on final design dimensions. However, the material of the CS was still assumed to be A36 steel.

The second local submodel based on final design dimensions was a three-dimensional shell model of the area near the equipment hatch and thickened reinforcement plate (LEHS). In this case, boundary conditions on the edge of the local mesh were applied directly from the global three-dimensional shell analysis. Stress and strain concentrations occur in this area due to a dramatic jump in thickness from the SCV wall to the reinforcement plate and because a material interface at which two dissimilar steels are welded together also lies in this region.

Finally, during on-site inspection of the SCV model, point measurements of the thickness of the SCV wall near the reinforcement plate indicated that the material had been thinned such that the as-built thickness was less than that specified in the design. Because this area had already been identified as one in which high strains occurred, a representation of the as-built wall thinning was incorporated into the local three-dimensional shell model of the equipment hatch (LEHSTh). Because the extent of the area over which the thinning occurs in the SCV model is not known, the thinning effect could only be approximated.

2. Test Article Description

The steel containment vessel (SCV) model, which incorporates some of the major features of a boiling water reactor (BWR) Mark II containment, was built in Japan by Hitachi Works, Ltd. and shipped to Sandia National Laboratories (SNL). At SNL, the model was enclosed in a contact structure (CS) made of carbon steel. The CS was designed to allow a minimum nominal gap of 18 mm between the exterior surface of the SCV model and the interior surface of the CS. The SCV/CS assembly will be tested within a fragment barrier designed to contain by-products of a catastrophic failure of the SCV. The fragment barrier is below grade and consists of a reinforced concrete floor and walls and a structural roof. Photos of the SCV model and the SCV/CS assembly on the test site at SNL are shown in Figure 2-1 and Figure 2-2.

2.1 Geometry

The geometries of the SCV model and the CS are described in detail in the following two subsections.

2.1.1 Steel Containment Vessel

The SCV model is scaled 1:4 in all wall thicknesses and 1:10 in overall geometry from a prototype Japanese BWR Improved Mark II containment. Whereas the design pressure of the prototype containment is 0.31 MPa (45 psig), the scaled design pressure for the mixed-scale SCV model is 0.78 MPa (113 psig).

Figure 2-3 shows an outline schematic of the SCV model with the CS. Detailed Hitachi drawings of the model are included in Appendix A. The SCV model consists of a number of sections with different wall thicknesses. Except at the knuckle, all thickness variations in the SCV model occur on its exterior surface so that the interior surface is smooth. Included in the SCV model is an equipment hatch opening with a thickened reinforcement plate. The hatch is not to scale, and the hatch cover is welded shut. In addition, the flanges of the top head (drywell head) are represented by a single thick steel ring scaled to match the hoop stiffness of the scaled flanges. The SCV model also includes several stiffeners and a material change interface where dissimilar steels are welded together with a full penetration weld. For convenience, the various sections of the model have been given names (for example, the "spherical shell," the "lower conical shell," and the "knuckle") as shown in Figure 2-3. These names will be used throughout this report to refer to various locations on the model.

The portion of the SCV model above the ring support girder approximates the major features of an actual containment, but the lower portion of the model (i.e., the bottom head below the upper flange of the ring support girder, including the access hatch and other openings) does not. These parts of the model merely complete the pressure boundary. The SCV model was designed to ensure that neither leakage nor failure will occur below the upper flange of the ring support girder during testing, and that deformations in those areas will be negligible.

2.1.2 Contact Structure

Japanese Improved Mark II BWR containments consist of a steel containment vessel surrounded by a reinforced concrete shield building. (US containments are typically constructed of reinforced concrete with a steel liner.) Under severe accident loadings, it is anticipated that the steel containment vessel will grow until it contacts the surrounding shield building. The CS included as part of this test was intended only to allow investigation of the response of the SCV model against an almost rigid surrounding structure during pressurization, so that the behavior of the SCV was more representative of the expected behavior of actual plants. The CS was not designed to simulate the effects of the concrete shield building in physical plants.

The CS was designed to remain essentially elastic (i.e., only local yielding is permitted) until the SCV reaches an internal pressure of approximately 10 times its design pressure. Figure 2-3 shows the SCV/CS assembly. The CS was welded to the ring support girder with a partial penetration weld. Design drawings of the CS are also included in Appendix A.

The CS was designed to provide a minimum gap of 18 mm between the exterior surface of the SCV and the interior surface of the CS. This dimension was selected to ensure that at least one of the following criteria was met before contact occurred, despite reasonable variations due to fabrication difficulties and tolerances:

1. deformation in the conical section equals the scaled gap dimension (9 mm) between an actual BWR Mark II containment and its concrete shield building;
2. deformation in the knuckle region equals two times the scaled gap dimension;
3. strain measured by any functioning surface strain gage exceeds 5% (including the sum of membrane and bending strain and any strain concentrations).

The gap was also designed with the intent that generalized contact between the SCV and the CS would be made prior to structural failure of the SCV.

2.2 Materials

Materials used in the design of the SCV model and contact structure are described in the following two sections, respectively.

2.2.1 SCV Model

The portion of the model above the ring support girder is constructed of SGV480 steel and SPV490 steel. SGV480 steel is the material above the material change interface, and SPV490 steel is the lower material. Standard properties for these materials (Table 2-1) were supplied by Nuclear Power Engineering Corporation (NUPEC) of Japan. In addition, NUPEC provided results of standard uniaxial tests performed on specimens taken from the SCV material. These data are included in Appendix B.

The bottom surface of the ring support girder is spot welded to four steel support legs. These legs are bolted to the floor of the fragment barrier constructed to house the model.

2.2.2 Contact Structure

In the final design (Appendix A), the CS is constructed of 38 mm-thick, SA516 Grade 70 steel with a nominal yield strength of 258 MPa and an nominal ultimate strength of 476 MPa. The CS was fabricated by Chicago Bridge & Iron Services, Inc.

2.3 As-Built Features

Several measurements of the as-built SCV model and the CS were made. Measurements taken of the SCV before installation of the CS included thickness and radius of the SCV wall at several points around the circumference for various elevations. After the CS was installed, the gap between the exterior surface of the SCV model and the interior surface of the CS was also measured at several locations.

2.3.1 SCV Wall Thicknesses

Thickness measurements were made at Hitachi before shipment of the model to SNL. Details of these measurements are included in Appendix C. In general, the as-built SCV model is 5% to 10% thicker than the design. This would indicate that the actual hoop strains would be lower at a given pressure than those predicted by the finite element models based on design dimensions. However, near some of the weld lines, an occasional measurement indicates a thickness slightly (2% to 3%) less than the design. There is no way of knowing how localized this thinning is since there is a large distance between measurements.

Thickness measurements were also taken at SNL after installation of the model in the fragment barrier. Measurements made at SNL focused near weld seams where evidence of grinding was visible and near the equipment hatch. These measurements are also included in Appendix C. The measurements near the

Table 2-1. Nominal Material Properties

Property	SGV480	SPV490
Minimum yield strength	265 MPa	490 MPa
Tensile strength	480 to 590 MPa	610 to 735 MPa
Minimum elongation after fracture	17%	18% for 9 mm plate 25% for 17.5 mm plate

equipment hatch indicated an area of significantly thinned material, albeit of unknown extent. These data were used to study the effects of local wall thinning in a detailed finite element analysis of the area around the equipment hatch.

2.3.2 External Radii

On-site measurements of external dimensions of the SCV model were made by Chicago Bridge & Iron Services, Inc. prior to construction of the CS. The reported data shown in Appendix C give the radii measured from a calculated mean centerline at 45-degree increments around the circumference of the SCV at each of several elevations. These data indicate that, in nearly all the sections below the conical to spherical transition region, the radii vary less than 0.3% around the circumference. (Only one point in the lower conical section has a higher variation, which still is only 0.55%.)

2.3.3 Gap Dimensions

Appendix C also includes the results of measurements done by SNL on the gap between the exterior surface of the SCV model and the interior surface of the CS after installation. The only area in which the gap is less than the 18 mm design is near the top of the contact structure. Therefore, localized contact might initiate in this region somewhat earlier than predicted in the finite element analyses. However, this should not have a significant effect on the model behavior. Except near the equipment hatch, the gap varies from roughly 20 to 25 mm, which is greater than the 18 mm of the design but significantly less than the "worst case" scenario of 34 mm. This worst case scenario was investigated by finite element analyses prior to the contact structure design and is described in Section 5.3 of this report. The gap around the top of the equipment hatch is significantly larger at 27 to 33 mm but still below the 34 mm case investigated by axisymmetric analyses. Because all as-built gap dimensions fall within the bounds examined by the 18 mm and 34 mm axisymmetric analyses, additional analyses using specific as-built gap dimensions were not warranted.

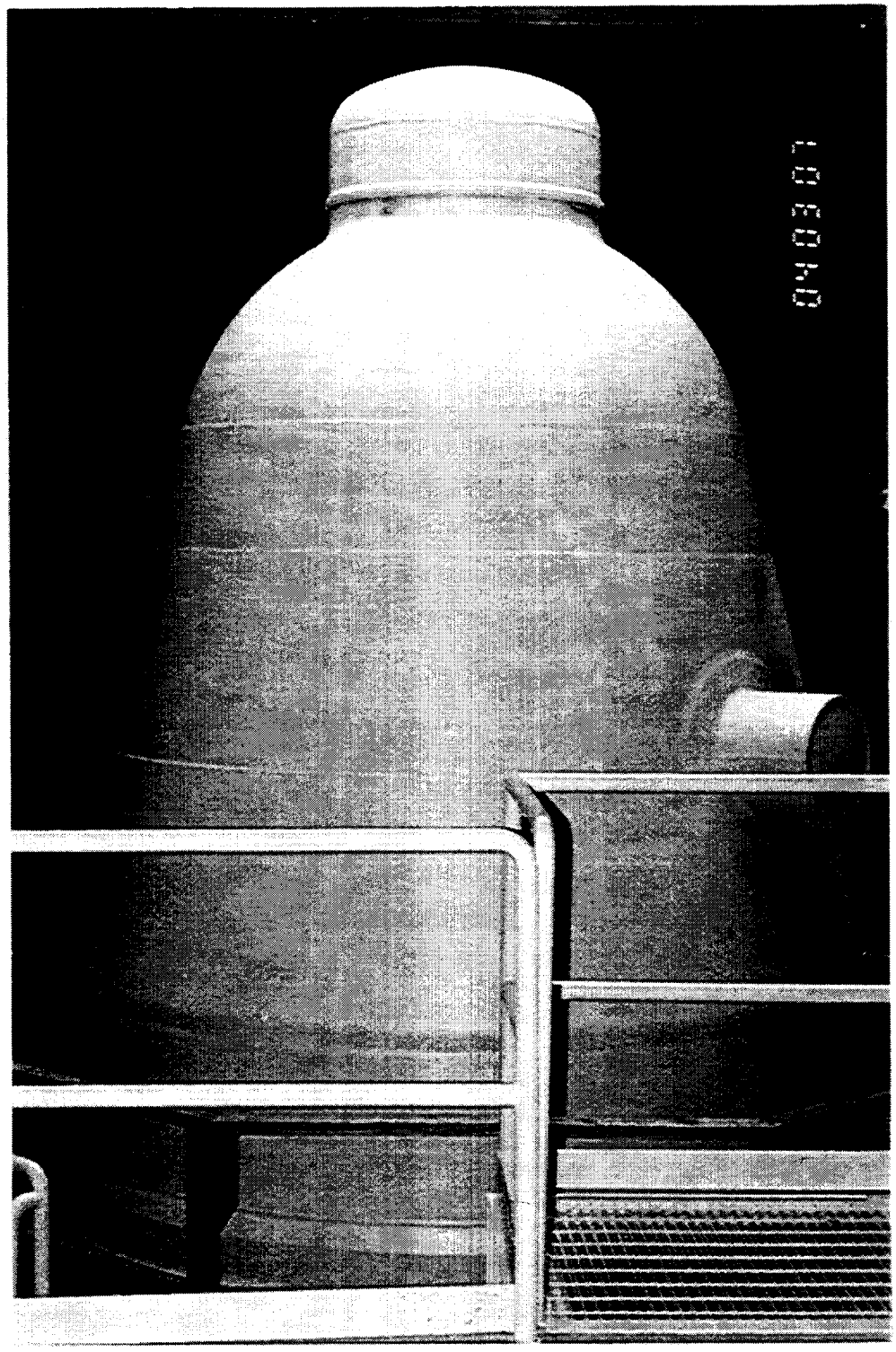

Figure 2-1. Photo of the SCV model on site at Sandia National Laboratories in Albuquerque, New Mexico.

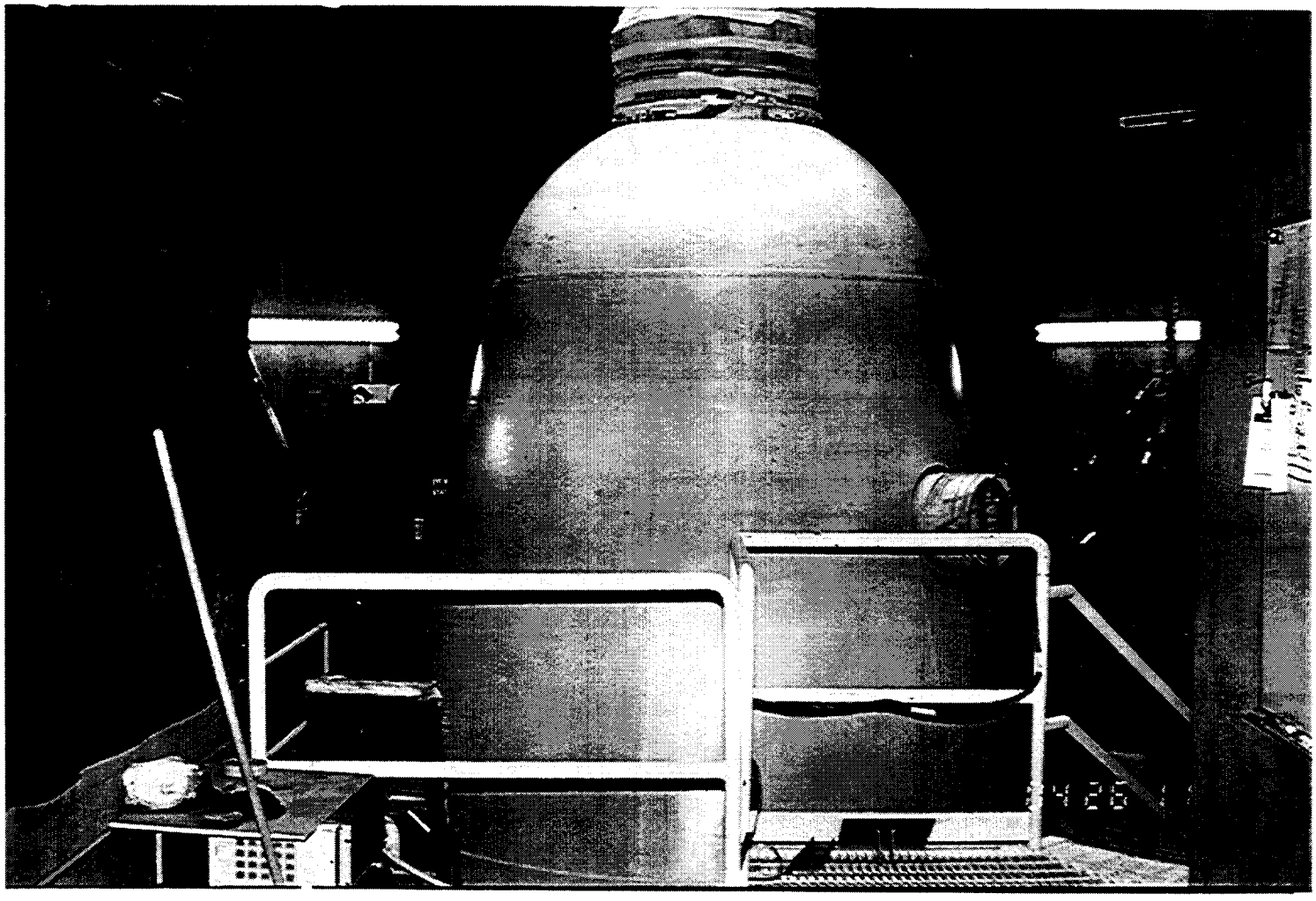

Figure 2-2. Photo of the SCV/CS assembly on the test site.

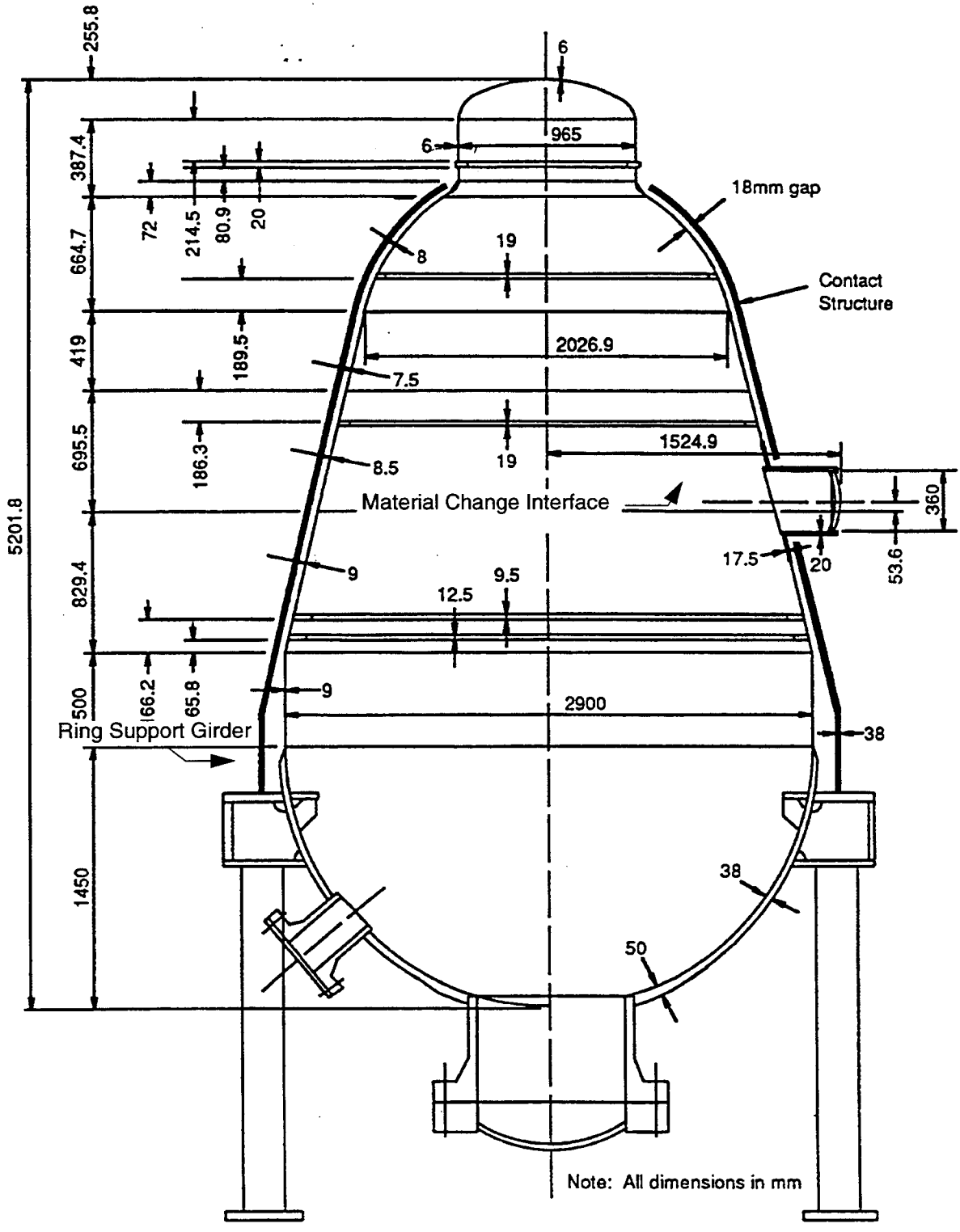

Figure 2-3. Schematic drawing of the SCV/CS assembly.

3. Test Description

The steel containment vessel/contact structure (SCV/CS) assembly was subjected to monotonically increasing static internal pressure as described briefly in this section. Further details of the test sequence and the pressurization system are contained in the project test plan[1].

3.1 Pressure Supply

For the internal pressurization test of the SCV model, the pressure source consists of liquid nitrogen that is gasified and regulated to a constant pressure and temperature. The temperature of the nitrogen gas inside the SCV model is maintained to within ±3°C of the ambient temperature (15°C). This relatively constant gas temperature is achieved by setting the temperature at the pressure source location. Additional heating, if needed, is supplied by heaters before the nitrogen gas enters the model.

3.2 Pressurization Sequence

The pressurization sequence of the SCV test follows a monotonic rise of the internal pressure inside the SCV model until the model fails or the pressure level reaches 15.9 P_d (12.4 MPa, 1800 psig). The pressurization test will be terminated when the SCV model experiences a structural failure in terms of a catastrophic failure or a significantly large tear. If the SCV model leaks from the occurrence of multiple small cracks, then the pressurization system may not be able to maintain a constant pressure inside the model. At this time the SCV model will have experienced a functional failure, and the test will be terminated.

The internal pressurization test has three distinct stages in its test sequence:

1. first stage (0 - 4.6 P_d)
2. second stage (4.6 P_d)
3. third stage (4.6 P_d - model failure or 15.9 P_d)

where P_d is the scaled design pressure (0.78 MPa). The entire test sequence is shown in Figure 3-1.

3.2.1 First Stage (0 - 4.6 P_d)

According to preliminary analysis results[2,3], the conical section of the SCV model expands one scaled gap dimension of 9 mm at an internal pressure of approximately 4.6 P_d, and the structure behaves essentially in the elastic domain throughout this stage. The end of the first stage of the test will occur when the average displacement of any array of four displacement transducers (0°, 90°, 180°, and 270°) at a given elevation is equal to 9 mm, regardless of the pressure.

3.2.2 Second Stage (4.6 P_d)

This pressure condition is held at a constant level for 30 minutes. During this stage, the SCV model behaves as a stand-alone structure; no contact occurs between the SCV model and the CS.

3.2.3 Third Stage (4.6 P_d – model failure or 15.9 P_d)

The SCV model behaves in the plastic domain throughout this stage. As the pressure continues to increase, the SCV model will take a longer time at each pressure step to arrive at a state of steady structural response. Accordingly, the incremental pressure rise for each step will be reduced, and the dwell time will be increased.

---

[1] Luk, V.K., "Steel Containment Vessel Model Test Plan," Project Report No. R-SN-S-003, Rev. B, Sandia National Laboratories, Albuquerque, NM, December 1996.

[2] Porter, V.L., "Analysis of SCV Model Pressurization using Typical Material Properties," Sandia memorandum to V.K. Luk, January 18, 1994.

[3] Porter, V.L., "Three-Dimensional Analysis of Equipment Hatch," Sandia memorandum to V.K. Luk, February 22, 1995.

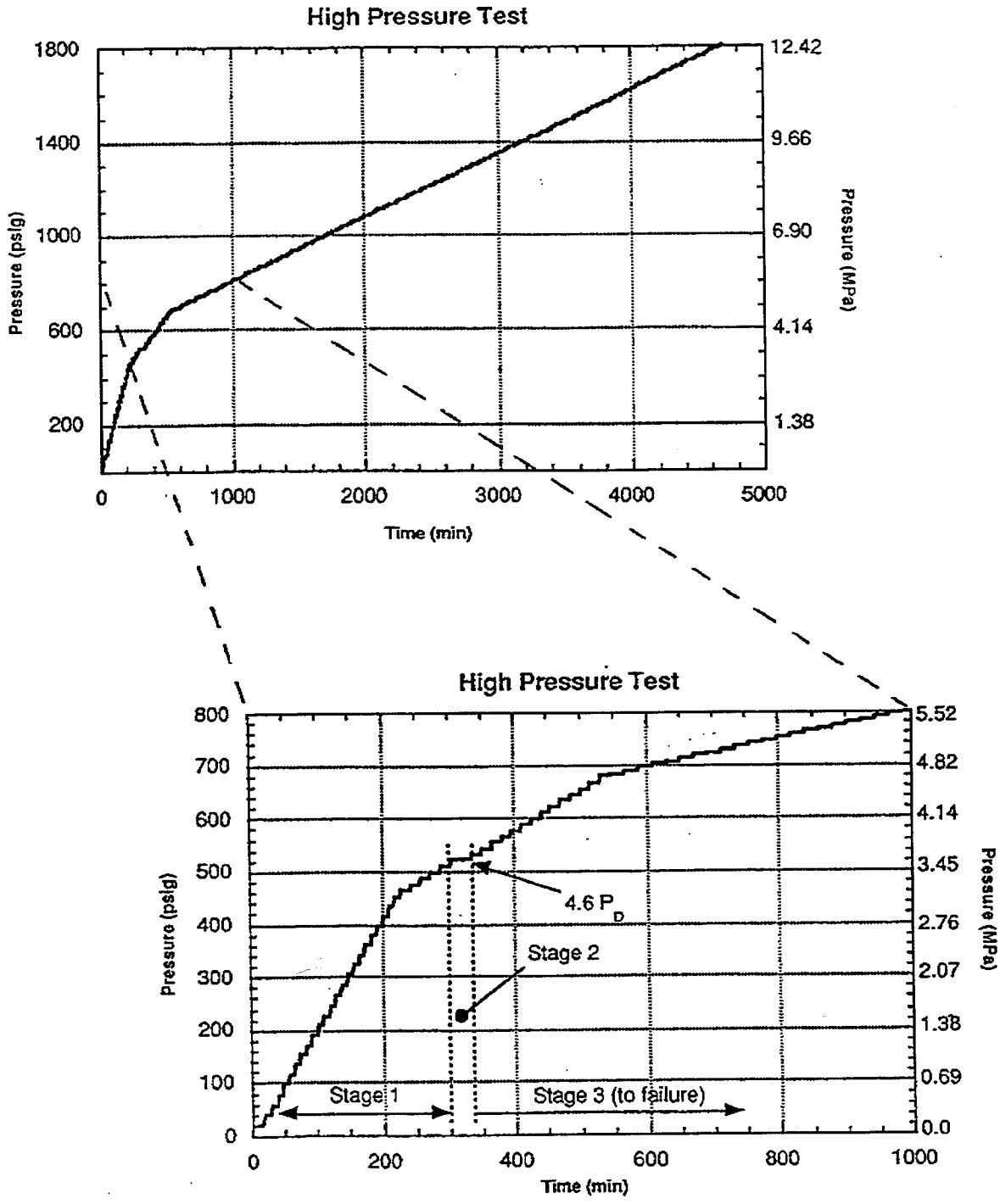

Figure 3-1. Pressurization sequence for the high pressure test.

4. Finite Element Model Development

The finite element models described in this section were preliminary analyses used to develop confidence in the models eventually used for pretest predictions. Finite element analyses of the actual containment were used to select the element types. Early analyses of the steel containment vessel (SCV) model were used for a parametric study of the effects of including a contact structure (CS) in the test and the effects of friction between the two structures on SCV behavior. These early models of the SCV were based on nominal material properties for SGV480 and SPV490 steels obtained from published literature. Also described in this section are finite element models of uniaxial test specimens used to extrapolate the data obtained from uniaxial tests of the actual materials used in the SCV construction.

4.1 Selection of Element Types

Two-dimensional axisymmetric analyses are useful tools for capturing the global response of the SCV model and contact structure because the only non-axisymmetric feature is the equipment hatch. In addition, axisymmetric shell elements are convenient because their inherent coordinate systems have axes through the wall thickness and along the meridional direction of the shell. A question was raised about the accuracy of shell elements in areas of stress concentration due to the thickness variations in the SCV wall. An extensive study of the behavior of axisymmetric shell elements, compared to axisymmetric continuum elements, showed that the shell elements did indeed adequately model the transitions in wall thickness[4,5,6,7,8]. However, additional axisymmetric continuum element analyses were indicated in the top head region at the knuckle and the flange where more drastic thickness variations occur. The preliminary axisymmetric analyses also indicated that the two-node axisymmetric shell elements performed much better than the three-node elements, especially in the presence of contact, as long as the linear elements were sufficiently small to represent the curved surfaces in the model. Hence, all subsequent two-dimensional shell analyses were performed using two-node axisymmetric shell elements.

Global three-dimensional discretization of the SCV model and CS was required to get boundary conditions for local studies focused on the equipment hatch. Shell elements were the only feasible choice for these global three-dimensional analyses because the number of continuum elements required to sufficiently represent bending in the thin wall of the vessel would be extremely high. Four-node shell elements capable of representing finite membrane strains were used in these three-dimensional computations. For the local analysis around the equipment hatch, a fine mesh of these elements was used to ensure adequate representation of the geometry.

4.2 Friction Studies

This section documents early scoping studies regarding the behavior of the SCV model with an exterior CS. Both the influence of CS stiffness and of the amount of friction between the vessel and the CS were investigated. ABAQUS, Version 5.2 (1993a) was used for the computations described in this section.

4.2.1 Finite Element Model Description

All simulations described in this section were preliminary axisymmetric analyses of the SCV model with a conceptual representation of the CS that preceded the actual design (Porter, 1994)[9,10]. The finite element model is shown in Figure 4-1. The finite element mesh for the SCV model consisted of 273 two-node axisymmetric shell elements for the shell walls, ring stiffeners, and top and bottom rings of the ring

4 Thorne, B.J., "Accuracy of Axisymmetric Shell Calculations for Steel Containment Vessels," Sandia memorandum to R.A. Watson, May 11, 1992.

5 Thorne, B.J., "Further Thought on Stress Concentration at Thickness Changes," Sandia memorandum to M.P. Bohn, February 1, 1993.

6 Thorne, B.J., "High Resolution Finite Element Calculations to Investigate the Effect of Stress Concentrations at Thickness Changes on the Response of the MK-II Steel Containment Vessel," Sandia memorandum to R.A. Watson, March 10, 1993.

7 Thorne, B.J., "Steel Containment Vessel Analysis Efforts during January and February 1993," Sandia memorandum to R.A. Watson, March 24, 1993.

8 Thorne, B.J., "Comparison of ABAQUS Torispherical Head Calculations with Kirk and Gill Data," Sandia memorandum to R.A. Watson, April 12, 1993.

9 Porter, V.L., "SCV Model Pressurization with a Surrogate Steel Shield Structure," Sandia memorandum to V.K. Luk, February 11, 1994.

10 Porter, V.L., "Further Investigation of Friction Effects for Shielded SCV Model," Sandia memorandum to V.K. Luk, May 4, 1994.

support girder. Gusset plates used for stiffeners of the ring support girder, the top head flange, and the bottom head flange were modeled with 116 four-node axisymmetric quadrilaterals. The CS consisted of 86 two-node axisymmetric shell elements. The CS geometry in these analyses was based on an early conceptual design that completely enclosed the SCV model with gap dimensions based on one-tenth scale of the gap in the actual plant.

The symmetry boundary condition of no radial displacement was imposed on the two nodes which lie on the axis of symmetry of the model as depicted in Figure 4-1. The model was constrained in the vertical direction by fixing the vertical displacement at the node on the bottom outside corner of the ring support girder, so all vertical displacement results are relative to this point. This point was chosen because the SCV model is supported on legs attached to the underside of the ring support girder. The legs themselves were assumed to be rigid and thus were not included in the finite element model.

Gusset plates were welded between the upper and lower rings of the ring support girder to provide it with significant shear and bending resistance. To include the effect of the 32 gusset plates in the axisymmetric finite element model, we modeled them as a solid ring with an orthotropic material model and a reduced Young's modulus. The ring representing the gusset plates was assumed to have no stiffness in the hoop direction. The reduced stiffness in the axial and radial directions was obtained by multiplying Young's modulus of the actual material by the ratio of the actual area of the gusset plates to the area of the solid ring in the axisymmetric finite element analysis.

Note that the CS is attached to the top ring of the ring support girder at one node. Because both the top ring of the ring support girder and the CS are modeled with shell elements, this common point has only one rotational degree-of-freedom. In other words, the rotation of this node is constrained by both the CS and the ring, which is a realistic representation. Common shell nodes also enforce similar rotational constraints where the rings of the ring support girder and all internal ring stiffeners are attached to the SCV model.

Pressure was applied to the entire interior surface of the SCV model. The CS was only loaded through contact with the SCV model and its connection to the ring support girder. Contact between the two structures was modeled with two-node, axisymmetric slide line elements superimposed on the SCV model shell elements. When contact occurs between the nodes of these elements and the elements on the CS, a stress is induced in the slide line elements in the direction of the normal. A tangential stress is also introduced if a non-zero coefficient of friction is specified.

The steel vessel was constructed of SPV490 and SGV480 steels. Because test data for the actual materials used in the model were not yet available at the time of these analyses, previously reported values from the published literature were used (Isozaki et al., 1986). The reported stress-strain behavior for these two materials was converted to true stress and true strain (Figure 4-2). The ends of the plotted curves represent behavior at the maximum load because conversion to true stress and strain is not possible beyond this point without knowing the reduction in cross-sectional area at the point of necking in the sample. The finite element code assumes perfect plasticity (no hardening) beyond the strains plotted in the figure.

In the first analysis, the CS was assumed to be nearly rigid by giving it a very high elastic stiffness and not allowing it to yield. Zero friction was assumed between the SCV wall and the CS. A second set of two analyses assumed the CS was constructed of SGV480 with the material response shown in Figure 4-2. In these analyses, the CS is referred to as "flexible" only to differentiate these analyses from the previous analysis with the "rigid" CS. For this set, both a frictionless model and a model assuming a coefficient of friction (μ) of 0.25 between the vessel wall and the CS were analyzed. Finally, in order to isolate the effects of friction on vessel behavior, a third set of simulations was run using the model with the rigid representation of the CS with coefficients of friction ranging from 0.01 to 0.5 by increments of 0.1.

The results discussed in this section of the report have been selected to demonstrate only the effects of CS rigidity and the effects of the amount of friction. More detailed results of model behavior based on later finite element models that more closely represent the final design SCV/CS are described in later sections.

4.2.2 Results

Figure 4-3 shows the finite element discretization of the top head and knuckle regions of the SCV model. The upper part of Figure 4-3 shows the part of the top head

where the cylindrical shell transitions to the spherical head. The first element above the top head flange is element number 156. The lower part of the figure shows the knuckle region. The knuckle itself consists of 10 elements numbered 130 to 139.

Results for the SCV response in the top head and knuckle regions are shown in Figure 4-4 through Figure 4-9. Figure 4-4 and Figure 4-5 show the history for the vertical displacement at the top of the SCV model. This displacement is caused by the strains in the top head itself as well as meridional membrane strains in the SCV wall from the top head flange down to the ring support girder, the point at which the vertical displacement is constrained. The latter meridional strains cause vertical rigid body motion of the top head above the flange. Figure 4-4 and Figure 4-5 show that the vertical displacement at the apex was the same for all simulations up to an internal pressure of 5.0 MPa. This is approximately the pressure at which full contact was achieved between the SCV model and the CS along the entire surface from the knuckle down to the top of the lower cylindrical shell. Above this pressure, the effects of friction and the rigidity of the CS on the top head displacement became more noticeable. Beyond an internal pressure of 11.0 MPa, the vertical displacement increased very rapidly due to extensive yielding near the center of the top head.

It is interesting to note that the displacement for the frictionless case was the lowest. In addition, all values of friction coefficient from 0.2 to 0.5 resulted in approximately the same vertical displacement, with 0.10 only slightly less. In all the analyses, the lower cylindrical shell yielded, leading to large radial expansion in this region which tends to pull down the containment wall above this section, thus decreasing the vertical displacement of the top head. However, if sufficient friction exists between the wall of the SCV model and the CS, this effect will be very localized near the lower cylindrical shell. Hence, the radial expansion in the lower cylindrical shell should have the greatest influence on the top head displacements in the case with the least amount of friction. Thus, the frictionless analysis should have the smallest vertical displacement at the apex as indicated in Figure 4-5.

Figure 4-6 and Figure 4-7 show the distribution of equivalent plastic membrane strain in the top head from the element just above the top head flange (element 156) to the element at the center of the top head (element 195) at an internal pressure of 6.0 MPa (for clarity, every other element is represented by a symbol on the plots). Neither the stiffness of the CS nor the amount of friction appeared to influence the plastic strain in the top head. Therefore, the analyses results are identical. This similarity in strains indicates that the difference in vertical displacements at the apex of the top head after contact is established between the SCV model and the CS (as shown in the previous two figures) is due to differences in vertical rigid body motion of the top head flange caused by meridional strain below the flange; it is not due to differences in strain in the top head itself. It further indicates that the thick top head flange serves as a constraint against radial motion that is not affected by the presence of a CS.

Figure 4-8 and Figure 4-9 show the response in the knuckle region of the SCV model for various coefficients of friction. The knuckle region consists of elements 128 to 149, while the knuckle itself includes elements 130 to 139. Locations of element numbers indicated on the plots are depicted in Figure 4-3.

The effects of friction on the hoop strain are shown in Figure 4-8 and the effects on meridional strain in Figure 4-9, both for 6.0 MPa internal pressure. These results show that the only major difference was in the hoop strain. The hoop strain decreased as the coefficient of friction was increased. In particular, the results for the frictionless analysis showed significantly higher hoop strains than any of the analyses with non-zero friction in the knuckle region.

Figure 4-10 shows the finite element discretization in the upper and lower conical sections, as well as the location of the thickness changes and the material transition. Even though the equipment hatch could not be included in these axisymmetric analyses, its location is indicated because the global axisymmetric response is important in this region.

Figure 4-11 through Figure 4-16 show some selected analysis results in the upper and lower conical sections. The upper conical section contains elements 74 through 109, and the lower conical section consists of elements 34 to 73. For clarity, only every other element is represented by a symbol. Locations for all these elements are shown in the schematic in Figure 4-10.

The effects of friction on the hoop and meridional strain components in the upper conical section are shown in Figure 4-11 and Figure 4-12, respectively, at

an internal pressure of 6.0 MPa. The only notable difference shows in Figure 4-11, where the hoop strain for the frictionless case is higher than any of the cases that included non-zero friction. However, the value of the coefficient of friction between 0.1 and 0.5 appears to make little difference.

Results for the lower conical section are shown in Figure 4-13 and Figure 4-14. The effects of friction in this section of the model are basically the same as in the upper conical section. The major effect of friction appears in the hoop strain component, with the case of frictionless contact exhibiting a higher hoop strain than any of the non-zero friction analyses.

Figure 4-15 and Figure 4-16 show the vertical displacements at the elevation on the axisymmetric model corresponding to the top of the equipment hatch. The effects of friction were much more dramatic in this area. In fact, the presence of friction actually reversed the direction of the final vertical displacement at the top of the equipment hatch. This dramatic difference between a frictionless and a non-zero friction contact for internal pressures higher than 5.0 MPa was mainly due to deformations occurring in the lower cylindrical shell at these pressures. The lower cylindrical shell experienced large radial expansion at pressures beyond 5.0 MPa which, in the case of no friction, caused the vertical displacement of the equipment hatch to reverse direction and become negative when the pressure exceeded about 6.3 MPa. However, in the case of non-zero friction above a value of 0.2, the contact between the SCV model and the CS provided constraint against this tangential downward motion. In the presence of friction, the equipment hatch moved upward following the general conical shell deformation of the CS. Increasing the coefficient of friction above 0.2 had little effect on the vertical displacement at the elevation corresponding to the top of the equipment hatch.

Figure 4-17 shows the finite element discretization of the lower cylindrical shell area of the SCV model. The upper mesh shows the elements in the area where the SCV model transitions from the lower cylindrical shell to the lower conical wall section. The lower mesh shows the transition from the very thick spherical bottom head to the lower cylindrical shell. Element number 200 is the last element of the bottom head and element number 1 is the first element of the SCV model in lower cylindrical shell. Element 264 is the first element of the CS where it attaches to the exterior ring support girder.

Figure 4-18 and Figure 4-19 show results for the response in the lower cylindrical shell of the model. As in the upper and lower conical regions, the effects of friction are visible only at an internal pressure higher than 5.0 MPa. The major effect occurs in the hoop strain component and is significantly different only for the case of a completely frictionless contact.

4.2.3 Effect of Friction on the Uplift Force

The amount of uplift that the CS imparts to the outer ring support girder can be estimated from the meridional stress in the CS at a point immediately above the support. Multiplying the meridional membrane stress by the cross-sectional area of the CS element just above the support girder (element 264 in Figure 4-17) gives the total uplift load. Figure 4-20 shows the uplift force for the two flexible structures (the force in the "rigid" structure is meaningless). Note that this is the total force exerted on the entire circumference of the ring. The results indicate that the effect of friction is to reduce the uplift force on the ring support girder.

4.2.4 Conclusions from Friction Analyses

Comparison of the results of these analyses demonstrated obvious differences between the models with no friction and those with some friction. However, the actual value of friction coefficient between 0.1 and 0.5 made little difference. Because the surfaces in the actual SCV model and CS are not lubricated, some friction can be assumed to be present. Therefore, all subsequent pretest prediction analyses described in Section 5, Section 6, and Section 7 were run using a coefficient of friction of 0.2.

4.3 Material Models

One of the most important components of any finite element analysis is the model of material behavior. The material model consists of two parts: the material data and the constitutive model. This section describes the methods used to ensure the best possible material modeling with the test data provided.

Material data in the form of results from tensile test specimens of the actual materials used in the SCV model construction were provided by Hitachi[11,12] and are included in Appendix B. These data consist of measured load vs. elongation over a specified gage length up to the point of necking in the specimen. Over this range, load can be converted to engineering and true stress, and elongation can be converted to engineering and true strain by the use of simple analytical equations. However, the tensile tests represent only a simple unidirectional loading, while the SCV model is a complicated, three-dimensional object that will experience a multi-directional stress field under internal pressure and contact. Therefore, local true stresses experienced in the model may well be above those at maximum load of a tensile test specimen, and the data must be extrapolated by a rational method.

Furthermore, a constitutive model that best represents the entire range of extrapolated test data must be selected. Mild steels such as those that compose the SCV model are commonly represented by elastic-plastic materials with isotropic hardening. However, the form of the hardening curve is extremely important when attempting to model a structure far into the plastic region. In particular, the correct form for the hardening curve is essential for failure prediction (Wellman and Salzbrenner, 1992). It must be noted that these material models do not directly address failure. Failure must be treated in a post-processing step separate from the finite element analysis.

The true stress-true strain data from the uniaxial tests were used to fit a theoretical hardening curve such as a power law or inverse hyperbolic sine law[13]. In addition to capturing the measured behavior up to maximum load, prediction of the behavior of the SCV up to failure requires reasonable extrapolations of the true stress-true strain data beyond maximum load. The tensile tests were simulated using a finite element model to verify the behavior after maximum load. This section describes the procedure used to fit the material models to the tensile test data and to obtain reasonable extrapolations beyond maximum load.

4.3.1 Conversion of Test Data to True Stress and True Strain

In a tensile test, the engineering strain, e, is written in Equation 4.1:

$$e = \frac{l - l_o}{l_o} \tag{4.1}$$

where l_o represents the initial gage length of the test specimen and l represents the current gage length of the test specimen. The engineering stress, s, is calculated directly from the load using Equation 4.2:

$$s = \frac{F}{A_o} \tag{4.2}$$

where F is the axial load on the tensile test specimen and A_o is the original cross-sectional area. The true strain, ε, is defined as

$$\varepsilon = \ln \frac{l}{l_o} \tag{4.3}$$

which is valid only for a homogeneous deformation over the gage length, and the true stress, σ, is defined as

$$\sigma = \frac{F}{A} \tag{4.4}$$

where A is the instantaneous cross-sectional area. By rearranging Equation 4.1 and combining with Equation 4.3, the true strain may be written in terms of the engineering strain:

$$\varepsilon = \ln(l + e) \tag{4.5}$$

By using the constant volume relationship, $A_o L_o = AL$, and combining Equation 4.2 and Equation 4.4, the true stress may be written in terms of the engineering stress:

$$\sigma = s(l + e) \tag{4.6}$$

Equation 4.5 and Equation 4.6 assume that the volume is constant, the stress is uniform through the cross-section, and the deformation is homogeneous throughout the gage length. However, at the point of maximum load in the tensile test, the deformation localizes, necking occurs, and the assumption of homogeneous deformation throughout the gage length

[11] 14th Task Group Meeting Notes, CTG-14-04, November 16, 1994.
[12] Fax from Hitachi, December 20, 1994.
[13] Carter, P.A., "Extrapolation of Hitachi Tensile Test Data," Sandia memorandum to V.K. Luk, June 6, 1995.

is violated. In addition, the stress distribution is no longer uniform through the cross-section. So, Equation 4.5 and Equation 4.6 are not valid beyond maximum load. Although the engineering stress decreases after necking because less load can be carried across the reduced cross-section, the true stress continues to increase (Dieter, 1986).

4.3.2 Procedure for Extrapolation of Test Data

The following procedure was used to obtain the necessary data. First, two different hardening plasticity models were fit to the experimental true stress-true strain data, which were available only up to maximum load, using a MATLAB (1992) curve fitting routine. These two models were chosen for their ability to accurately capture the hardening behavior of most steels. The first model is the power law hardening model shown in Equation 4.7 (Stone, 1997):

$$\sigma_e - \sigma_{ys} = A\left\langle \bar{\varepsilon}^p - \varepsilon_L \right\rangle^n \tag{4.7}$$

where A and n are the constants calculated from the curve fit, σ_e is the effective stress, σ_{ys} is the yield stress, $\bar{\varepsilon}^p$ is the equivalent plastic strain, and ε_L is the Luder's strain or yield plateau. The use of the brackets, $\langle\ \rangle$, denotes the Heaviside function where the expression enclosed in the brackets takes the value of the enclosed expression when positive and otherwise is zero. The second model uses the inverse hyperbolic sine function and is shown in Equation 4.8:

$$\sigma_e - \sigma_{ys} = A\sinh^{-1}\left(B\left\langle \bar{\varepsilon}^p - \varepsilon_L \right\rangle\right) \tag{4.8}$$

where A and B are the constants calculated from the curve fit.

After determining which of the two hardening models provided the best fit to the data from each set of tensile tests, each set of tensile tests was simulated using the appropriate constitutive relation in the SANTOS finite element program (Stone, 1997). Figure 4-21 shows the axisymmetric finite element model used. Only the top half of the length of the round bar was modeled because it is symmetric about the plane normal to the axis of the specimen at the center of the gage length. To ensure that the localized deformation occurs at the center of the gage length, the diameter was reduced by 0.5–1.0% at the plane of symmetry at the bottom boundary to provide an initial geometric imperfection. The specimen is restrained in the y-direction at the plane of symmetry, and displacements were imposed in the y-direction at the free end.

As shown in Equation 4.1, the engineering strain is obtained by dividing the change in the gage length or displacement by the original gage length. The load on the specimen can be converted to engineering stress by dividing by the original cross-sectional area as in Equation 4.2. The load-displacement data from the finite element analysis of the tensile test specimen were converted to engineering stress-strain data and compared to the engineering stress-strain data supplied by Hitachi in an attempt to verify the post-peak behavior. If the data from the finite element analysis did not correlate well with the Hitachi data, a new curve fit was tried and a new finite element analysis performed. This iterative process was repeated until reasonable post-peak behavior was obtained.

Hitachi performed a set of four tensile tests for each of the 11 different material/thickness combinations (two in the rolling direction and two in the transverse direction) for a total of 48 tests (one batch of tests was repeated). Table 4-1 summarizes the results of the curve fitting for the different SGV480 thicknesses; Table 4-2 summarizes the results of the curve fitting for the SPV490 thicknesses. For the SGV480 materials, the inverse hyperbolic sine law model worked best, while the power law worked best for the SPV490 materials.

Figures 4-22 through 4-32 consist of two plots each. The upper plot shows the true stress-true strain tensile test data sets along with the selected curve fit for each thickness of each material in the SCV model. The bottom plot in each figure shows the corresponding engineering stress-engineering strain data with the output of the finite element analysis of the tensile test. In other words, the top curves represent the fit of the constitutive model to the test data, and the bottom curves show the quality of the extrapolation of the test data beyond maximum load. The curves representing the finite element analyses using the theoretical constitutive models continue indefinitely because these models do not address failure. Failure must be assessed as a separate post-processing step after the finite element analysis of the SCV model is performed.

Table 4-1. Summary of Material Parameters – SGV480

Batch Designation	Location	Material	Thick-ness (mm)	σ_{ys}, Yield Strength (MPa)	A, Hardening Constant, (MPa)	B, Strain Constant	ε_L, Luder's Strain
RT12/ RT34	Top Head, Top Head Shell	SGV480	6.0	404.9	153.7	15.36	0.01
RT56	Upper Conical Shell	SGV480	7.5	404.2	147.5	15.36	0.01
RT78	Upper Spherical Shell	SGV480	8.0	386.5	148.0	16.70	0.01
RT910	Middle Conical Shell	SGV480	8.5	399.8	145.0	17.03	0.01
RT1112	Stiffening Ring	SGV480	9.5	409.6	139.2	17.71	0.01
RT1314	Stiffening Ring	SGV480	12.5	383.6	142.1	18.25	0.01
RT1516	Stiffening Rings (2)	SGV480	19.0	378.7	126.0	23.83	0.01
RT1718	Top Flange, Hatch Covers (2), Hatch Sleeve	SGV480	20.0	379.8	122.0	25.43	0.02
RT1920	Knuckle	SGV480	28.0	371.6	110.9	33.20	0.01

Table 4-2. Summary of Material Parameters – SPV490

Batch Designation	Location	Material	Thickness (mm)	σ_{ys}, Yield Strength (MPa)	A, Hardening Constant, (MPa)	n, Strain Exponent	ε_L, Luder's Strain
RT2122	Lower cylindri-cal shell, Lower Conical Shell	SPV490	9.0	660.0	390.0	0.45	0.015
RT2324	Bottom Flange, Bottom Head, Stiffening Ring, Ring Support Girder, Gusset Plates	SPV490	17.5	598.9	450.0	0.48	0.01

4.3.3 Implementation into ABAQUS

ABAQUS requires two options to specify an elastic-plastic material model: *ELASTIC, where the user specifies the elastic modulus and Poisson's ratio; and *PLASTIC, which specifies a metal plasticity model with a von Mises or Hill yield surface. For this option, the user must specify the yield stress as a function of plastic strain, as a series of data pairs, each consisting of a true stress and corresponding log plastic strain value. The stress-strain curves generated by the material parameters given in Table 4-1 and Table 4-2 were converted to series of true stress-plastic strain data pairs for input into ABAQUS.

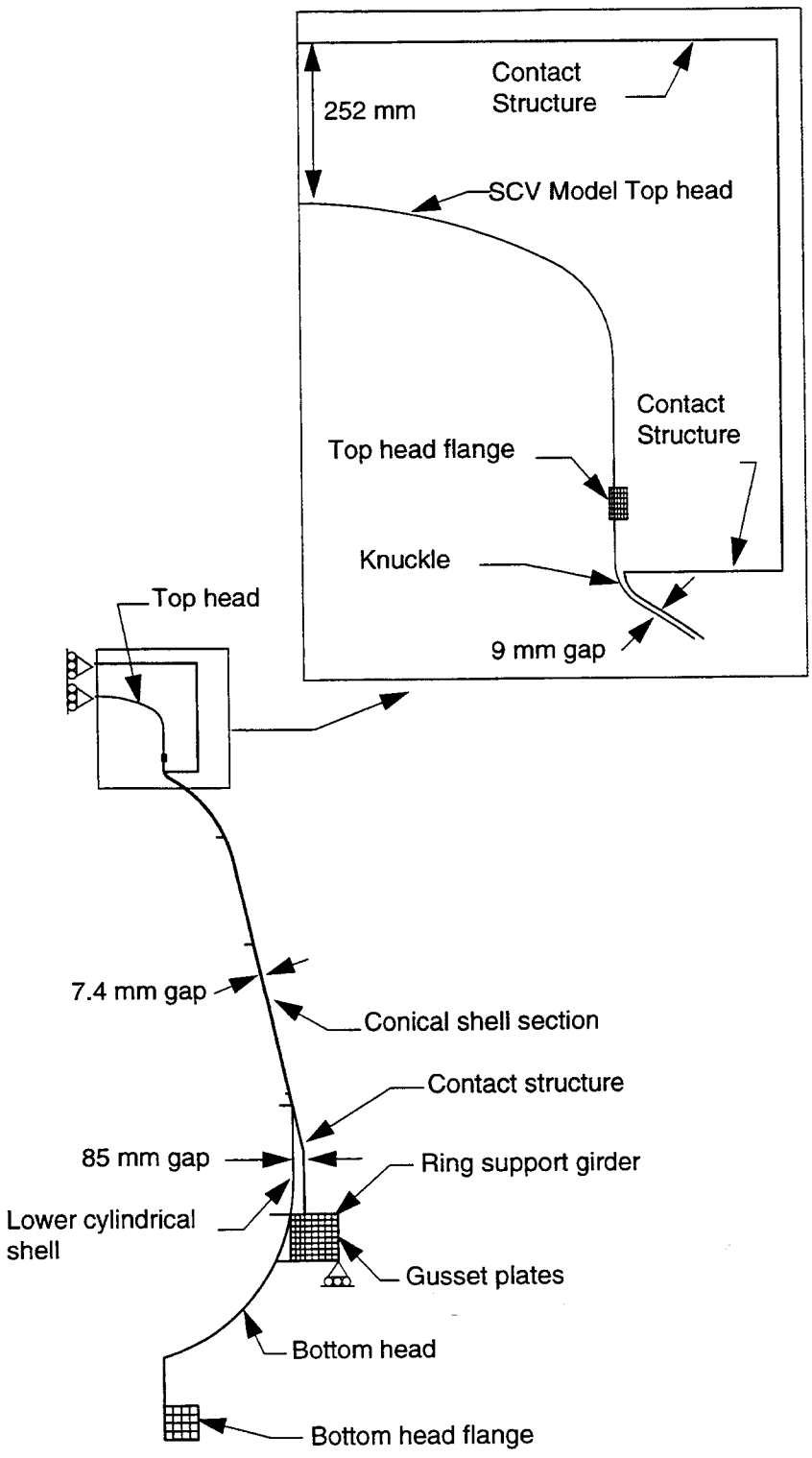

Figure 4-1. Axisymmetric finite element model of SCV with contact structure at a one-tenth scaled gap from undeformed SCV.

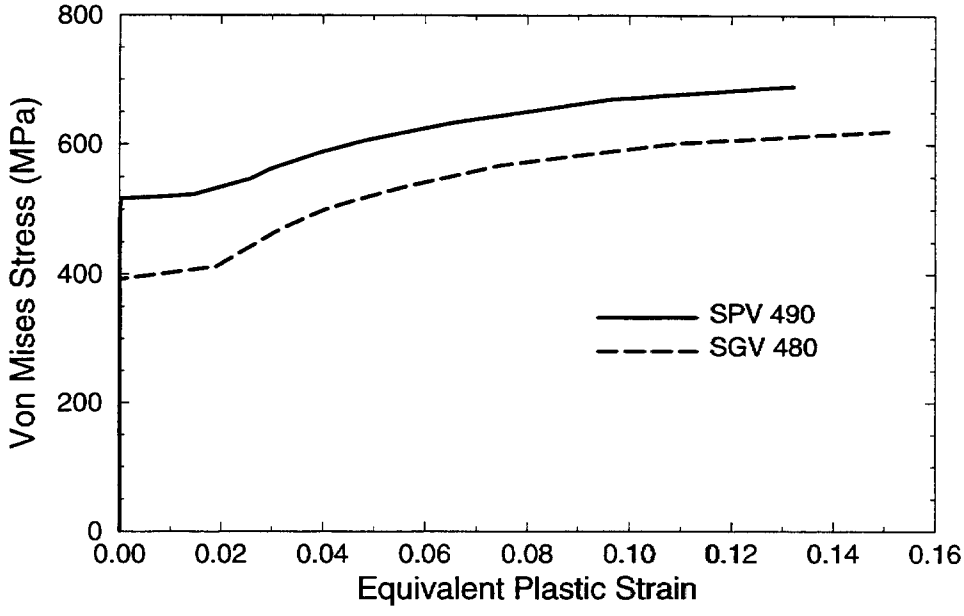

Figure 4-2. True stress — true strain response of SGV480 and SPV490 (Isozaki et al., 1986).

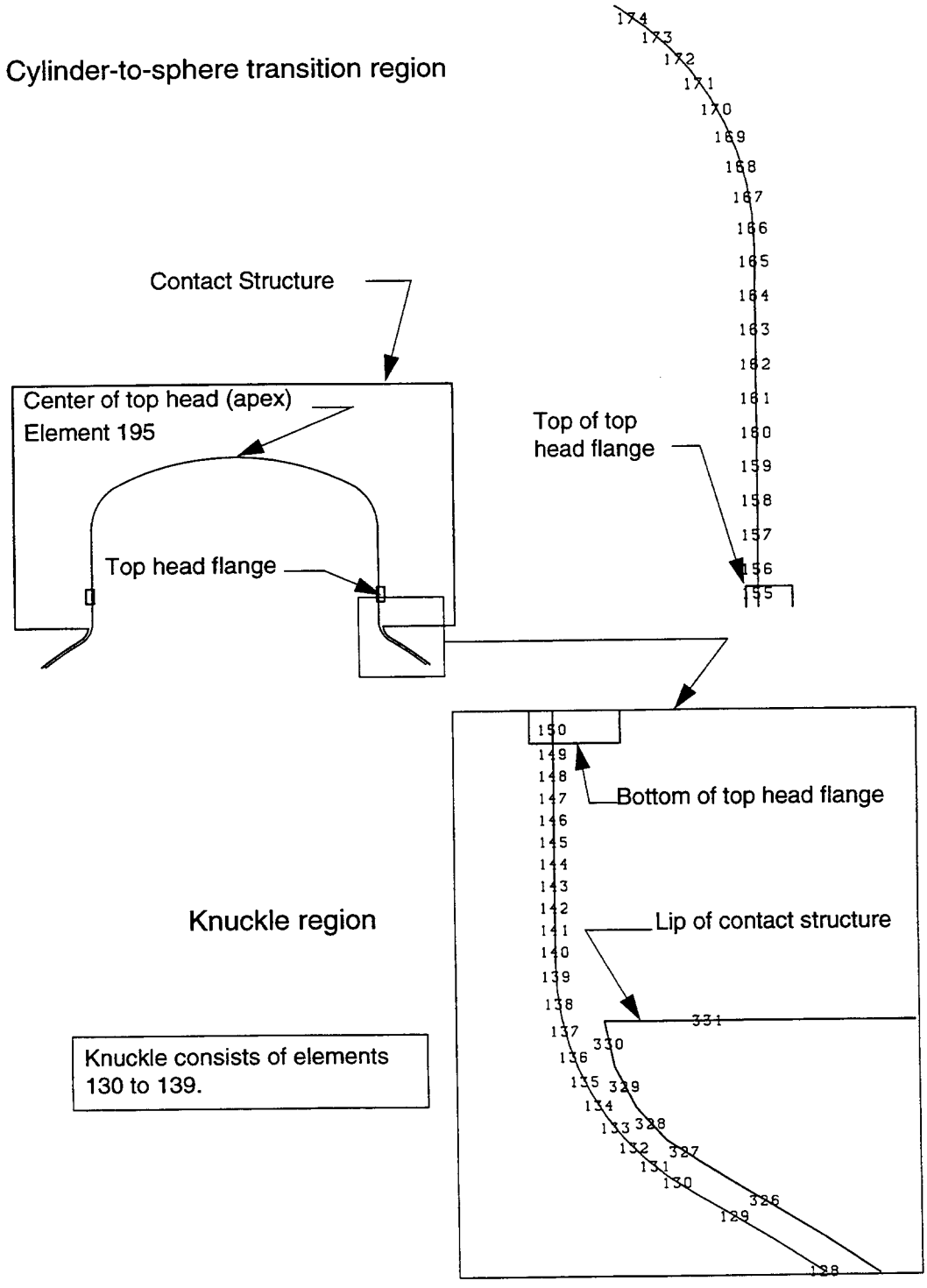

Figure 4-3. Preliminary axisymmetric finite element discretization of top head and knuckle region.

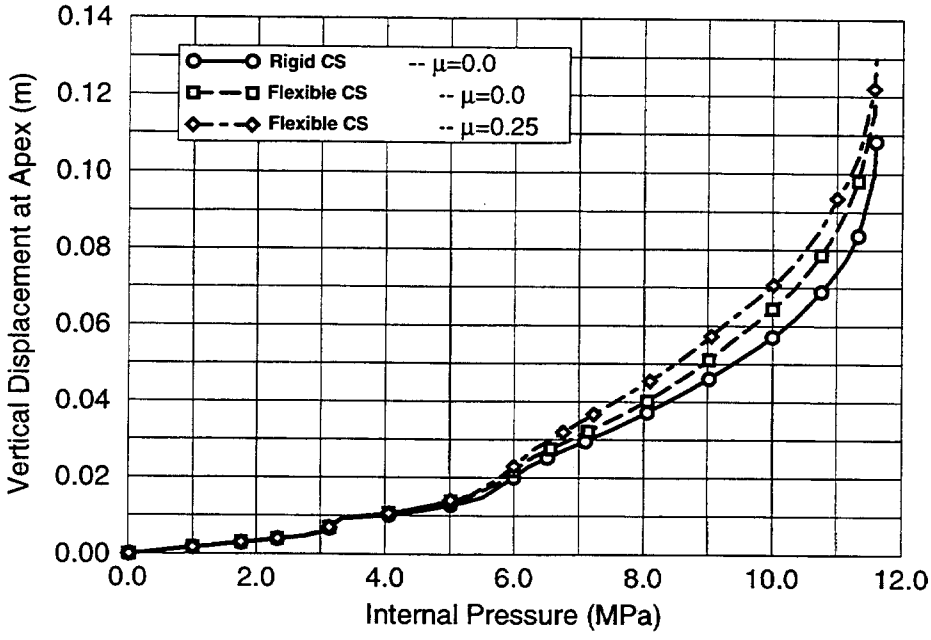

Figure 4-4. Vertical displacements at apex of top head (see Figure 4-3 for key to location).

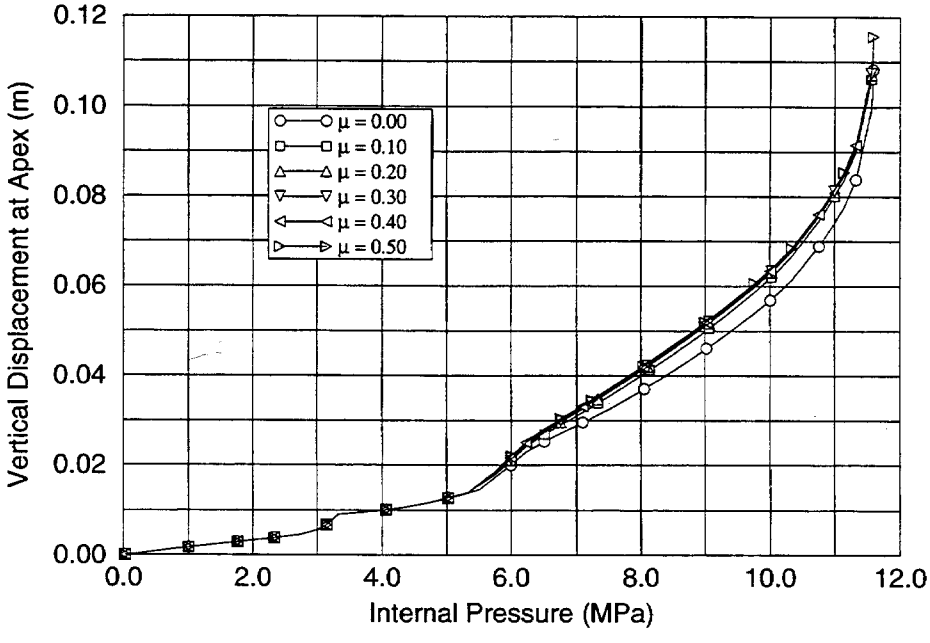

Figure 4-5. Vertical displacement at apex of SCV model for various amounts of friction (see Figure 4-3 for key to location).

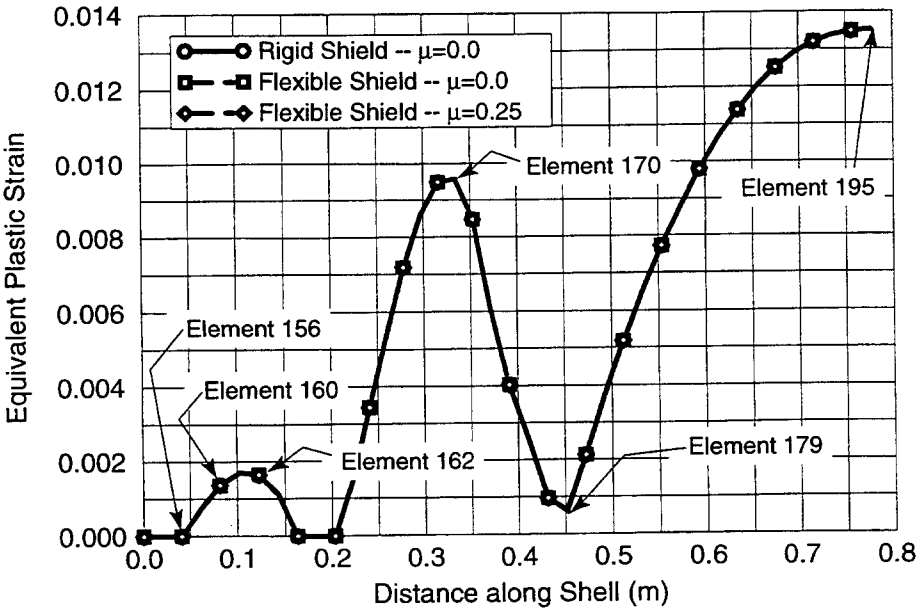

Figure 4-6. Equivalent plastic strain in top head above the flange at an internal pressure of 6.0 MPa. Element locations shown in Figure 4-3.

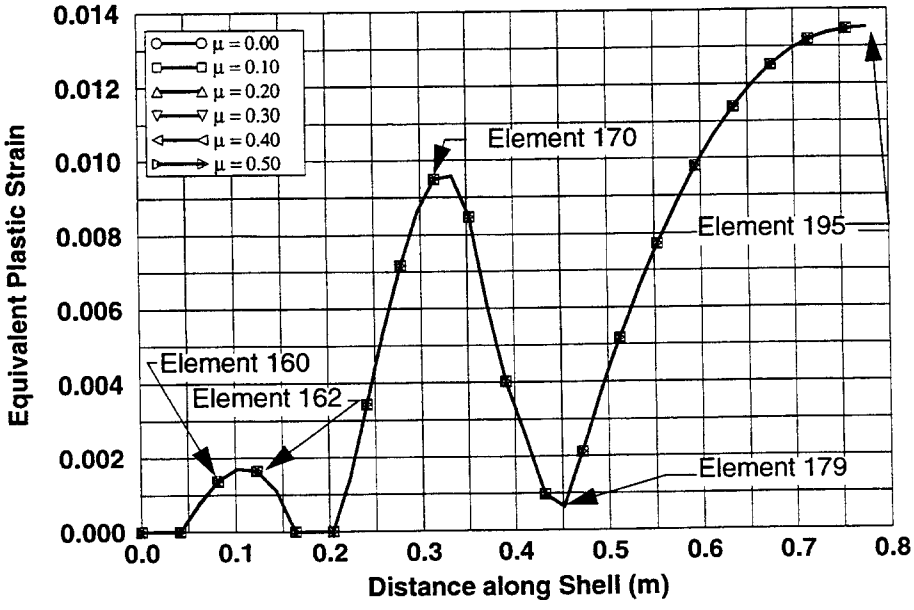

Figure 4-7. Effect of friction on plastic strain in top head at an internal pressure of 6.0 MPa. Element locations shown in Figure 4-3.

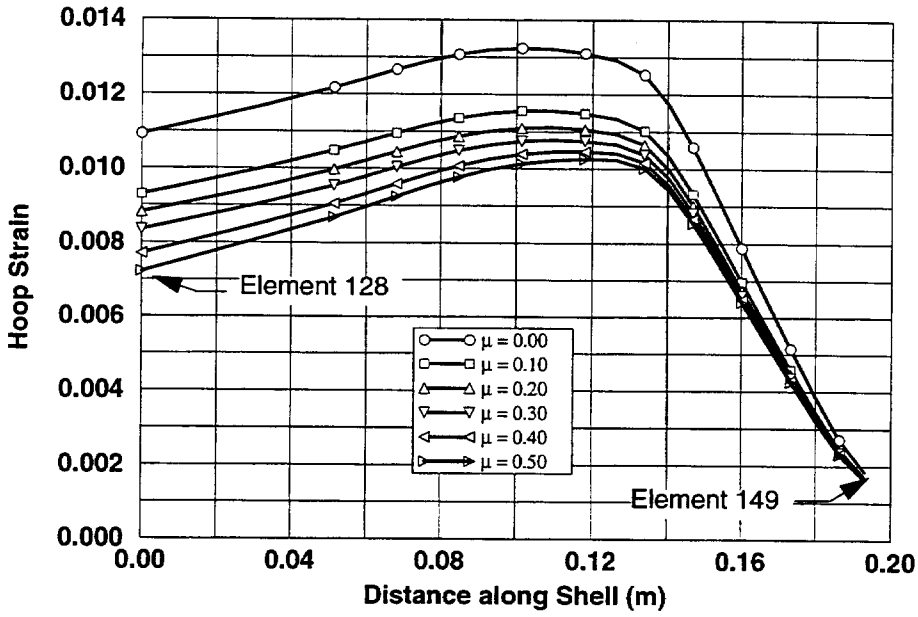

Figure 4-8. Effect of friction on hoop strain in the knuckle region at an internal pressure of 6.0 MPa. Element locations shown in Figure 4-3.

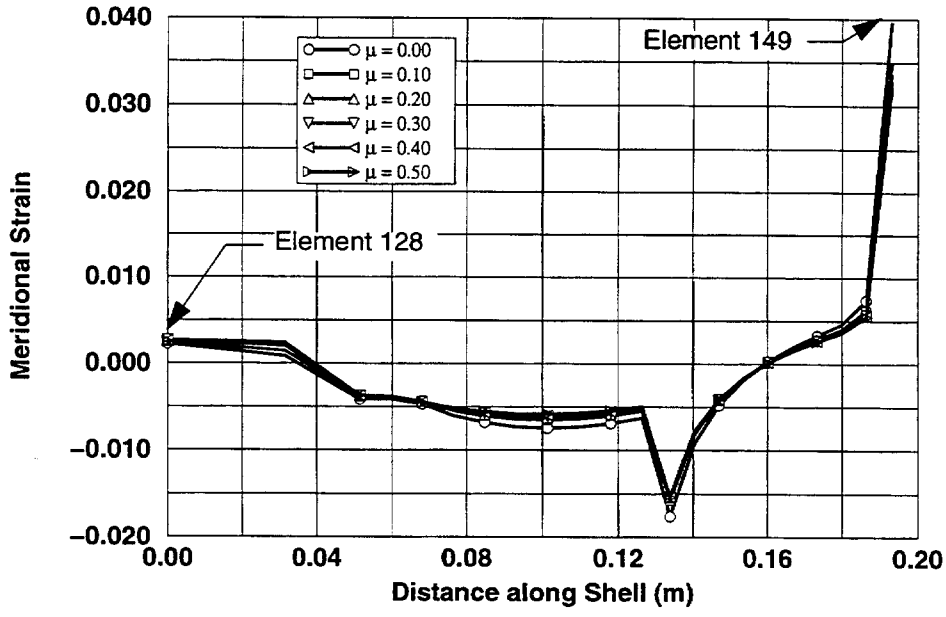

Figure 4-9. Effect of friction on meridional bending strain in the knuckle region at an internal pressure of 6.0 MPa. Element locations shown in Figure 4-3.

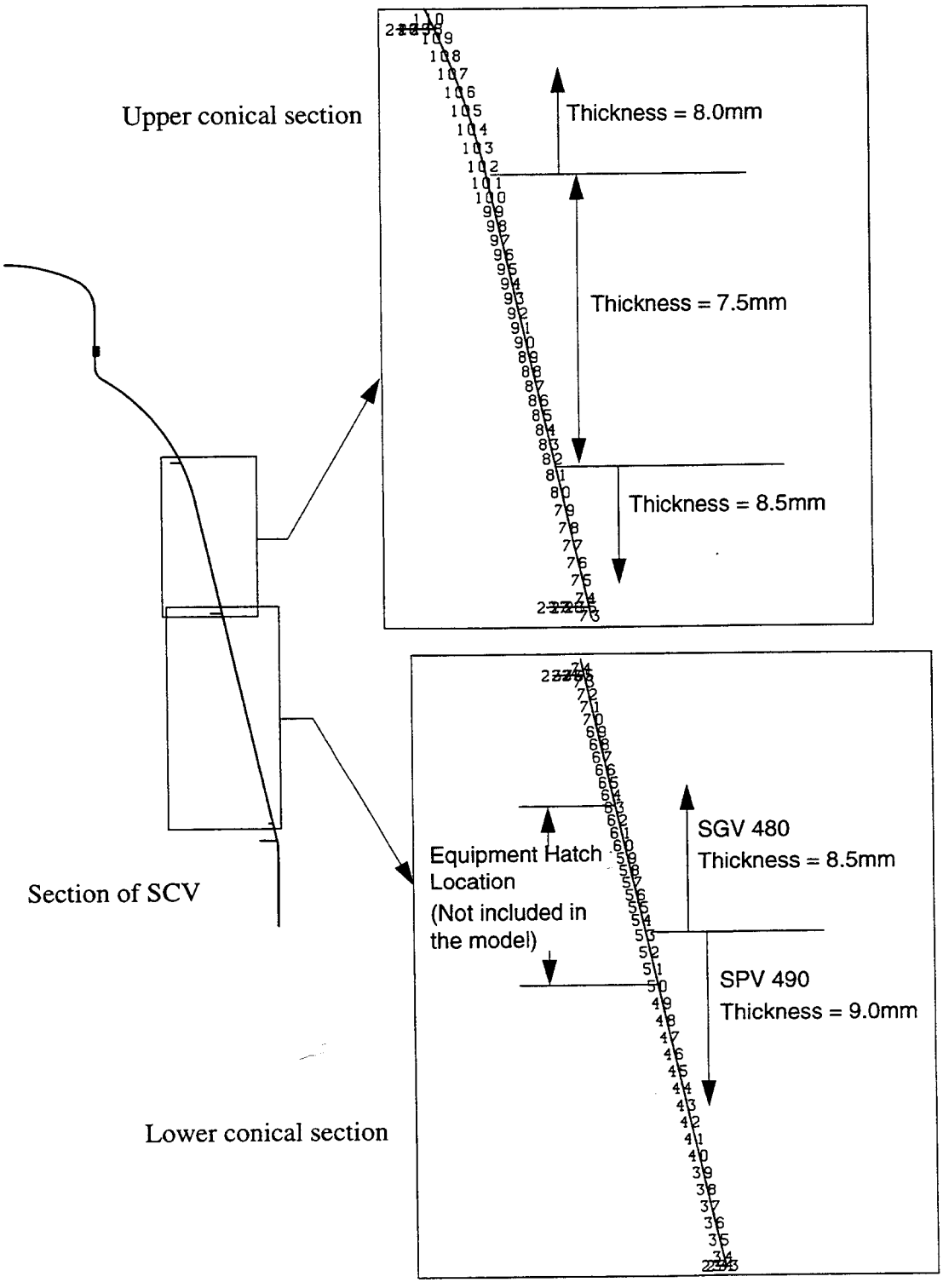

Figure 4-10. Preliminary axisymmetric finite element mesh of conical section (contact structure not shown).

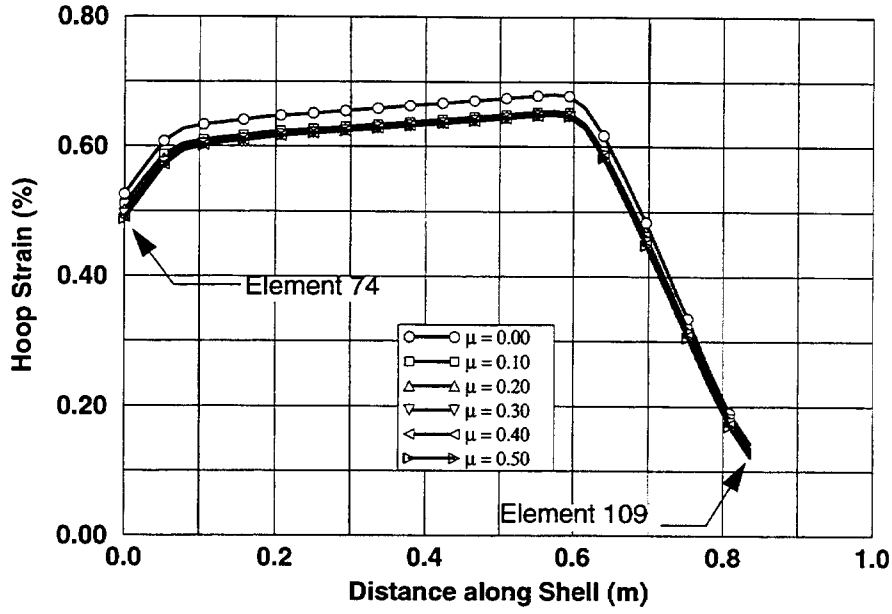

Figure 4-11. Effect of friction on hoop strain in the upper conical section at an internal pressure of 6.0 MPa. Element locations shown in Figure 4-10.

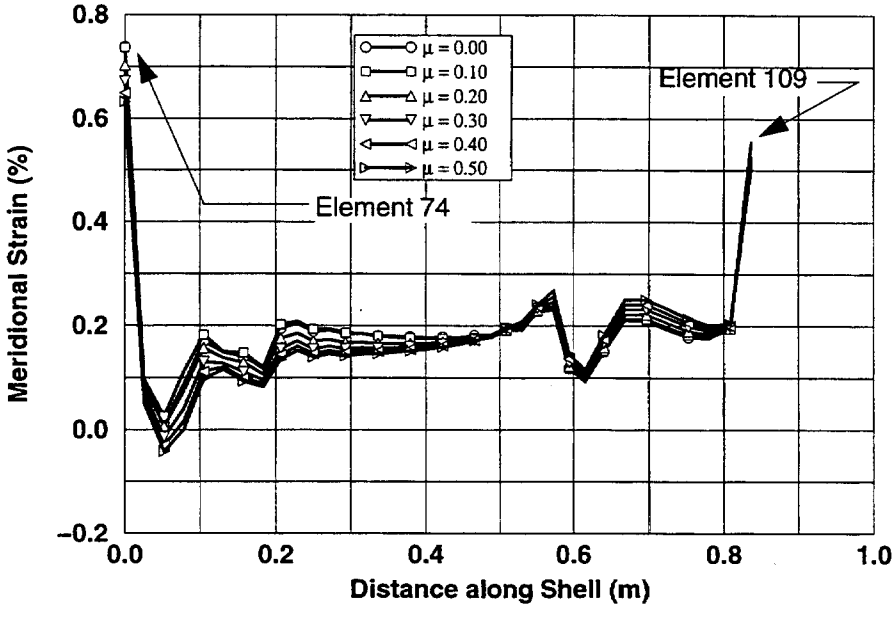

Figure 4-12. Effect of friction on meridional strain in the upper conical section at an internal pressure of 6.0 MPa. Element locations shown in Figure 4-10.

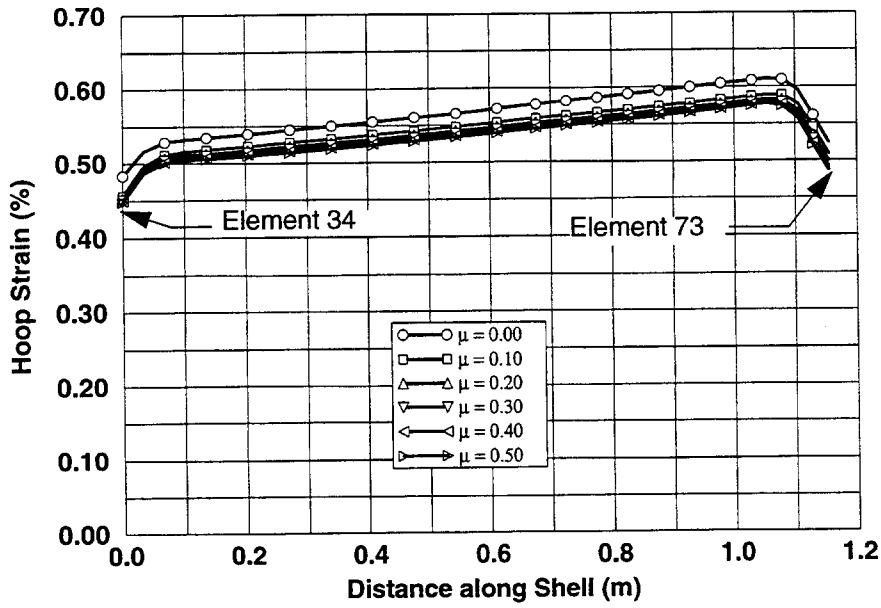

Figure 4-13. Effect of friction on hoop strain in the lower conical section at an internal pressure of 6.0 MPa. Element locations shown in Figure 4-10.

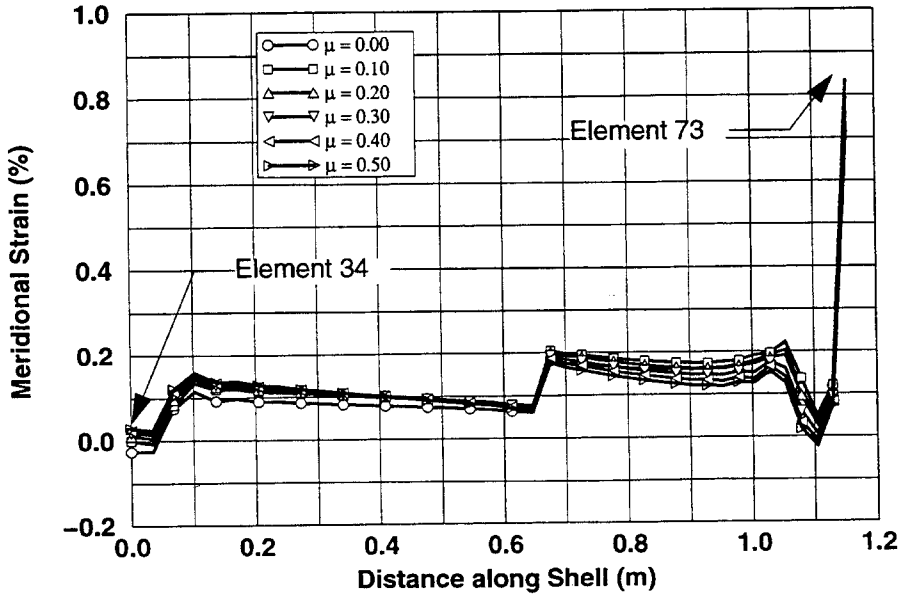

Figure 4-14. Effect of friction on the meridional bending strain in the lower conical section at an internal pressure of 6.0 MPa. Element locations shown in Figure 4-10.

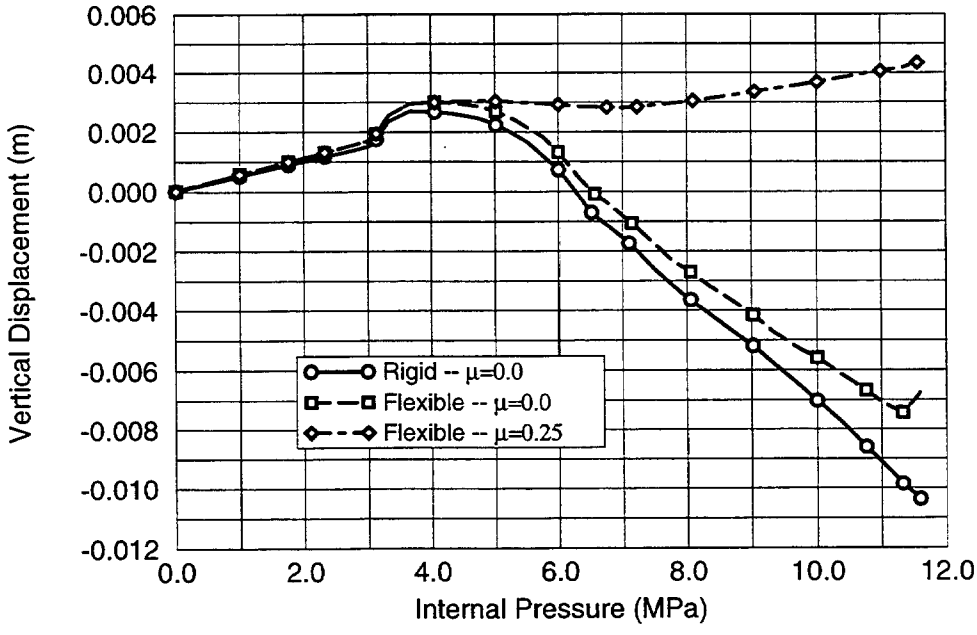

Figure 4-15. Displacement of elevation corresponding to the top of the equipment hatch. Equipment hatch location shown in Figure 4-10.

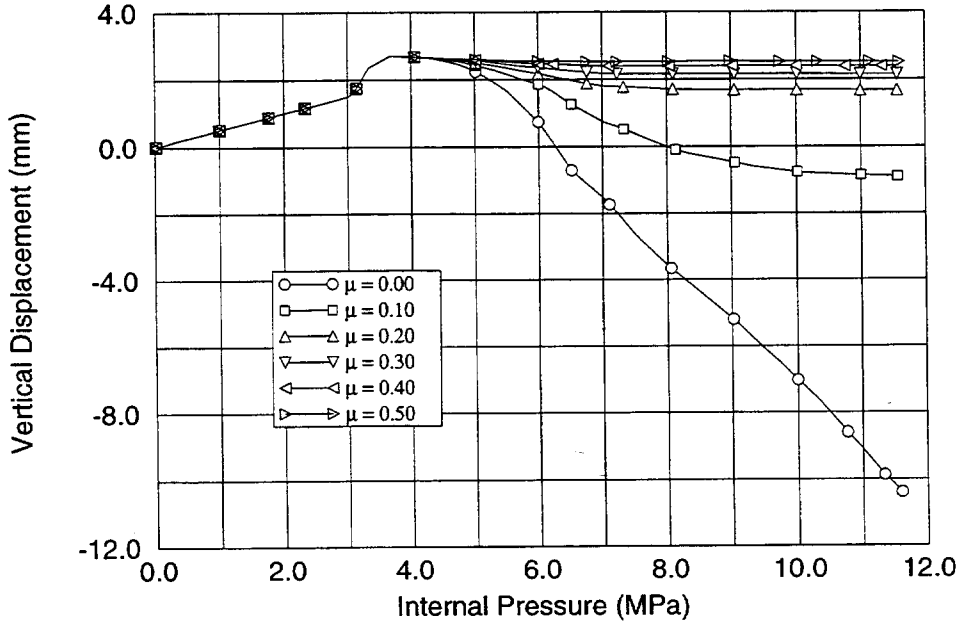

Figure 4-16. Vertical displacement at the elevation corresponding to the top of the equipment hatch for various values of friction. Equipment hatch location shown in Figure 4-10.

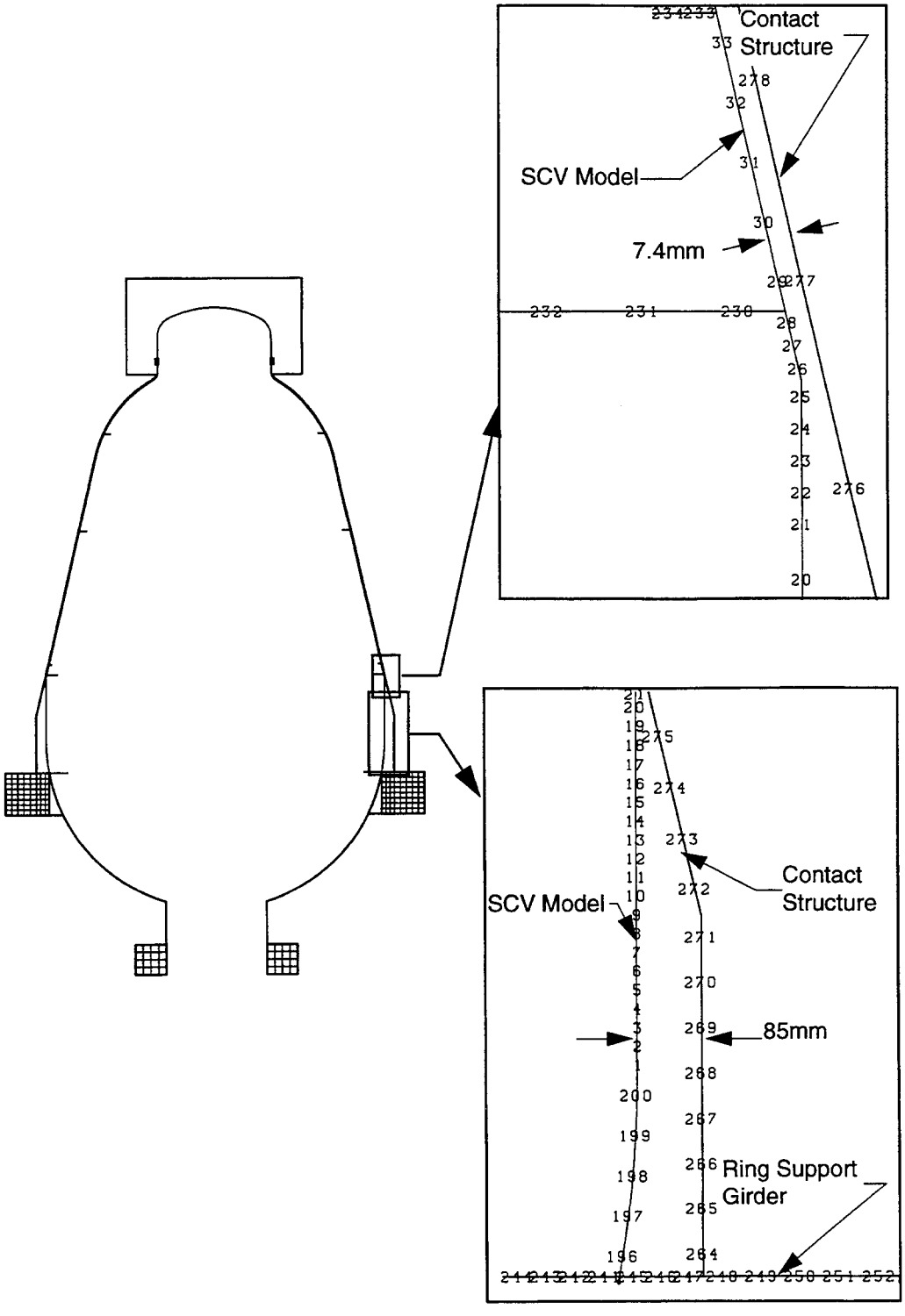

Figure 4-17. Preliminary axisymmetric finite element discretization of lower cylindrical section.

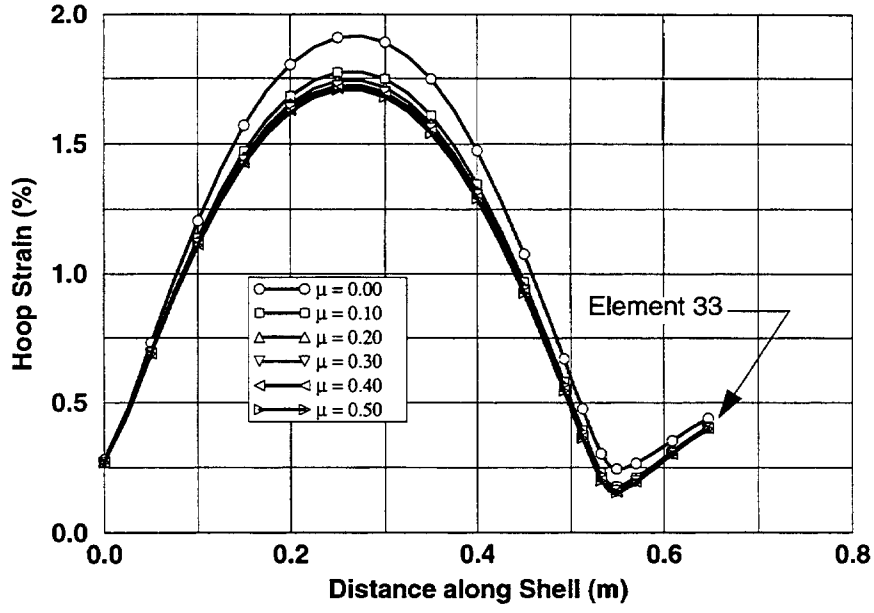

Figure 4-18. Effect of friction on hoop strain in the lower cylindrical shell at an internal pressure of 6.0 MPa. Element locations shown in Figure 4-17.

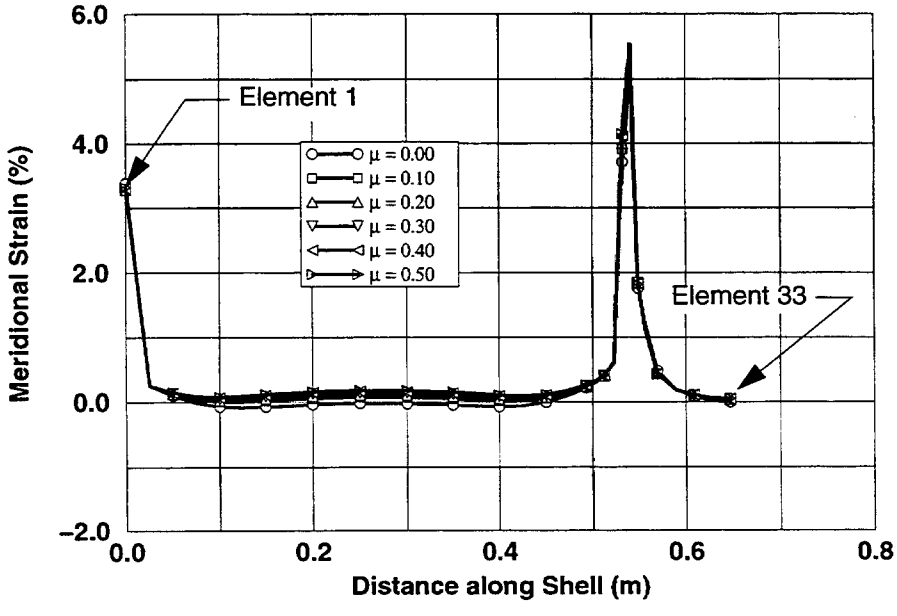

Figure 4-19. Effect of friction on meridional bending strain in the lower cylindrical shell at an internal pressure of 6.0 MPa. Element locations shown in Figure 4-17.

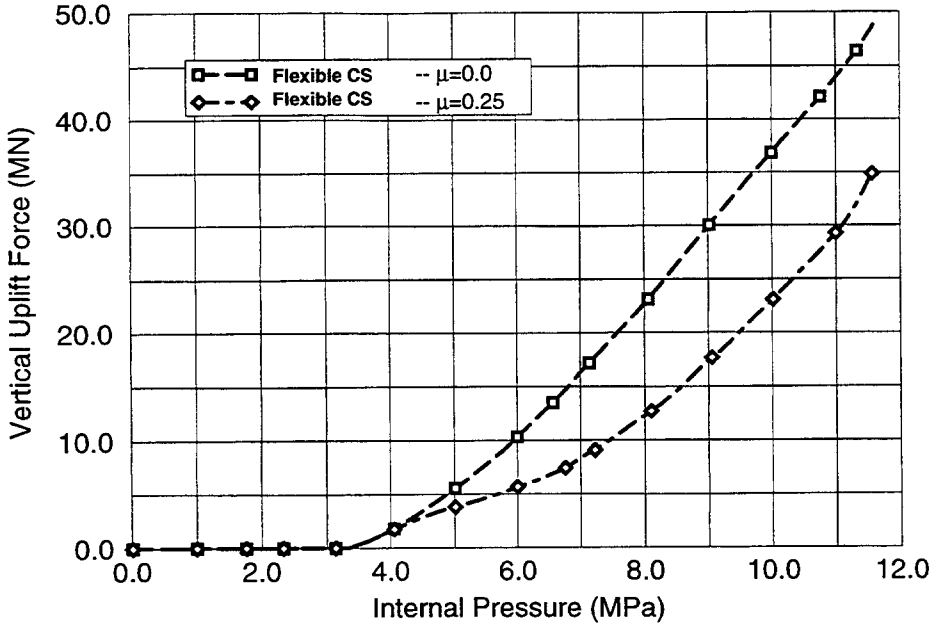

Figure 4-20. Uplift force on the ring support girder from the contact structure (from meridional stress in element 264). Element locations shown in Figure 4-17.

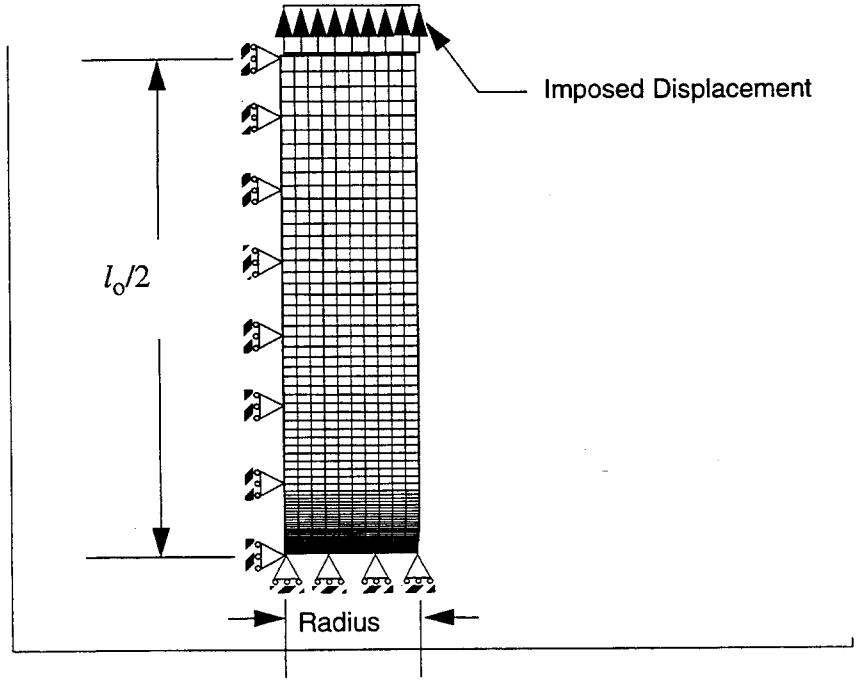

Figure 4-21. Axisymmetric finite element model of typical tensile test specimen.

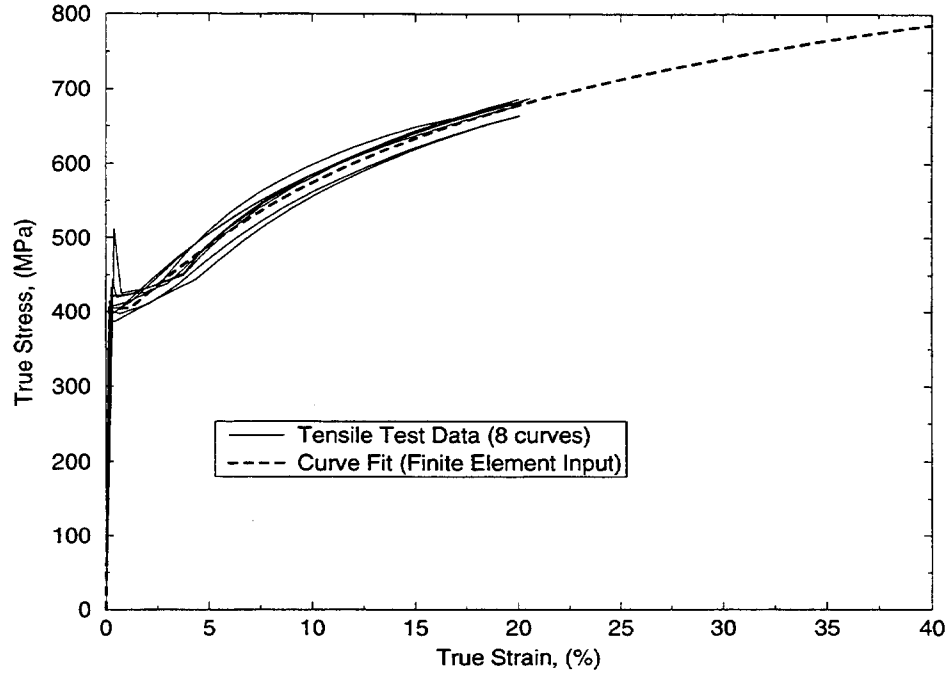

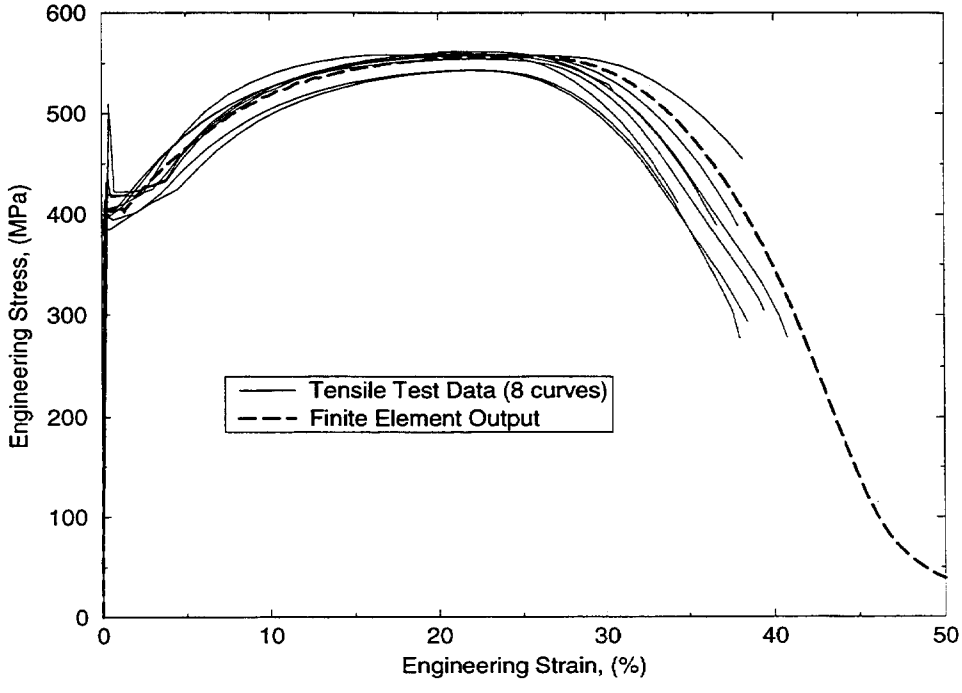

Figure 4-22. Material - SGV480; Thickness - 6.0 mm; Location - Top Head, Top Head Shell. Top: True Stress and Strain. Bottom: Engineering Stress and Strain.

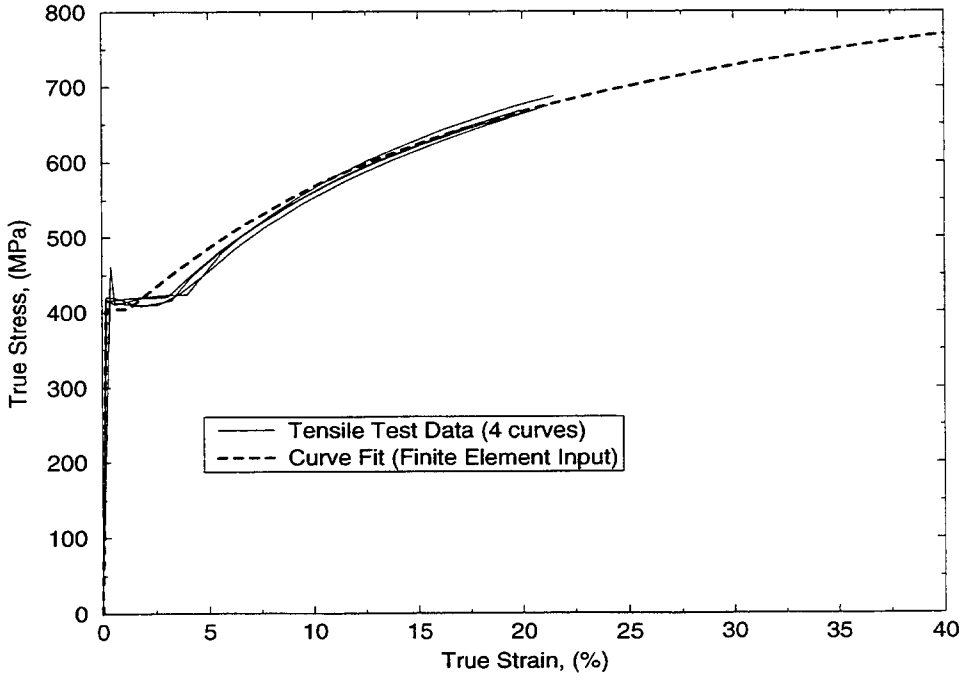

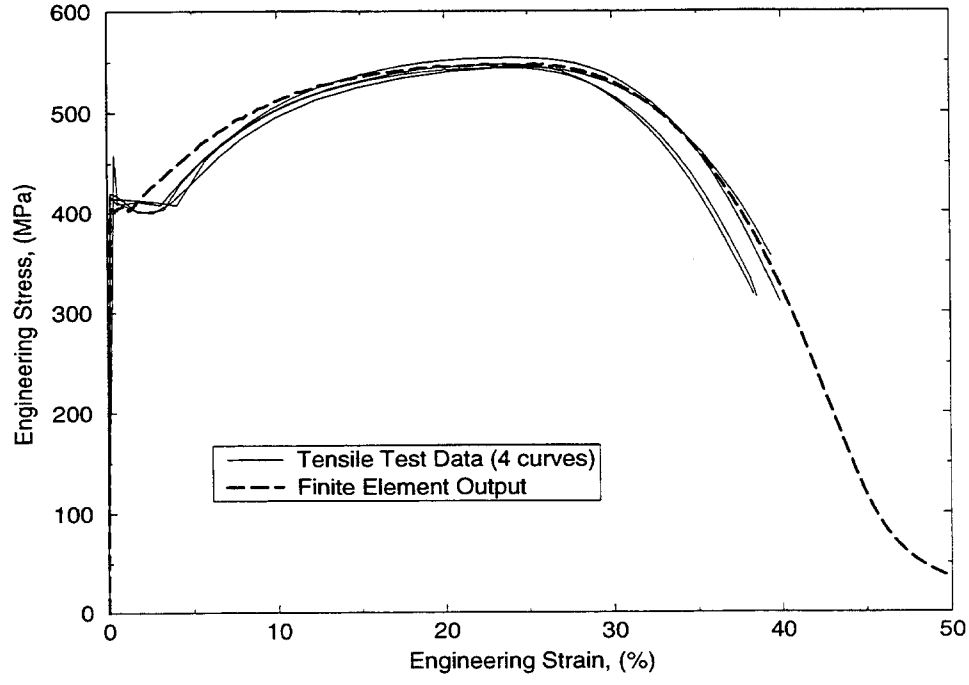

Figure 4-23. Material - SGV480; Thickness - 7.5 mm; Location - Upper Conical Shell. Top: True stress and strain. Bottom: Engineering stress and strain.

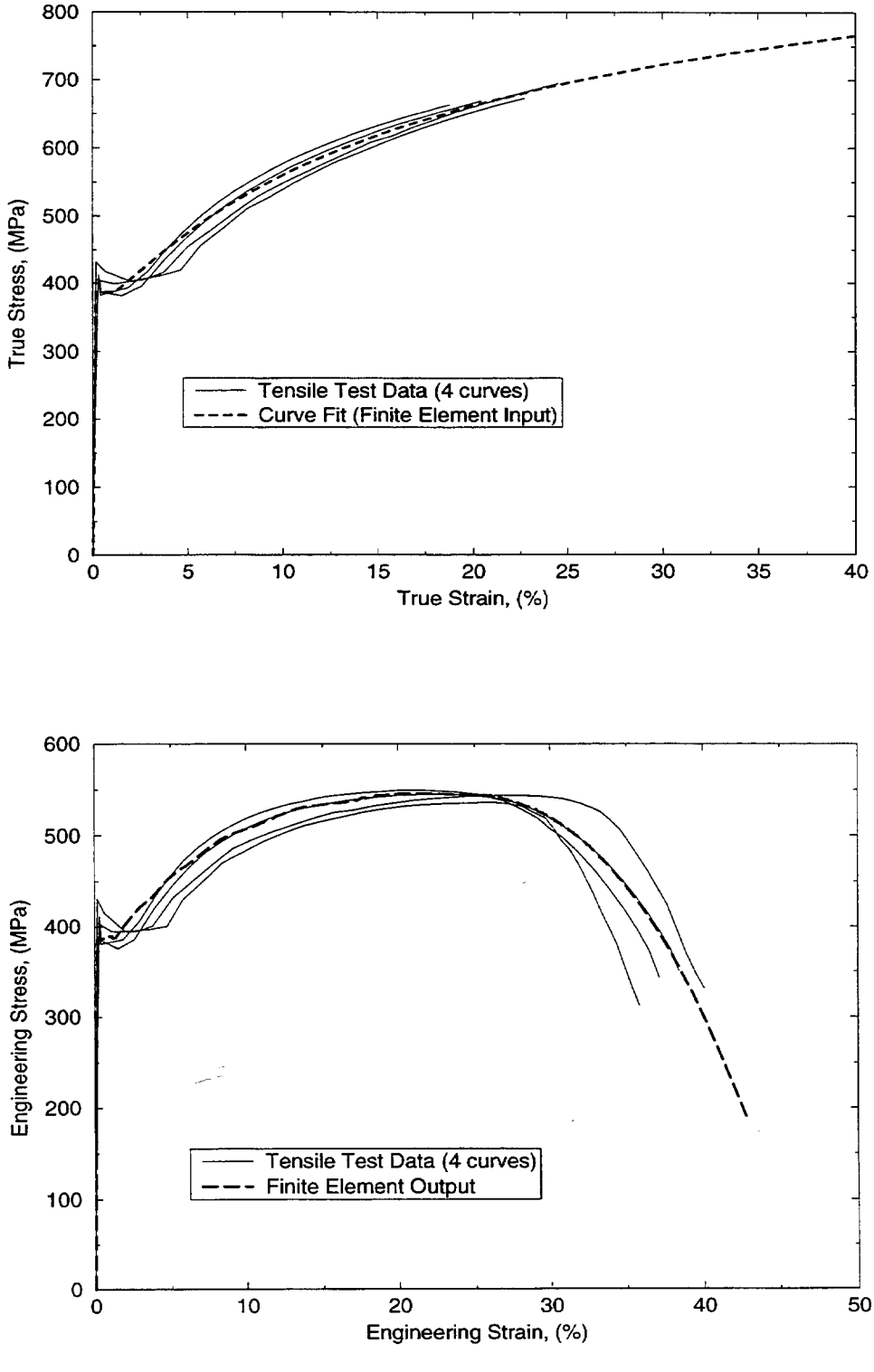

Figure 4-24. Material - SGV480; Thickness - 8.0 mm; Location - Upper Spherical Shell. Top: True stress and strain. Bottom: Engineering stress and strain.

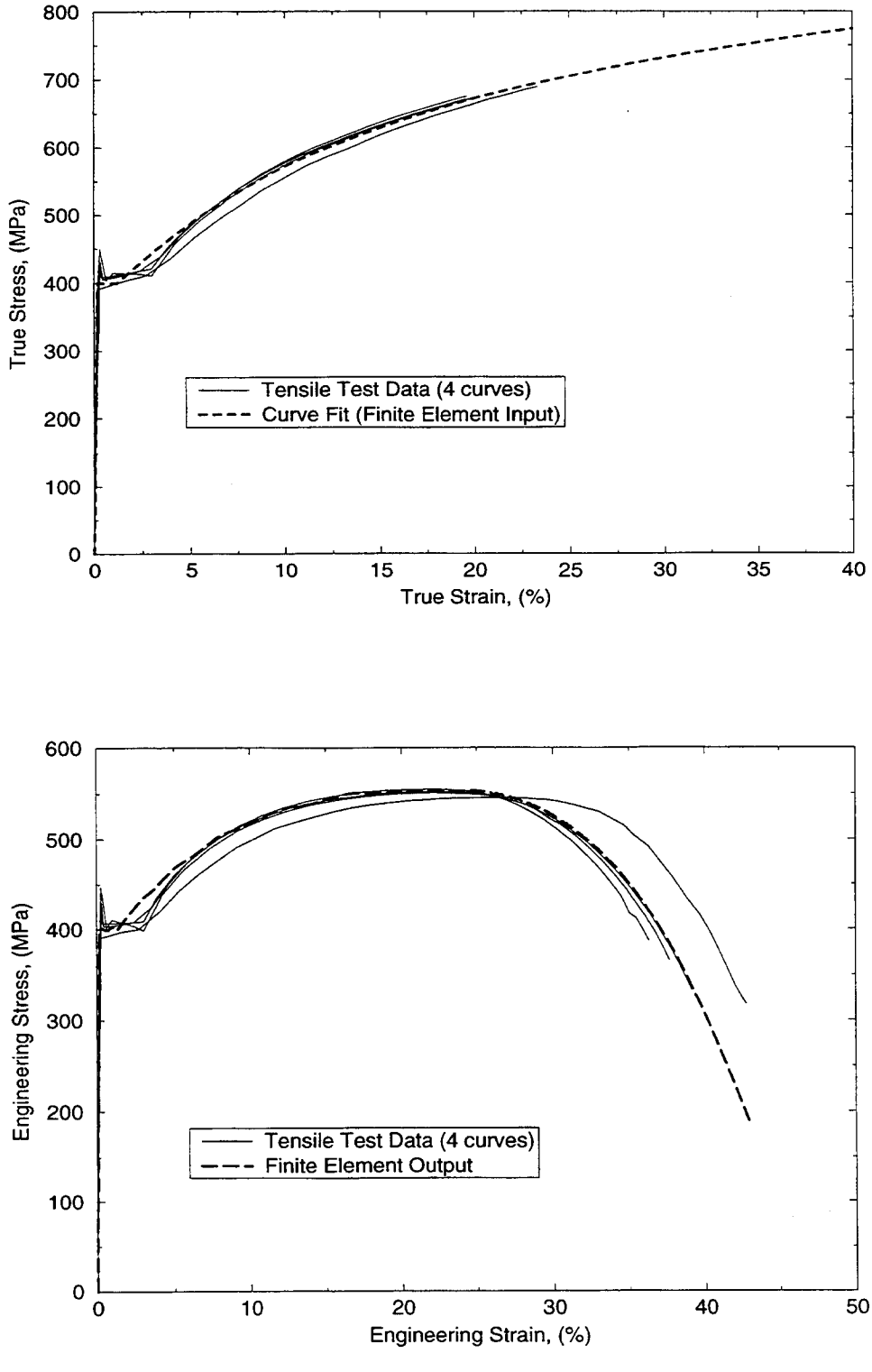

Figure 4-25. Material - SGV480; Thickness - 8.5 mm; Location - Middle Conical Shell. Top: True stress and strain. Bottom: Engineering stress and strain.

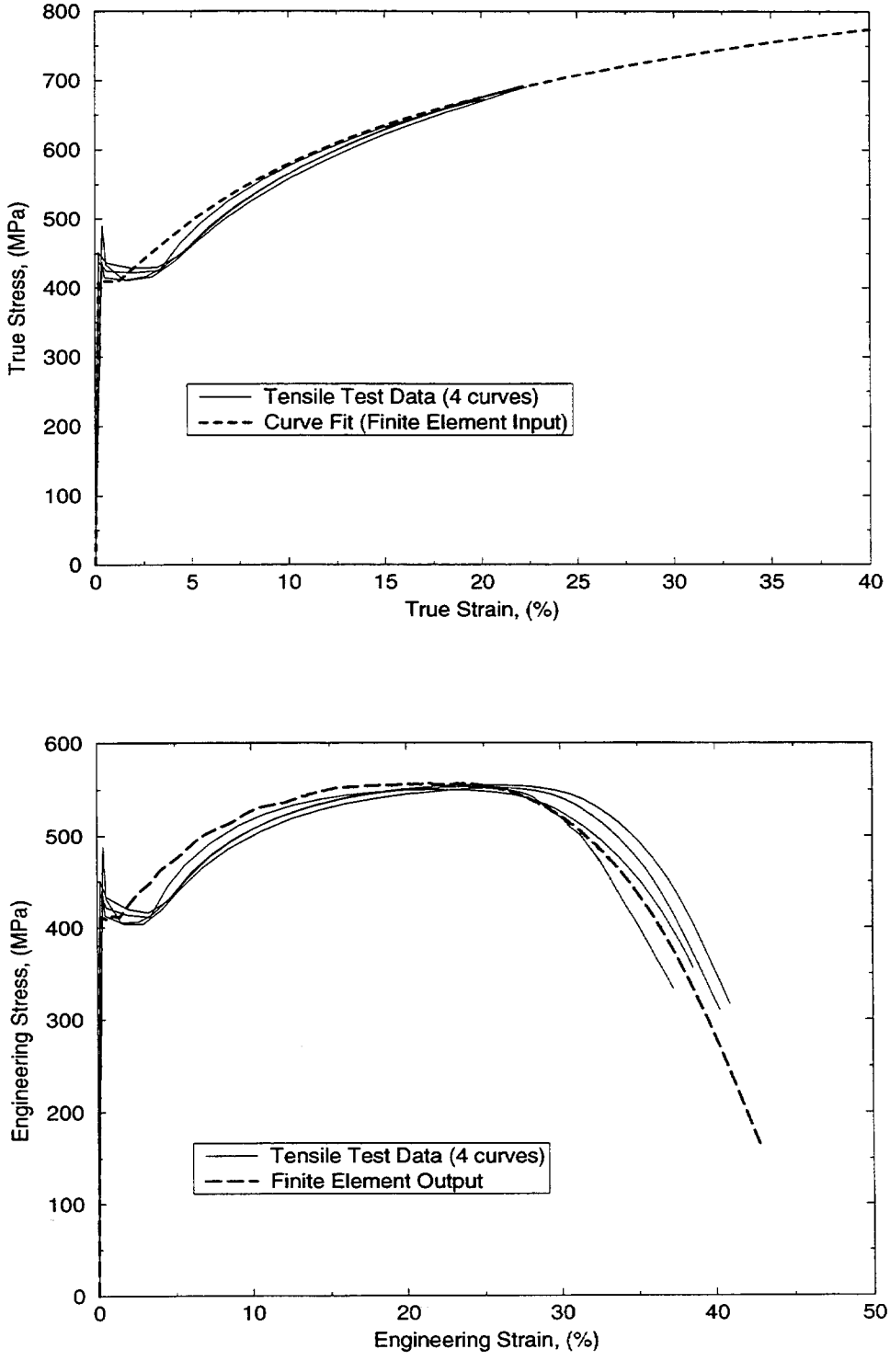

Figure 4-26. Material - SGV480; Thickness - 9.5 mm; Location - Stiffening Ring. Top: True stress and strain. Bottom: Engineering stress and strain.

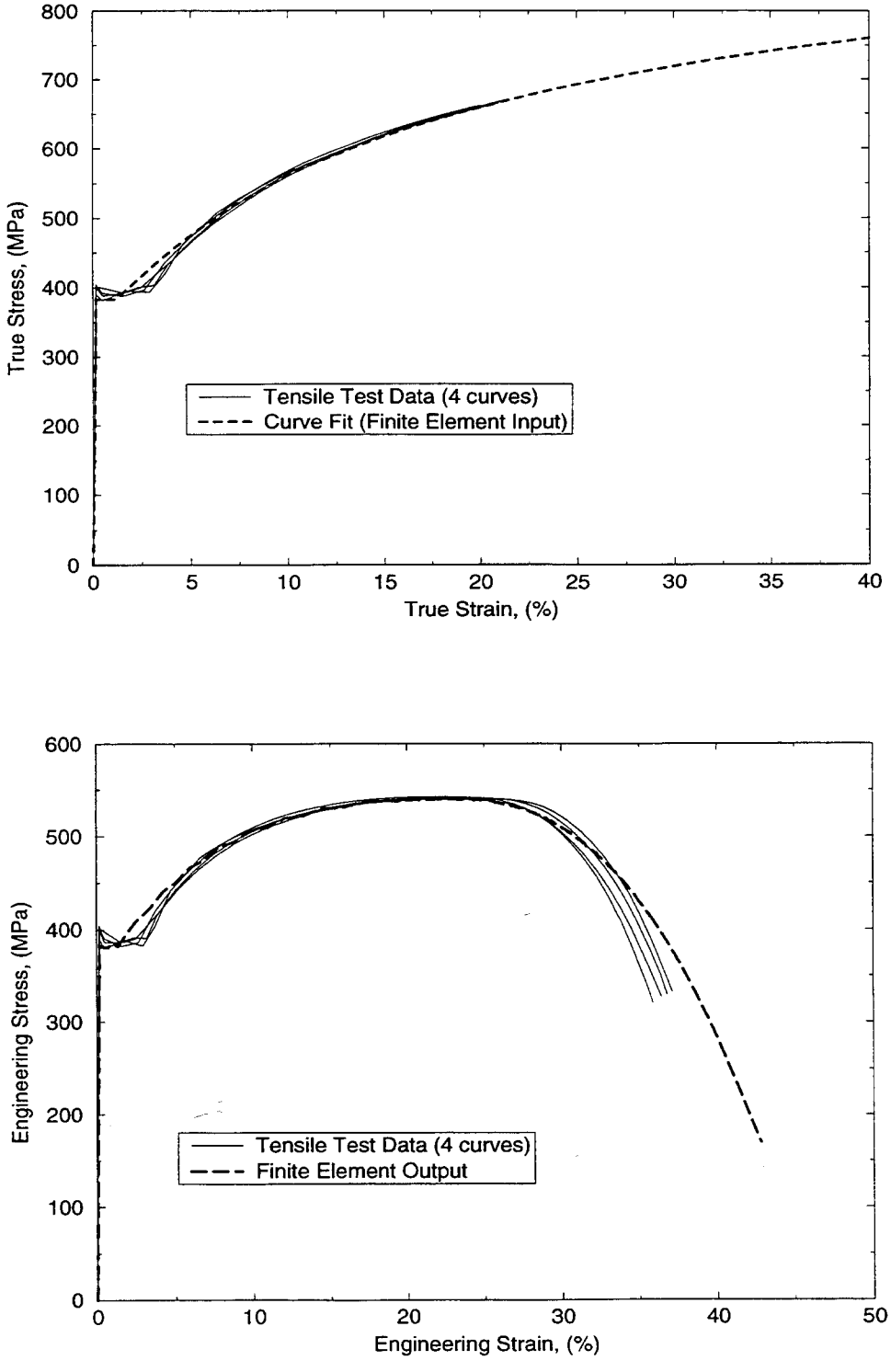

Figure 4-27. Material - SGV480; Thickness - 12.5 mm; Location - Stiffening Ring. Top: True stress and strain. Bottom: Engineering stress and strain.

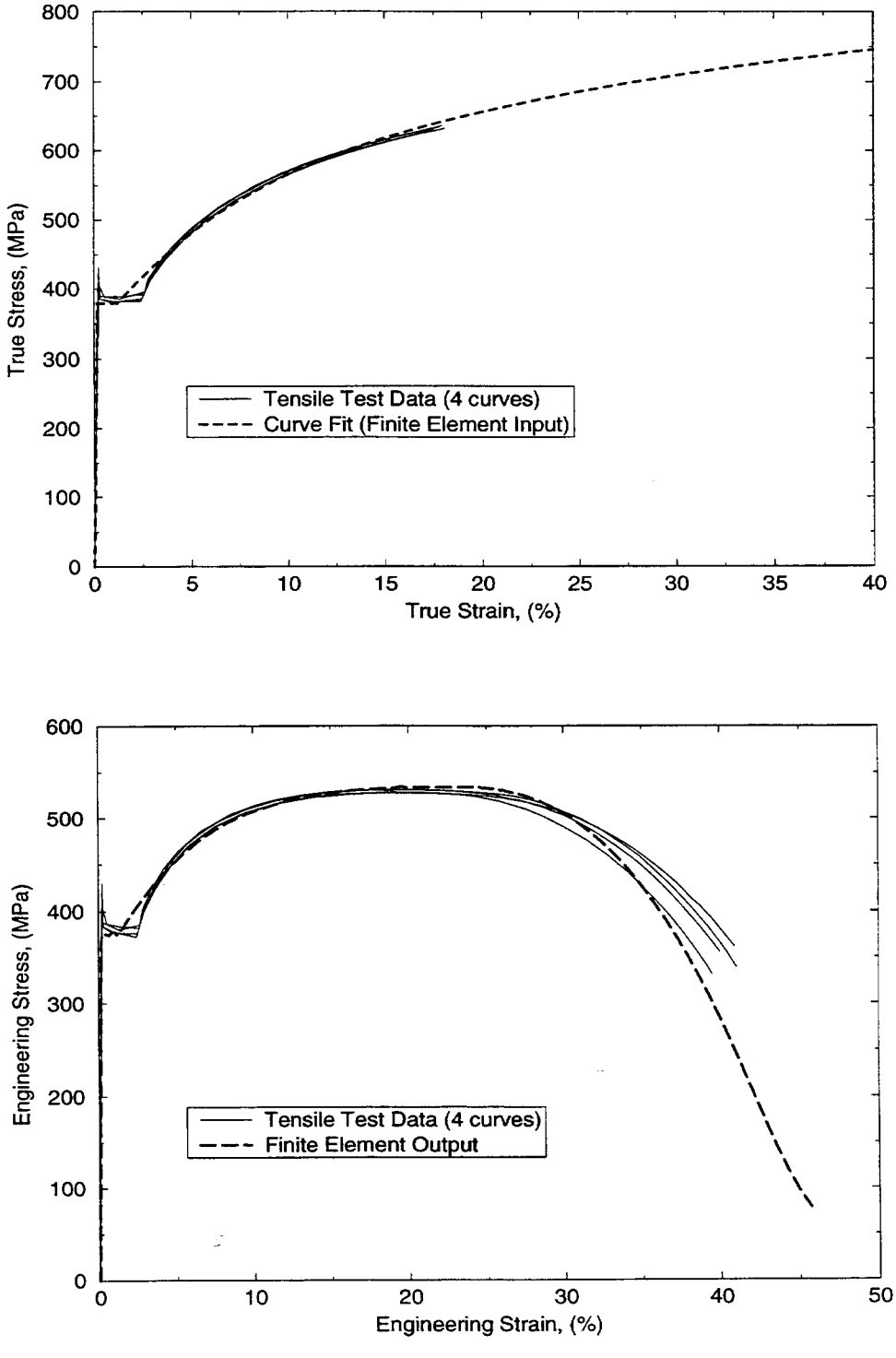

Figure 4-28. Material - SGV480; Thickness - 19.0 mm; Location - Stiffening Rings (2). Top: True stress and strain. Bottom: Engineering stress and strain.

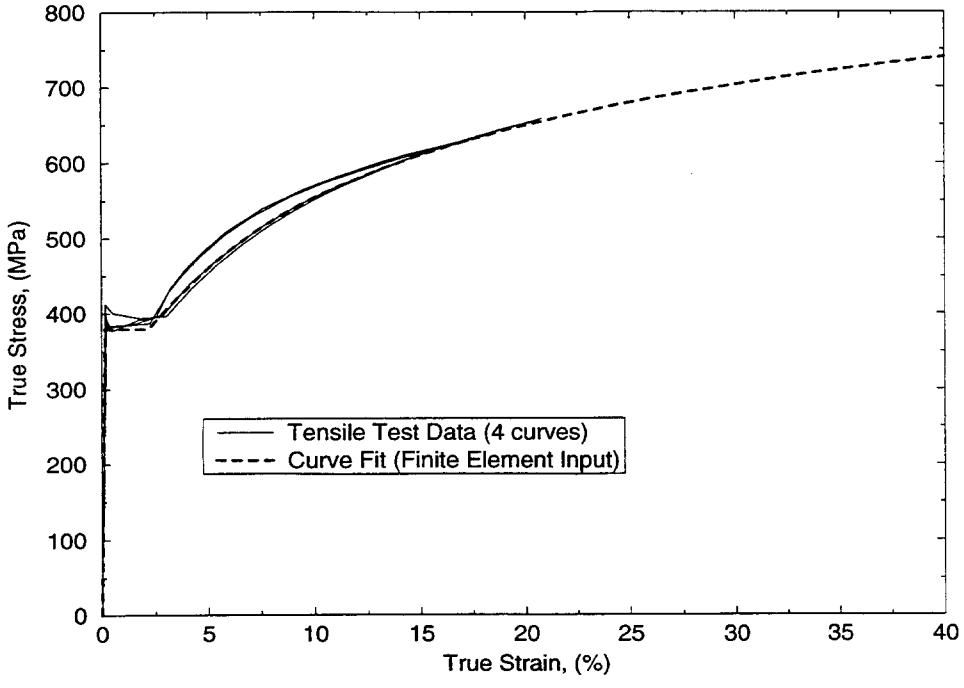

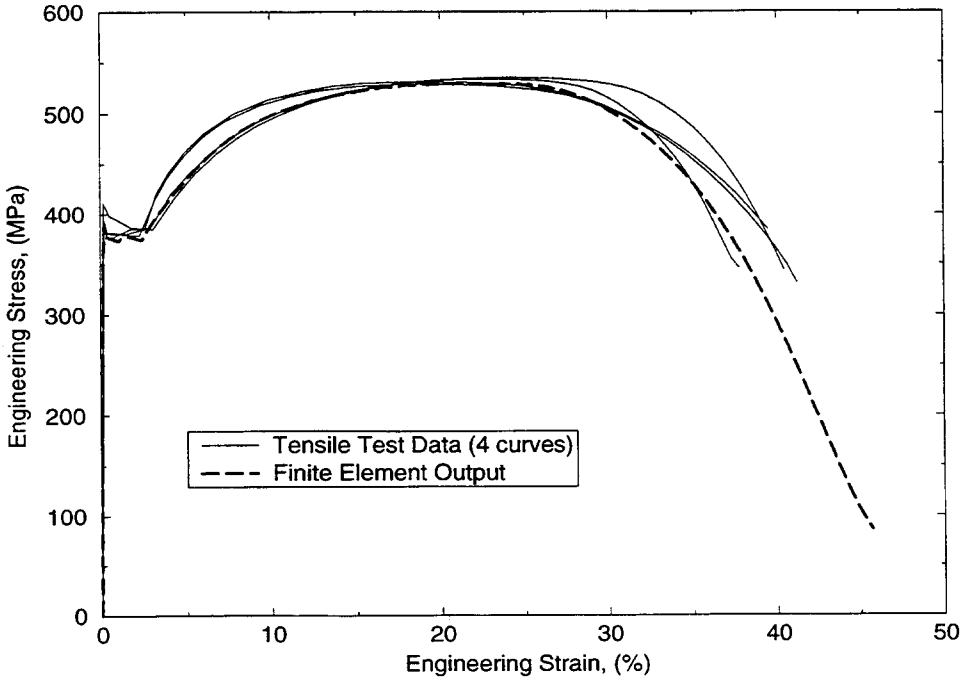

Figure 4-29. Material - SGV480; Thickness - 20.0 mm; Location - Top Flange, Hatch Covers (2), Hatch Sleeve. Top: True stress and strain. Bottom: Engineering stress and strain. Top Flange.

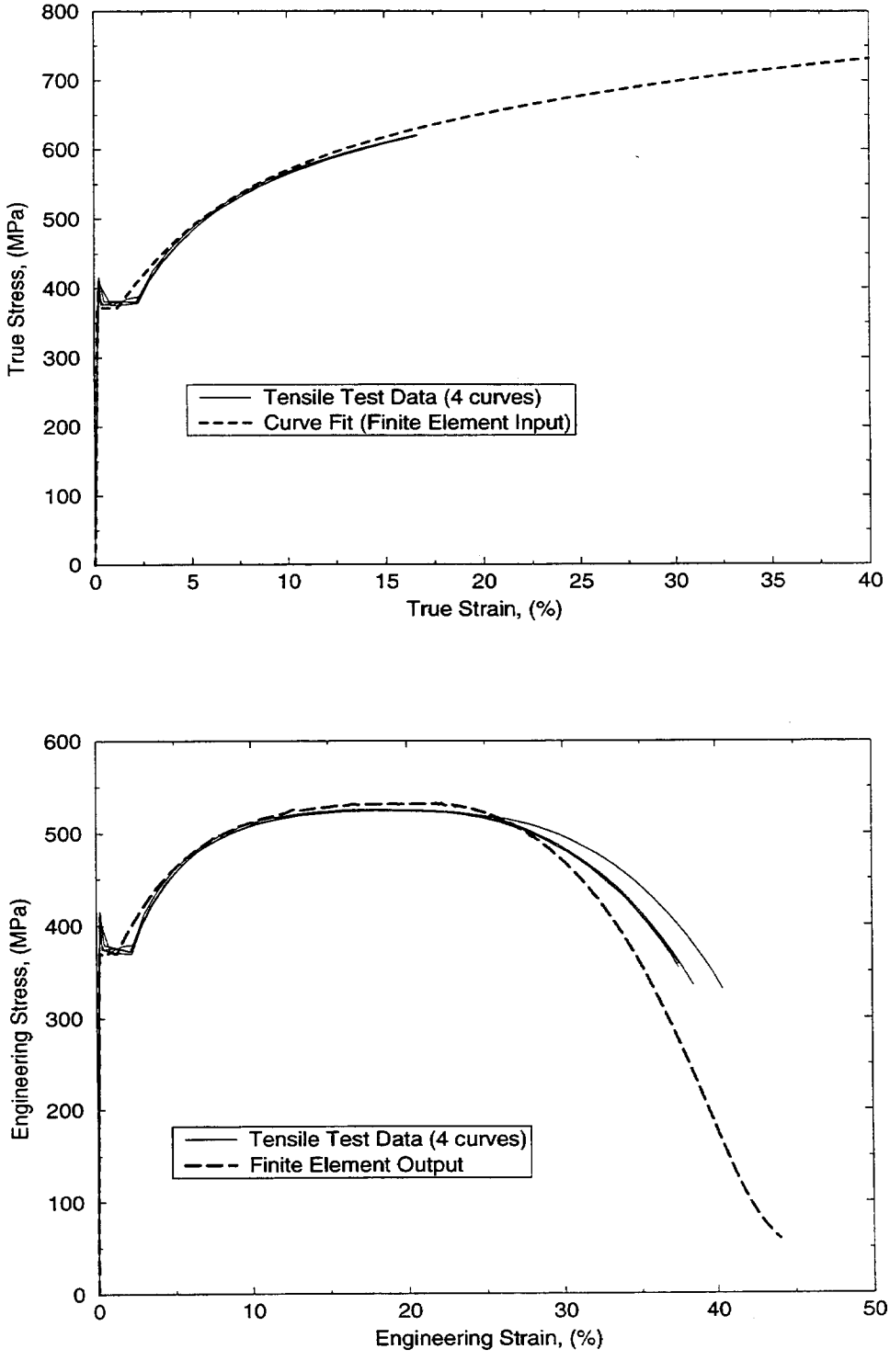

Figure 4-30. Material - SGV480; Thickness - 28.0 mm; Location - Knuckle. Top: True stress and strain. Bottom: Engineering stress and strain.

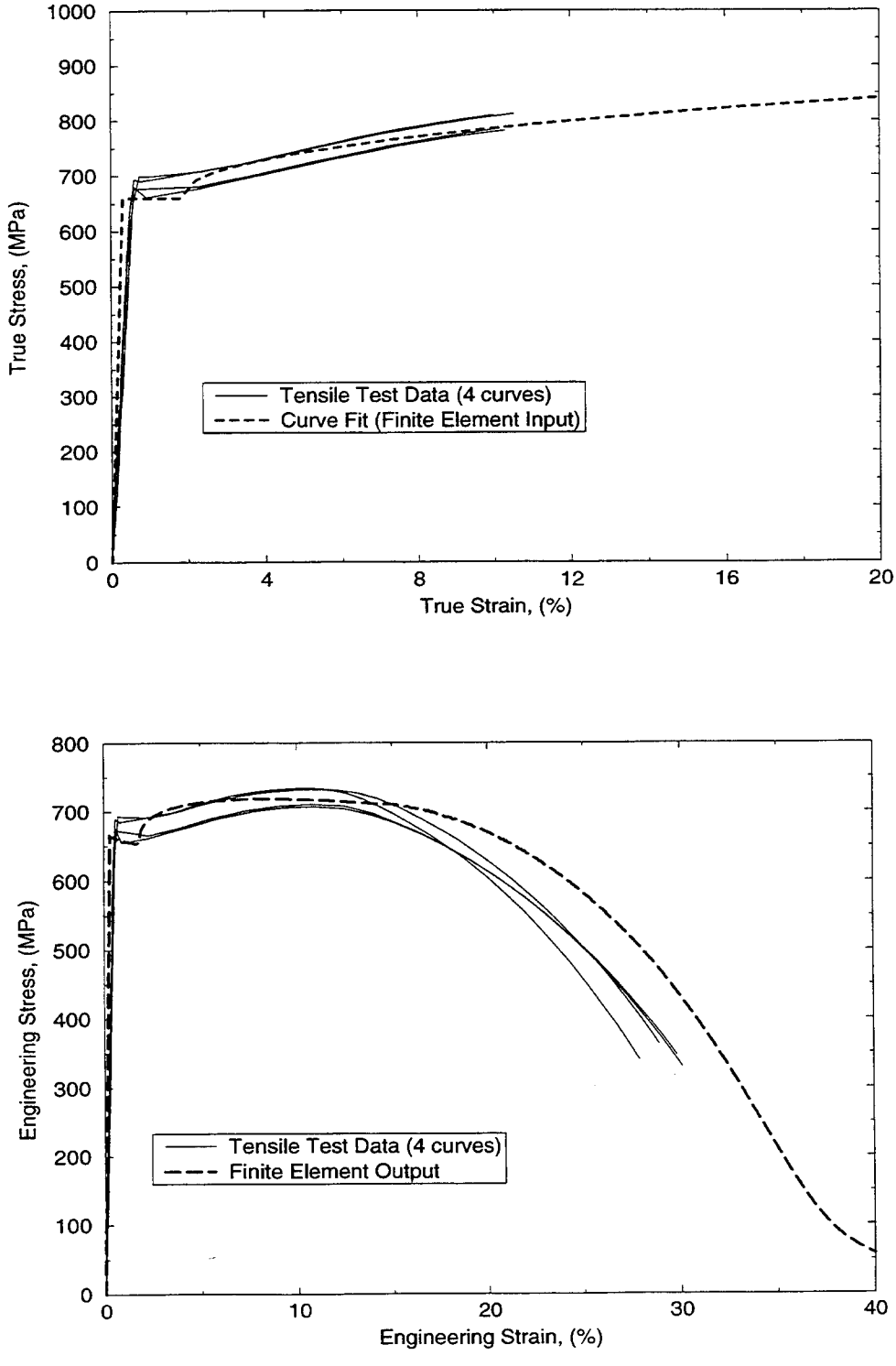

Figure 4-31. Material - SPV490; Thickness - 9.0 mm; Location - Lower Cylindrical Section, Lower Conical Shell. Top: True stress and strain. Bottom: Engineering stress and strain.

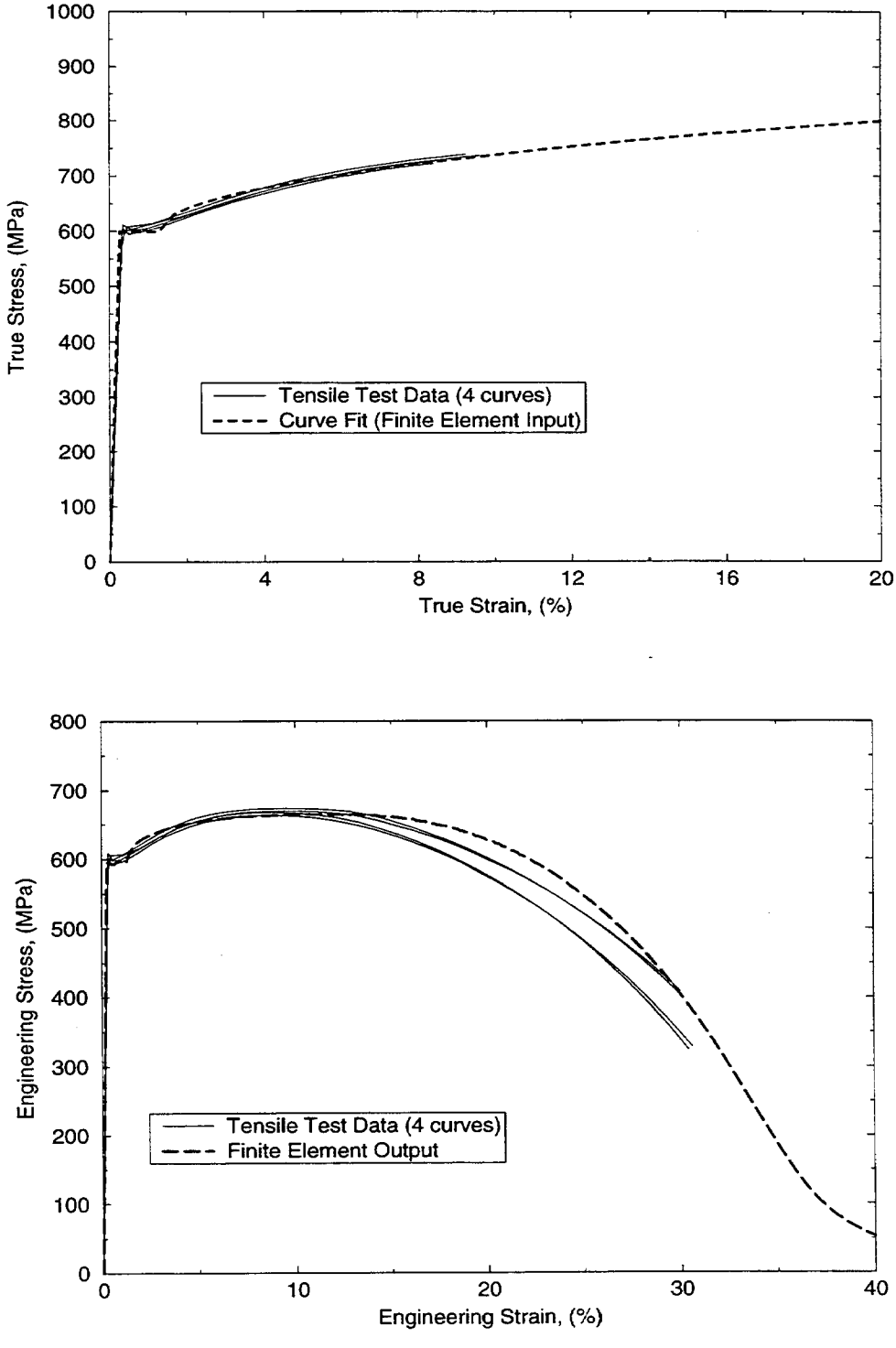

Figure 4-32. Material - SPV490; Thickness - 17.5 mm; Location - Bottom Flange, Bottom Head, Stiffening Ring, Ring Support Girder, Gusset Plates. Top: True stress and strain. Bottom: Engineering stress and strain.

5. Global Axisymmetric Analyses

The analyses described in this section were used to provide guidance for the design of the contact structure (CS). Two axisymmetric finite element models were developed, one with an 18 mm gap and another with a 34 mm gap. These analyses also provided insight about the distribution of strain throughout the meridional distance along the steel containment vessel (SCV) wall in areas away from the location of the equipment hatch. Both models described in this section used the uniaxial test data with the extrapolations described in the previous section. Because the objective of these axisymmetric analyses was primarily to support the CS design (and not for prediction of failure), they were terminated at 8 MPa internal pressure or roughly 10 P_d.

5.1 Finite Element Model Description

The basic finite element model of the SCV and CS for the axisymmetric analyses appears in Figure 5-1[14]. To support the CS design effort, two different gap dimensions, 18 mm and 34 mm, were examined. The CS was designed with a nominal gap of 18 mm, but fabrication tolerances could have resulted in gaps of 34 mm in some areas. The uniform 34 mm gap in the axisymmetric analysis provided a bound on the worst case.

Two-node axisymmetric shell elements were used for the SCV walls, ring stiffeners, and rings of the support girder. Four-node axisymmetric quadrilaterals were used for the flanges, gusset plates, and the CS. Two-node axisymmetric contact elements were superimposed on the shell elements at the midsurface of the wall of the SCV to model the contact between the SCV and the CS. The total number of elements used was approximately 1600 for both the 18 mm case and the 34 mm case. Based on the earlier parametric studies described in Section 4.2.1, the coefficient of friction used for these analyses was μ=0.2[15], so that when contact occurs, a tangential stress is induced in the contact elements in addition to a normal stress. Axisymmetric boundary conditions were imposed on the node at the top of the hemispherical dome of the SCV as well as at the bottom hatch cover. The model was also constrained in the vertical direction at the bottom outside corner of the ring support girder. The loading consisted of pressure on the interior of the SCV and self-weight of the entire structure. The material models are described in detail in Section 4.3. All computations were performed with the commercial finite element code ABAQUS, Version 5.3 (ABAQUS, 1993b).

Gusset plates are welded between the upper and lower rings of the ring support girder to provide it with significant shear and bending resistance. To include the effect of the 32 gusset plates in the axisymmetric finite element model, we modeled them as a solid ring with an orthotropic material model and a reduced Young's modulus. The ring representing the gusset plate was assumed to have no stiffness in the hoop direction. The reduced stiffness in the axial and radial directions was obtained by multiplying Young's modulus of the actual material by the ratio of the actual area of the gusset plates to the area of the solid ring modeled in the axisymmetric finite element analyses.

Because the global axisymmetric analyses were performed before the design of the CS was finalized, there are two important differences between the CS as modeled in these analyses and in the final design. The first difference is that the CS was fabricated from SA516 Grade 70 steel rather than A36 steel represented in the analyses. SA516 has a slightly higher yield (258 MPa [38 ksi] compared to 245 MPa [36 ksi] for the A36) and also a slightly higher ultimate strength (476 MPa [70 ksi] compared to 408 MPa [60 ksi] for A36) (Hucek, 1985). Because the weaker A36 steel CS remained essentially elastic (i.e., only local yielding occurred) in these analyses, it is unlikely that the change in material will significantly affect the results. The other important difference lies in the geometry of the CS near the knuckle of the SCV. Figure 5-2 details the differences between the as-modeled and the final design geometry for the part of the CS adjacent to the knuckle. Note the gap at the top of the knuckle in the final design of the structure is nearly twice that of the model: 38 mm compared to 18 mm. The final design geometry near the knuckle is included in the local

[14] Carter, P.A., and Key, S.W., "Axisymmetric Analyses of the SCV Model," Sandia memorandum to V.K. Luk, November 2, 1995.

[15] Porter, V.L., "Further Investigation of Friction Effects for Shielded SCV Model," Sandia memorandum to V.K. Luk, May 4, 1994.

axisymmetric analysis of the top head described later in Section 7.1.

5.2 Results – 18 mm Case

This section describes results for the case of a uniform 18 mm gap between the SCV model and the CS. In these analyses, the CS is modeled with A36 steel based on preliminary designs, but because it is designed to remain essentially elastic throughout the test, the response of the SCV model should not be much different for the CS constructed of SA516 Grade 70 steel in the final design.

5.2.1 Displacement History

Figure 5-3 and Figure 5-4 show the displacement histories at the boundary condition locations. The apex of the hemispherical dome on the top head and the bottom of the bottom hatch cover are the locations where the axisymmetric boundary conditions are applied. The vertical displacement as a function of internal pressure is plotted in Figure 5-3. The scaled design pressure (P_d) for the model is 0.78 MPa (113 psi). The vertical displacement of the apex of the hemispherical dome increases linearly until after 3 P_d where the slope increases. At 5 P_d, when the vertical displacement is just over 15 mm, the effect of the CS becomes apparent as the slope decreases significantly. Above 7 P_d, the slope increases once again due to yielding in the top head. At 10 P_d the maximum displacement at the apex is approximately 46 mm. The bottom hatch cover displaces linearly downward such that the displacement at 10 P_d is approximately -2 mm. The horizontal displacement in Figure 5-4 at the bottom of the ring support girder is relatively small in comparison to the displacements shown in Figure 5-3. The displacement is linear until contact initiates at just over 5 P_d, where it continues to increase to a maximum of nearly 0.4 mm at 10 P_d.

5.2.2 Contact History

Figure 5-5 and Figure 5-6 show the gap closure history as a function of the meridional distance along the SCV wall (distance along the shell reference line) starting with x = 0 at the bottom of the lower cylindrical shell and ending at the top of the knuckle (refer to Figure 5-1). The initial gap from the lower conical section to the knuckle region is 18 mm. When contact has occurred the gap distance is equal to zero.

Figure 5-5 shows data for 4, 5.1 and 6 P_d. The gap closes rapidly from P = 4 P_d until first contact occurs in the knuckle region at P = 5.1 P_d. As will be shown later, this is due primarily to the growth of plastic strain in the middle and upper conical sections as well as in the knuckle region. Immediately after contact in the knuckle region, contact occurs in the upper conical section, and at 6 P_d, contact has also occurred in the middle conical section. By 8 P_d, contact has also spread to the lower conical section (Figure 5-6). When the internal pressure reaches 10 P_d contact has initiated in the spherical section, and has propagated significantly in all other areas, although no contact occurs at any of the stiffeners.

5.2.3 Strain History - SCV

Figure 5-7 shows the hoop and meridional strains at the middle surface for two pressures, 5.1 P_d and 8 P_d, as a function of distance along the SCV wall up to the top of the middle conical section. At first contact, 5.1 P_d, the strain field is dominated by hoop strains in free field regions away from any discontinuities. This shows that the deformation in this region is dominated by radial expansion. At 8 P_d, the meridional strain in the material just below the material interface is in compression, and the distribution of hoop strain is nearly constant in both the lower and the middle conical sections due to the constraint imposed by the CS. At 10 P_d (Figure 5-8), the hoop and meridional strains continue to follow the same trend as in Figure 5-7. The maximum meridional strain at this pressure is approximately 2.1% at the stiffener while the maximum hoop strain is approximately 1.9% in the lower cylindrical shell.

Figure 5-9 shows the membrane hoop and meridional strain components at 5.1 P_d and 8 P_d as a function of distance for the SCV wall beginning at the bottom of the upper conical section (x = 0) and ending at the top of the knuckle. At 5.1 P_d the maximum hoop strain is roughly 2% and occurs in the knuckle region, while the minimum meridional strain is in the knuckle and shows a compressive strain of approximately -0.7%. In the upper conical section, hoop strains dominate the meridional component with a local maximum occurring in the middle of the upper conical section. The hoop and meridional components of strain are nearly equal in the spherical section which is consistent with the theoretical elastic stress field in a pressurized sphere – uniform tensile stresses in all directions (Gere and

Timoshenko, 1984). At 8 P_d the maximum value of hoop strain remains in the knuckle and has increased to 2.5% and the meridional component has decreased slightly to -0.8% (compression) in the same location. The maximum hoop strain in the upper conical section has not increased significantly due to the restraint of the CS in this location, although the magnitudes of the hoop strain near the top and bottom of the upper conical section have increased such that the distribution is nearly uniform throughout the upper conical section. Plasticity has begun to govern the strain field in the spherical section as shown by the significant increase in hoop strain relative to the meridional component. The meridional component increased only slightly throughout the entire domain with the maximum value of 0.5% occurring at the stiffener. Figure 5-10 shows the hoop and meridional components at 10 P_d. The hoop strains have not increased significantly in the upper conical section due to the presence of the CS. At the stiffener location and above it in the spherical section where contact has not yet occurred, the hoop strains have increased significantly although the maximum for the entire domain is about 3% in the knuckle. The meridional strains have generally increased except at the knuckle where they have decreased to roughly -1% (compression).

To illustrate the compressive strains in the knuckle, Figure 5-11 shows the hoop and meridional stress history at the middle surface for an element in the knuckle. The dominant tensile hoop stress causes a compressive strain in the meridional direction. This is a Poisson's effect, which can be easily verified using Hooke's law for plane stress (Gere and Timoshenko, 1984).

Figure 5-12 shows the definitions of the different sections in the top head. Figure 5-13 shows the meridional and hoop components of strain as a function of distance from the bottom of the cylindrical portion of the top head just above the knuckle up to the apex of the dome for 5.1 P_d and 8 P_d. At both pressures, the largest hoop strains occur in the lower cylindrical section where it connects to the knuckle. The top flange limits the hoop strains to nearly zero for both load steps but creates a meridional strain concentration in the element immediately below the top flange that is over 1.2% at 5.1 P_d and over 2% at 8 P_d. The rest of the meridional strain field at 5.1 P_d consists of relatively small strains with uniform distribution. At 8 P_d, significant meridional strains occur in transition from the cylindrical portion of the top head to the hemispherical dome. Here the meridional component is in tension due to membrane stretching from the uplift of the dome. The hoop component is in compression as a result of this section being pulled radially inward by the dome. Figure 5-14 shows the meridional and hoop components at 10 P_d. Here the radial compression effect is even more pronounced although the maximum values for each component remain in the cylindrical section between the knuckle and the top flange. Figure 5-15 shows the equivalent plastic *membrane* (middle surface) strain as a function of the meridional distance along the SCV wall from the bottom of the lower cylindrical shell to the top of the knuckle for three different internal pressures. The figure shows that significant plastic strains do not develop in the SCV wall until after 4 P_d. The plastic membrane strain in the SCV wall grows considerably from 4 P_d to 5.1 P_d, the pressure where contact first occurs. The maximum membrane strain in the SCV wall is approximately 1.8%. The rate of increase in membrane strain with increasing pressure has obviously been slowed by the interaction with the CS. Figure 5-16 shows the plastic membrane strain at two higher internal pressures. At 8 P_d the maximum strain in the SCV wall is approximately 2.6% just below the knuckle. At 10 P_d the maximum plastic strain in the SCV wall is about 3.1% at the same location. Uniform distribution occurs in the lower, middle, and upper conical sections at both pressures due to the widespread contact in these areas.

Figure 5-17 shows the equivalent plastic *surface* strains as function of distance along the SCV wall. At 5.1 P_d the maximum plastic surface strain of 3.3% occurs on the exterior surface just below the knuckle region. The maximum plastic surface strain at 10 P_d has shifted to the location just below the 12.5 mm stiffener where the top of the lower cylindrical section meets the bottom of the lower conical section. The magnitude of this interior surface strain is about 7%. Large differences in magnitude between the interior and exterior surface strains indicate bending due to a discontinuity such as a stiffener.

Figure 5-18 shows the equivalent plastic membrane strain as a function of meridional distance starting with $x = 0$ at the top of the knuckle up to the apex of the top head for three internal pressures. At 4 P_d there is a small amount of plastic strain due to the thickness and curvature discontinuity at the knuckle interface. At 5.1 P_d, the strain has significantly increased to approximately 1.5% because of the discontinuity at the knuckle. At this pressure the maximum plastic strain in

the transition from the cylindrical region of the top head to the hemispherical dome is about 0.05%. At 6 P_d, the strain has increased slightly near the knuckle discontinuity, and the strain in the transition region is more than 0.2%. Figure 5-19 shows data for the same locations for 8 P_d and 10 P_d. At 8 P_d plastic strains have developed in each region except for the top flange. At 10 P_d the strain is more than 3.3% just above the knuckle, nearly 1% in the cylindrical portion above the top flange, approximately 1.5% in the transition region from the cylindrical portion to the hemispherical dome, and over 4% at the apex of the hemispherical dome.

In Figure 5-20 the plastic surface strains are plotted along the meridional distance from the top of the knuckle to the apex of the hemispherical dome. At 5.1 P_d the maximum surface strain is on the interior surface in the region adjacent to the top flange and has a magnitude of nearly 5%. At 10 P_d, the strain at the same location has nearly doubled to more than 9%. Plastic surface strain has also accumulated in the cylindrical portion above the top flange, in the transition region from the cylinder to the dome, and in the dome itself. The character of the bending changes from the cylindrical section, where the exterior surface has the higher strains, to the transition region, where the interior surface strains are higher, to the hemispherical dome, where the exterior surface strains are higher again.

Figure 5-21 shows the equivalent plastic membrane strain history for one element from each of the four stiffeners. Locations of the stiffeners are shown in Figure 2-3. The elements plotted are those with the highest plastic strain at 10 P_d. The element with the highest plastic strain was also the element located on the innermost ring of the stiffener, i.e., the element at the smallest radius. The 19 mm stiffener in the upper conical section is clearly the worst case, although the maximum strain at 10 P_d is just under 1.5%. This stiffener yields at 4.9 P_d, well before the other stiffeners, and strain increases at a greater rate after yielding. The other 19 mm stiffener has the second highest plastic strain at 10 P_d although it does not yield until about 8.0 P_d. The 9.5 mm stiffener yields at 6.3 P_d, but its maximum plastic strain never exceeds 1%. The 12.5 mm stiffener yields the latest of all, at about 8 P_d, and reaches a maximum plastic strain of only 0.6% at 10 P_d.

Figure 5-22 shows the hoop and meridional components of strain for the element from Figure 5-21 with the highest maximum plastic strain (element #1300 in the 19 mm stiffener in the upper conical section). The hoop component is in tension for the entire pressurization due to the radial expansion of the ring. The meridional component (in the horizontal direction) is in compression due to a Poisson's effect. Elements from the other stiffeners show similar behavior.

In Figure 5-23, the equivalent plastic strain and the hoop and axial components are plotted as a function of internal pressure for an element in the top flange. As with the stiffeners, this particular element was chosen because it had the highest plastic strain at 10 P_d relative to the other elements in the top flange. This element was located on the inside ring on the bottom of the top flange. The hoop component is in tension because of the radial expansion of the cylindrical portion of the top head, and the axial component is in compression due to Poisson's effect. The hoop strains are linear up to about 4.0 P_d and then increase more rapidly due to yielding in the cylindrical section located just below the flange. The rate of increase in hoop strain then decreases again from 5.1 P_d to about 8.5 P_d due to the spread of contact along the SCV wall. Finally, the hoop strain increases more rapidly once again above 8.5 P_d due to yielding of the flange. Analogous changes in slope occur in the compressional meridional strains. Plastic strains in this element are small relative to other locations in the model; the maximum value at 10 P_d is less than 0.3%.

5.2.4 Strain History - CS

Figure 5-24 shows the equivalent plastic strains and the hoop and axial components of strain for the element with the highest plastic strain at 10 P_d. This element is located in the top row of elements on the inside surface of the CS adjacent to the knuckle. This element did not yield until nearly 7.7 P_d and reached a maximum strain of roughly 0.6%. The behavior of the axial and hoop components was similar to the behavior observed in the top flange. No other locations in the CS developed plastic strains, even up to a pressure of 10 P_d.

5.2.5 High Plastic Strain Locations

Figure 5-25 compares the equivalent plastic *membrane* strain history for two elements: one from the spherical section and the element at the apex of the top head. These elements were chosen because of their high plastic membrane strains relative to other elements and also because they show little or no bending behavior.

The element from the spherical section yields at roughly 4.5 P_d but does not begin to accumulate any appreciable plastic strain until about 7 P_d. After 8.6 P_d, when this particular element comes in contact with the CS, it accumulates very little additional plastic strain, for a total of approximately 2.5% at 10 P_d. The element at the apex of the top head yields late relative to the first element, after 7 P_d, but accumulates plastic strain much more quickly, reaching a value of 4.7% at 10 P_d, which is the maximum plastic membrane strain magnitude for the entire structure.

Figure 5-26 shows the equivalent plastic *surface* strain history for three elements: the element at the transition from the lower cylindrical shell to the lower conical section, the element immediately below the top flange, and the element immediately above the knuckle. Note that the first two elements are evaluated at the interior surface of the SCV wall and the last one is evaluated at the exterior surface. These elements were chosen because they have high magnitudes of surface strain as well as large differences between the interior and exterior surface values, indicating bending-dominated behavior. The interior of the element from the lower conical section adjacent to the lower cylindrical shell yields at roughly 3.5 P_d, but because it is composed of the higher yield material and is relatively close to the overly stiff bottom head, it never contacts the CS and thus continues to accumulate plastic strain. This element seems to be pivoting radially outward from the point where the curvature changes from cylindrical to conical, because the cylindrical section is stiffer.

The interior surface of the element immediately below the top flange reaches a maximum surface strain of over 9%, which is the maximum plastic surface strain for the entire structure. This element never contacts the CS, although the effect of global contact on this element at 5 P_d is evident. This element attaches to the extremely stiff top flange, and as the cylindrical section between the knuckle and the top flange expands radially outward this element bends outward, accumulating a large amount of plastic strain on the inside surface. However, the element immediately above the knuckle does not show similar behavior. In this element, the exterior surface shows the higher strain. Because the knuckle displaces radially outward much more than the top flange, the element adjacent to the knuckle is pulled outward such that its outside surface is in tension. This element reaches a maximum value of roughly 8.5%, which is the maximum exterior surface strain reached in the structure.

5.3 Results - 34 mm Case

Contact first occurs for the 34 mm case at 5.5 P_d (compared with 5.1 P_d for the 18 mm case) in the upper conical section. The strains in the middle conical section, knuckle, and lower conical section continue to increase rapidly until contact occurs in these areas at 5.7 P_d, 6.1 P_d, and 7.4 P_d, respectively. Unlike the 18 mm case, the plastic membrane strain in the spherical section is highest at higher pressures, reaching a maximum of approximately 5.5% at 10 P_d. For the surface plastic strains, the behavior is similar to the 18 mm case. The cylindrical section just below the top flange has the highest value, a maximum of approximately 12% at 10 P_d, because the outward expansion of the cylindrical section is restrained by the stiffer top flange.

Figure 5-27 shows the gap closure history as a function of the meridional distance along the SCV wall starting with x = 0 at the bottom of the lower cylindrical shell and ending at the top of the knuckle (same as Figure 5-5 and Figure 5-6 for the 18 mm gap) at 5.5 P_d, 8 P_d, and 10 P_d. The first location of contact is in the upper conical section at 5.5 P_d, followed by the middle conical section at 5.7 P_d, followed by the knuckle at 6.1 P_d. By 8 P_d, contact is widespread in the lower, middle, and upper conical sections (similar to Figure 5-15 and Figure 5-16 for the 18 mm gap). By 10 P_d, the area of contact has continued to spread in these areas, and contact has also initiated in the spherical section.

Figure 5-28 shows the equivalent plastic *membrane* strain as a function of distance along the SCV wall for three internal pressures (5.5, 8, and 10 P_d). The upper conical section has the highest magnitude of membrane strain at first contact, approximately 3.4%, but by 8 P_d the knuckle has the highest magnitude of strain, approximately 4.8%. At 10 P_d the strain in the knuckle has increased to over 5.5%, the strain in the upper conical section has a maximum value of 4.4%, and the maximum strain in the middle conical section is slightly over 3.6%. The distributions of plastic strains at all pressures above 5.5 P_d are qualitatively similar to the 18 mm gap analysis, but at a magnitude approximately twice as large. However, none of the strains is large enough to indicate global failure before 10 P_d.

Figure 5-29 compares the equivalent plastic membrane strain history for two elements: one from the spherical section and the element at the apex of the top head (same as Figure 5-25 for the 18 mm case). These elements were chosen because of their high plastic membrane strains relative to other elements and also because they show little or no bending behavior. The element from the spherical section yields after 4.5 P_d and quickly accumulates plastic strain up to 9.1 P_d, where it contacts the CS and the growth of plastic strain is greatly reduced. The behavior of the element at the apex of the top head is nearly identical to the same element in the 18 mm case. After yielding at roughly 7 P_d, the element rapidly accumulates 4.5% plastic strain by 10 P_d.

Figure 5-30 shows the plastic *surface* strain for three elements: the element at the transition from the lower cylindrical shell to the lower conical section, the element immediately below the top flange, and the element immediately above the knuckle. These are the same three elements that were discussed for the 18 mm case in Figure 5-26, and they show similar behavior. The first location, the interior of the element from the lower conical section adjacent to the lower cylindrical shell, reaches a maximum strain of just under 9% at 10 P_d, compared to 7.5% for the 18 mm case. The next location, the interior surface of the element immediately below the top flange, reaches a maximum surface strain of over 12%, compared to over 9% for the 18 mm case. This is also the location of maximum plastic surface strain for the entire structure. The drastic slope change at 6 P_d is caused by global contact between the SCV and the CS, although the element itself never contacts the CS. The larger 34 mm gap allows this element to reach over 11% plastic surface strain at contact compared to less than 5% for the 18 mm case. The behavior at the last location is similar to the same element in the 18 mm case. The exterior surface of this element reaches a maximum of just over 9% strain compared to almost 8.5% for the 18 mm case.

5.4 Summary

The axisymmetric analysis with a uniform 34 mm gap indicated that contact would occur at 5.5 P_d, compared to 5.1 P_d indicated by the 18 mm gap analysis. Above 5.5 P_d, the maximum strains in the part of the SCV wall shielded by the CS for the 34 mm gap were roughly twice those for the 18 mm gap, a direct consequence of the fact that the gap is approximated twice the size. However, in neither case did the level of strains indicate global axisymmetric failure of the vessel even at 10 P_d. Strains in the top head are nearly the same for both cases. It must be noted that nothing can be inferred from these analyses about non-axisymmetric strain levels, i.e., the local strain concentrations near the equipment hatch, which may be strongly affected by the local gap dimension.

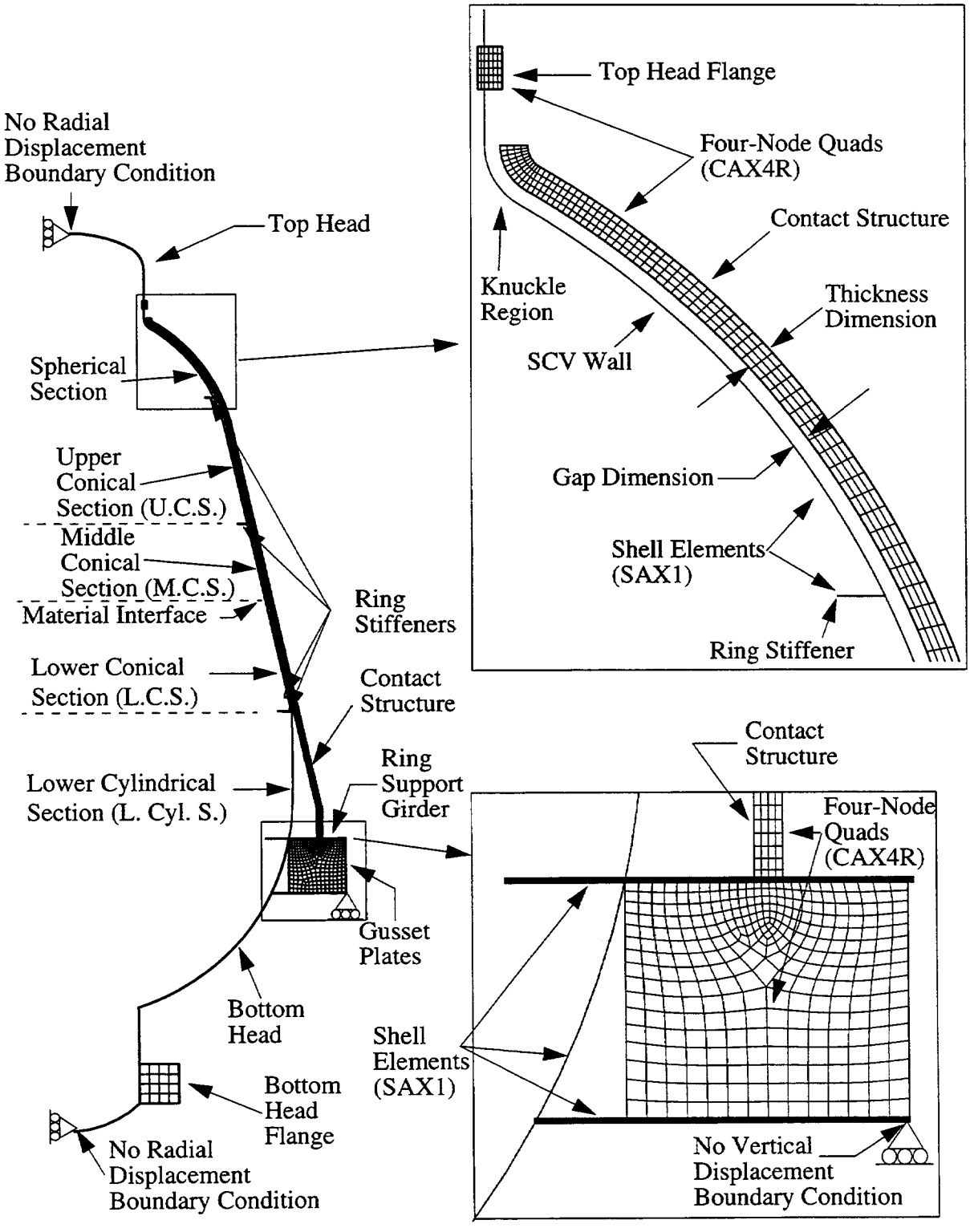

Figure 5-1. Axisymmetric finite element model showing knuckle and ring support girder details.

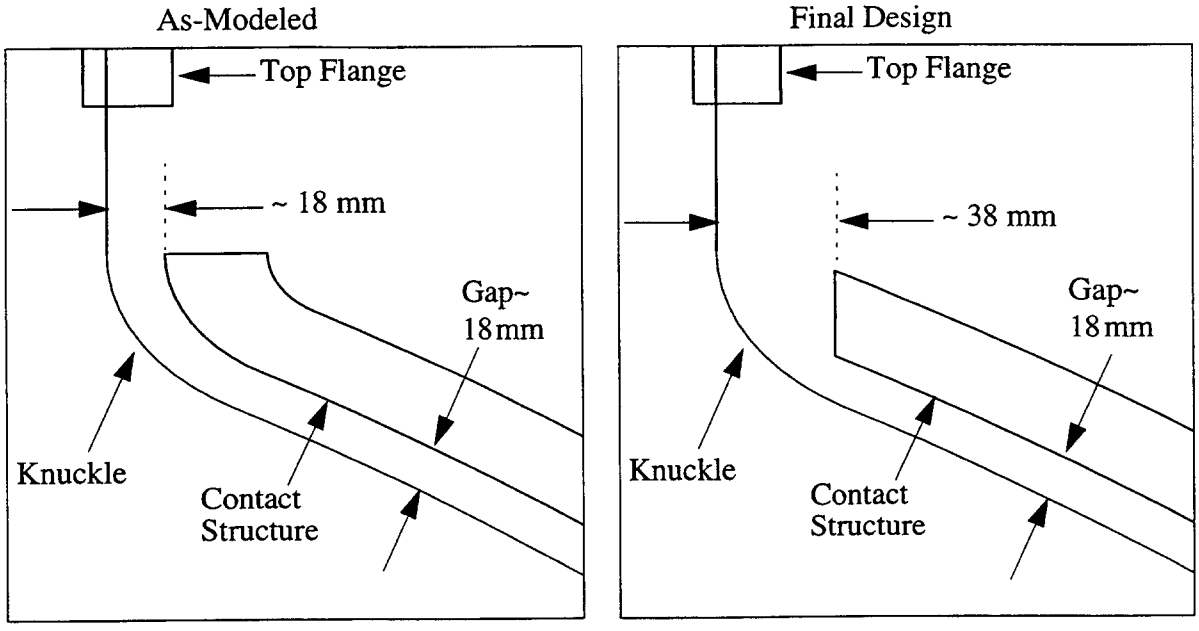

Figure 5-2. Comparison of as-modeled and final design details in contact structure near the SCV knuckle.

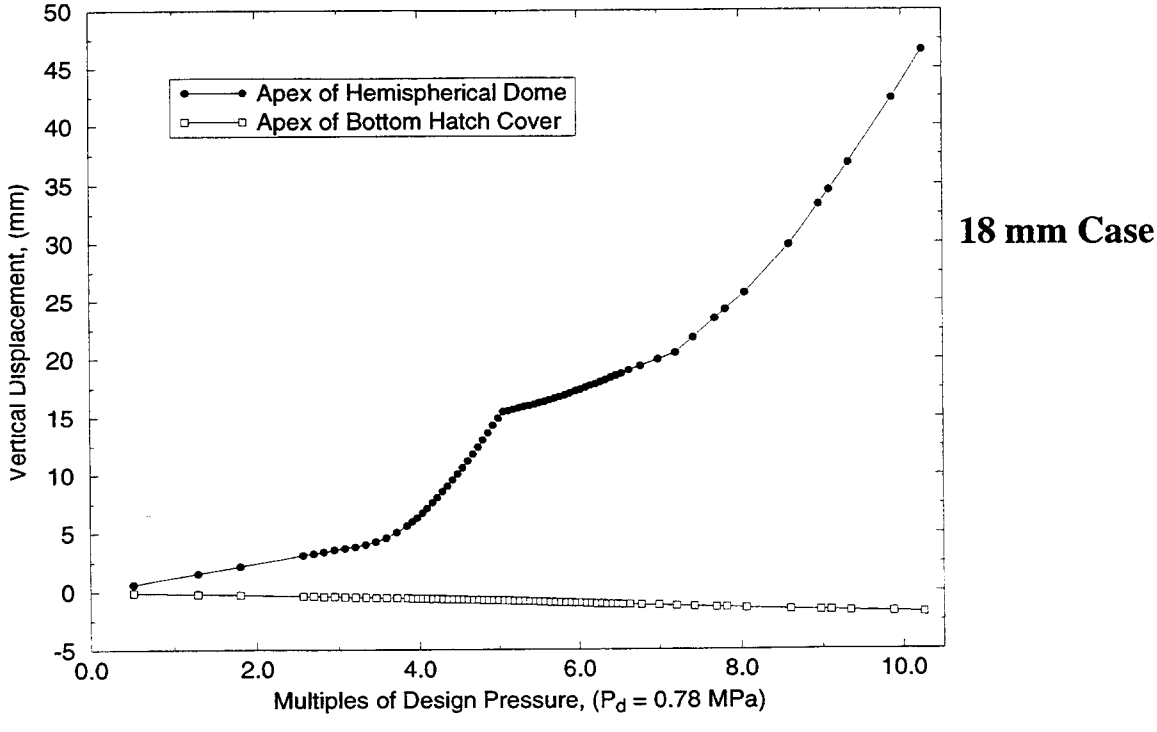

Figure 5-3. Vertical displacement history of nodes at apex of top head and apex of bottom hatch cover. Both nodes have axisymmetric boundary conditions.

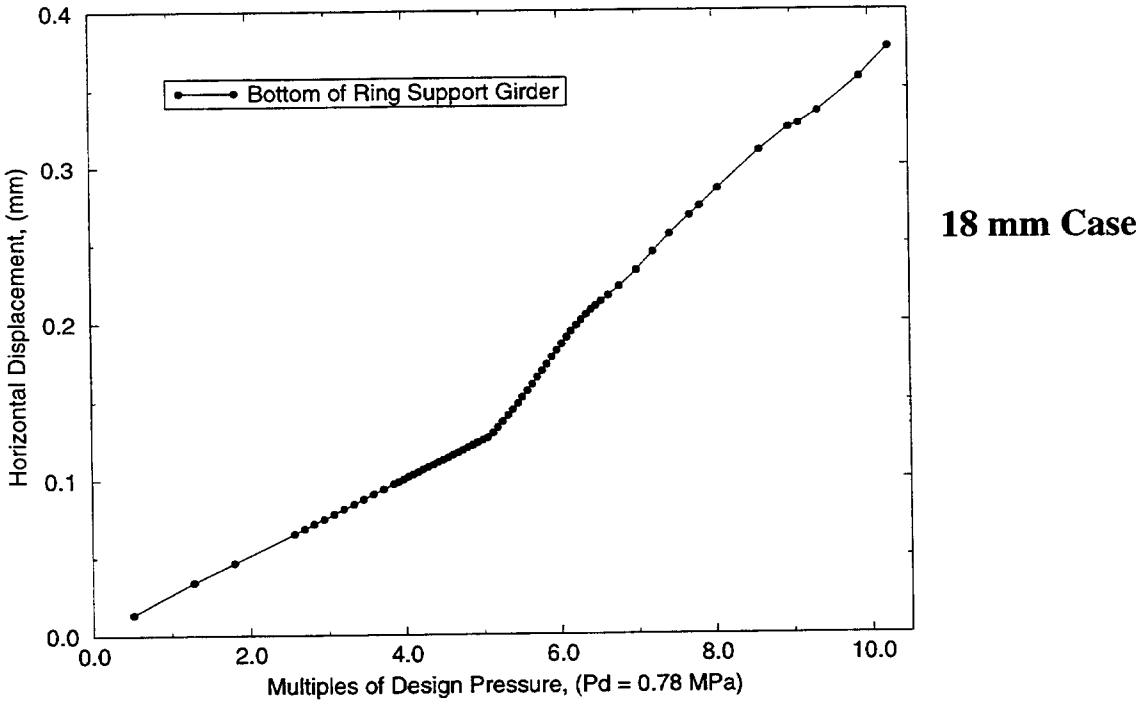

Figure 5-4. Horizontal displacement history of node at bottom of ring support girder. This node is restrained in the vertical direction.

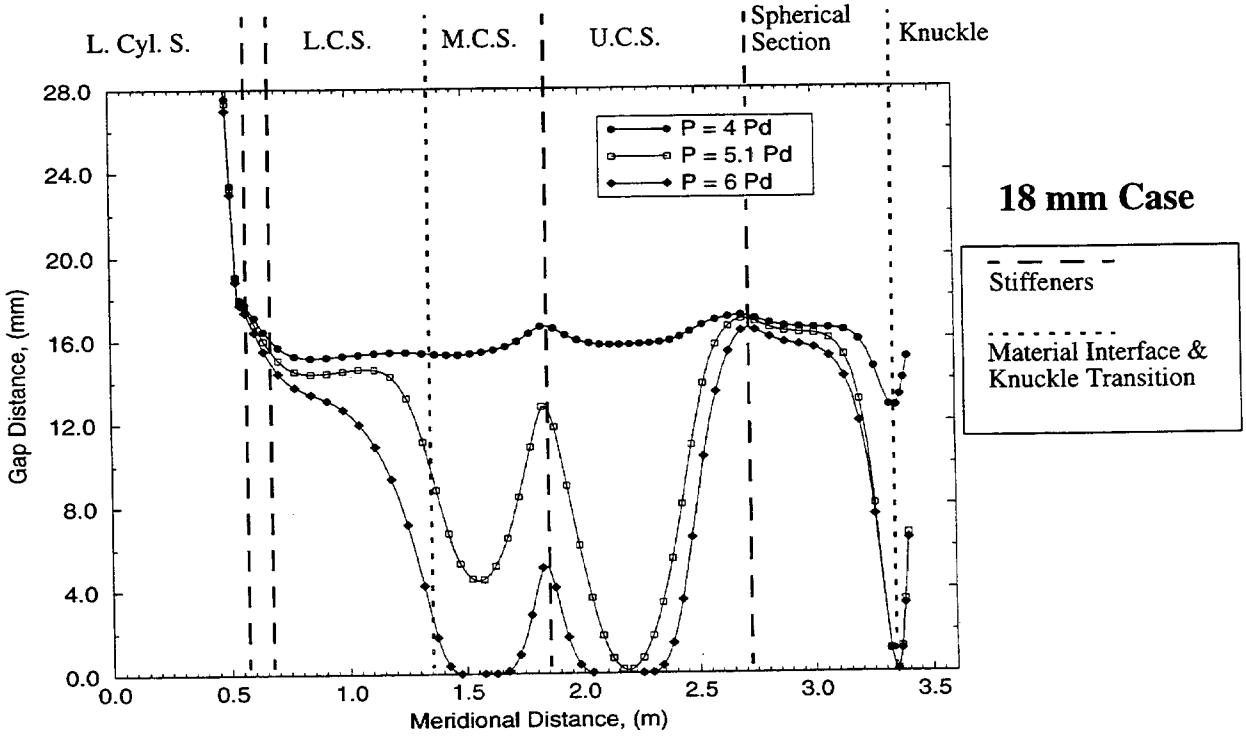

Figure 5-5. Gap closure distance along the SCV wall from the lower cylindrical section to the top of the knuckle at 4, 5.1, and 6 P_d. Locations (L.Cyl.S., etc.) are shown in Figure 5-1.

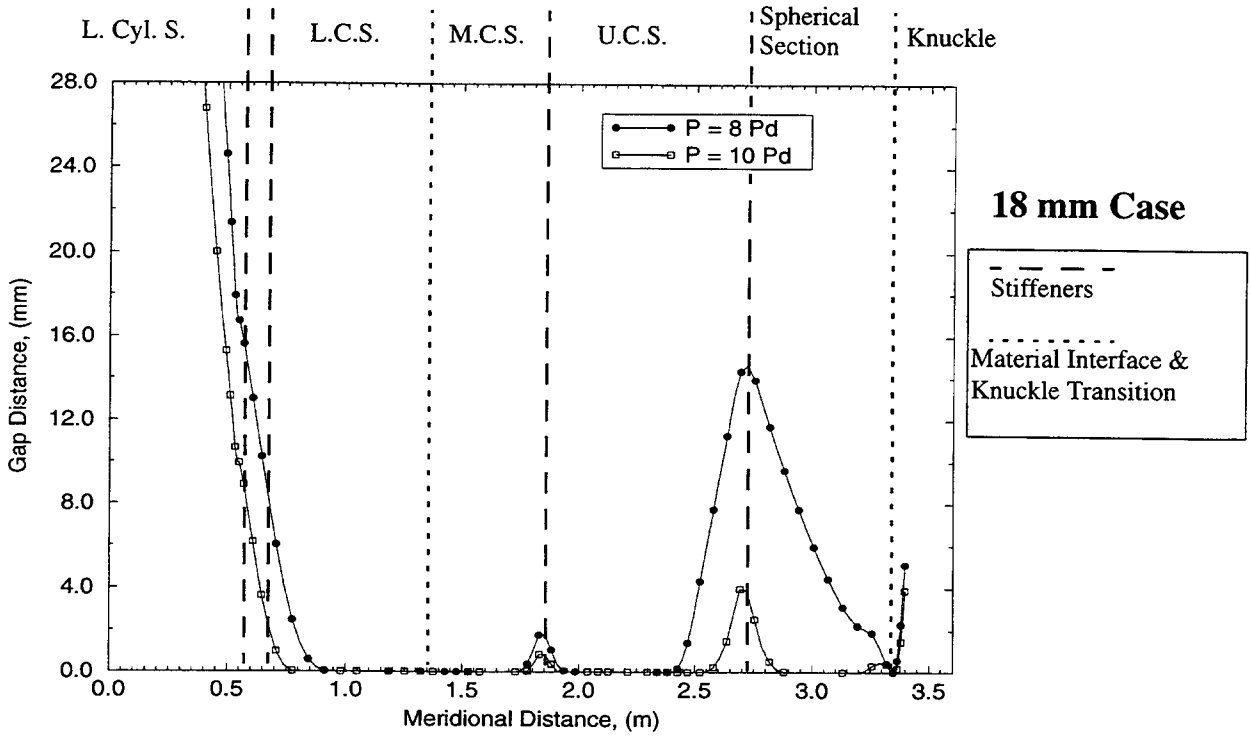

Figure 5-6. Gap closure distance along the SCV wall at 8 and 10 P_d. Locations (L.Cyl.S., etc.) are shown in Figure 5-1.

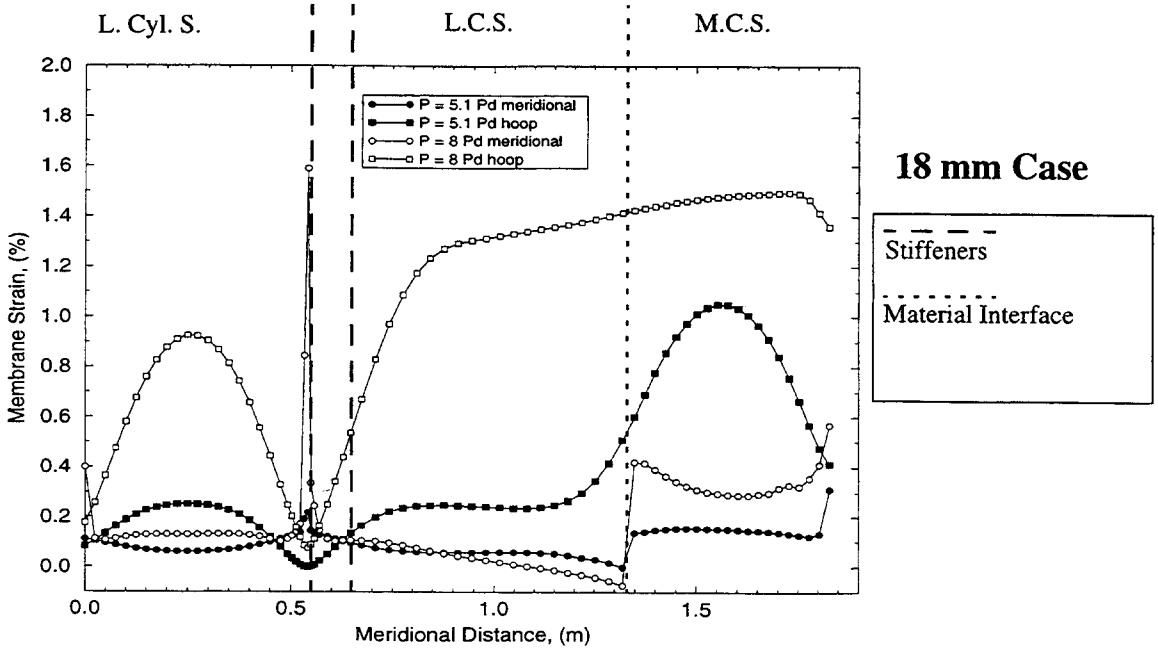

Figure 5-7. Meridional and hoop strain components (middle surface) along the SCV wall from the lower cylindrical section to the middle conical section at 5.1 and 8 P_d. Locations (L.Cyl.S., etc.) are shown in Figure 5-1.

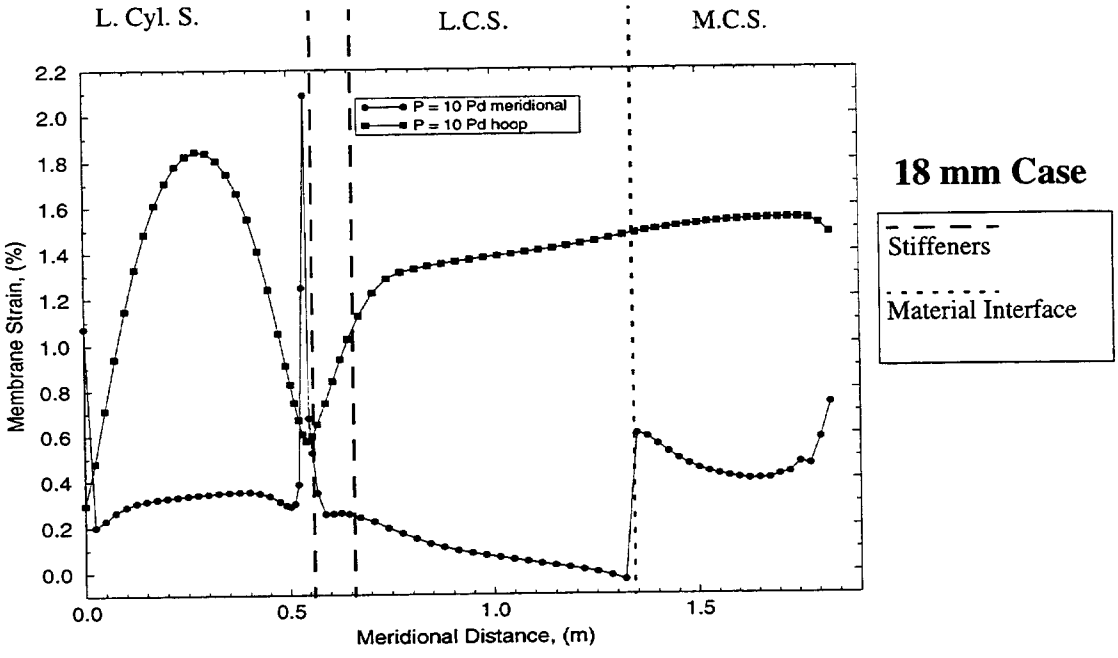

Figure 5-8. Meridional and hoop strain components (middle surface) along the SCV wall from the lower cylindrical section to the middle conical section at 10 P_d. Locations (L.Cyl.S., etc.) are shown in Figure 5-1.

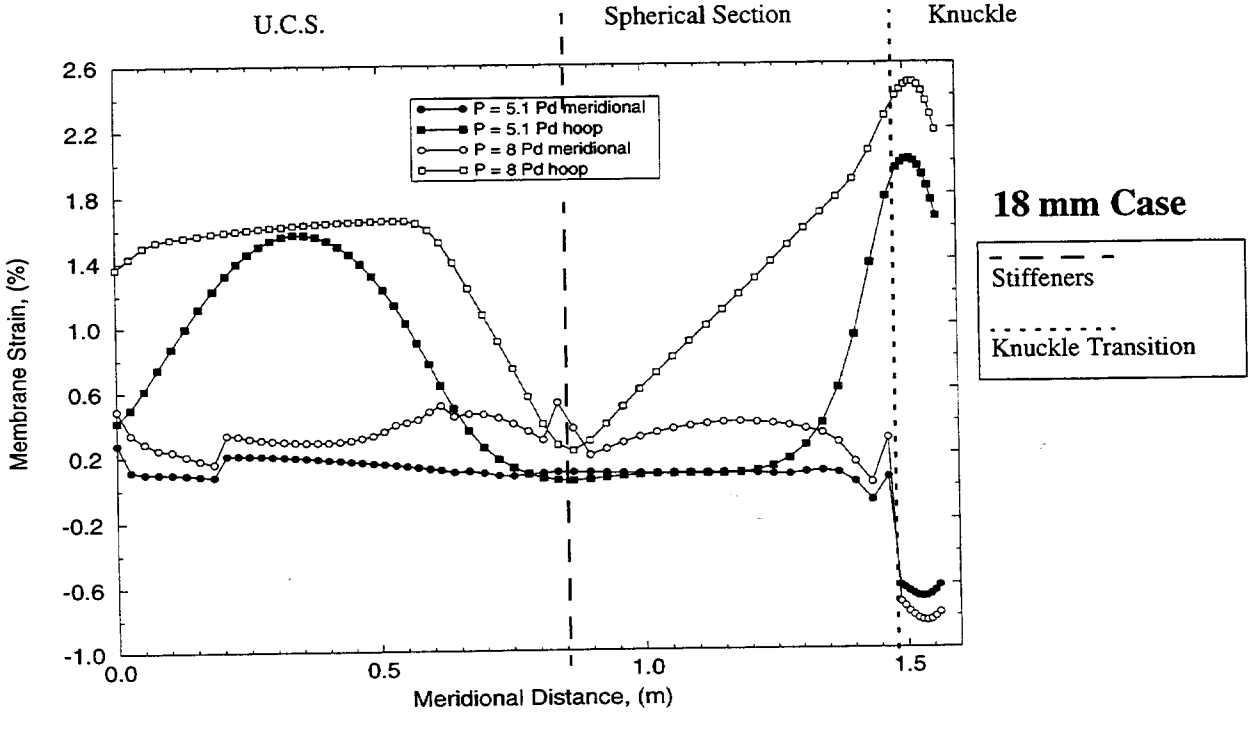

Figure 5-9. Meridional and hoop strain components (middle surface) along the SCV wall from the upper conical section to the knuckle at 5.1 and 8 P_d. Locations (U.C.S., etc.) are shown in Figure 5-1.

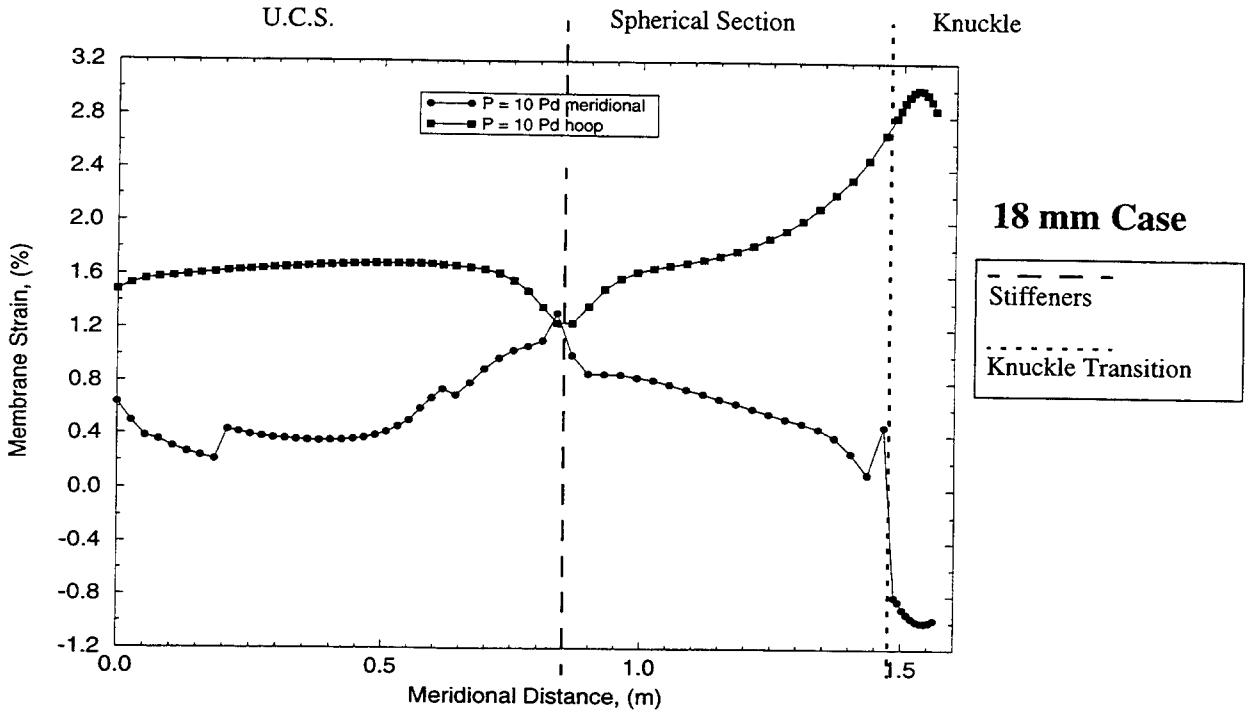

Figure 5-10. Meridional and hoop strain components (middle surface) along the SCV wall from the upper conical section to the knuckle at 10 P_d. Locations (U.C.S., etc.) are shown in Figure 5-1.

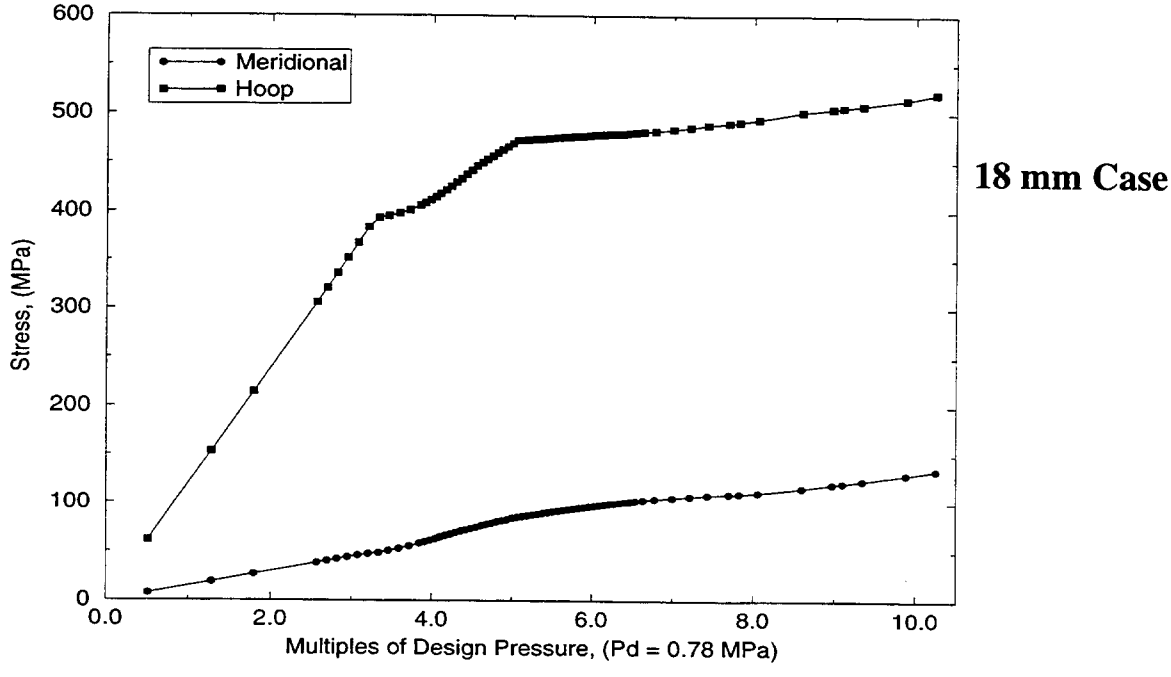

Figure 5-11. Stress history for one element in the middle of the knuckle showing meridional and hoop components at the middle surface.

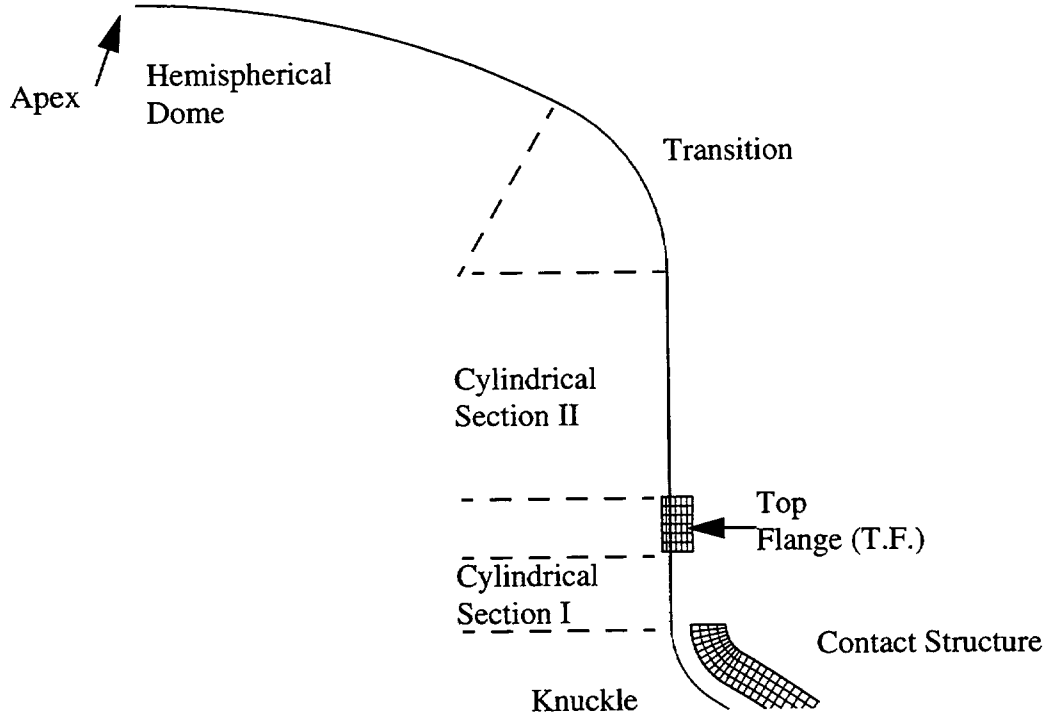

Figure 5-12. Detail of top head with labels showing Cylindrical Section I, Top Flange, Cylindrical Section II, Transition, and Hemispherical Dome.

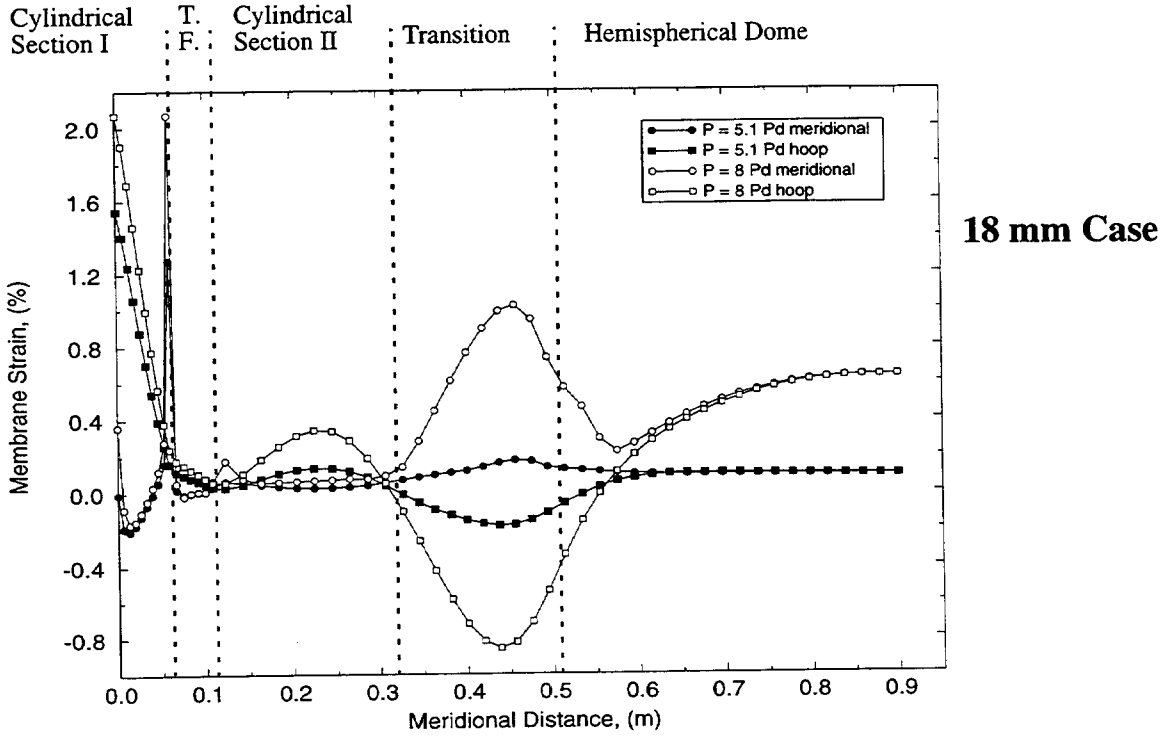

Figure 5-13. Meridional and hoop strain components (middle surface) from the top of the knuckle to the apex of the hemispherical dome at 5.1 and 8 P_d.

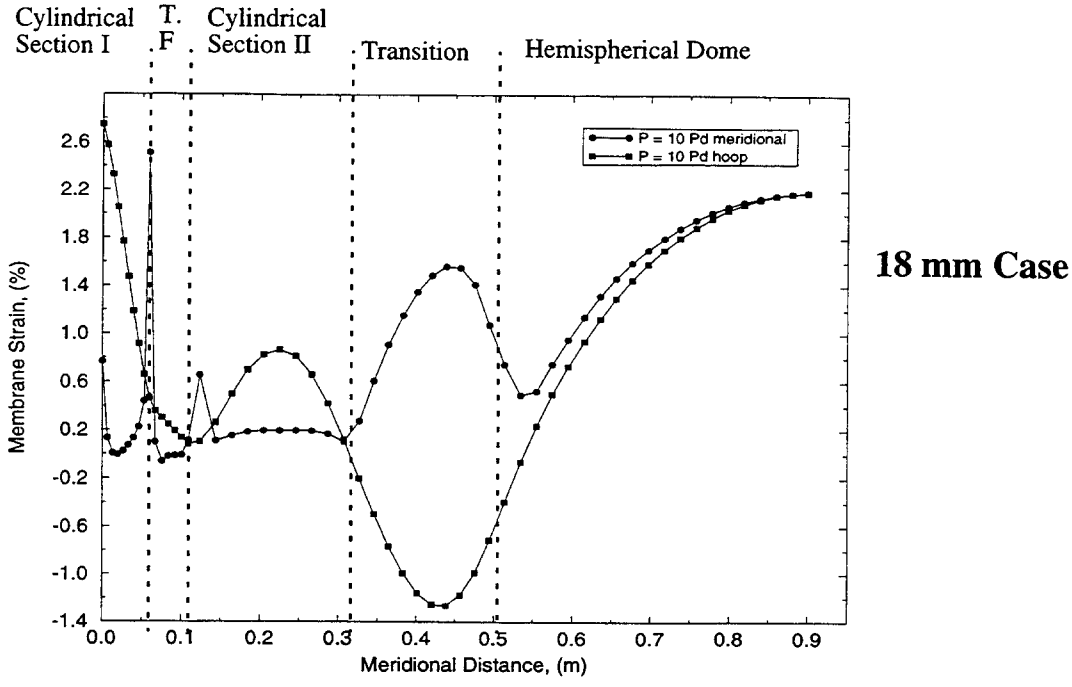

Figure 5-14. Meridional and hoop strain components (middle surface) from the top of the knuckle to the apex of the hemispherical dome at 10 P_d. Locations are shown in Figure 5-12.

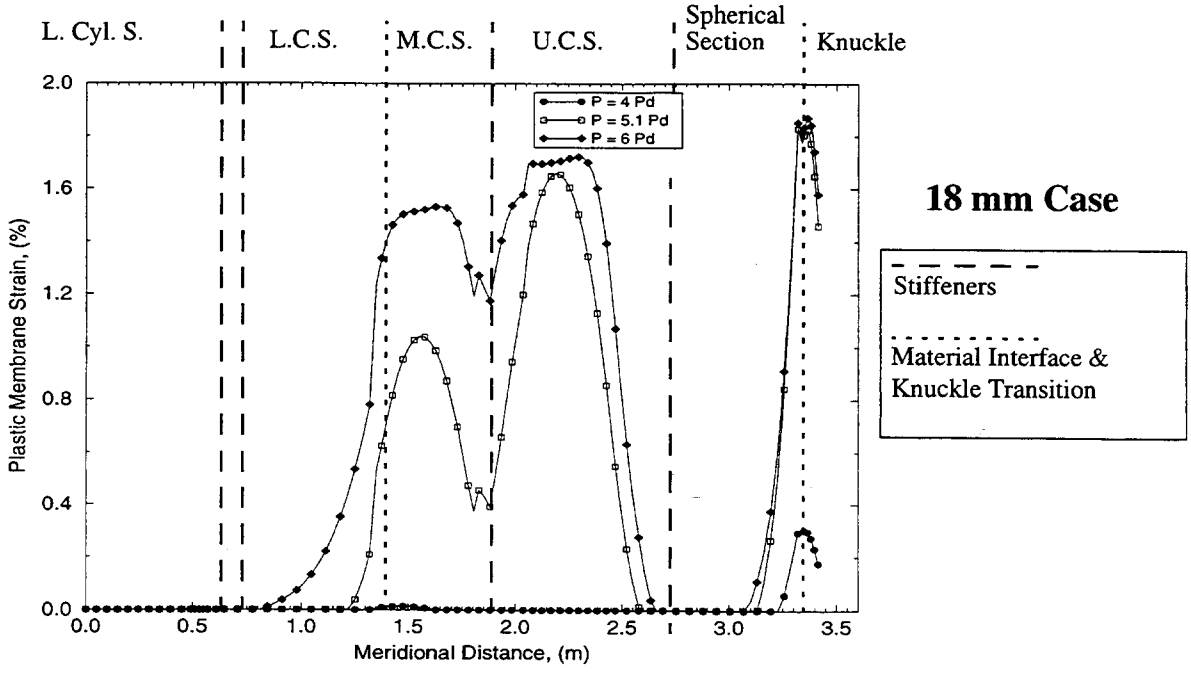

Figure 5-15. Plastic membrane strain along the SCV wall from the lower cylindrical section to the knuckle at 4, 5.1, and 6 P_d. Locations (L. Cyl. S., etc.) are shown in Figure 5-1.

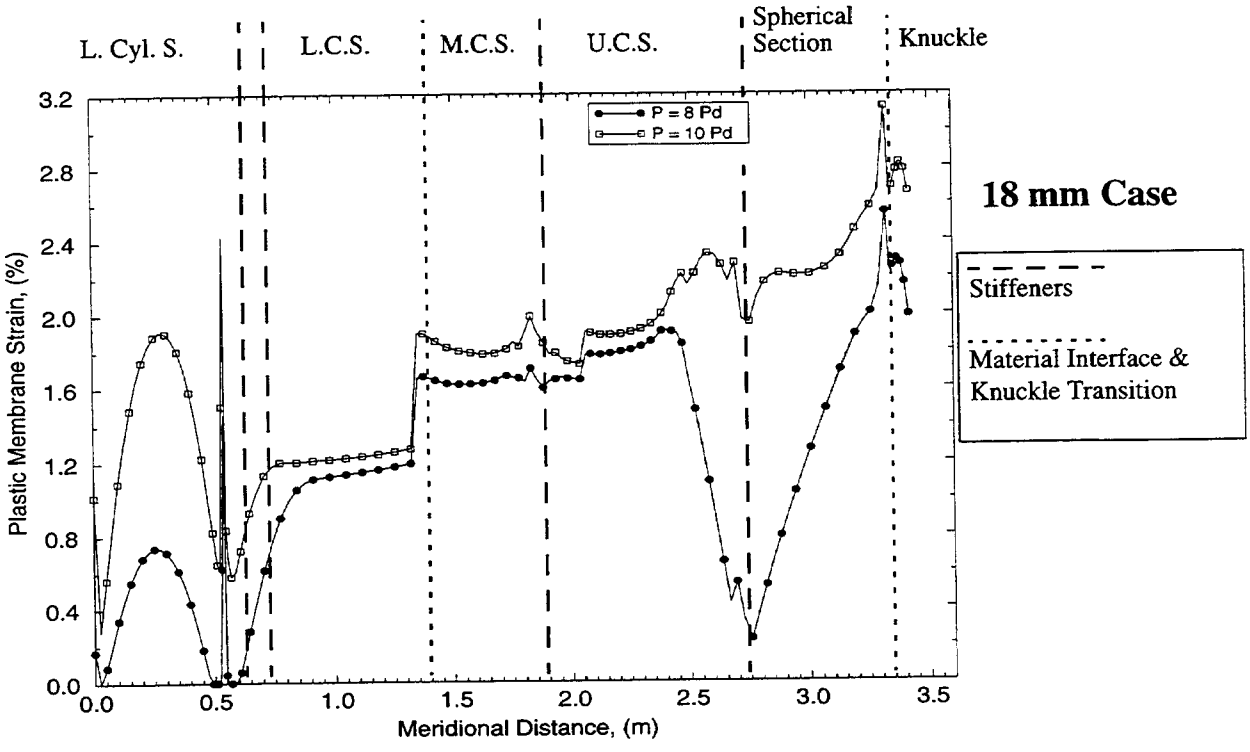

Figure 5-16. Plastic membrane strain along the SCV wall from the lower cylindrical section to the knuckle at 8 and 10 P_d. Locations (L. Cyl. S., etc.) are shown in Figure 5-1.

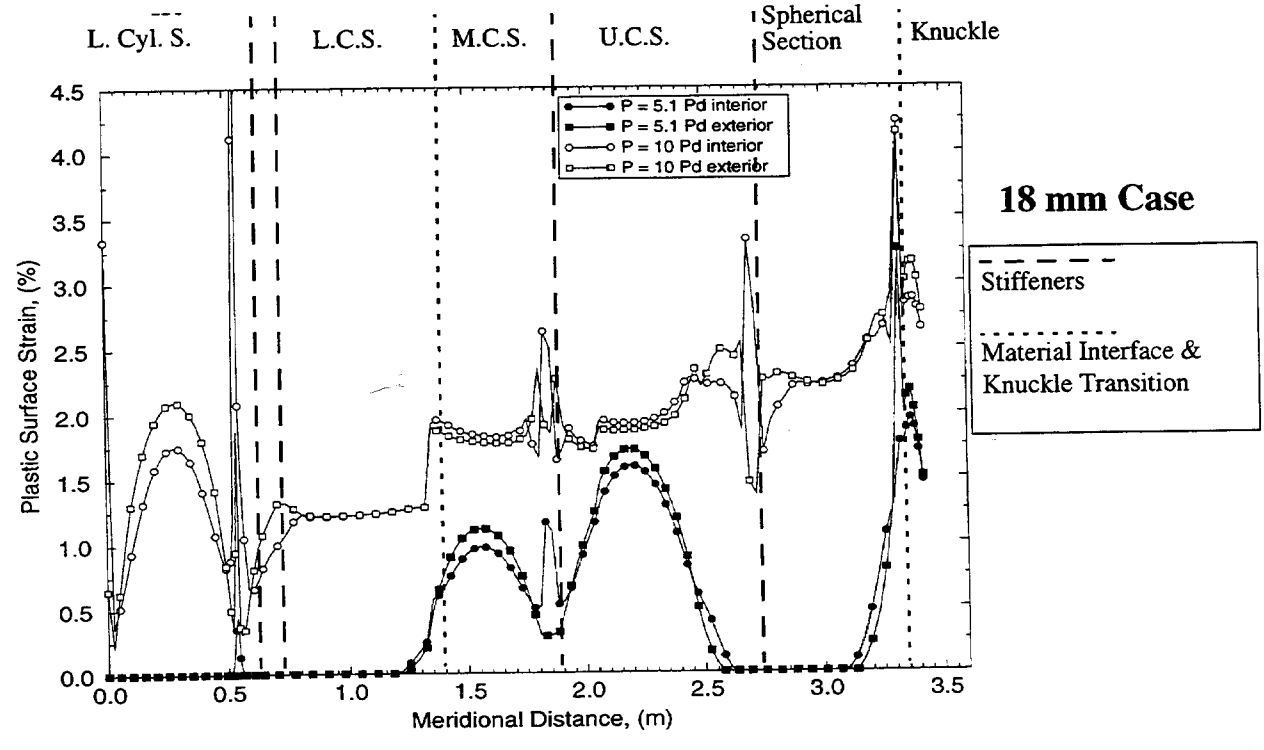

Figure 5-17. Plastic surface strain along the SCV wall from the lower cylindrical section to the knuckle at 8 and 10 P_d. Locations (L. Cyl. S., etc.) are shown in Figure 5-1.

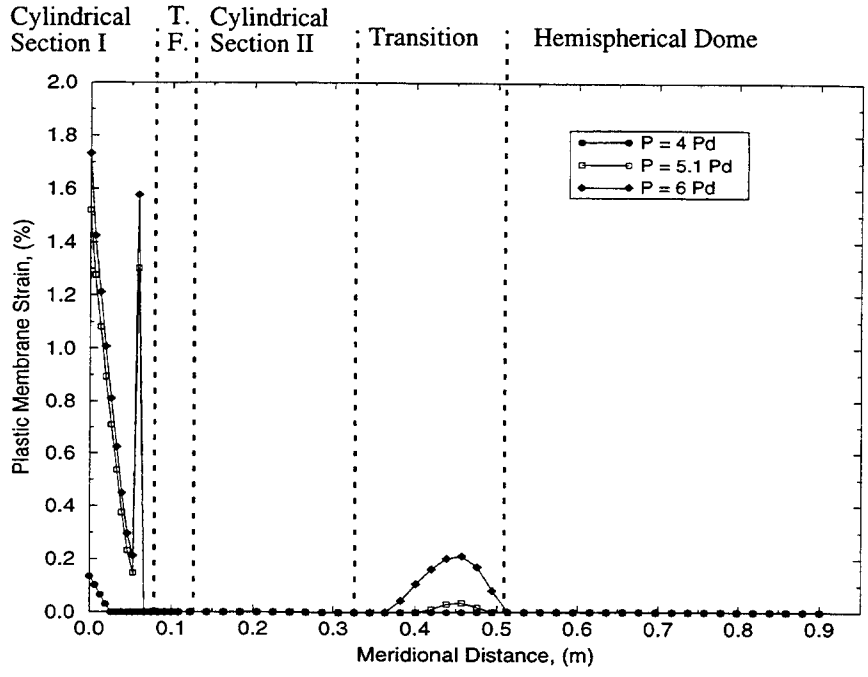

Figure 5-18. Plastic membrane strain as a function of meridional distance from the top of the knuckle to the apex of the top head at 4, 5.1, and 6 P_d. Locations are shown in Figure 5-12.

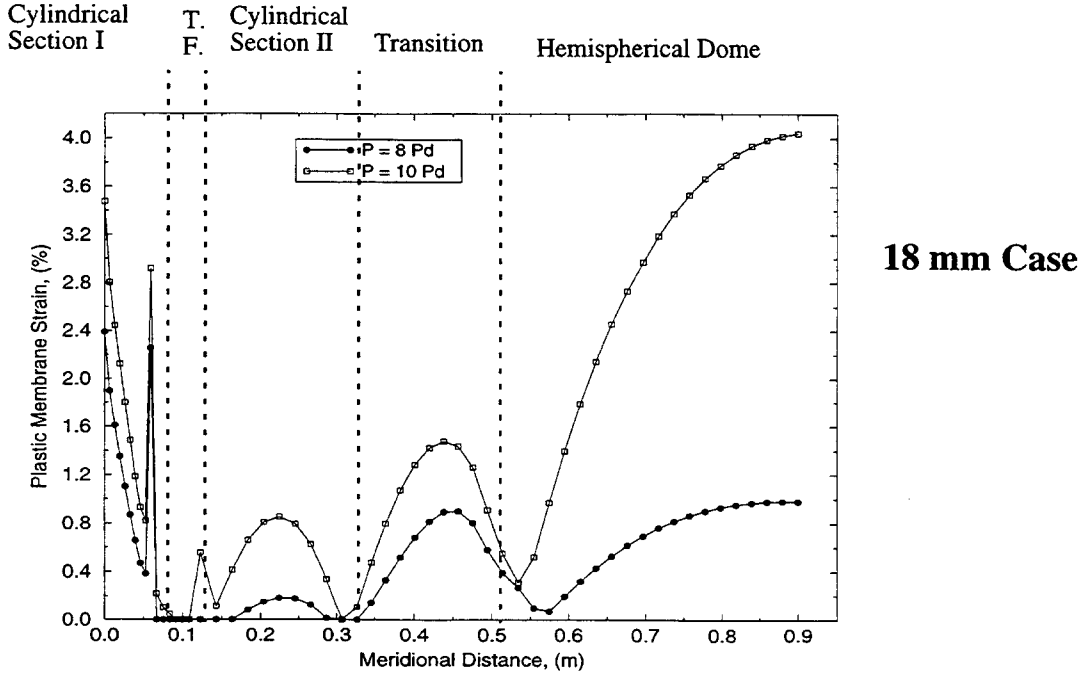

Figure 5-19. Plastic membrane strain as a function of meridional distance from the top of the knuckle to the apex of the top head at 8 and 10 P_d. Locations are shown in Figure 5-12.

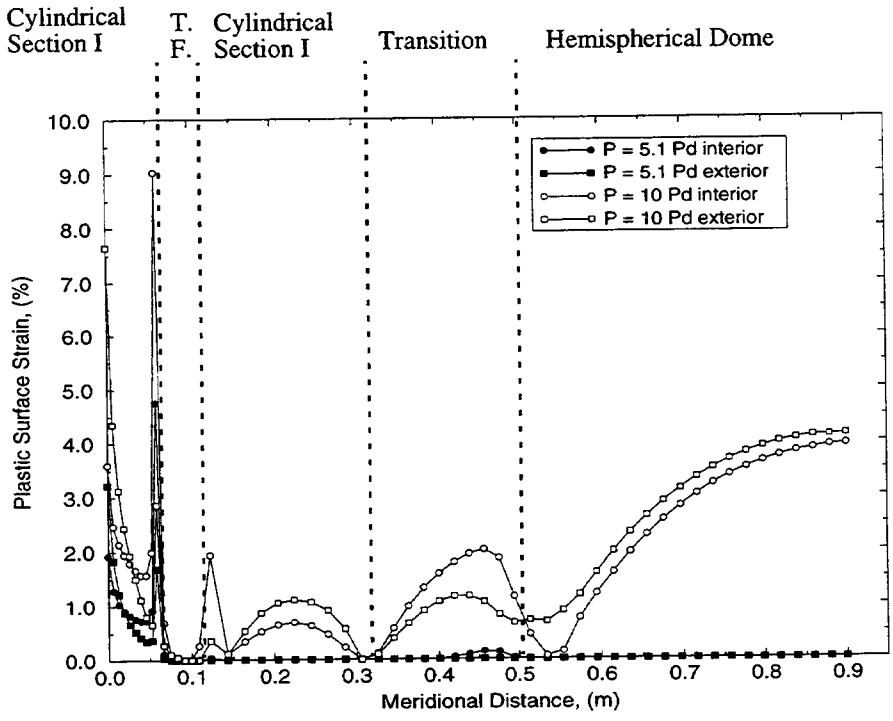

Figure 5-20. Plastic surface strain as a function of meridional distance from the top of the knuckle to the apex of the top head at 5.1 and 10 P_d. Locations are shown in Figure 5-12.

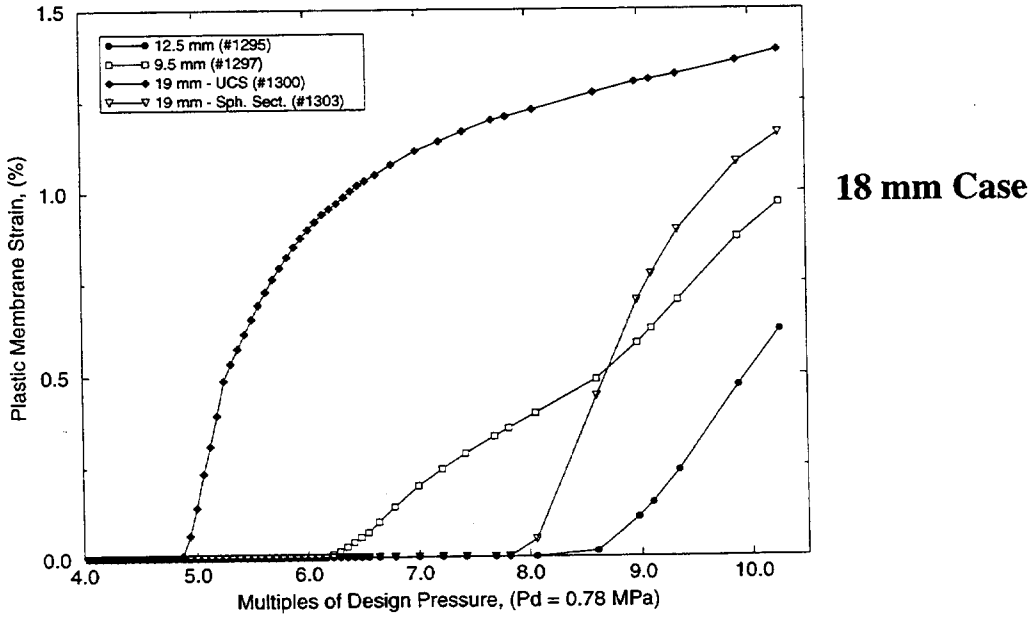

Figure 5-21. Plastic membrane strain history for the element with the highest equivalent plastic strain magnitude in each of the four SCV wall stiffeners.

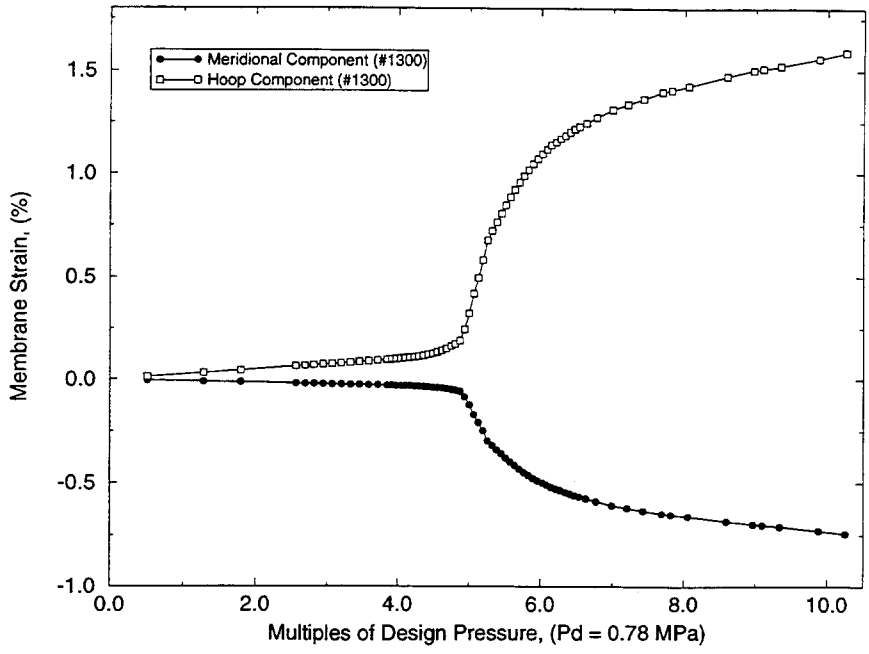

Figure 5-22. Meridional and hoop component strain history for the element with the highest plastic strain history of all of the stiffeners (from the 19 mm stiffener in the U.C.S).

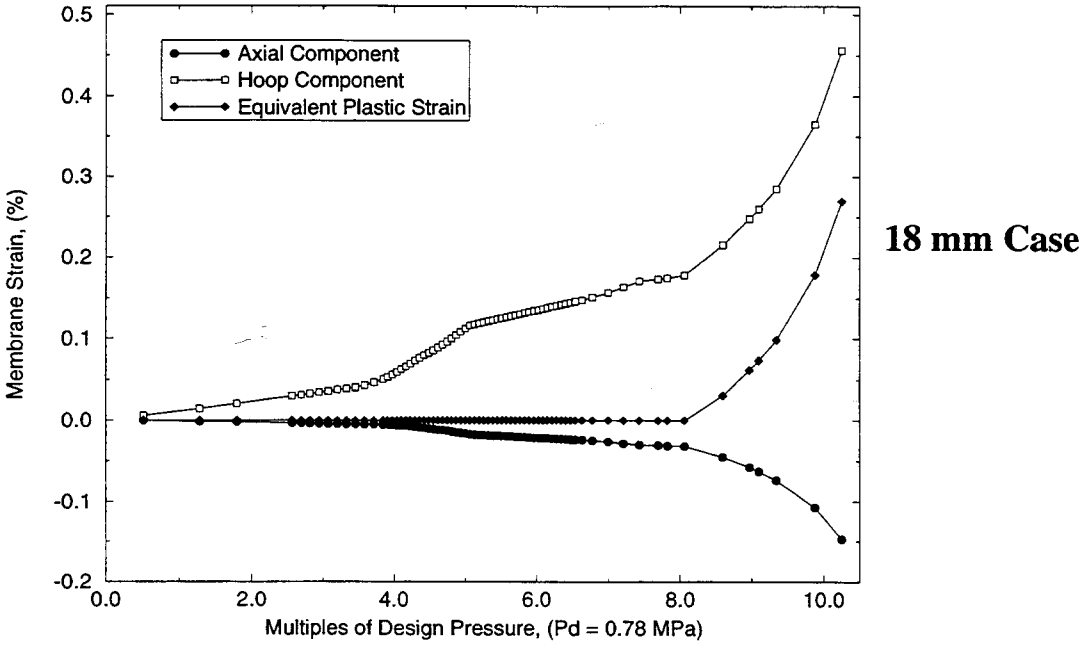

Figure 5-23. Axial, hoop, and equivalent plastic strain for the element with the highest equivalent plastic strain in the top flange.

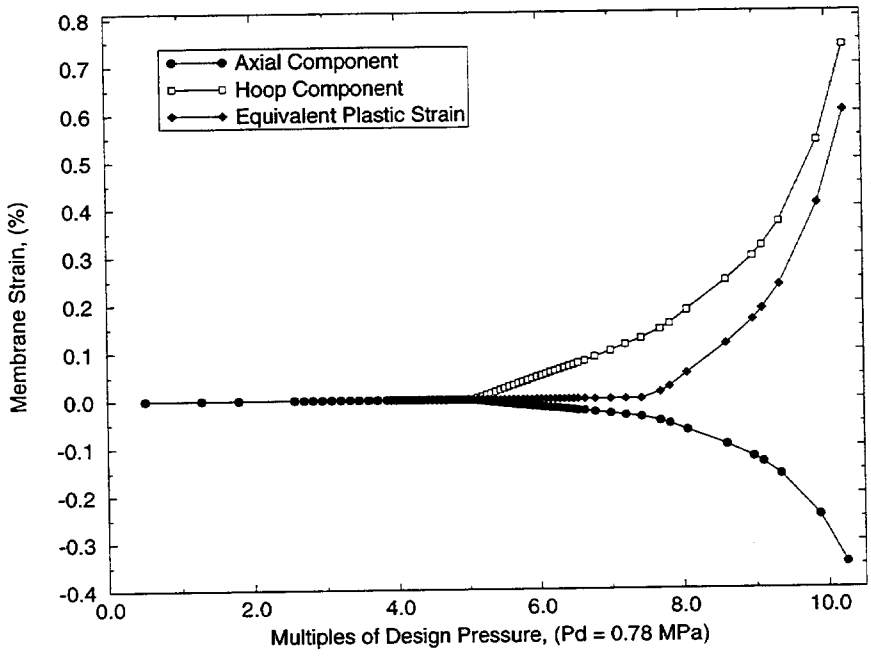

Figure 5-24. Axial, hoop, and equivalent plastic strain for the element with the highest equivalent plastic strain in the contact structure.

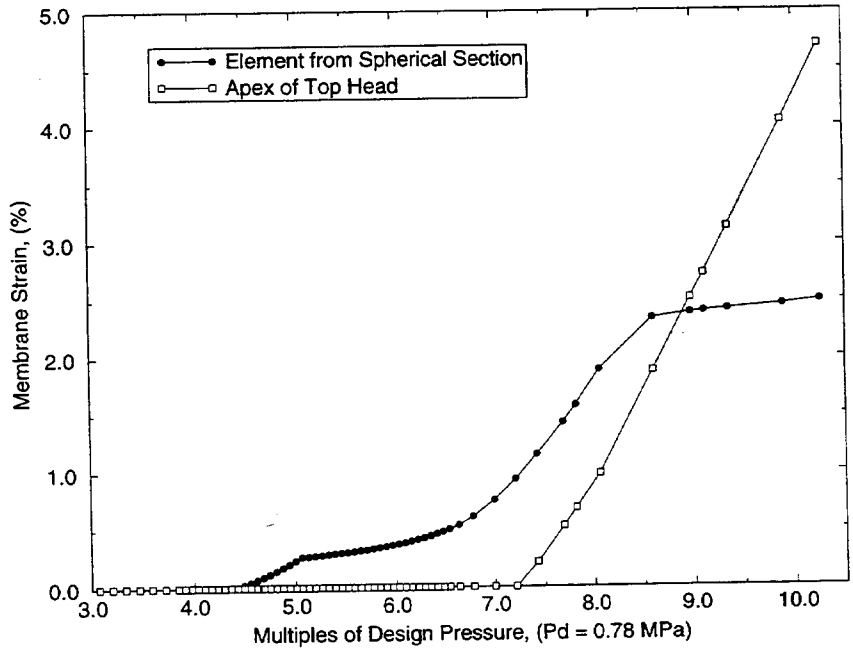

Figure 5-25. Equivalent plastic membrane strains for two representative elements. The element at the apex of the top head has the highest plastic membrane strain for the entire structure.

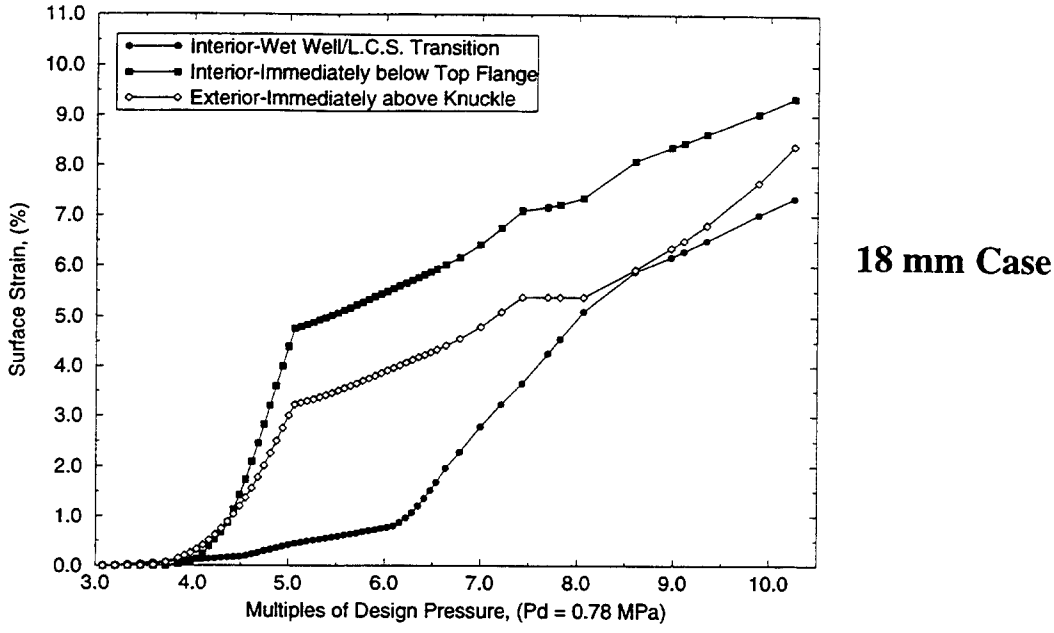

Figure 5-26. Equivalent plastic surface strains for three representative elements. The interior surface of the element immediately below the top flange has the highest plastic surface strain for the entire structure.

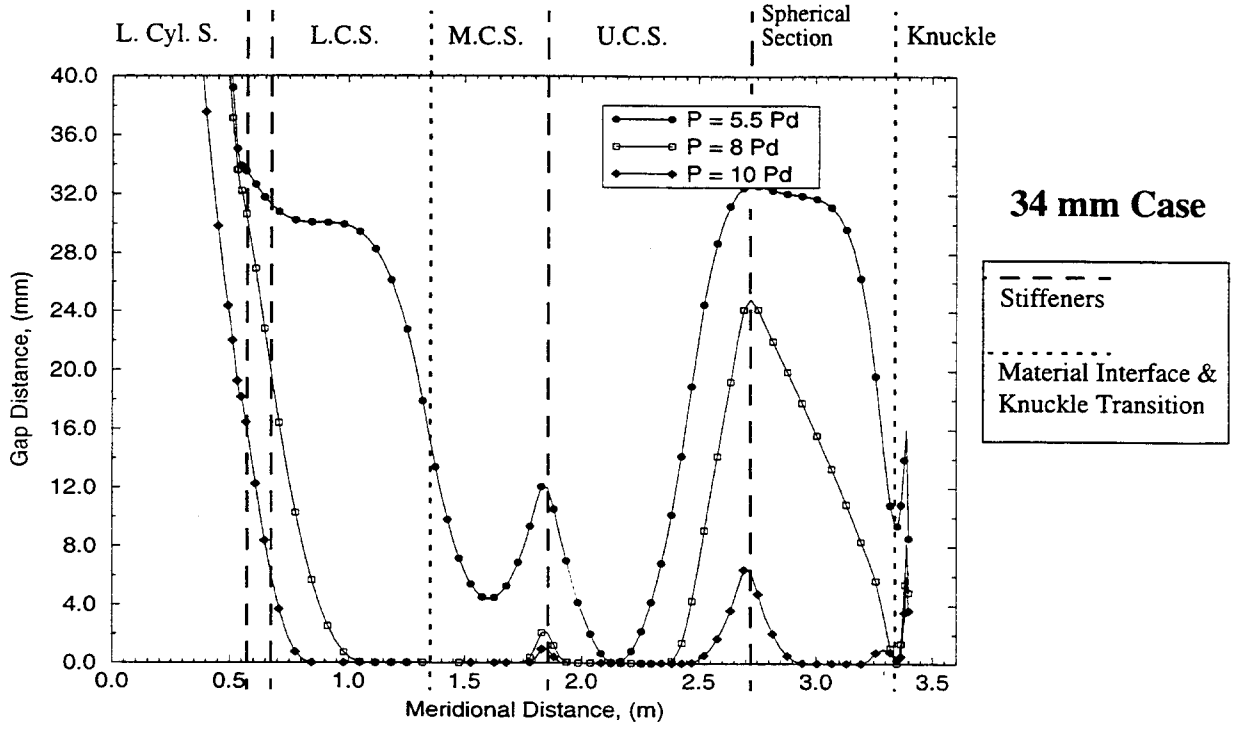

Figure 5-27. Gap closure distance along the SCV wall from the lower cylindrical section to the top of the knuckle at 5.5, 8, and 10 P_d. Locations (L. Cyl. S., etc.) are shown in Figure 5-1.

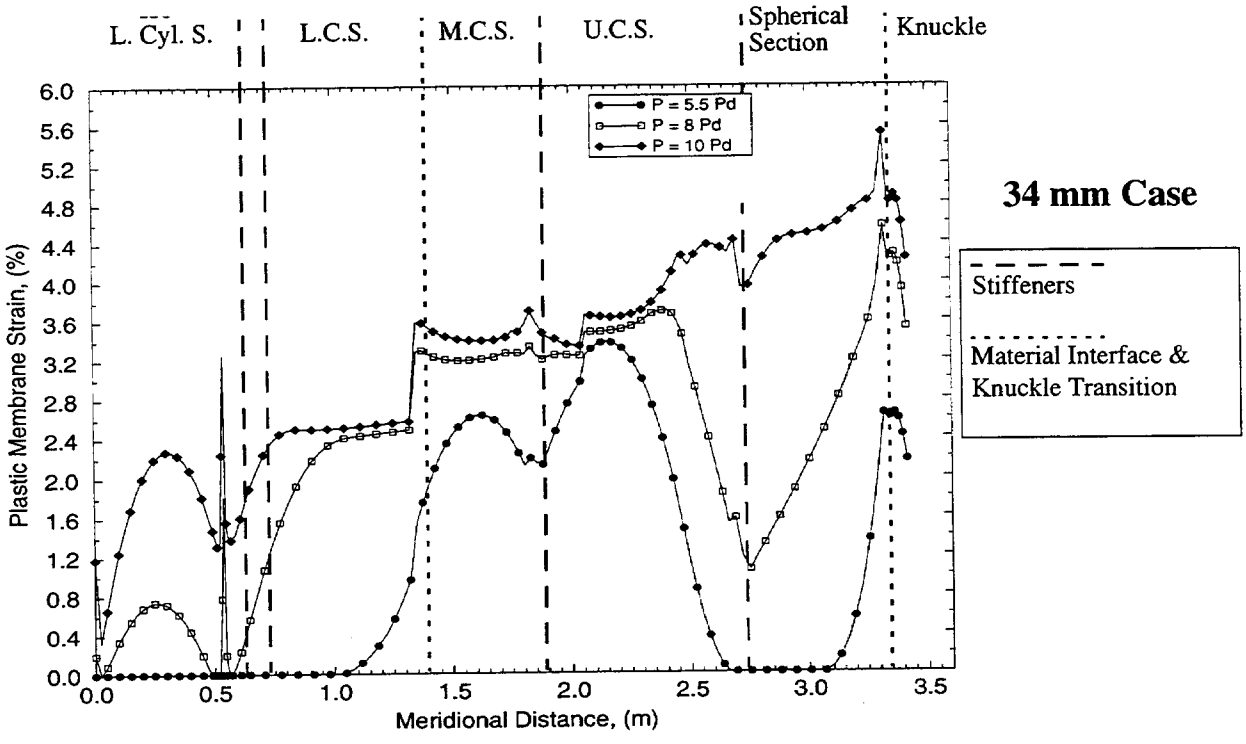

Figure 5-28. Equivalent plastic membrane strain as a function of meridional distance from the lower cylindrical section to the top of the knuckle at 5.5, 8, and 10 P_d. Locations (L. Cyl. S., etc.) are shown in Figure 5-1.

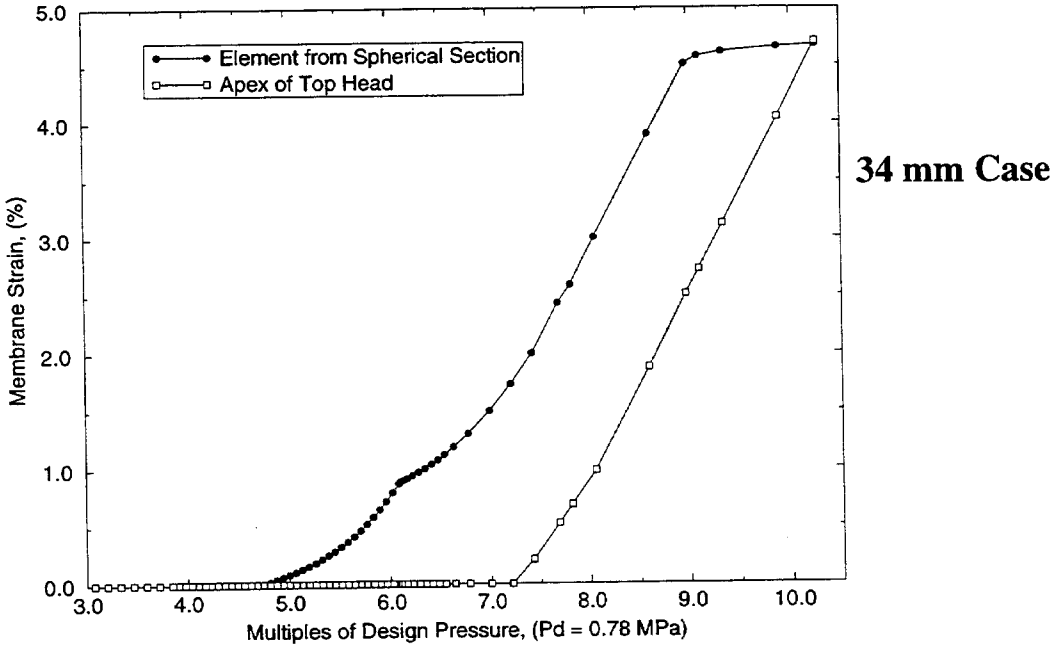

Figure 5-29. Equivalent plastic membrane strains for two representative elements.

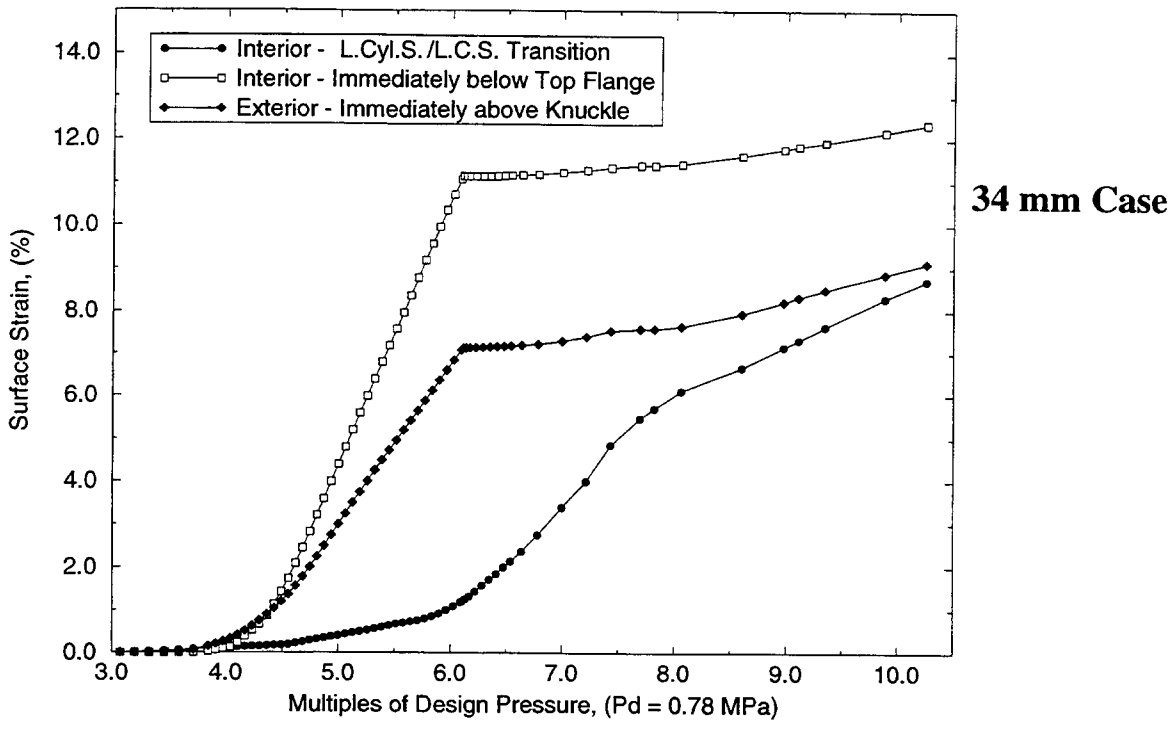

Figure 5-30. Equivalent plastic surface strains for three representative elements. The interior surface of the element immediately below the top flange has the highest plastic surface strain for the entire structure.

6. Global Three-Dimensional Shell (G3DS) Analysis

A global three-dimensional shell analysis was the only way to assess the steel containment vessel (SCV) behavior including the equipment hatch explicitly in the model. In addition to providing insight into global model behavior, this model also provided the boundary conditions for the local three-dimensional models described in Section 7.

6.1 Finite Element Model Description

The finite element model of the SCV and contact structure (CS) for the G3DS model appears in Figure 6-1. The half-symmetry model used approximately 4800 four-node reduced integration shell elements with finite membrane strain capability (ABAQUS S4R elements). The only non-axisymmetric detail of the SCV/CS assembly and this finite element model is the equipment hatch. Symmetric boundary conditions were imposed on all nodes lying in the vertical (*x-y*) plane passing through the centerline of the equipment hatch, and vertical displacements were constrained at the support locations on the underside of the ring support girder. The loading consisted of gravity and internal pressure, and the analysis ran until it failed to converge at approximately 12.7 MPa internal pressure or slightly over 16.3 P_d. The nominal gap between the SCV and the CS was 18 mm. For this model, the available small sliding formulation was deemed appropriate because the relative sliding of the SCV and CS was assumed to be small. The friction coefficient, discussed previously in Section 4.2.1, was μ=0.2. Computations for this model were performed with ABAQUS/Standard, Version 5.4 (1994).

The thickened equipment hatch insert plate was constructed such that it is flush with the inside surface of the SCV. The resulting thickness eccentricity poses a problem when using shell elements in ABAQUS because there is no way to explicitly model a shell with uneven material distribution about a reference line. A simple elastic test case showed that using the *SHELL SECTION, COMPOSITE option in ABAQUS is an accurate way of implicitly modeling the eccentricity at the equipment hatch insert plate[16]. The equipment hatch insert plate was modeled as a composite shell with three layers. As shown in Figure 6-2, the eccentricity was introduced by making the middle layer the same thickness (t_w) as the adjacent material and then placing two layers with the same thickness on either side, such that the total thickness of the middle and outer layers is equal to the insert plate thickness (t_p). The middle and outside layers were given the modulus of elasticity for the equipment hatch insert plate (measured from the Hitachi tensile tests in Appendix B), $E_{plate} \sim 216 \times 10^9$ Pa, while the inner composite layer was given a dummy modulus of $E_{dummy} \sim 1$ Pa. This formulation makes the stiffness of the inner layer of the composite shell negligible with respect to the other two layers.

Because of the eccentricity at the insert plate, the gap between the insert plate in the SCV model and the as-designed CS is reduced considerably from 18 mm to approximately 9 mm. However, because the contact algorithm uses the centerline of both the composite shells in the SCV insert plate and the regular shells in the CS as the reference, the eccentricity formulation described above does not represent the smaller gap. The gap between the insert plate and the CS in the finite element model remains 18 mm rather than 9 mm.

As with the axisymmetric model described in Section 5.1, there were two important changes made late in the design of the CS that were not incorporated in this model. The CS material and its geometry near the knuckle of the SCV in the global three-dimensional shell model were the same as in the axisymmetric model (see Figure 5-2 for knuckle details). It is unlikely that the difference in materials would significantly affect the results. However, the geometry near the knuckle is especially important and is modeled more accurately and completely in a local axisymmetric continuum model of the top head described in Section 7.1.

6.2 Results

Table 6-1 summarizes the yielding and contact events for the global three-dimensional shell analysis. Results for deformed shape, contact history, and high strain or critical areas are discussed in the following sections.

[16] Carter, P.A., "Eccentricity Test Case," Sandia memorandum to V.K. Luk and M.F. Hessheimer, July 17, 1995.

Table 6-1. Summary of Yielding/Contact Events for Global 3-D Shell (G3DS) Model

Internal Pressure	Event
0 - 2.3 MPa	Elastic behavior
2.3 MPa	Local yielding in top/bottom of E/H sleeve at attachment to insert plate
2.3 MPa	Local yielding at middle conical section attachment to E/H insert plate
2.7 MPa	Yielding in knuckle
2.8 MPa	Local yielding at bottom of E/H insert plate
3.0 MPa	Local yielding in upper conical section above E/H
3.1 MPa	Yielding in middle conical section around circumference
3.4 MPa	Yielding in upper conical section around circumference
3.7 MPa	Yielding in lower conical section near insert plate
3.9 MPa	Yielding in lower conical section around circumference
4.1 MPa	Contact initiates in the SCV in the upper conical section and knuckle
4.1 MPa	Circumferential contact in upper conical section
4.3 MPa	Circumferential contact in middle conical section
4.7 MPa	Yielding in lower cylindrical shell around circumference
5.1 MPa	Yielding in dome of top head
5.3 MPa	Circumferential contact in lower conical section
5.5 MPa	Yielding in spherical section (away from knuckle)
6.6 MPa	Contact initiates in spherical section
11.3 MPa	Circumferential contact in lower cylindrical shell

6.2.1 Displacements

Figure 6-3 shows the deformed shape of the SCV at six different pressure levels. All displacements have been magnified by a factor of five. For clarity, the CS, ring support girders, and gusset plates are not shown. At 3 MPa, when only localized yielding has occurred, very little deformation is discernible. At 4.1 MPa, when contact first occurs, there is noticeable deformation in the upper and middle conical sections. The effect of the stiffeners is evident in the upper conical section as it tries to expand outward but is restrained by two 19 mm stiffeners. The knuckle shows deformation in both the outward (radial) and vertical directions, while the top head and top head flange deform nearly exclusively in the vertical direction. The equipment hatch also appears to be rotating outward and downward at this pressure. By 6 MPa, most of the upper and middle conical sections are contacting the CS. The outward expansion of the lower cylindrical shell is now apparent. At 8 MPa it is clear that the CS is arresting further radial expansion of most of the SCV. The apex and the cylindrical portion of the top head, which are not shielded by the CS, are showing excessive amounts of deformation. At 10 MPa, which is nearly 13 multiples of the design pressure, the only locations where further deformations are clear are the top head and the lower cylindrical shell.

Vertical displacement at the apex of the top head and horizontal displacement at the center of the equipment hatch cover are shown in Figure 6-4. Displacements at both locations are linear until approximately 3.0 MPa. From 3.0 MPa to approximately 4.0 MPa, the vertical

displacement of the apex increases more rapidly due to yielding in the SCV wall. When contact initiates in the knuckle region and upper conical section, the meridional strains are constrained so the rate of vertical displacement at the apex decreases significantly. At 5.1 MPa, yielding begins in the top head so the vertical displacement at the apex increases rapidly. Similarly, the horizontal displacement at the equipment hatch increases rapidly from approximately 3.1 to 5.5 MPa due to yielding in the lower and middle conical sections. Above 5.5 MPa, local contact occurs at the equipment hatch centerline thus restraining further radial growth.

6.2.2 Contact History

Figure 6-5 shows the progression of contact. Only the part of the SCV that is shielded by the CS is displayed. Dark areas indicate contact while light areas indicate no contact. The first plot shows contact initiating in the upper conical section and the knuckle. The area of contact has increased considerably at 5 MPa to include the middle conical section, and by 6 MPa contact includes the lower conical section. By 8 MPa, the spherical section has made uniform circumferential contact except near the upper 19 mm stiffener, which is still arresting the radial growth of the SCV. At 10 MPa, the only area of the SCV that has not contacted the CS is the lower cylindrical shell where the initial gap is well over 100 mm.

6.2.3 Strains

Figure 6-6 and Figure 6-7 show locations at which various components of free-field strains are discussed. These strains are plotted in Figure 6-8, Figure 6-9, and Figure 6-10. In all locations, the hoop strain increases rapidly when yielding occurs, and then becomes nearly constant when contact occurs. The highest level of hoop strain occurs in the upper conical section because the gap dimension is the same but the radius of the containment vessel is smaller than in the lower sections. Some bending is evident in Figure 6-9 as shown by the difference in interior and exterior strains near the material interface and in Figure 6-10 at the midheight of the upper conical shell.

Figure 6-11 shows transition areas at which strains are plotted in Figure 6-12 through Figure 6-14. Of particular interest in these areas near stiffeners are the meridional strains at the interior and exterior surfaces. Differences in the strains at the two surfaces indicates the amount of bending strain. Near the lower stiffeners (Figure 6-12), bending becomes quite pronounced above 5.1 MPa, after yielding in the lower cylindrical shell. However, the gap in this area is quite large, so contact does not occur until 11.3 MPa. Above this pressure, the bending strain is slightly reduced. At the material change interface (Figure 6-13), the bending strains are not as pronounced although bending is evident between 4.0 and 8 MPa. Above the latter pressure, local contact occurs with the CS so the bending strain is severely restricted. Similar bending behavior occurs at the middle stiffener as shown in Figure 6-14.

6.2.4 Critical Plastic Strain Areas

Contour plots of equivalent plastic strain indicated three locations with high strains that dictated further study. Figure 6-15 compares the three locations which consistently displayed the highest plastic strains throughout the history: (1) the junction of the equipment hatch insert plate and the material change interface; (2) the apex of the top head; and (3) the knuckle region. The element at the knuckle and at the material change interface near the insert plate yields at roughly the same time, but the element at the knuckle contacts first, thus the plastic strain for this element levels out earlier in the loading. Because both elements are eventually shielded by the CS, neither accumulates nearly as much plastic strain as the apex of the top head. The apex yields at 5.1 MPa, compared to 2.5 MPa for the other two locations, but the amount of plastic strain quickly surpasses that accumulated at the other two locations, reaching a value of nearly 40% before the analysis fails to converge at just over 12.7 MPa. To assess the importance of these critical areas, refined models for both the top head, including the knuckle, and the area near the equipment hatch insert plate were created and are discussed in Section 7.

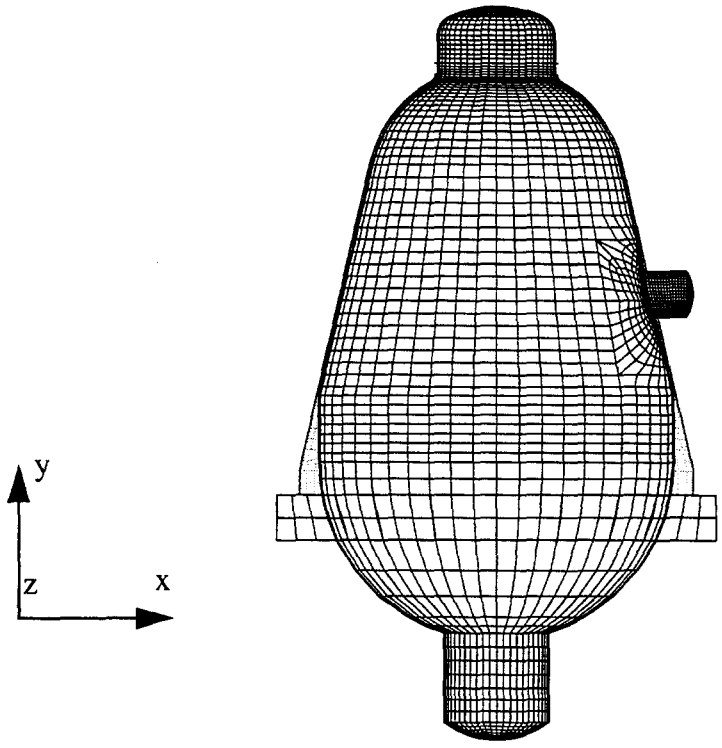

Figure 6-1. Global 3-D Shell (G3DS) model mesh. Note: contact structure appears behind SCV.

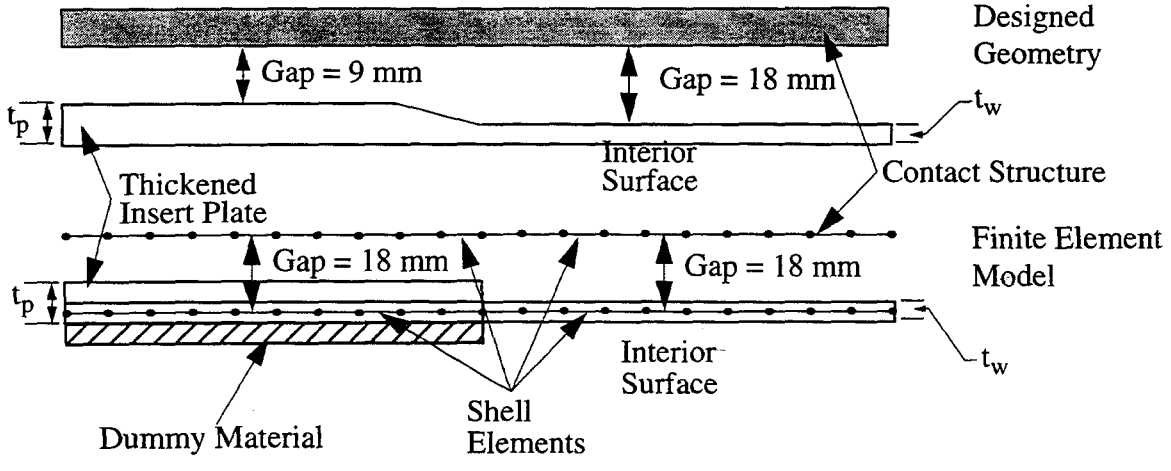

Figure 6-2. Cross section of thickened equipment hatch insert plate and attached conical section showing as-designed geometry (top) and as-modeled geometry (bottom) using shell elements.

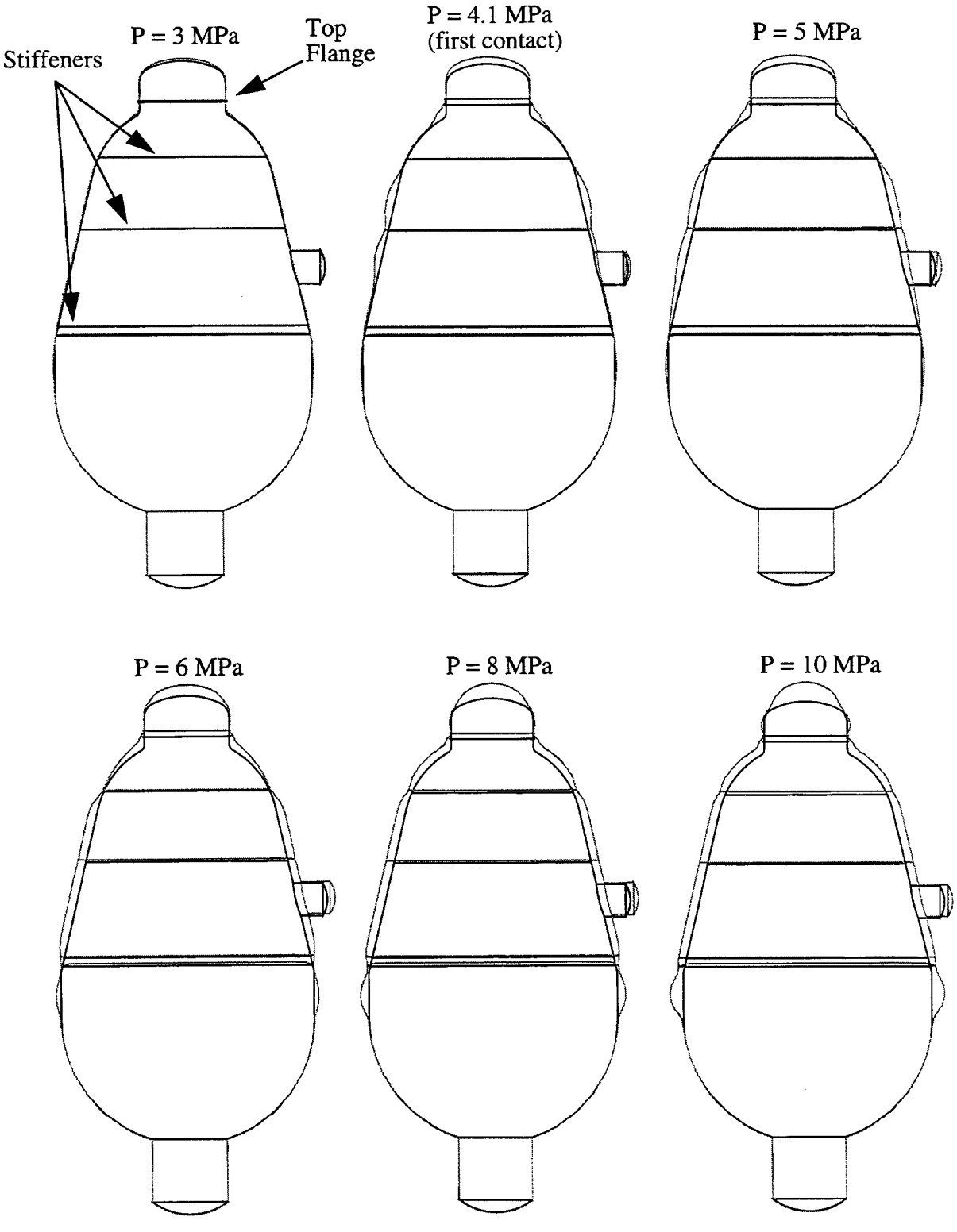

Figure 6-3. Deformed shape of G3DS at six pressure levels. Contact structure, ring support girders, and gusset plates are not shown. Displacements are magnified by five.

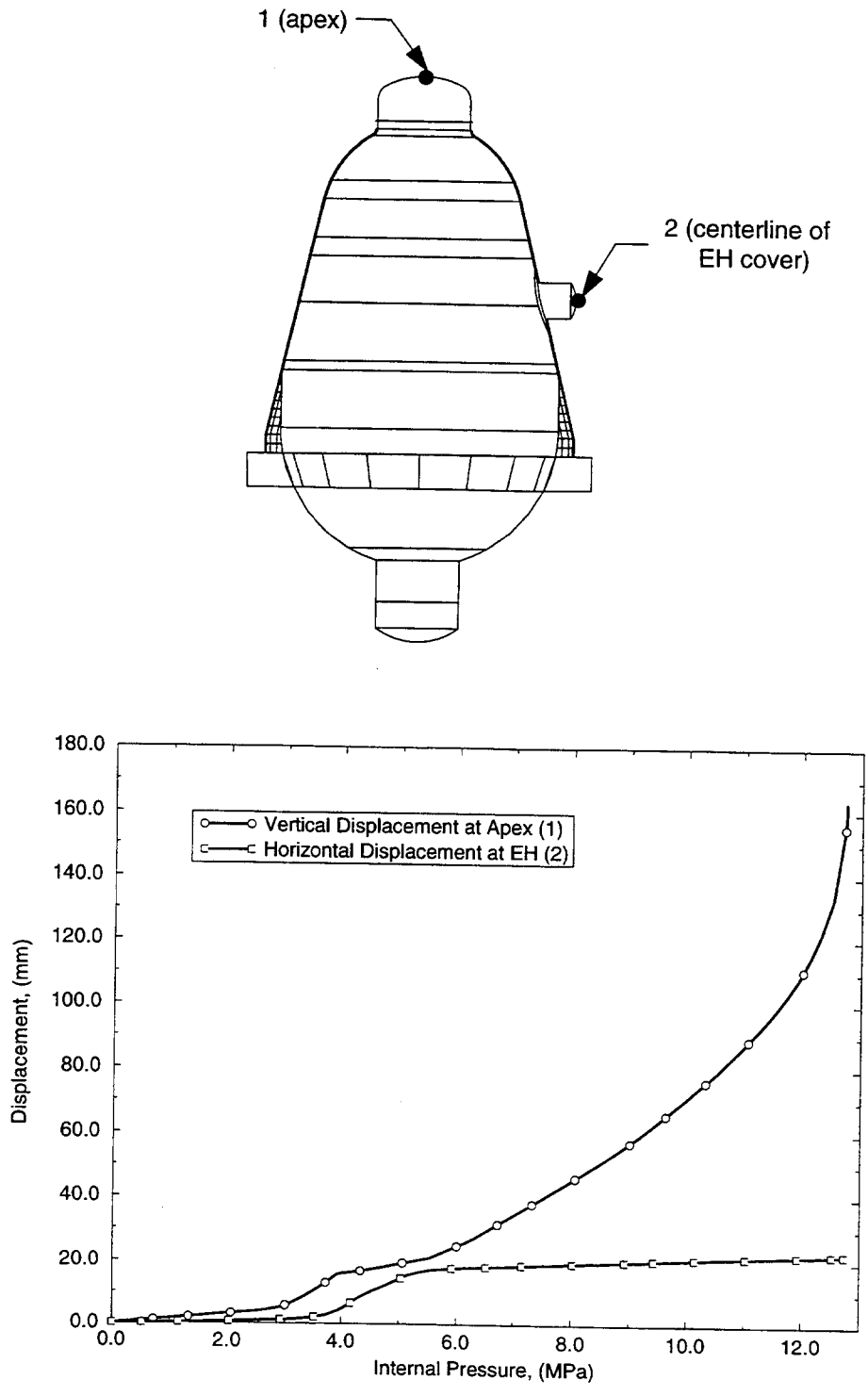

Figure 6-4. Displacements at apex and at the equipment hatch.

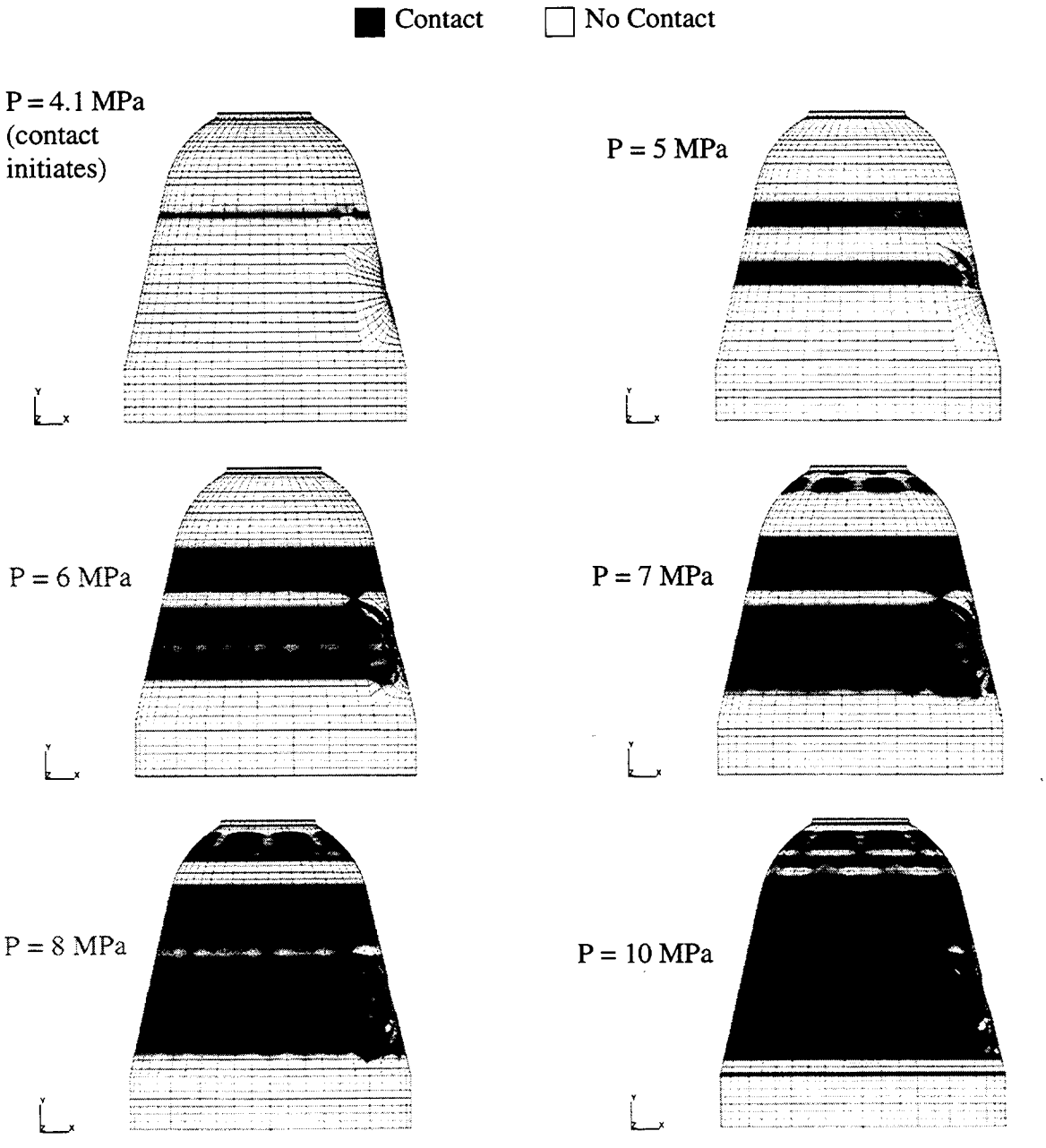

Figure 6-5. Contact evolution.

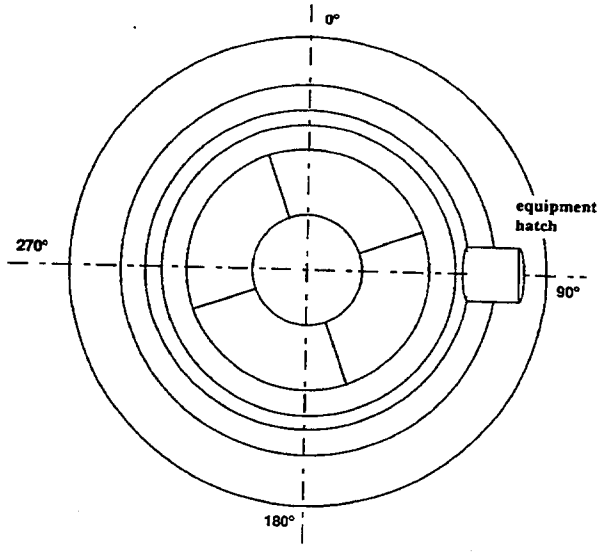

Figure 6-6. Top view of SCV model showing angular coordinates.

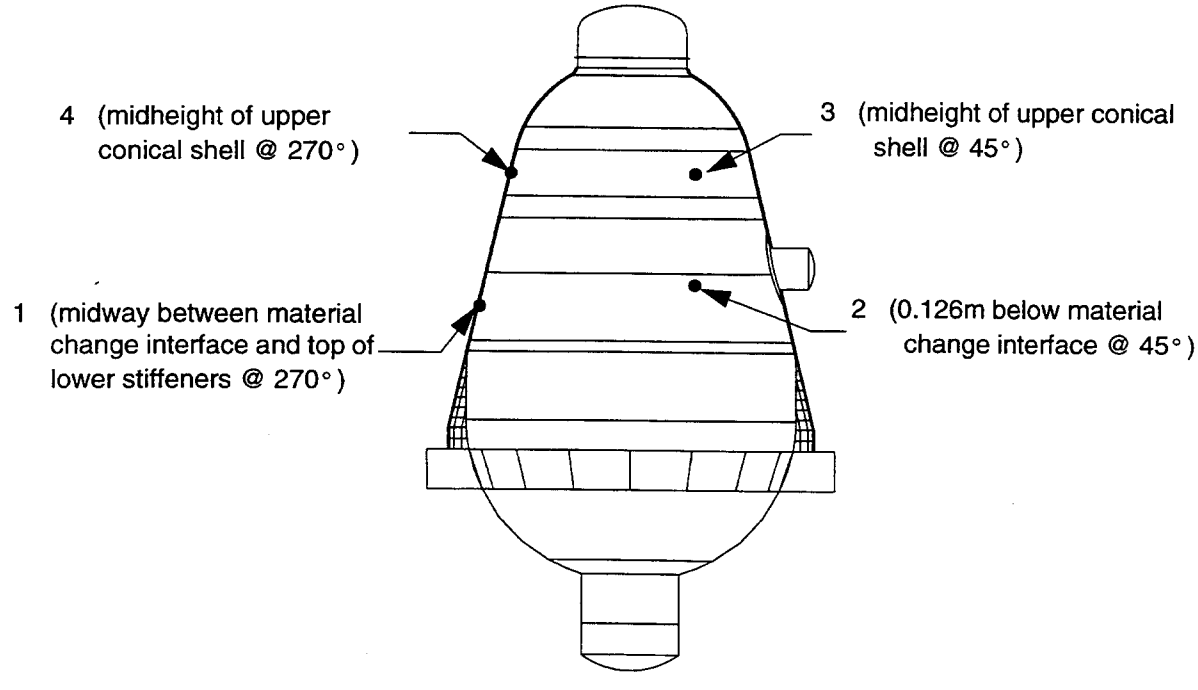

Figure 6-7. Free-field strain locations.

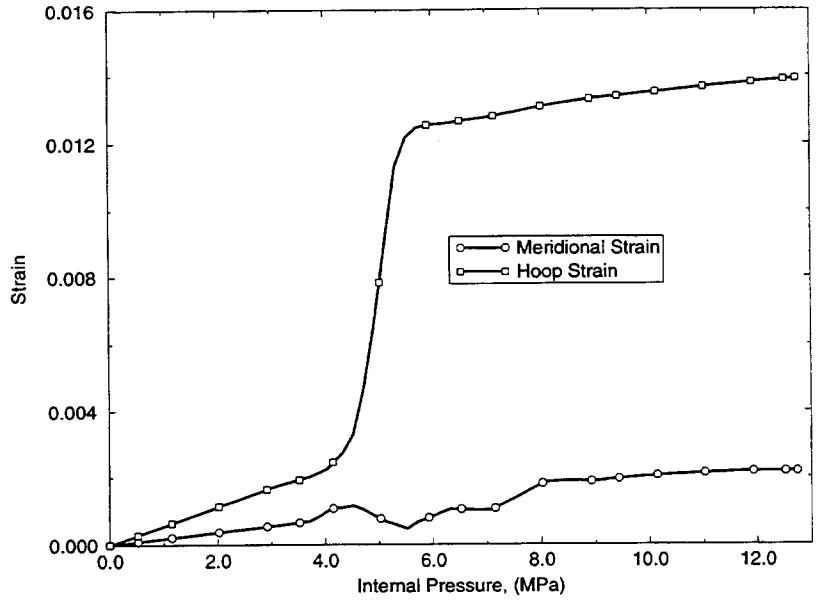

Figure 6-8. Meridional and hoop strain history at interior surface in lower conical shell (Point 1 in Figure 6-7).

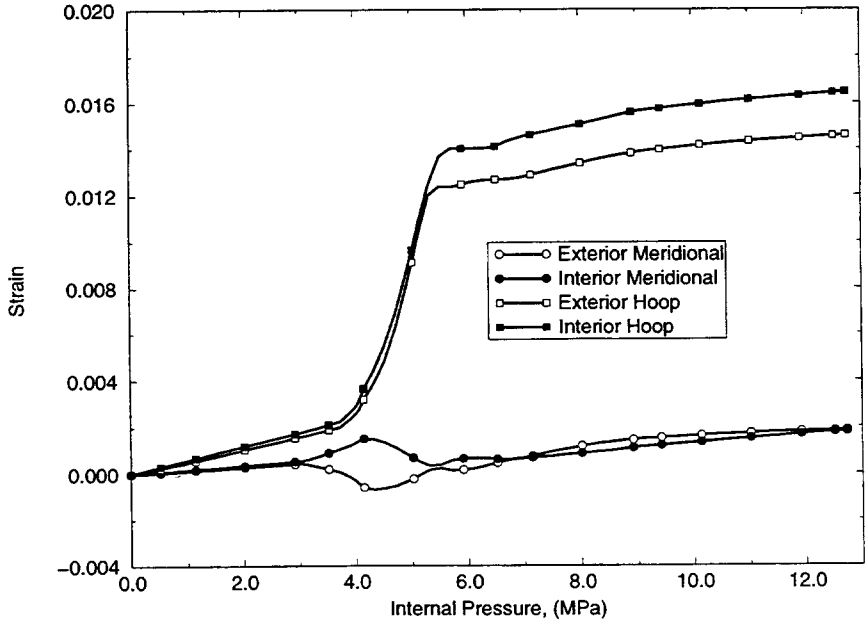

Figure 6-9. Meridional and hoop strain history at exterior and interior surfaces in lower conical shell (Point 2 in Figure 6-7).

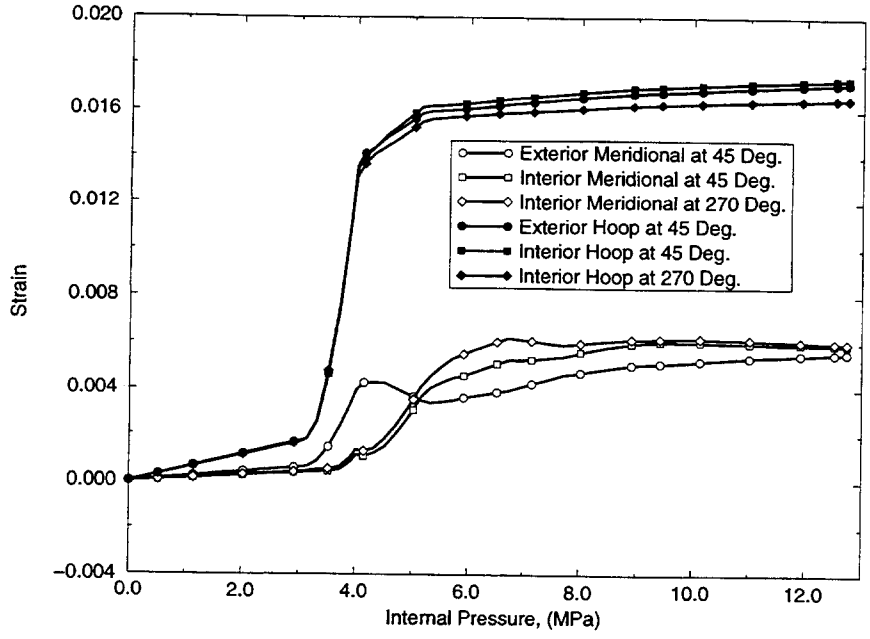

Figure 6-10. Meridional and hoop strain history at exterior and interior surfaces in upper conical shell (Points 3 and 4 in Figure 6-7).

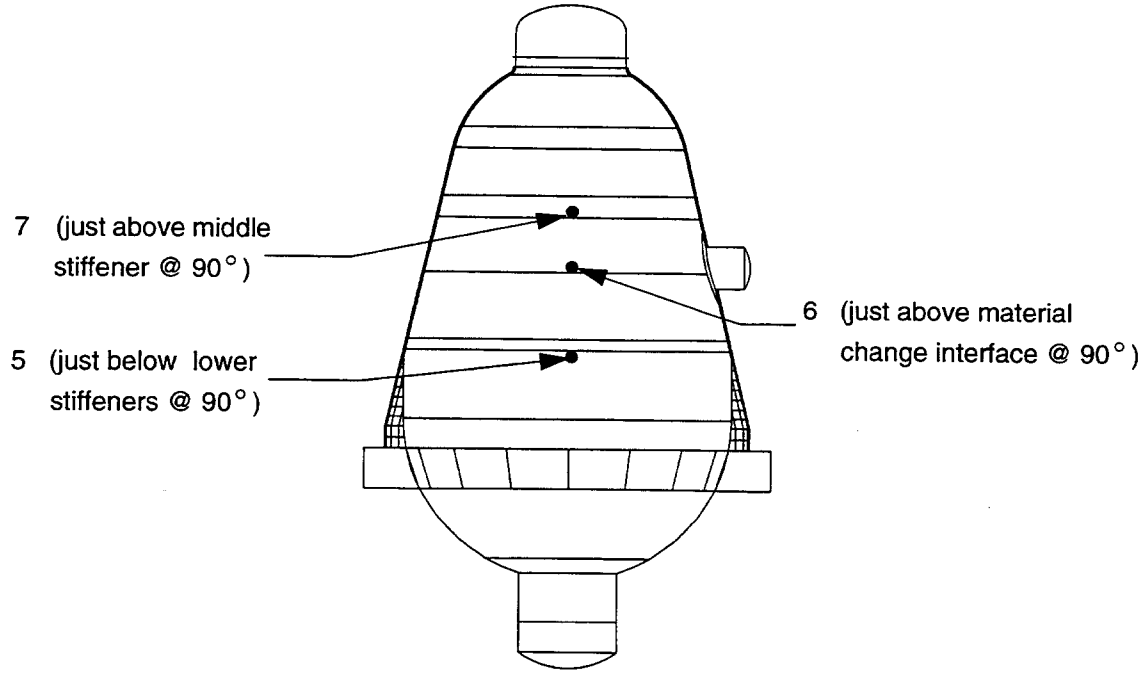

Figure 6-11. Transition area strain locations.

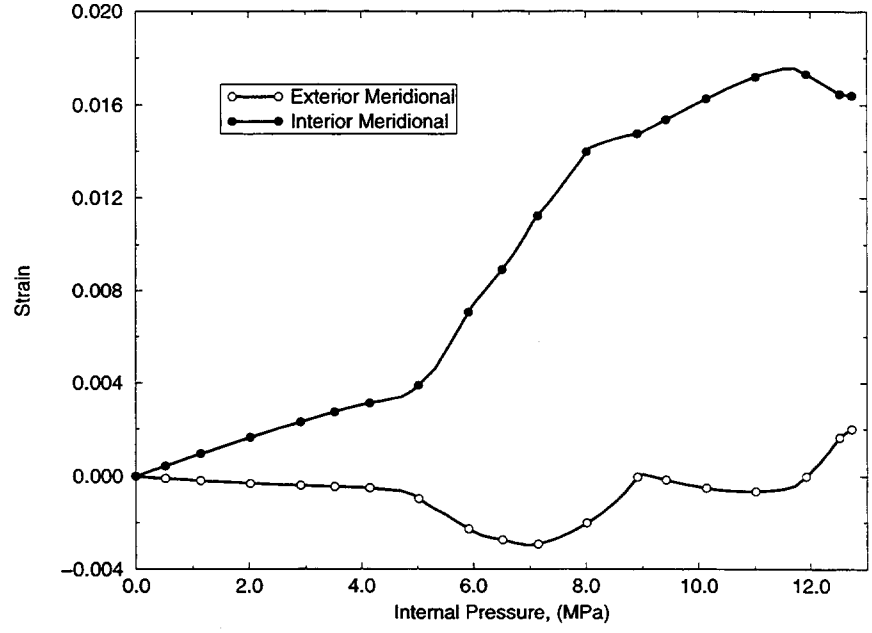

Figure 6-12. Meridional strain history at exterior and interior surfaces just below lower stiffeners (Point 5 in Figure 6-11).

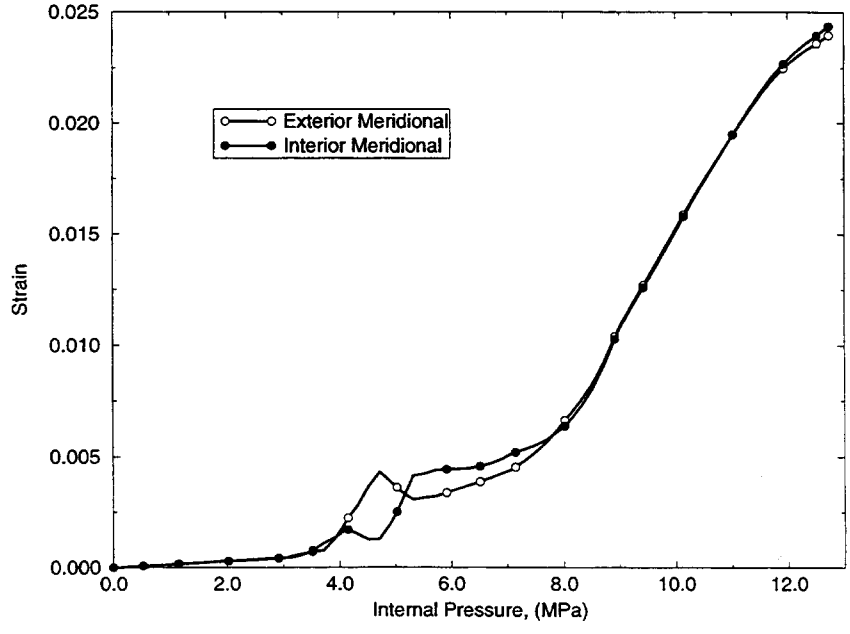

Figure 6-13. Meridional strain history at exterior and interior surfaces just above material change interface (Point 6 in Figure 6-11).

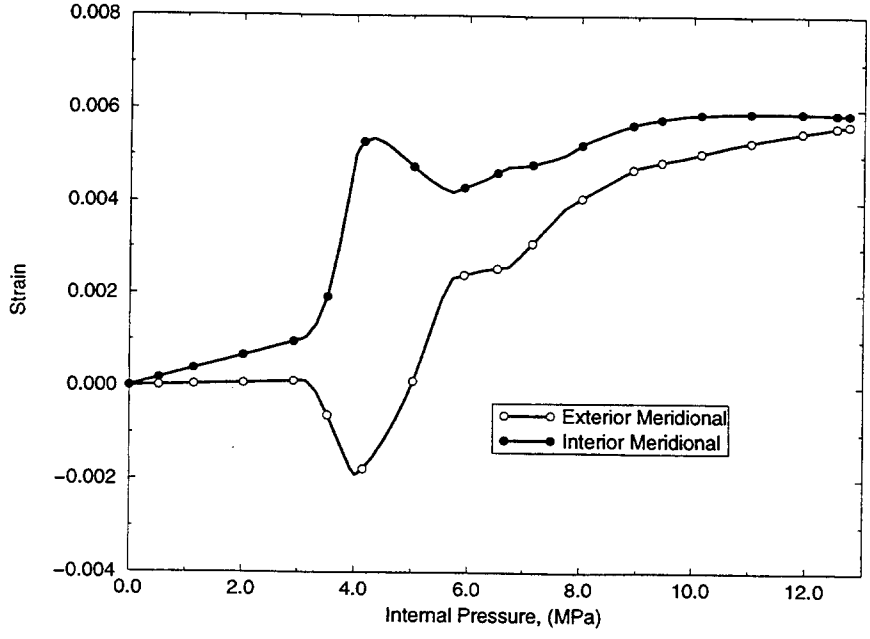

Figure 6-14. Meridional strain history at exterior and interior surfaces just above middle stiffener (Point 7 in Figure 6-11).

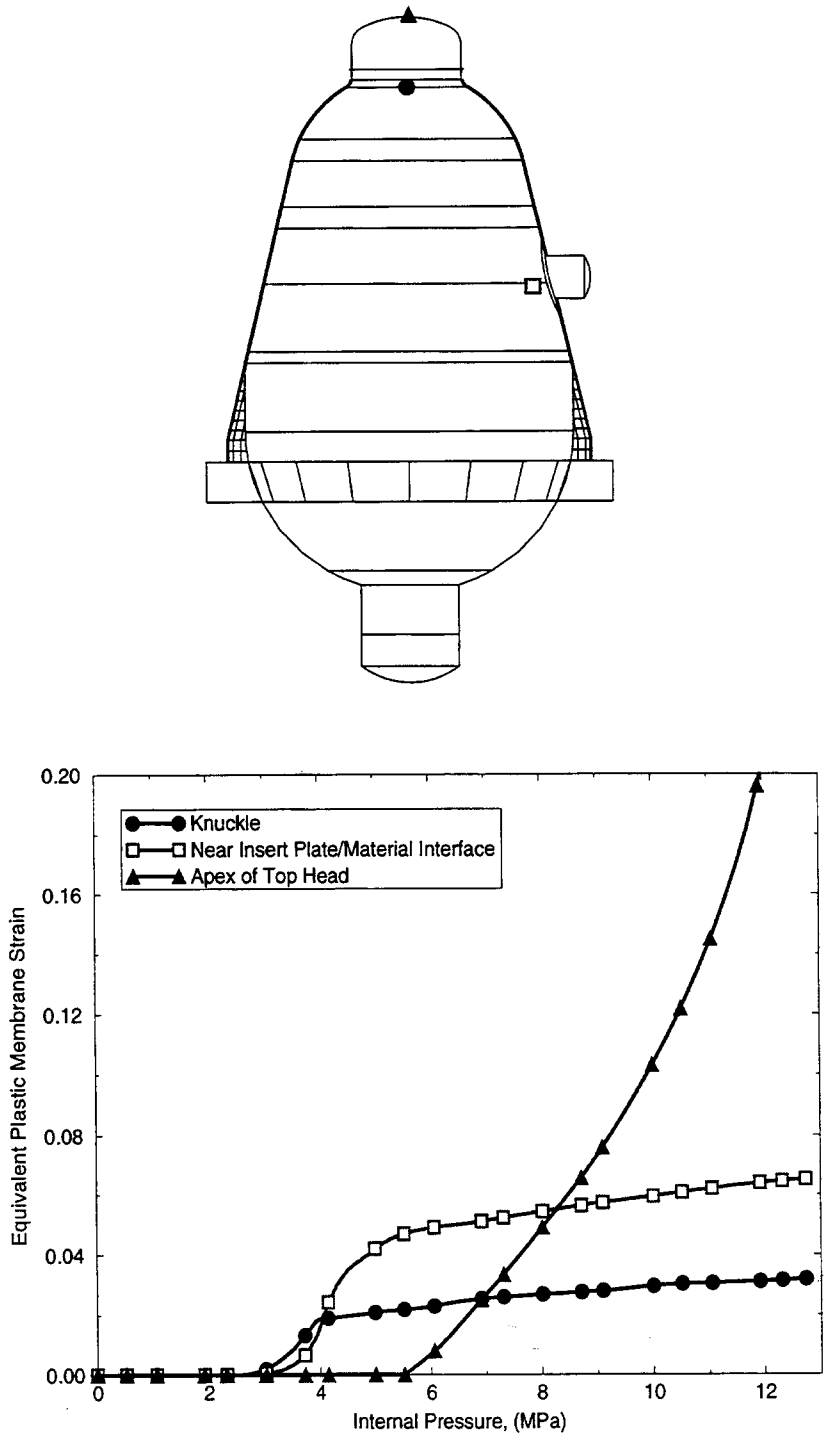

Figure 6-15. Equivalent plastic membrane strain for three critical locations in the global 3-D shell (G3DS) model as a function of internal pressure. Locations of strains are shown in top drawing.

7. Detailed Local Analyses

Local analyses of the top head and the area around the equipment hatch were performed in order to incorporate more refined meshes in areas of high strain. In each case, boundary conditions on the edge of the refined local mesh were obtained from the global three-dimensional shell (G3DS) analysis described in Section 6.

The local submodel of the top head is an axisymmetric model with a fine mesh of continuum elements in the shell wall in order to more accurately model the thick knuckle and flange regions. It also incorporates the final design geometry of the contact structure (CS) in this area.

Two local submodels of the equipment hatch area were developed, both with three-dimensional shell elements. The first model is based on exactly the same geometry as that in global three-dimensional shell model. The only difference is that the mesh near the thickened reinforcement plate around the equipment hatch is significantly refined. The second submodel uses the same refined mesh but also incorporates an approximation of wall thinning discovered during on-site inspection of the steel containment vessel (SCV) model. Neither of these submodels utilized as-built information on gap size.

All material properties in these models were obtained from the uniaxial test data as described in Section 4.3.

7.1 Top Head Including Knuckle Region (LTHAXC)

One critical area requiring further study as indicated by the global models was the top head region including the knuckle. For this area, a local axisymmetric continuum model was created that included the most recent as-designed geometry of both the SCV and the CS from the top head apex down to the upper 19 mm stiffener.

7.1.1 Finite Element Model Description

Figure 7-1 shows the Local Top Head Axisymmetric Continuum Model. The model used 7200 four-node reduced integration, axisymmetric continuum elements (ABAQUS CAX4R elements) and five two-node thin or thick linear shell elements (ABAQUS SAX1 elements). Axisymmetric boundary conditions were imposed at the apex of the top head. At the lower bound of the model, rotations and displacements from the G3DS model were applied to the shell nodes in a manner similar to the *SUBMODEL option in ABAQUS. However, ABAQUS does not allow the submodel option to be used when changing from a three-dimensional model to a two-dimensional axisymmetric model, so the process was conducted manually. The displacement and rotation histories from the appropriate nodes on the global shell model were applied with the *USER SUBROUTINE option, which provides the user with a way to prescribe the magnitude of any degree of freedom using FORTRAN code. Multi-point constraints were used to transition from the shell elements to the continuum elements. As with the other models, the loading consisted of internal pressure and gravity. The contact definition for this model was basically the same as the previous models (the coefficient of friction was $\mu = 0.2$) except that the small sliding formulation was not specified. For this case, ABAQUS defaults to a finite sliding formulation, which allows arbitrary separation, sliding, and rotation of the surfaces.

As mentioned in Section 5.1 and shown in Figure 5-1, the design of the CS was changed after the global axisymmetric and three-dimensional shell models were completed. However, the local continuum model of the top head described in this section includes those design modifications. Because continuum elements were used throughout the model, the geometry was more accurately modeled, especially near the top head flange and the knuckle.

7.1.2 Displacements

Figure 7-2 shows the deformation of the top head submodel. The first three plots are the deformed shape of the entire model at three different internal pressures, while the last six are close-ups of the knuckle/top head flange region with some additional pressure steps included. The displacements are *not* magnified. First contact occurs at 3.2 MPa at the knuckle as it expands radially outward to meet the corner of the CS. At 6 MPa bending of the cylindrical section of the top head from the bottom of the top head flange is apparent, and at 8 MPa bending around the top of the top head

flange is beginning. The vertical growth of the dome is also significant at 8 MPa. Note that the top head flange shows almost no radial expansion at 8 MPa. The overly stiff behavior of the top head flange and the rapid radial expansion of the knuckle create bending locations with significant plastic strains (Section 7.3.4). Figure 7-3 shows displacement and strain locations in top head.

Vertical displacement of the apex of the dome is plotted in Figure 7-4. This displacement is nearly identical to the same displacement that was obtained from the G3DS model (Figure 6-4). Because the top head submodel has a very fine mesh and therefore simulates more flexibility than the global model, the internal pressure reaches a maximum value of only 12.1 MPa rather than the 12.7 MPa indicated in the global analysis, and the maximum displacement is higher at this pressure.

7.1.3 Strains

Results for strain components in the top head are plotted in Figure 7-5 to Figure 7-7 for the locations shown in the diagram in Figure 7-3. As noted previously, the difference in strains at the interior and exterior surfaces indicates the amount of bending strain. Thus significant bending strain is present just below the top head flange for pressures greater than 3.0 MPa as shown in Figure 7-5. Some bending strain is also evident just below the knuckle (Figure 7-6). In the spherical section, the hoop and meridional components are nearly equal until significant yielding occurs at 5.4 MPa. Above 7.0 MPa, these strain components are significantly higher than those computed in the global three-dimensional shell analysis for any of the other free-field areas.

7.1.4 Critical Plastic Strain Areas

Figure 7-8 plots the strains from the critical locations from the top head submodel as a function of internal pressure. The five locations can be broken down into three areas: the apex of the top head, the top head flange, and the knuckle. After 8 MPa, all five locations show similar strain histories except for the element below the knuckle. The primary differences in the strain histories appear early in the loading.

The exterior surface of the apex of the top head yields late in the history at about 5 MPa compared to the other elements. Since this location is not protected by the CS, the growth of plastic strain is rapid up to a maximum of over 34% at an internal pressure of 12 MPa.

The overly stiff behavior of the top head flange can probably be attributed to the mixed scaling of the SCV (1:4 ratio thickness; 1:10 ratio on overall size). This causes large bending strains in the elements just below and above the top flange on the interior surface. The element just above the top flange behaves similarly to the apex of the top head except that it yields sooner. The element just below the top flange accumulates more plastic strain early in the loading but otherwise behaves similarly to the first two elements.

The element at the interface between the top of the knuckle and the cylindrical section of the top head on the exterior surface accumulates still more plastic strain early in the loading but then appears to be temporarily affected by the CS at just over 3 MPa. The last location under consideration is the element at the interface between the bottom of the knuckle and the spherical section on the exterior surface. It accumulates more plastic strain than all the other elements until it contacts the CS at just over 3 MPa. The effect of the CS on this element is much more apparent as this element reaches a maximum strain of only 12% compared to nearly 34% for the apex and 24% for the other elements.

7.2 Equipment Hatch Area As Designed (LEHS)

The second critical area indicated by the G3DS analysis was the area near the thickened reinforcement plate around the equipment hatch. This area also includes the material change interface. This section describes a local submodel based on final design information.

7.2.1 Finite Element Model Description

The model (Figure 7-9) used 4800 four-node reduced integration shell elements with finite membrane strain capability (ABAQUS S4R elements). The boundary conditions were imposed using the *SUBMODEL option. Submodeling in ABAQUS is used to study a local part of a model with a refined mesh based on interpolation of the solution from an initial, G3DS onto the nodes on the appropriate parts of the boundary of the submodel. Figure 7-10 compares the global model mesh and the local submodel mesh. For this particular

analysis all nodes on the boundary of the submodel were "driven" by the results from the G3DS model. The loading consisted of gravity and internal pressure. The coefficient of friction used for this model was the same as in previous models, μ=0.2. The eccentricity of the equipment hatch insert plate was also modeled as described in Section 6.1. Because this model uses results from the global model, the model was allowed to run up only to 12.7 MPa, the point where the global model failed to converge. Computations for this model were performed with ABAQUS, Version 5.4 (1994).

7.2.2 Contact History

Figure 7-11 shows the evolution of contact for the equipment hatch submodel. As before, black areas indicate contact, white areas indicate no contact. The elements on the border of the model are gray because they are "driven" nodes and so are not included in the contact algorithm. Contact first occurs at 4.2 MPa in the middle conical section. Contact propagates toward the insert plate at 5 MPa and by 6 MPa has contacted a large part of the insert plate and has spread to the lower conical section (below the material interface). At 8 MPa the contact is widespread throughout the model.

7.2.3 Critical Plastic Strain Area

This model was developed to study the junction of the equipment hatch insert plate and the material interface after the global model indicated potentially high strains in this area. Figure 7-12 compares the equivalent plastic membrane strains from the two models at the same location: the element in the 8.5 mm wall (middle conical section) that is adjacent to the equipment hatch insert plate and to the 9.0 mm wall (lower conical section). These elements are indicated in the figure. In the global model this element is approximately 60 mm by 30 mm in size; in the local submodel the element in the corresponding location is 11 mm by 11 mm. Qualitatively the behavior of the two elements is similar. Quantitatively, the element in the local submodel reaches strains nearly 50% higher than the global model: 9% in the submodel compared to approximately 6.5% in the global model. The difference is best explained by the submodel's ability to measure more accurately the strain concentration because of its finer mesh.

7.3 Equipment Hatch As Built (LEHSTh)

The last analysis performed was used to study the effects of thinned areas near the junction of the equipment hatch insert plate and material change interface. This model is the same as the previously described local equipment hatch submodel, except that an approximation of wall thinning has been included.

7.3.1 Finite Element Model Description

Figure 7-13 shows the basic finite element model used to study the effects of thinning. The model is the same as the previous equipment hatch submodel except that the measured thicknesses near the junction of the equipment hatch insert plate and the material interface were input explicitly using the *NODAL THICKNESS option in ABAQUS, Version 5.5 (1995). This model was intended only to study the thinned area near the equipment hatch insert plate and so does not include any other as-built information.

The as-built measurements given in Appendix C indicate that the nominal thicknesses of the as-built SCV are 5% to 10% thicker than the designed configuration of the SCV, while two locations on either side of the equipment hatch insert plate are up to 22% *thinner* than the designed configuration on which all the finite element models are based. Changing the nominal thickness in the finite element submodel was not an option because the submodel used boundary conditions from the global model, which was based on the original, as-designed thicknesses. Accommodating the thinning in the finite element model, the measured thickness from the thinned areas from the SCV was converted to a percentage of the nominal measured thickness. Then these percentages were used to calculate the input thicknesses for the thinned locations in the finite element model.

7.3.2 Contact History

The contact behavior for this model is nearly the same as for the previously discussed equipment hatch submodel without wall thinning (Figure 7-11).

7.3.3 Strains

The four points near the equipment hatch reinforcement plate are depicted in Figure 7-14. Strains are plotted in

Figure 7-15 through Figure 7-17. All these points occur in the SGV480 material. As Figure 7-15 indicates, the maximum principal strain at 67.5 degrees is significantly higher than that at 45 degrees for internal pressures above 3 MPa. The strain at 45 degrees reaches its maximum value at around 4.0 MPa when contact occurs in this region. However, the strain at 67.5 degrees continues to grow above this pressure, eventually reaching nearly 7%. As Figure 7-16 illustrates, the meridional strains near the top of the reinforcement plate show substantial bending behavior. Both the exterior and the interior strain increase rapidly at around 3.8 MPa, but then increase more slowly after 4 MPa because contact has occurred. However, on both surfaces the meridional strain again increases rapidly, reaching a maximum of 3.5% at 12.7 MPa. The hoop strains just to the right of the reinforcement plate (plotted in Figure 7-17) also show some bending behavior after yielding has initiated (3.8 MPa).

Finally, strain components are plotted in Figure 7-18 at two more points near the reinforcement plate where pretest inspection revealed thinned wall material. Both points are located in the SPV490 material below the material change interface indicated by the weld line. At these two points, both the meridional and the hoop strains are significantly higher than the points discussed above in the SGV480 material, particularly at Point 17 which is closer to the thickness transition at the edge of the reinforcement plate.

7.3.4 Critical Plastic Strain Areas

Figure 7-19 compares the critical strain area from this submodel with wall thinning to the global shell and the submodel without wall thinning. This is the same figure as Figure 7-12 with the data from the LEHSTh model added. Qualitatively each curve represents the same behavior: the element yields at between 3 and 4 MPa and accumulates plastic strain very quickly until it reaches the CS between 5 and 6 MPa. The primary difference between each curve is the amount of plastic strain accumulated prior to contact. The effect of the thinned section is apparent, as the slightly thicker and higher yield SPV490 material now shows the greatest accumulation of plastic strain.

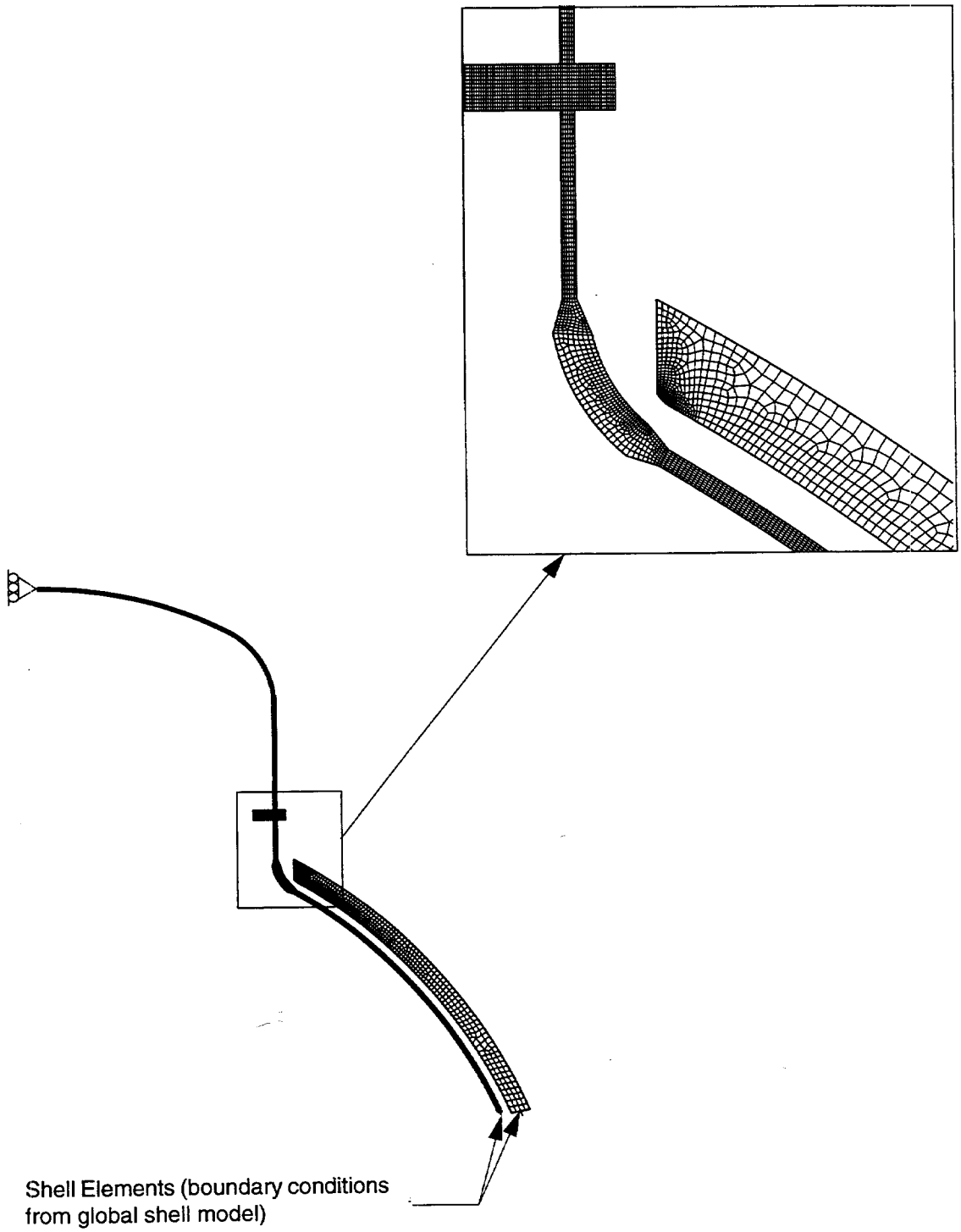

Figure 7-1. Local Top Head Axisymmetric Continuum Model with close-up of knuckle and top head flange.

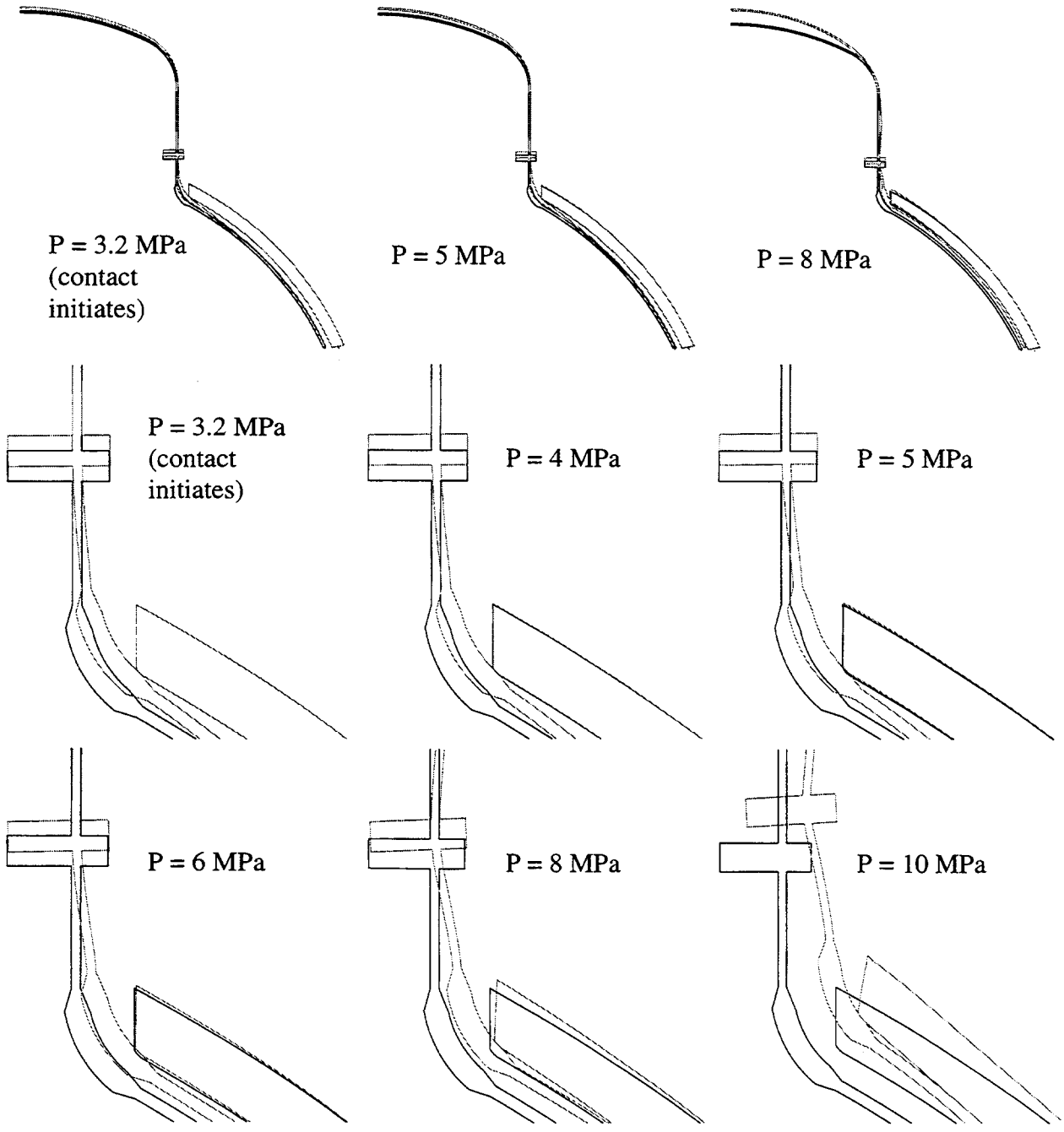

Figure 7-2. Deformed shape plots of Local Top Head Axisymmetric Continuum Model with close-up of knuckle/top head flange. The displacements are not magnified.

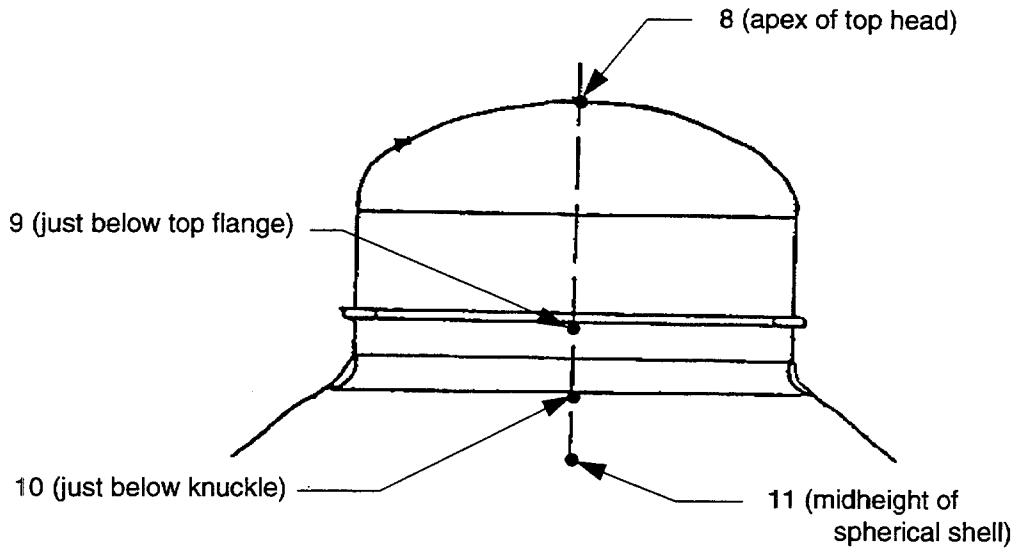

Figure 7-3. Displacement and strain locations in top head.

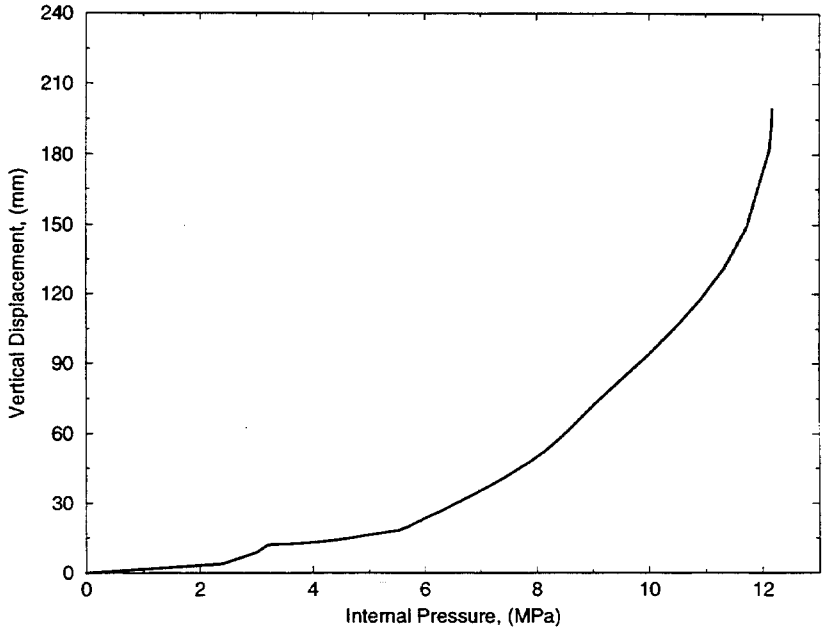

Figure 7-4. Vertical displacement at apex of top head from local top head model (Point 8 in Figure 7-3).

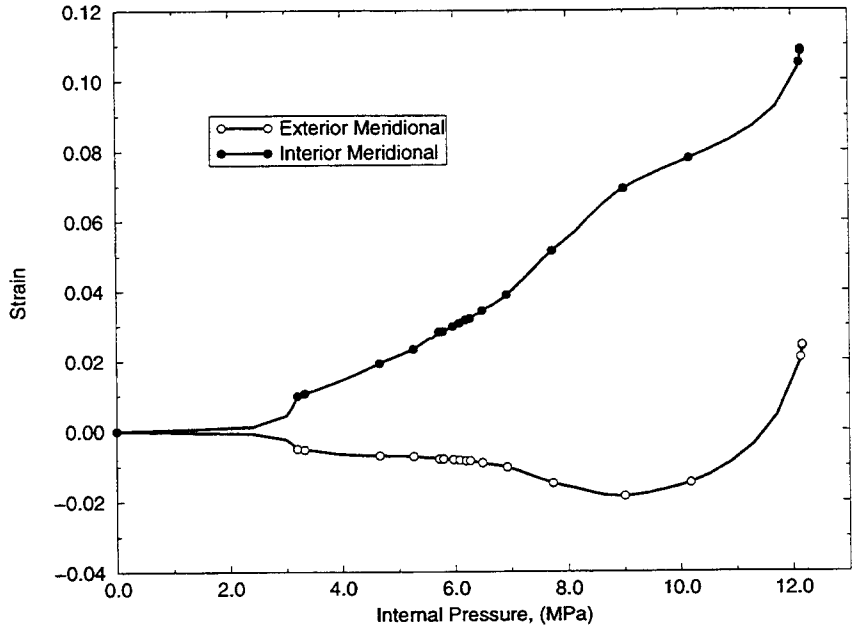

Figure 7-5. Meridional strains at exterior and interior surfaces just below top head flange (Point 9 in Figure 7-3).

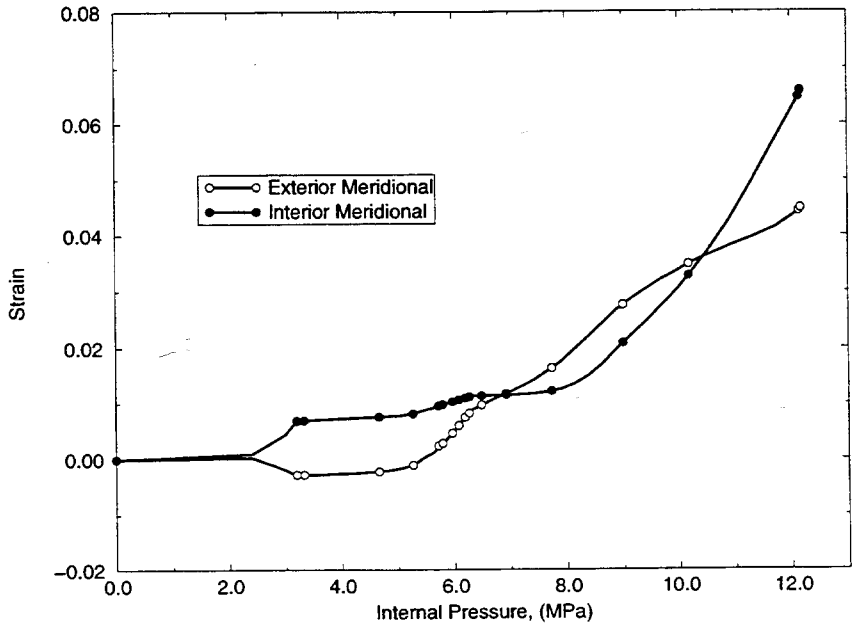

Figure 7-6. Meridional strain at exterior and interior surfaces just below knuckle (Point 10 in Figure 7-3).

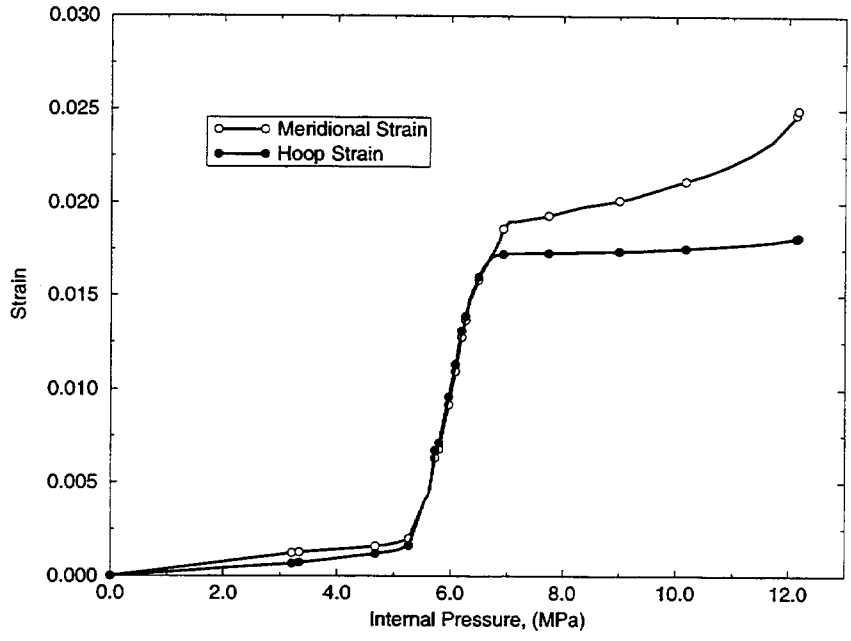

Figure 7-7. Meridional and hoop strains at interior surface at midheight of the spherical shell (Point 11 in Figure 7-3).

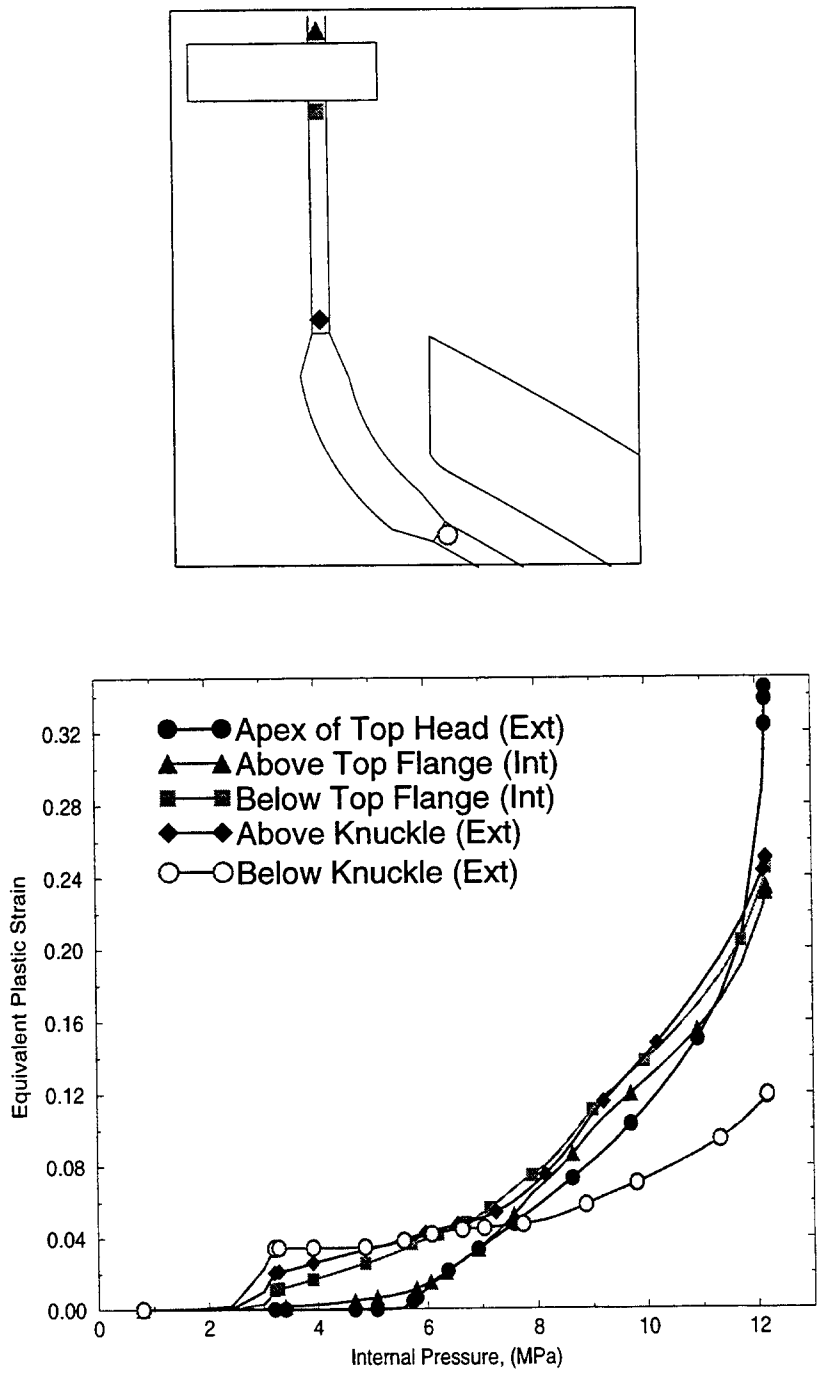

Figure 7-8. Comparison of critical high strain areas from the LTHAXC model. Four of the locations are indicated in the top diagram; the other location is the apex of the top head (bottom plot).

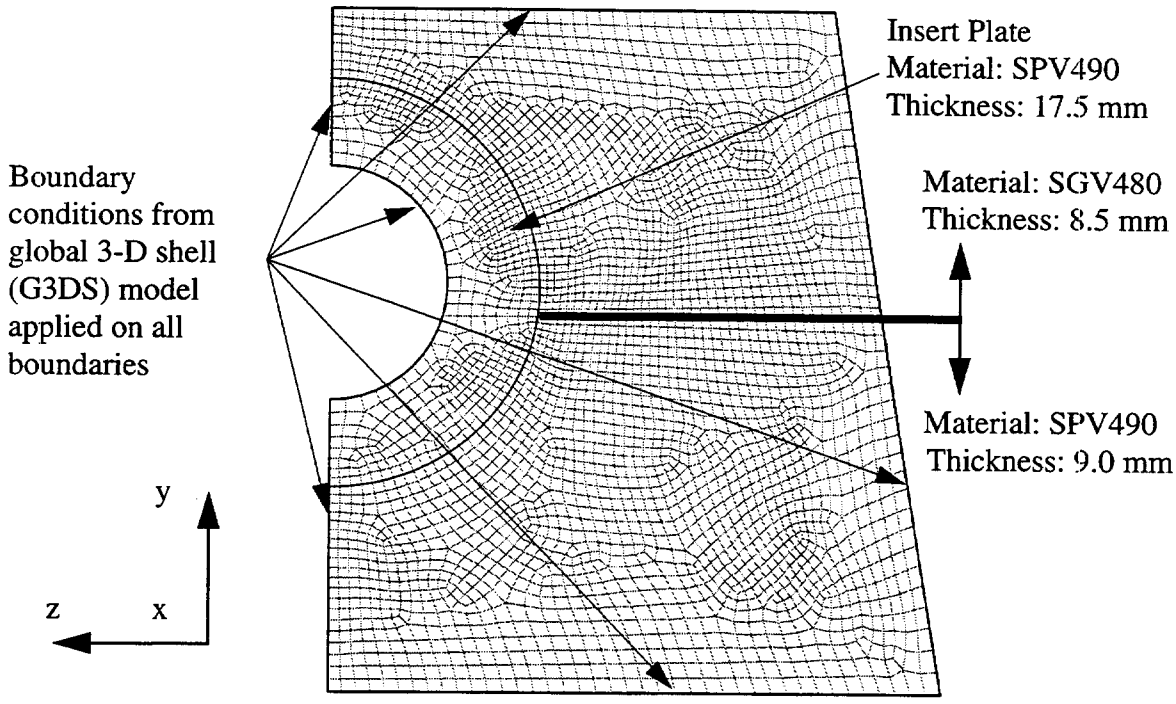

Figure 7-9. LEHS (Section 7.2) model mesh (contact structure not shown).

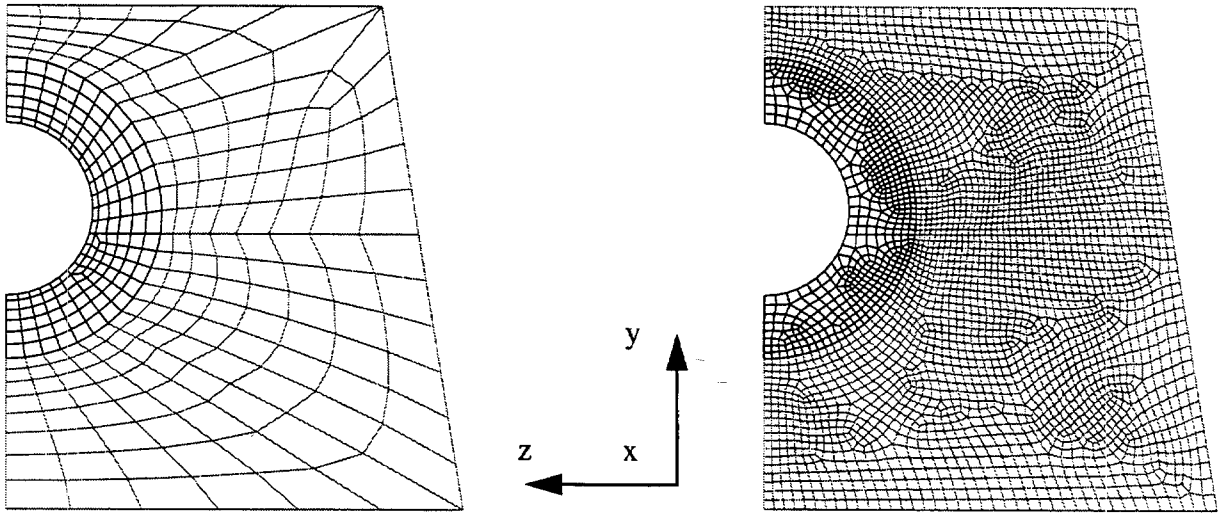

Figure 7-10. Comparison of G3DS mesh at left and equipment hatch submodel at right. The increase in mesh density in the submodel is roughly a factor of 10.

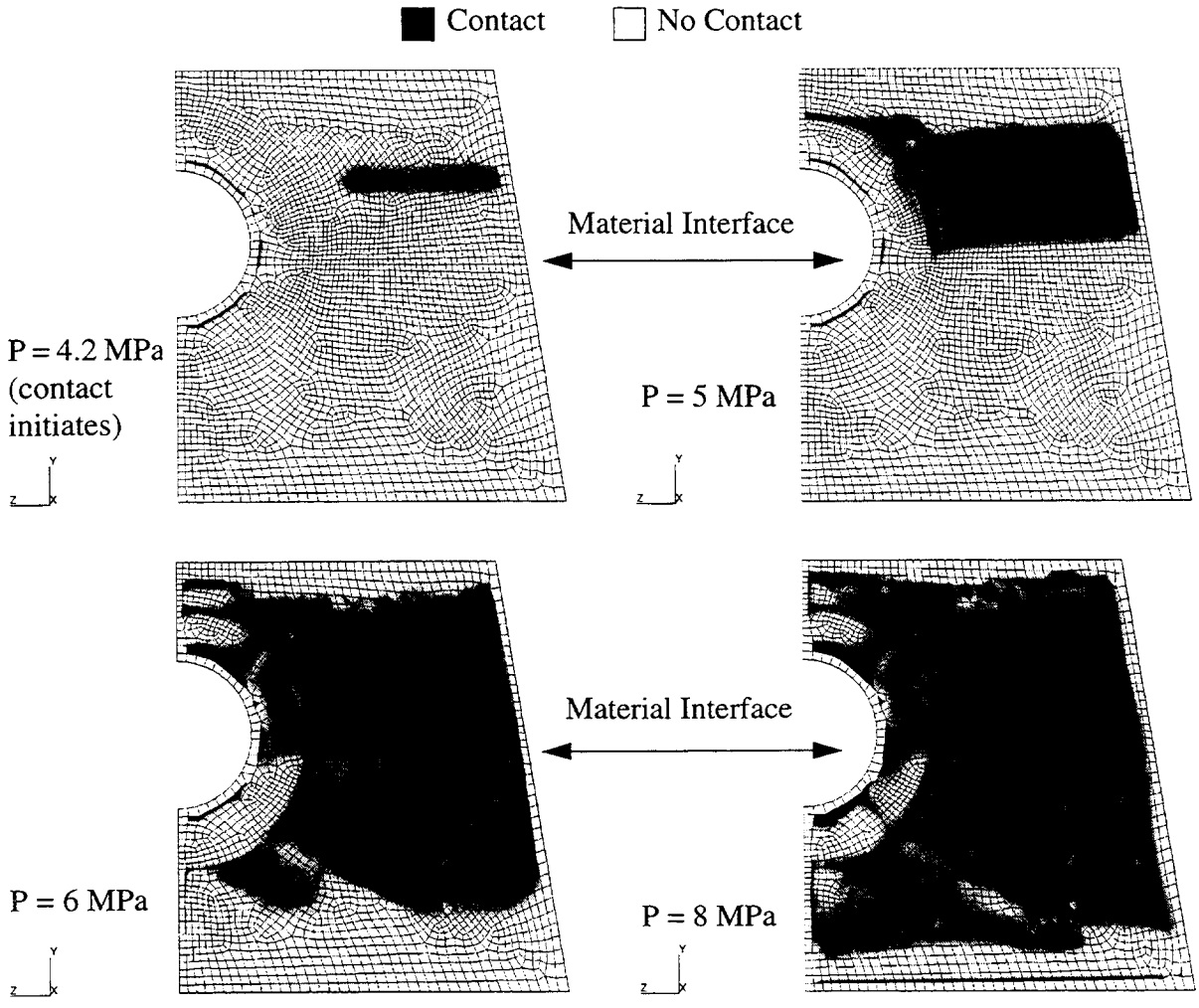

Figure 7-11. Evolution of contact for equipment hatch submodel.

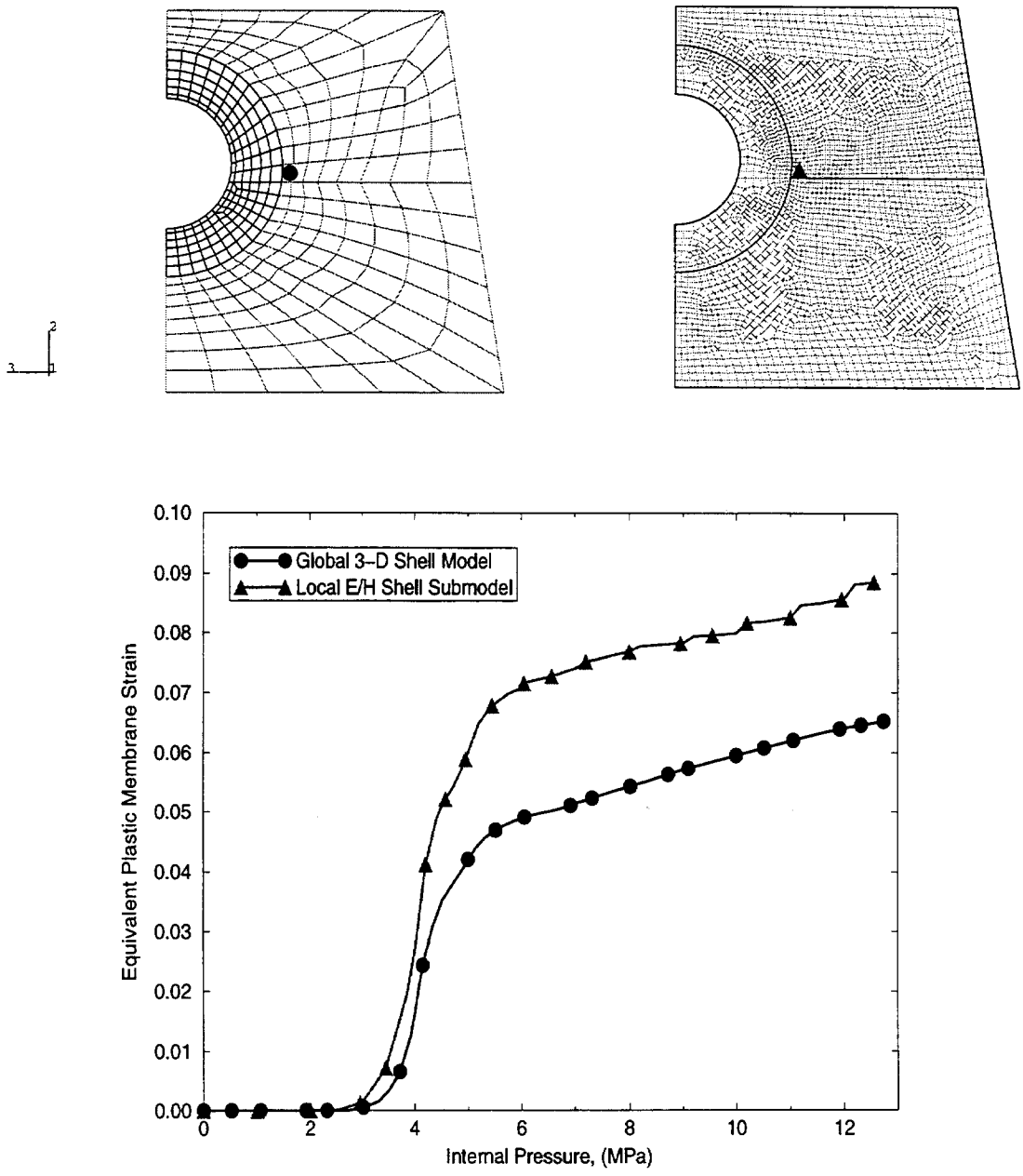

Figure 7-12. Comparison of critical area elements from G3DS and LEHS (Section 7.2.3) models with element locations indicated in the diagrams at top.

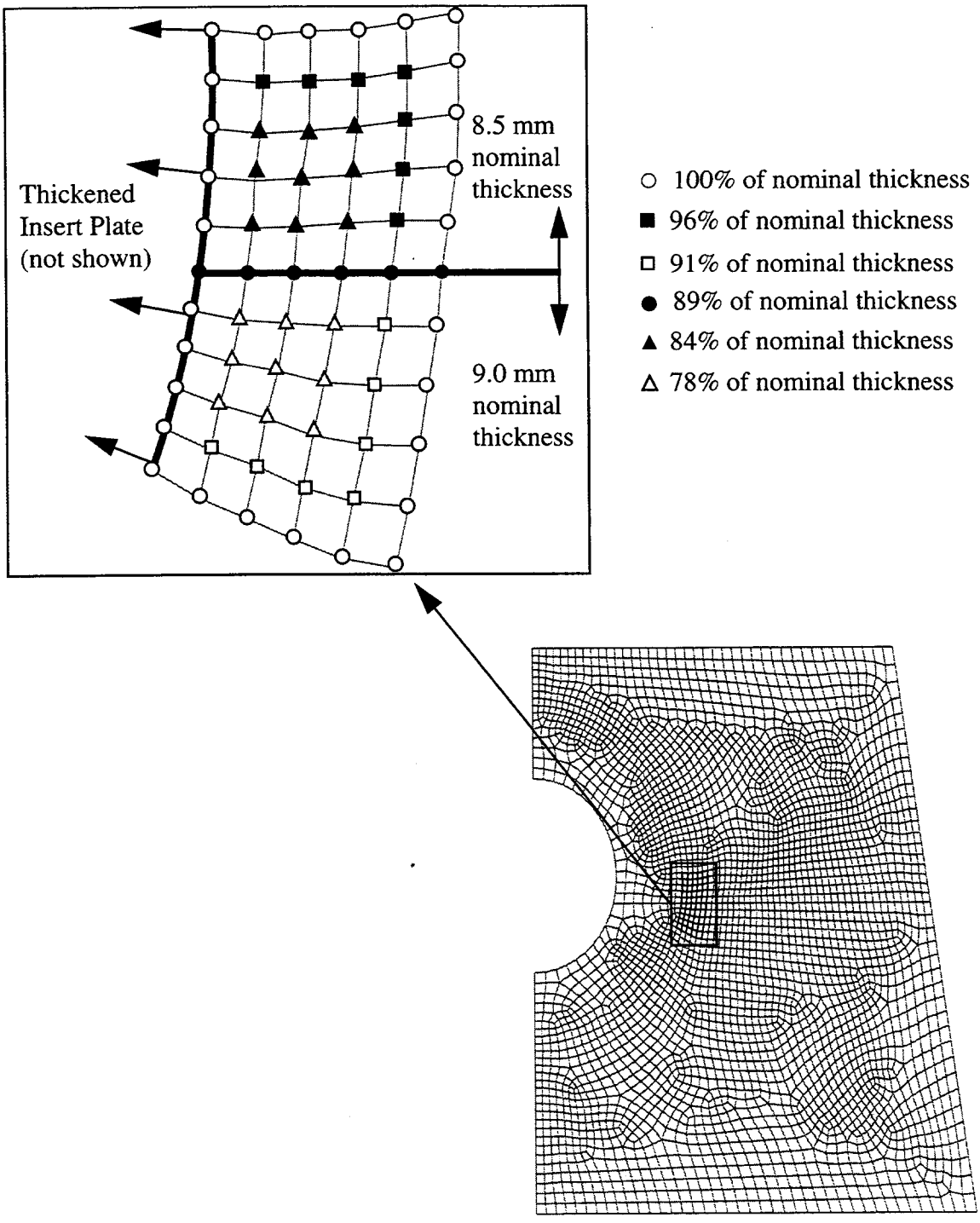

Figure 7-13. Diagram showing the equipment hatch submodel at lower right (contact structure not shown) with a detail of the thinned area at upper left. Values for thickness reduction, shown as percentages, are superimposed on the appropriate nodes.

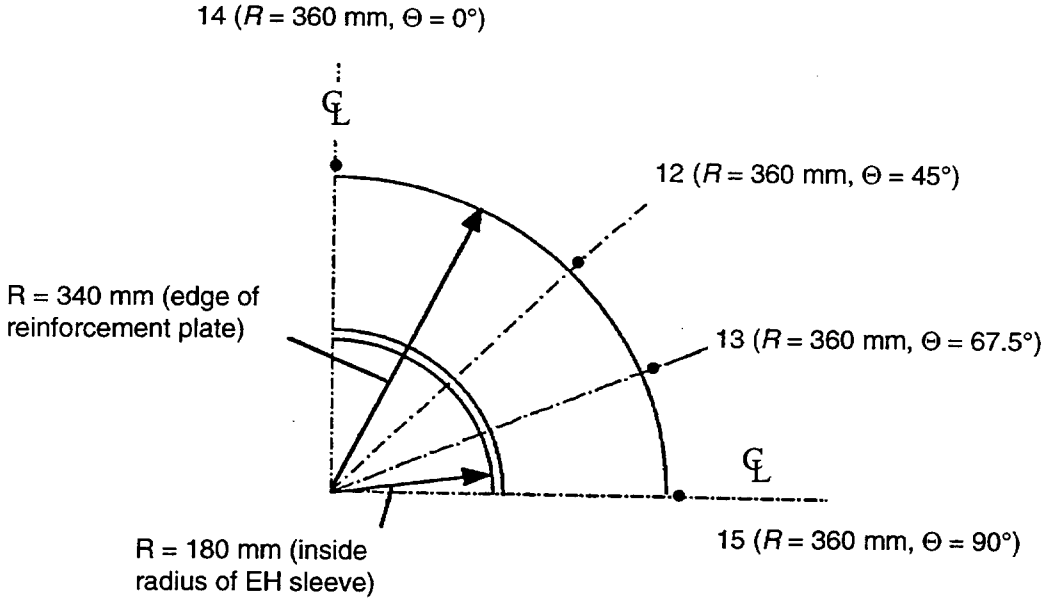

Figure 7-14. Strain locations in area around equipment hatch insert plate.

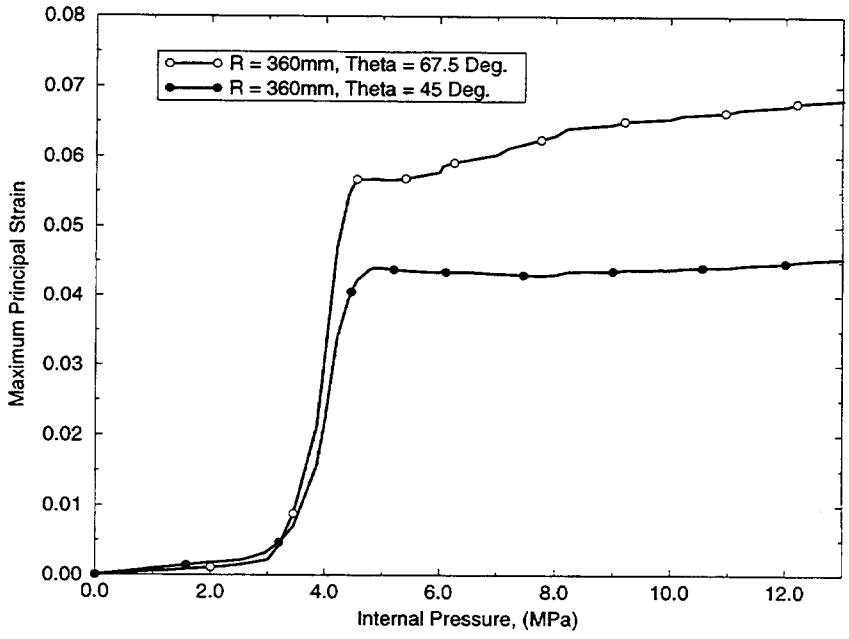

Figure 7-15. Maximum principal strain near the equipment hatch reinforcement plate (Points 12 and 13 shown in Figure 7-14).

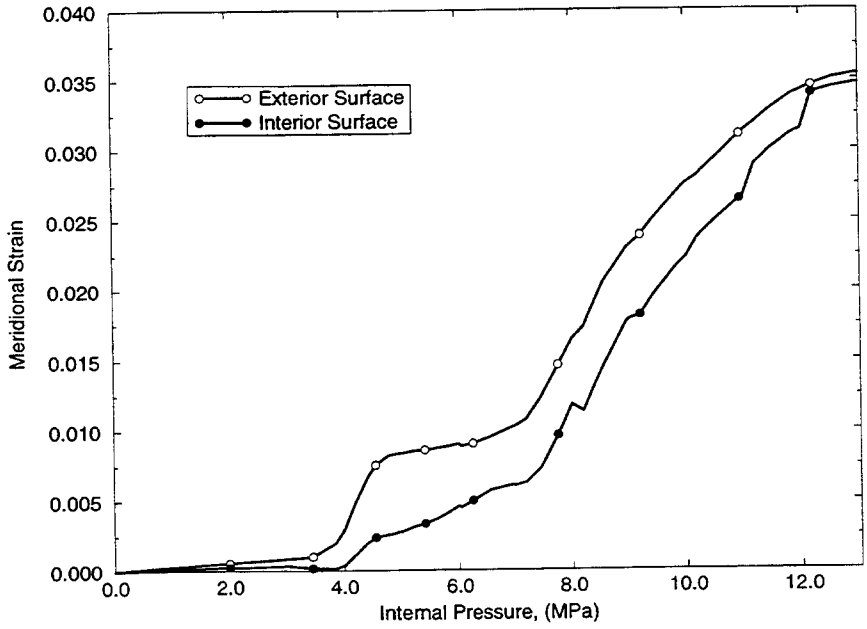

Figure 7-16. Meridional strain at the exterior and interior surfaces at the top of the equipment hatch insert plate (Point 14 in Figure 7-14).

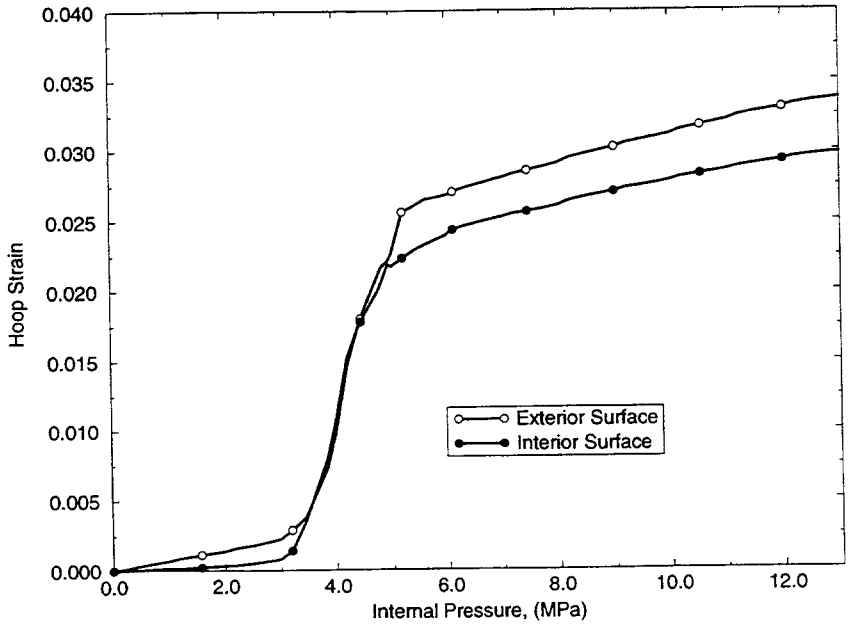

Figure 7-17. Hoop strain at the interior and exterior surfaces at the side of the equipment hatch insert plate (Point 15 in Figure 7-14).

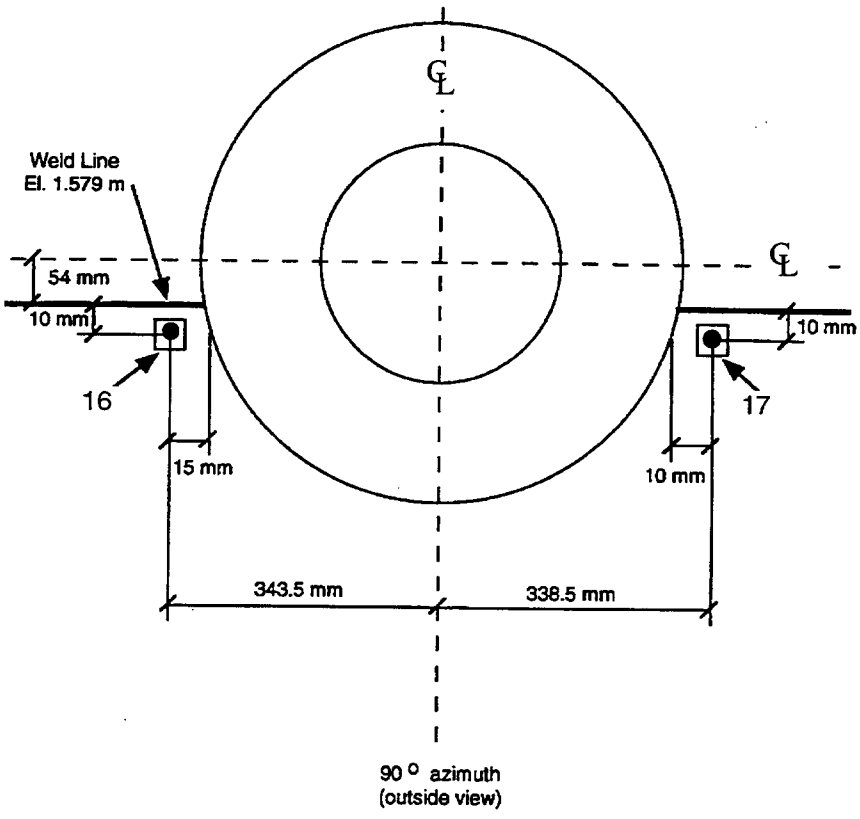

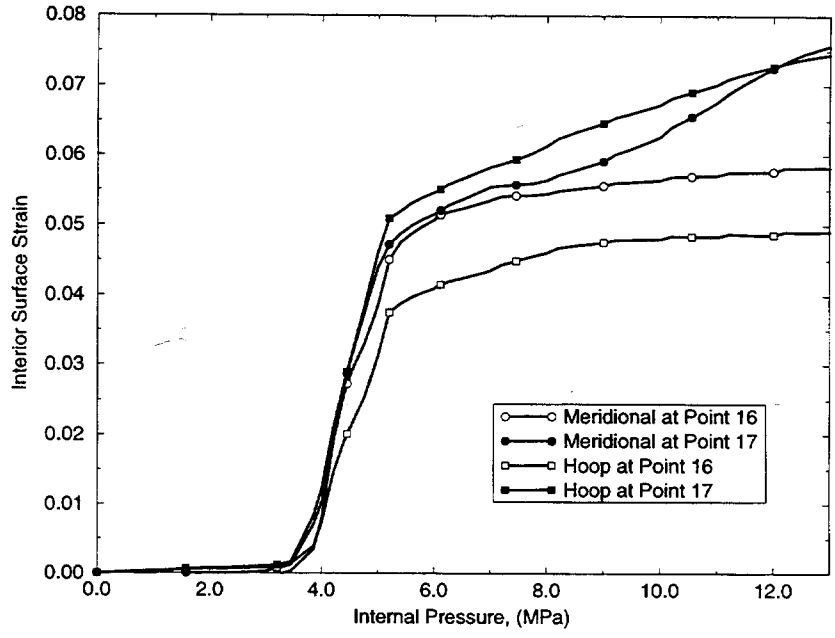

Figure 7-18. Meridional and hoop strain at two points on the interior surface in the thinned area near the equipment hatch reinforcement plate (Points 16 and 17 in diagram above).

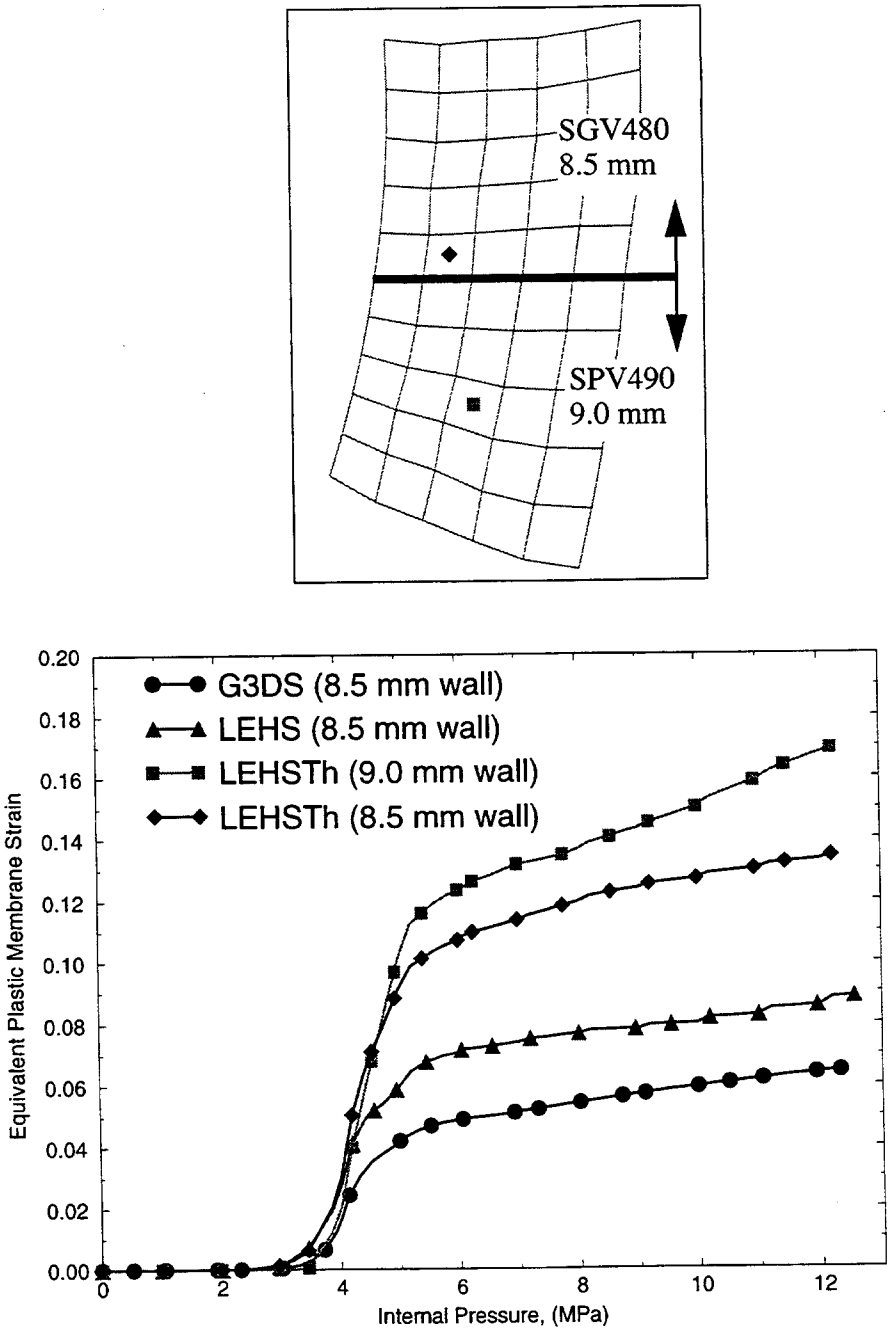

Figure 7-19. Comparison of high-strain locations from the G3DS model, the LEHS model (Section 7.2), and the LEHSTh model (Section 7.3). Locations from the LEHSTh model are shown at the top. See Figure 7-12 for locations from other models.

8. Assessment of Potential Failure Modes

In this section we assess several possible failure modes of the steel containment vessel (SCV) model based on results of the finite element analyses. Failure of the SCV model is defined as inability to maintain pressure, due either to a catastrophic failure of the vessel or to a local tear that causes leakage. Because the SCV model has no bolted flanges or penetration covers, seal leakage is not considered. Furthermore, the SCV model has no known cracks of critical length that would lead to premature brittle fracture, so the discussion in this report is limited to ductile failure modes. The modes of failure that have been considered are buckling of the torispherical top head, global ductile rupture of the vessel (also referred to as plastic collapse), and local ductile tearing in areas of localized high strains.

8.1 Top Head Buckling

Considerable research has indicated from both experimental and analytical methods that some torispherical heads may be subject to non-axisymmetric buckling failures. Kalnins and Updike (1991) detail several publications on the subject. Torispherical heads with ratios of head thickness (t) to crown radius (L) less than 0.002 may be susceptible to buckling. Torispherical heads with t/L greater than 0.002 but less than 0.04 are much more likely to fail by axisymmetric plastic collapse (i.e., global ductile rupture) (Kalnins and Updike, 1991). For the SCV model,

$t = 6$ mm
$L = 873$ mm
$t/L = 0.0068 > 0.002$

Therefore, since t/L is significantly greater than 0.002, buckling of the torispherical top head was not considered a likely mode of failure.

8.2 Global Ductile Rupture

Global ductile rupture of a pressure vessel is an axisymmetric mode of failure that occurs when the free-field membrane von Mises stress reaches a critical value. The wall becomes thinner due to Poisson's ratio, but no alternate load path exists. Therefore, when the material cannot sufficiently harden to accommodate the additional stresses caused by the area reduction, it cannot carry the load. Rapid radial growth occurs and is followed by global ductile rupture. This phenomenon is analogous to necking in uniaxial test specimens.

As described in Section 2.1 and shown in Figure 2-3, most of the SCV model is enclosed within the contact structure (CS). The CS is a thick steel shell that severely restrains radial growth of the SCV model. Therefore, in areas where the SCV model contacts the CS, global ductile rupture was not a likely mode of failure. However, because the top head above the knuckle is not enclosed within the CS, global ductile rupture must be considered in this region. Because global rupture is an axisymmetric failure mode, results from the axisymmetric continuum analysis of the top head region described in Section 7.1 are used here.

Figure 8-1 shows a schematic of the top head. Global ductile rupture of the top head could occur in the torispherical shell or in either of the two cylindrical shell regions. Finite element analysis results for radial growth are shown in Figure 8-2 for the crown of the torispherical shell and in Figure 8-3 for both cylindrical shell sections. In each case, generalized yielding of the section is indicated by the initial slope reduction of the curve, which occurs at approximately 4.0 MPa internal pressure for the torispherical shell and at 6.0 MPa for the cylindrical shells. However, in all sections, substantial capacity remains after initial yielding due to hardening of the material. The onset of global ductile rupture is indicated by substantial radial growth with a small change in internal pressure, i.e., the internal pressure at which the radial growth reaches an asymptotic value. The finite element results indicate that this pressure is slightly above 12.0 MPa in all three sections of the top head.

8.3 Local Ductile Failure

A failure mode more likely than global ductile rupture for a complicated structure such as the SCV model is a local failure caused by localized high strains. Local high strains may occur near stiffeners, thickness transitions, and changes in geometry. These may be intentional features of the design or as-built features. Failure in local areas is highly dependent on the exact geometry of local features in the actual model. Therefore, predictions are much less reliable than those for global failure modes.

Figure 8-4 shows a comparison of local critical strain areas from the finite element analyses. Only the results from two local submodels, the equipment hatch with wall thinning (LEHSTh) and the local top head continuum (LTHAXC) models are shown. For comparison of locations with differing material properties, the strains for each location were normalized by their true strain at maximum load from the Hitachi tensile tests. Therefore, a y-value of 1.0 corresponds to the strain at necking from that material's uniaxial tensile test. The raw (unnormalized) data are plotted in Figure 7-8 and Figure 7-19.

When the strains are normalized, the primary candidate for failure location becomes clear: the 9.0 mm wall section just below the material interface and near the equipment hatch insert plate shown by the long dashes in Figure 8-4. The primary reason that this particular location stands out is the difference in the ductility between the SPV490 steel and the SGV480 steel. The true strain at maximum load for the SPV490 material is approximately 10%; the true strain at maximum load for the SGV480 material is approximately 20%. Thus, the SPV490 material in the thinned section (9.0 mm nominal thickness, lower conical section) at an internal pressure of 5 MPa has reached a plastic strain that in the uniaxial-stress tensile test led to necking.

Continued deformation in the thinned section is "displacement controlled." That is, the boundary around the plastic domain in the thinned section interacts with the adjacent thicker stiffer elastic sections as a "cut out" or opening with a nominally fixed membrane load. Further increases in internal pressure cause the boundary around the thin section to expand similarly to the way an unreinforced cut out or opening in a pressure vessel expands. The expansion of the opening imposes additional strain on the yielding thinned section.

While the shell element mesh used in the LEHSTh model has some ability to represent locally accelerated thinning, it does not have the refinement necessary to track the strain localization on the length scale exhibited in the tensile test. The nature of the strain state, biaxial tension, is also important for failure prediction. The analysis indicates that the total strain in the thinned section is very nearly equal in two directions (circumferential and radial directions with respect to the edge of the equipment hatch insert plate edge). Although a forming limit diagram for this material is not available, examination of a typical forming limit diagram for a low-carbon steel (Figure 8-5) shows the differences between the load path for a tensile test and the load path for the area under consideration (equal biaxial strain). In a typical tensile test, necking occurs at 2n, where n is the strain-hardening exponent. Equal biaxial extension produces a neck at 1.3n. Thus, significant localization of plastic flow with attendant tearing is expected in the thinned section when the normalized value of effective plastic strain reaches (1.3/2.0) = 0.65 or 65% of the necking strain from the tensile test. In Figure 8-4 this corresponds to approximately 4.5 MPa internal pressure for the location in the SPV490 material.

8.4 Conclusions

The pretest predictions of failure of the SCV model are dependent on details that were included in the analytical effort. In particular, local failure analyses are very dependent on as-built features incorporated into the analytical models. Results of a local analysis of the thinned section of the SCV wall near the equipment hatch reinforcement plate indicate that this area is the most vulnerable for failure. This analysis was based on an 18 mm gap in this region; it did not include the as-built gap dimensions which were somewhat larger. Given the early and rapid occurrence of plastic flow compared to other locations within the pressure vessel, the strains attained relative to the material's ductility, and the biaxial stress state, the finite element results indicate local ductile failure in the thinned section next to the equipment hatch insert plate near an internal pressure of 4.5 MPa. Global ductile rupture of the vessel is indicated in the top head at the much higher pressure of slightly more than 12 MPa.

An earlier failure at the equipment hatch or another location due to the presence of welding flaws or inclusions could not be ruled out because states of stress simultaneously produce plastic flow in at least four other locations in the pressure vessel (primarily the top head and knuckle regions). The weld metal and HAZ near the thinned areas introduce additional uncertainty. The yield strength and ductility of the weld metal is typically higher than the parent material, while the same properties in the HAZ are typically lower than the parent material. Brittle failure modes have not been considered in this analysis effort.

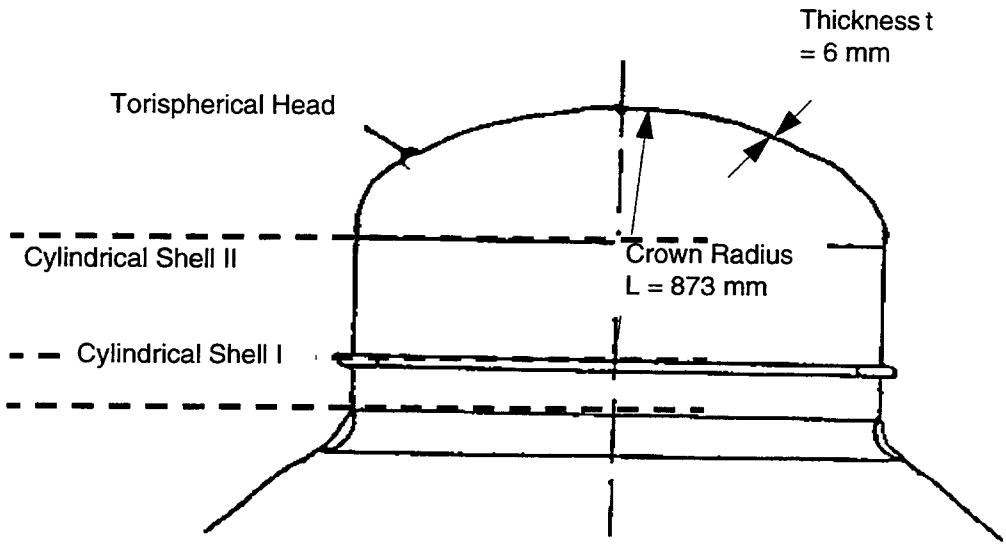

Figure 8-1. Schematic of the top head.

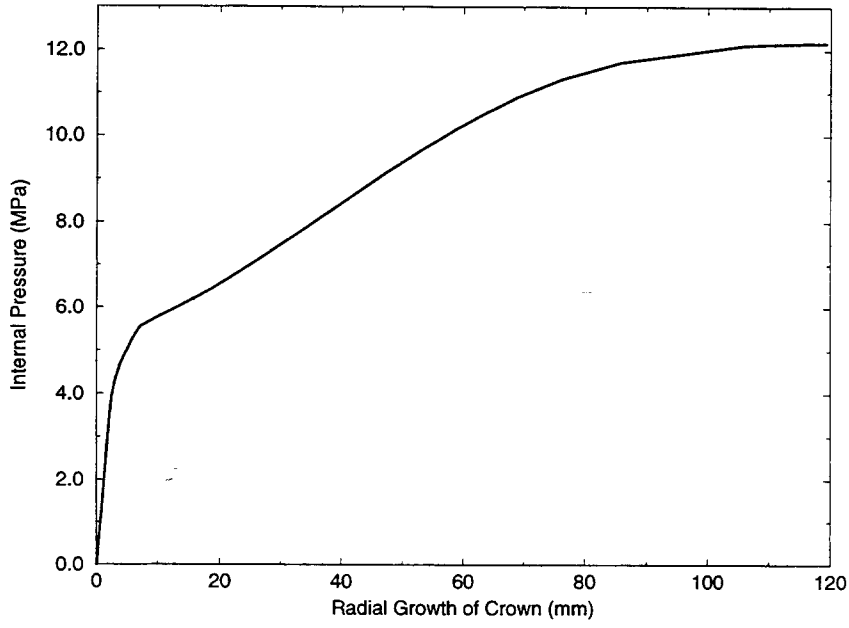

Figure 8-2. Radial growth at crown of torispherical head (see schematic Figure 8-1).

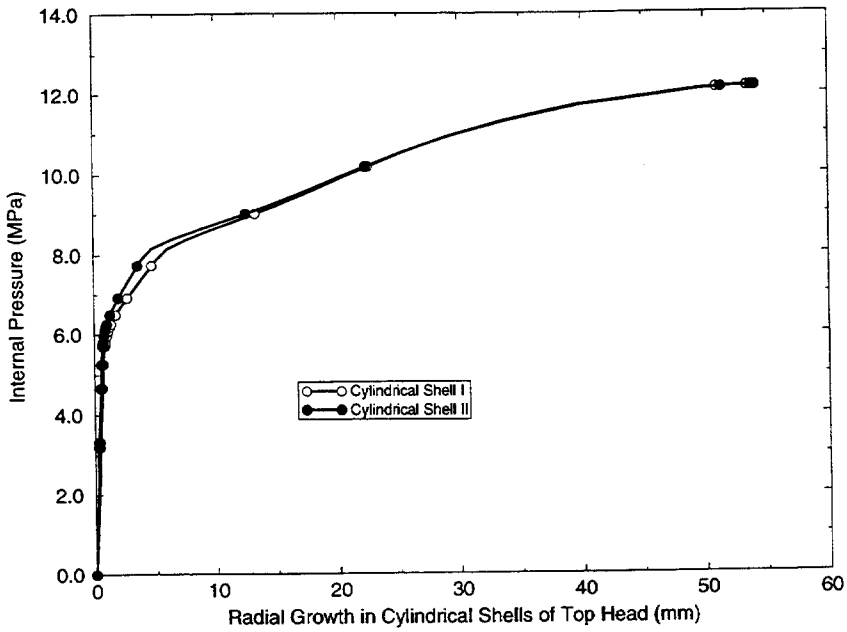

Figure 8-3. Radial growth in cylindrical sections of top head (shell sections shown in Figure 8-1).

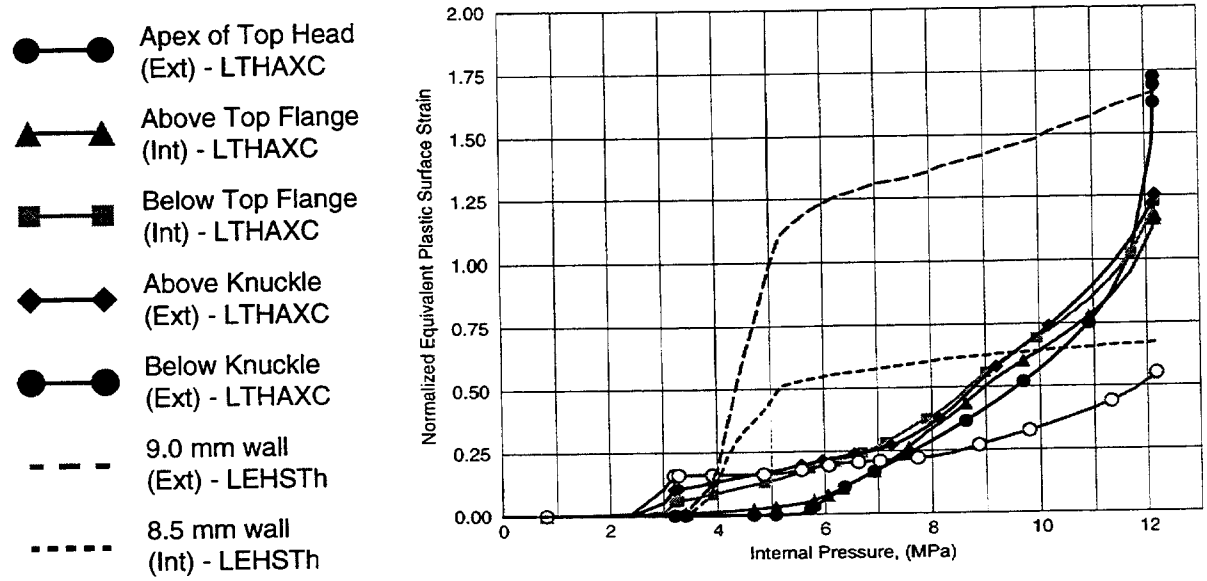

Figure 8-4. Normalized equivalent plastic strain from critical areas. Only critical areas from the local models are included because they are the most accurate. Strains have been normalized by each material's true strain at maximum load.

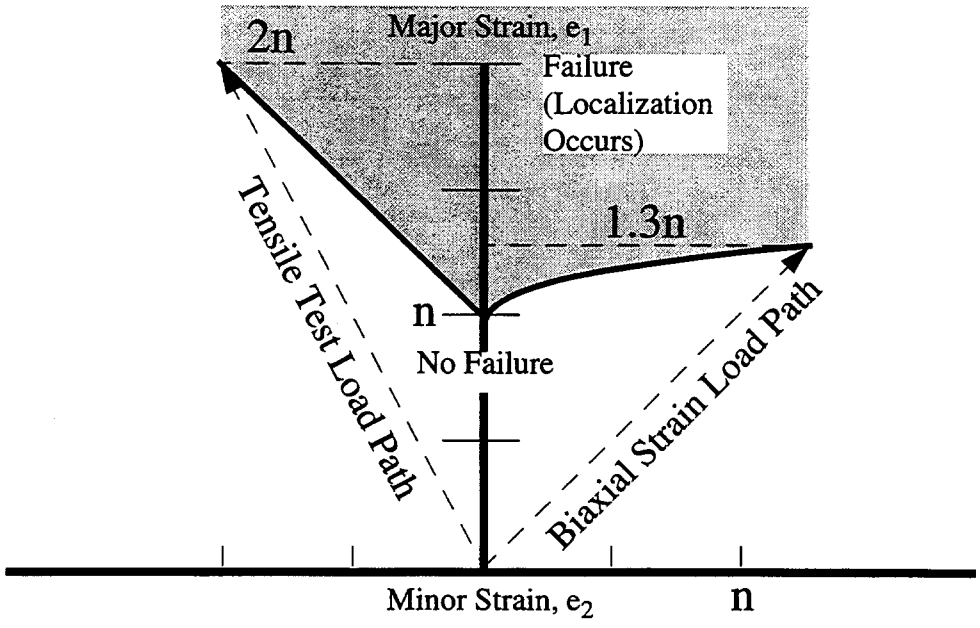

Figure 8-5. Typical forming limit diagram for low carbon steels. The strains below the curve are acceptable while those above the curve correspond to regions affected by local necking. Note the differences in major strain values between a tensile test load path and a biaxial strain load path (Hosford and Caddell, 1983).

9. Supplemental Computations for Design and Instrumentation Support

Several of the previously discussed finite element analyses were used to support the design of the model and the instrumentation system. This section describes additional analyses that were performed for these tasks.

9.1 SCV Model Design

Finite element computations were performed very early in the program to investigate the effects of the proposed mixed scaling (1:10 overall, 1:4 wall thickness). These included axisymmetric shell analysis of the unshielded, mixed-scale model[17] as well as analysis of an unshielded full-scale containment[18,19]. Comparison of these analyses showed that the proposed mixed-scale model would be an adequate representation of the overall behavior of the full-scale containment at a scaled pressure load. However, the relative increase in the wall thickness would have the effect of reducing the bending strains and would alter buckling characteristics in the top head. Therefore, this test should be regarded as a validation test for analysis methods that can then be used to analyze a full-scale containment vessel, but the test results cannot be directly applied to infer behavior of a full-scale containment.

9.2 Contact Structure

Early finite element axisymmetric shell analyses were also performed on the full-scale containment with a representation of a shield building in order to determine the effects that the inclusion of a contact structure (CS) would have on steel containment vessel (SCV) model behavior[19,20,21,22,23]. These computations used a rigid surface to model the CS in order to bound the problem and because no detailed information was available on the actual shield building. Table 9-1 summarizes the response of the shielded and unshielded containments in key locations. Results are presented at approximately 5% and 10% maximum strain because the original termination criteria were based on strain.

These results showed that the presence of a shield structure would have a significant effect on the behavior of the steel containment model. Maximum strains of 5% and 10% occurred at higher pressures in the shielded containment than in the unshielded. Furthermore, these maximum strains occur in different locations in the containment. In the shielded containment, the largest inelastic strains occurred in the top head, while in the unshielded containment the maximum strains occurred in the middle part of the conical section at lower pressure. Therefore, the inclusion of some type of CS in the scale model test was warranted.

Additional finite element analyses were performed to evaluate the thickness of the CS for the design effort[24]. These axisymmetric shell analyses showed that a 32-mm thick CS constructed of A36 steel would not experience large plastic strains over the range of the test.

9.3 Instrumentation Holes

The presence of the CS presented some additional challenges for the instrumentation on the exterior surface of the SCV model. To measure bending response of the SCV model, strain gages were required on both the interior and exterior surfaces at the same location. During the initial stages of pressurization, the SCV was not in contact with the outer structure so the strain gages on the exterior surface functioned normally. However, once the SCV made contact with

---

17 Porter, V.L., "Analysis of SCV Model Pressurization using Typical Material Properties," Sandia memorandum to V.K. Luk, January 18, 1994.

18 Thorne, B.J., "Steel Containment Vessel Calculation without Rigid Shield Building," Sandia memorandum to J.S. Ludwigsen, December 4, 1991.

19 Thorne, B.J., "Additional Information about Steel Containment Vessel Calculated Strains," Sandia memorandum to W.A. von Riesemann, December 12, 1991.

20 Thorne, B.J., "Review of 'Study on the Effect of Shield Building' HITA91-003," Sandia memorandum to J.S. Ludwigsen, November 22, 1991.

21 Thorne, B.J., "Steel Containment Vessel Calculation with Rigid Shield Building," Sandia memorandum to J. S. Ludwigsen, December 2, 1991.

22 Thorne, B.J., "Steel Containment Vessel Calculation to 4MPa," Sandia memorandum to R.A. Watson, July 21, 1992.

23 Thorne, B.J., "Calculations for Estimating Loads on the Shield Building," Sandia memorandum to R.A. Watson. November 20, 1992.

24 Carter, P.A., and Porter, V.L., "Contact Structure Design," Sandia memorandum to V.K. Luk, October 11, 1994.

Table 9-1. Behavior of Shielded and Unshielded MK-II Containment Vessel

Parameter	Unshielded	Shielded
Yield Pressure (MPa)	0.75	0.75
Pressure at First Contact (MPa)	N/A	0.84 (near top of equipment hatch)
At Approximately 5% Maximum Strain		
Pressure (MPa)	0.96	1.2
Maximum Strain at Knuckle (%)	5.2	2.2
Maximum Strain at Equipment Hatch (%)	2.9	0.6
Maximum Strain in Top Head (%)	-0.2	(5.2)
At Approximately 10% Maximum Strain		
Pressure (MPa)	1.25	1.4
Maximum Strain at Knuckle (%)	11	2.2
Maximum Strain at Equipment Hatch (%)	6.4	0.6
Maximum Strain in Top Head (%)	(6.1)	(8.9)
Note: All strain values are membrane strains. Meridional strains are denoted by enclosure in parentheses. All others are hoop strains.		

the CS, any strain gage in the area of contact eventually ceased to function. Therefore, measuring bending response beyond this point would not normally be possible. The solution to allow bending strain measurements to continue after contact has been established was to put small holes in the CS over a few of the gages on the exterior of the SCV as long as the holes were small enough that they would not affect the local behavior of the SCV model. Axisymmetric finite element analyses of a uniform load on a circular plate over a hole were performed to assess the effects such a hole in the CS would have on the strain in the SCV wall[25]. Results of analyses for both 1.5-inch and 2.0-inch diameter holes in the contact structure indicate that the bending strains introduced in the SCV wall by contact with the hole would be on the order of 4% or 5% of the membrane strains. Furthermore, the deflection due to the bending is less than 0.2 mm even in the worst case. This amount of localized bulging represents less than 3% of the wall thickness.

9.4 Inner Support Ring Adequacy

During construction and instrumentation of the SCV model, an inner ring in the bottom head provided support for two technicians and instrumentation equipment. Instrumentation continued to be supported by this ring during the test. Finite element results for the radial deformation and stress state in this ring during pressurization showed that the SCV model exhibits very little radial expansion in this region and is sufficiently strong to sustain the anticipated loads[26]. Furthermore, results of a simple closed-form analysis with both live and dead loads on the ring indicated that the ring was more than adequate to support the anticipated loads without significant vertical deflection.

[25] Porter, V.L., "Investigations of Potential Errors Introduced by Instrumentation Holes in the Contact Structure," Sandia memorandum to V.K. Luk, February 7, 1995.

[26] Porter, V.L., "Analysis of Inner Support Ring for SCV Model Test," Sandia memorandum to V.K. Luk, February 4, 1995.

10. Summary and Conclusions

This report documents the finite element analyses performed at SNL for support of design efforts and for pretest predictions of the behavior of a steel containment vessel (SCV) model to be tested in a joint program sponsored by Nuclear Power Engineering Corporation (NUPEC) of Japan and the Nuclear Regulatory Commission (NRC). The ABAQUS (1993b) general purpose finite element code was used for all structural analyses.

Preliminary axisymmetric analyses were used to characterize the behavior of the shielded mixed-scale model and for studies regarding the development of the finite element models to be used for later pretest predictions. As a result of these scoping computations, shell elements were used extensively in later models for prediction of model behavior during the test. In addition, the preliminary finite element analyses were used to perform a parametric study on the effects of friction between the SCV and the contact structure (CS). Results indicated that the magnitude of the friction coefficient between 0.1 and 0.5 had little effect on model behavior, although results from a frictionless analysis were substantially different. Because the SCV model and the CS are not lubricated surfaces, a friction coefficient of 0.20 was judged a reasonable assumption and used in all subsequent analyses. Finally, axisymmetric finite element analyses of uniaxial tensile test specimens were also used to extrapolate the material data provided by uniaxial tensile tests beyond maximum load to the stress ranges needed to extend the predictive analyses to the point of failure.

The structural analysis effort for pretest predictions of model behavior consisted of four basic finite element models with some analyses repeated with slight modifications. The results for first yield and for first contact for each of these analyses are summarized in Table 10-1. The first finite element model was a global axisymmetric shell element model. This model was run with two different gap dimensions (the nominal distance between the SCV and CS): 18 mm (the as-designed gap), designated as GAX18, and 34 mm (a worst-case-scenario gap), designated GAX34. All remaining analyses used the as-designed 18 mm gap dimension. The second model was a global three-dimensional shell element model (G3DS) whose only non-axisymmetric detail was the equipment hatch. Results from this model called for further study in two areas: (1) the area near the junction of the material change interface and the equipment hatch insert plate, and (2) the top head including the knuckle. The third model was a local axisymmetric continuum element model of the CS and the top head area of the SCV from the apex extending down to the upper 19 mm stiffener (LTHAXC). The last model was a locally refined shell element submodel of a cut-out of the material change interface/equipment hatch insert plate junction from the three-dimensional shell element model. This model was first run with design parameters (LEHS) and then rerun later with a representation of as-built shell thicknesses when they became available (LEHSTh).

Pretest predictions of failure of the SCV model are highly dependent on details that were included in the analytical effort. In particular, local analyses are very dependent on as-built features incorporated into the analytical models. Results of a local analysis of the thinned section of the SCV wall near the equipment hatch reinforcement plate indicate that this area is the most likely for failure. This analysis did not include the as-built gap dimensions which were somewhat larger than the 18 mm used in the design. Given the early and rapid occurrence of plastic flow compared to other locations within the pressure vessel, the strains attained relative to the material's ductility, and the biaxial stress state, the finite element results indicate local ductile failure in the thinned section next to the equipment hatch insert plate near an internal pressure of 4.5 MPa. Global ductile rupture of the vessel is indicated in the top head at the much higher pressure of slightly more than 12 MPa.

An earlier failure at the equipment hatch or another location due to the presence of welding flaws or inclusions could not be ruled out because there are states of stress simultaneously producing plastic flow in at least four other locations in the pressure vessel (primarily the top head and knuckle regions). The weld metal and HAZ near the thinned areas introduce additional uncertainty. The yield strength and ductility of the weld metal is typically higher than the parent material, while the same properties in the HAZ are typically lower than the parent material. Brittle failure modes have not been considered in this analysis effort.

Table 10-1. Summary of Pretest Analyses

	First Yield		First Contact	
Model Description	**Location**	**Pressure**	**Location**	**Pressure**
Global Axisymmetric -- 18 mm Gap (GAX18)	Knuckle	2.2 MPa	Knuckle/upper conical section	4.0 MPa
Global Axisymmetric -- 34 mm Gap (GAX34)	Knuckle	2.2 MPa	Knuckle/upper conical section	4.0 MPa
Global 3-Dimensional Shells (G3DS)	E/H sleeve at attachment to insert plate	2.3 MPa	Knuckle/upper conical section	4.1 MPa
Local Axisymmetric Continuum of Top Head (LTHAXC)	Knuckle	2.0 MPa	Knuckle	3.2 MPa
Local 3-Dimensional Shells of Equipment Hatch Area (LEHS)	Middle conical section adjacent to insert plate	2.6 MPa	Middle conical section	4.2 MPa
Local 3-Dimensional Shells of Equipment Hatch Area with Thinning (LEHSTh)	Above thinned section adjacent to insert plate	2.2 MPa	Middle conical section	4.2 MPa

11. References

ABAQUS User's Manual, Version 5.2, Hibbitt, Karlsson and Sorensen, Inc., Pawtucket, RI, 1993a.

ABAQUS/Standard User's Manual, Version 5.3, Hibbitt, Karlsson and Sorensen, Inc., Pawtucket, RI, 1993b.

ABAQUS/Standard User's Manual, Version 5.4, Hibbitt, Karlsson and Sorensen, Inc., Pawtucket, RI, 1994.

ABAQUS/Standard User's Manual, Version 5.5, Hibbitt, Karlsson and Sorensen, Inc., Pawtucket, RI, 1995.

Dieter, G E., *Mechanical Metallurgy*, Third edition, McGraw-Hill Book Co., New York, N.Y., 1986.

Gere, J.M., and Timoshenko, S.P., *Mechanics of Materials*, Second edition, PWS-Kent Publishing Co., Boston, MA, 1984.

Hosford, W.F., and Caddell, R.M., *Metal Forming: Mechanics and Metallurgy*, Prentice-Hall, Inc. Englewood Cliffs, N.J., 1983.

Hucek, H.J., ed., *Structural Alloys Handbook.* Vol. 1. Columbus, Ohio: Batelle's Columbus Laboratories, 1985.

Isozaki, T., Soda, K., Miyazono, S., "Structural Analysis of a Japanese BWR MARK-I Containment under Internal Pressure Loading," *Proceedings of the Third Workshop on Containment Integrity*, NUREG/CP-0076, SAND86-0618, August, 1986.

Kalnins, A., Updike, D.P., "New Design Curves for Torispherical Heads," Welding Research Council Bulletin, Bulletin 364, New York, June 1991.

Luk, V.K, and Klamerus, E.W., *Round Robin Pretest Analyses of a Steel Containment Vessel Model and Contact Structure Assembly Subject to Static Internal Pressurization*, NUREG/CR-6517, SAND96-2877. Albuquerque, NM: Sandia National Laboratories, 1996.

MATLAB Reference Guide, Version 4.2, The Mathworks, Inc., Natick, MA, 1992.

Porter, V.L., "Analyses of a Steel Containment Vessel with an Outer Contact Structure under Severe Internal Overpressurization Conditions," *Proceedings of the Third International Conference on Containment and Design*, Canadian Nuclear Society, Toronto, Canada, October, 1994.

Stone, C.M., *SANTOS: A Two Dimensional Finite Element Program for the Quasistatic, Large Deformation, Inelastic Response of Solids*, SAND90-0543. Albuquerque, NM: Sandia National Laboratories, 1997.

Wellman, G.W., and Salzbrenner, R., "Quasistatic Modeling and Testing of Exclusion Region Barrier Mock-Ups," SAND92-0024, Sandia National Laboratories, Albuquerque, NM, March 1992.

Appendix A

Steel Containment Vessel (SCV) Model and Contact Structure (CS) Drawings

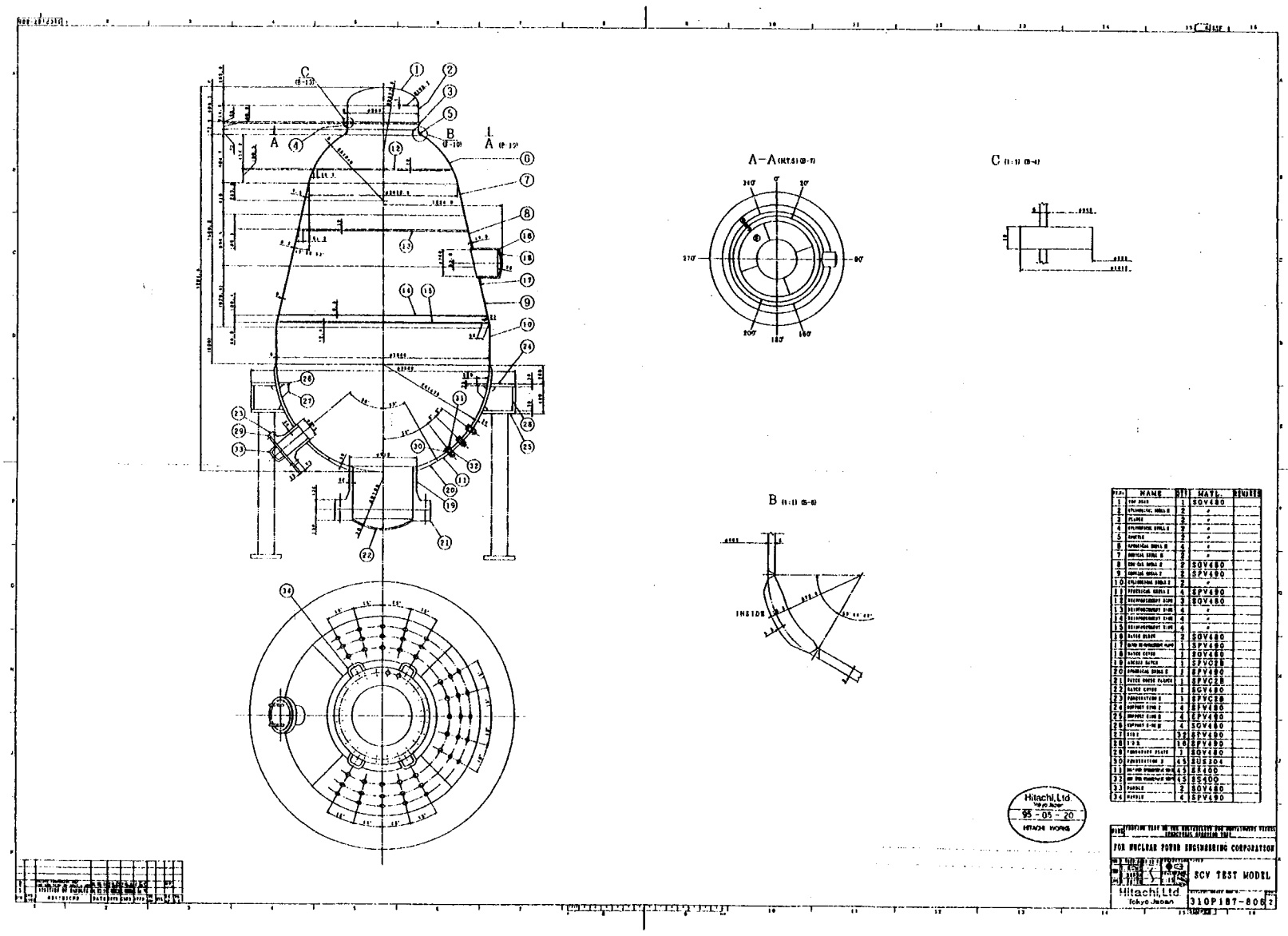

Figure A-1. Steel containment vessel (SCV) model - dimensional layout.

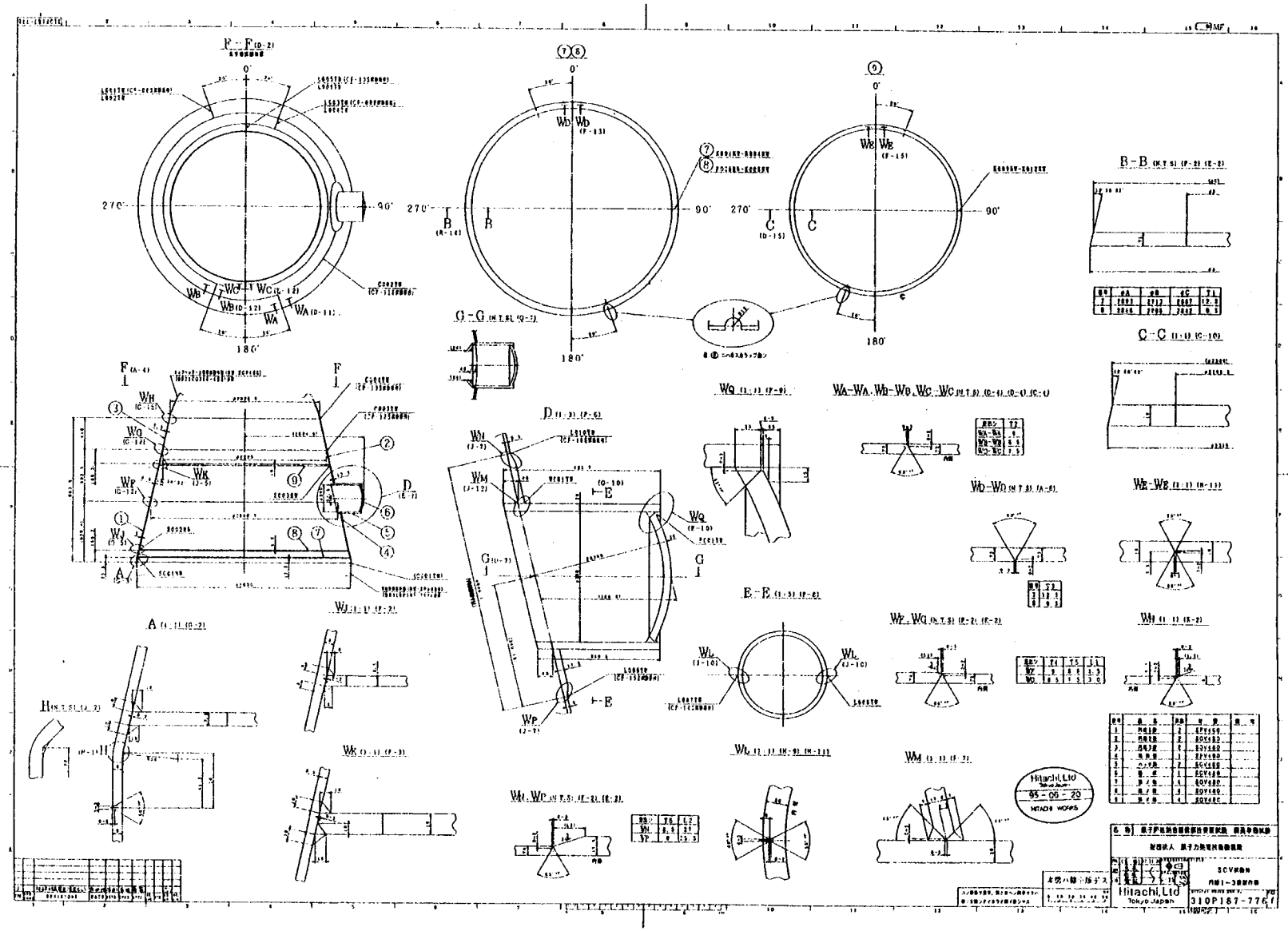

Figure A-2. Steel containment vessel (SCV) model - middle section.

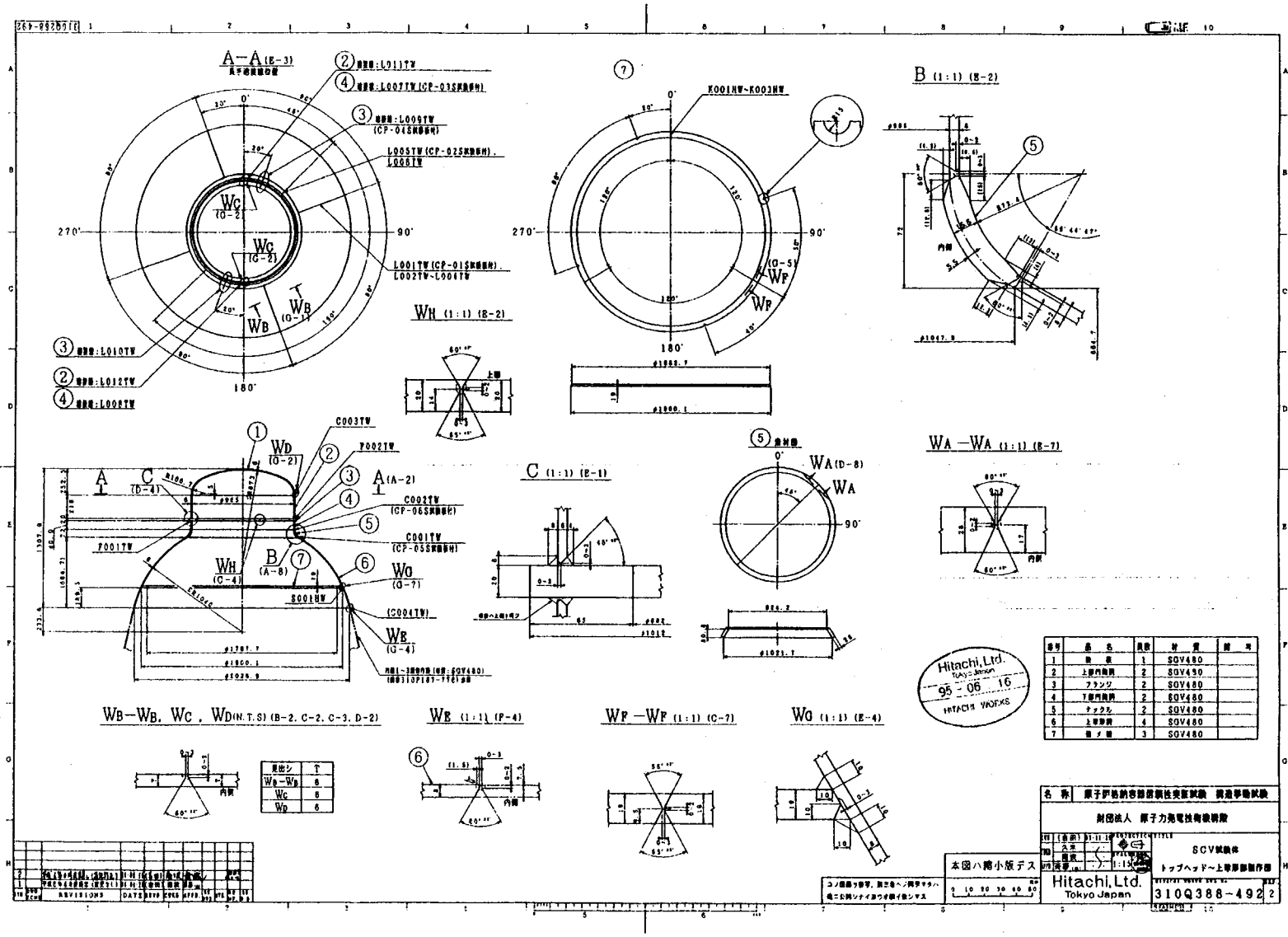

Figure A-3. Steel containment vessel (SCV) model - upper section.

Appendix B

Uniaxial Test Data

Table 1. Dimensions of Test Specimens

D (mm)	L (mm)	R (mm)	P (mm)
~14	50	15	60
~10	35	12	50
~6	21	10	35
~4	14	6	24
~3	11	4	20

L: Gage Length

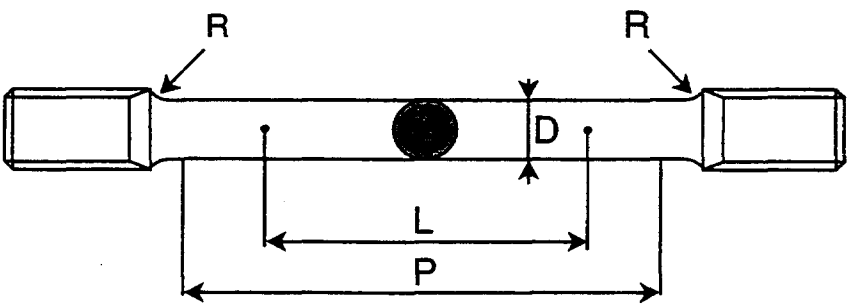

TRI-6403-012-0

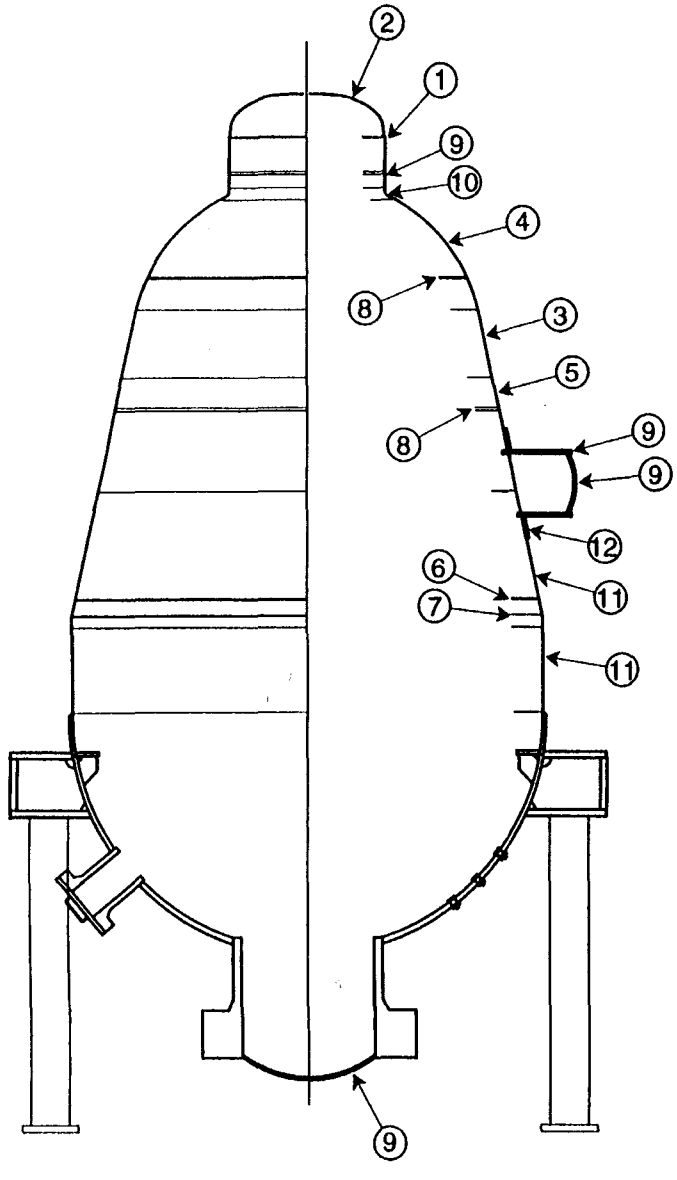

TRI-6403-013-0

Table 2. Outline of SCV Material Tests

Location	Material	Thickness (mm)	Table Number	Direction	Specimen Number
1 Top Head Shell	SGV480	6	4	Roll Rectangular	R1, R2 T1, T2
2 Top Head	SGV480	6	5	Roll Rectangular	R3, R4 T3, T4
3 Conical Shell 3	SGV480	7.5	6	Roll Rectangular	R5, R6 T5, T6
4 Spherical Shell	SGV480	8	7	Roll Rectangular	R7, R8 T7, T8
5 Conical Shell 2	SGV480	8.5	8	Roll Rectangular	R9, R10 T9, T10
6 Reinforcement Ring	SGV480	9.5	9	Roll Rectangular	R11, R12 T11, T12
7 Reinforcement Ring	SGV480	12.5	10	Roll Rectangular	R13, R14 T13, T14
8 Reinforcement Ring	SGV480	19	11	Roll Rectangular	R15, R6 T15, T6
9 Flange, Hatch Cover Hatch SLeeve	SGV480	20	12	Roll Rectangular	R17, R18 T17, T18
10 Knuckle	SGV480	28	13	Roll Rectangular	R19, R20 T19, T20
11 Cylindrical Shell Conical Shell	SPV490	9	14	Roll Rectangular	R21, R22 T21, T22
12 Hatch Reinforcement Plate	SPV490	17.5	15	Roll Rectangular	R23, R24 T23, T24

Table 3. Failure Results of Tensile Test

Location	Specimen #	Gage Length L (mm)	Elongation Lf (mm)	Elongation (%)	Initial Diameter D (mm)	Final Diameter Df (mm)	Reduction of Area (%)
1	R1	11.0	15.18	38.0	3.01	1.34	80.2
	R2	11.0	15.23	38.5	3.01	1.47	76.1
	T1	11.0	15.49	40.8	3.01	1.33	80.5
	T2	11.0	15.34	39.5	3.01	1.33	80.5
2	R3	11.0	15.17	37.9	3.01	1.50	75.2
	R4	11.0	15.20	38.2	3.02	1.51	75.0
	T3	11.0	14.78	34.4	3.00	1.52	74.3
	T4	11.0	15.03	36.6	3.00	1.54	73.6
3	R5	11.0	15.22	38.4	3.00	1.36	79.4
	R6	11.0	15.33	39.4	3.01	1.36	79.6
	T5	11.0	15.39	39.9	2.99	1.41	77.8
	T6	11.0	15.24	38.5	2.99	1.36	79.3
4	R7	14.0	19.61	40.1	4.02	1.92	77.2
	R8	14.0	19.02	35.9	4.02	1.99	75.5
	T7	14.0	19.20	37.1	4.01	2.02	74.6
	T8	14.0	19.38	38.4	4.02	2.07	73.5
5	R9	14.0	19.48	39.1	4.01	1.94	76.6
	R10	14.0	19.99	42.8	4.03	1.94	76.8
	T9	14.0	19.27	37.6	4.03	2.10	72.8
	T10	14.0	19.08	36.3	4.00	2.08	73.0
6	R11	14.0	19.64	40.3	4.02	1.80	80.0
	R12	14.0	19.73	40.9	4.00	1.82	79.3
	T11	14.0	19.40	38.6	4.01	2.08	73.1
	T12	14.0	19.22	37.3	4.02	1.99	75.5
7	R13	21.0	28.53	35.9	6.01	2.90	76.7
	R14	21.0	28.64	36.4	6.01	2.91	76.6
	T13	21.0	28.79	37.1	6.02	3.01	75.0
	T14	21.0	28.72	36.8	6.00	2.98	75.3
8	R15	35.0	49.33	40.9	10.00	5.16	73.4
	R16	35.0	48.83	39.5	10.01	5.09	74.1
	T15	35.0	49.00	40.0	10.01	5.15	73.5
	T16	35.0	49.37	41.1	10.00	5.12	73.8
9	R17	35.0	49.43	41.2	10.01	5.07	74.3
	R18	35.0	48.82	39.5	10.00	5.11	73.9
	T17	35.0	48.21	37.7	10.02	5.38	71.2
	T18	35.0	49.16	40.5	10.03	5.34	71.7
10	R19	50.0	69.26	38.5	14.01	7.38	72.3
	R20	50.0	70.22	40.4	14.01	7.28	73.0
	T19	50.0	68.78	37.6	14.00	7.54	71.0
	T20	50.0	68.76	37.5	14.01	7.57	70.8
11	R21	14.0	18.17	29.8	4.02	1.63	83.6
	R22	14.0	18.21	30.1	4.02	1.67	82.7
	T21	14.0	18.04	28.9	4.02	1.52	85.7
	T22	14.0	17.90	27.9	4.01	1.64	83.3
12	R23	35.0	45.50	30.0	10.01	4.36	81.0
	R24	35.0	45.48	29.9	10.01	4.42	80.5
	T23	35.0	45.64	30.4	10.01	4.48	80.0
	T24	35.0	45.71	30.6	10.01	4.42	80.5

Table 4. Location 1 Test Results - Upper Cylindrical Shell Above Top Flange (SGV480: Thickness 6 mm)

R1	Engr. Strain (%)	Engr. Stress (MPa)	True Strain (%)	True Stress (MPa)
1	0.000	0.0	0.000	0.0
2	0.004	7.5	0.004	7.5
3	0.017	34.9	0.017	34.9
4	0.035	73.9	0.035	74.0
5	0.053	113.1	0.053	113.1
6	0.071	152.2	0.071	152.3
7	0.089	191.4	0.089	191.6
8	0.107	230.6	0.107	230.8
9	0.125	270.0	0.125	270.3
10	0.143	309.2	0.143	309.6
11	0.161	348.1	0.161	348.7
12	0.179	387.6	0.179	388.3
13	0.459	384.3	0.458	386.1
14	1.854	400.1	1.837	407.5
15	3.110	412.8	3.082	425.6
16	4.506	424.8	4.407	444.0
17	5.622	443.8	5.469	468.7
18	6.878	463.3	6.652	495.1
19	8.134	479.5	7.820	518.6
20	9.390	492.8	8.975	539.1
21	10.647	503.6	10.117	557.2
22	11.903	512.6	11.246	573.6
23	13.159	520.0	12.362	588.5
24	14.415	526.0	13.466	601.9
25	15.671	531.1	14.558	614.4
26	16.927	535.2	15.638	625.7
27	18.183	538.2	16.706	636.0
28	19.439	540.7	17.763	645.9
29	20.695	542.2	18.809	654.4
30	21.951	543.1	19.845	662.3
31	22.230	543.2	20.073	663.9
32	22.649	543.1		
33	23.486	542.6		
34	24.463	541.0		
35	25.301	538.6		
36	26.138	534.6		
37	26.975	529.2		
38	27.952	520.8		
39	28.790	511.9		
40	29.627	501.6		
41	30.464	489.4		
42	31.441	472.7		
43	32.279	456.2		
44	33.116	437.4		
45	34.093	412.8		
46	34.930	388.1		
47	35.768	362.3		
48	36.605	336.4		
49	37.582	304.4		
50	38.001	277.5		

R2	Engr. Strain (%)	Engr. Stress (MPa)	True Strain (%)	True Stress (MPa)
1	0.000	0.0	0.000	0.0
2	0.004	7.3	0.004	7.3
3	0.011	22.0	0.011	22.0
4	0.027	56.7	0.027	56.7
5	0.043	91.5	0.043	91.5
6	0.059	126.3	0.059	126.4
7	0.075	161.3	0.075	161.4
8	0.091	195.8	0.091	196.0
9	0.107	231.0	0.107	231.3
10	0.123	266.2	0.123	266.5
11	0.140	301.2	0.140	301.6
12	0.156	336.0	0.156	336.5
13	0.172	371.1	0.171	371.7
14	0.185	398.7	0.184	399.5
15	0.185	400.3	0.184	401.0
16	0.712	394.4	0.709	397.2
17	2.116	402.4	2.094	410.9
18	3.521	420.5	3.460	435.3
19	4.925	445.1	4.807	467.0
20	6.330	466.0	6.137	495.5
21	7.734	483.0	7.449	520.3
22	9.138	496.8	8.744	542.2
23	10.543	508.1	10.023	561.7
24	11.947	517.0	11.285	578.8
25	13.352	524.4	12.532	594.4
26	14.756	530.1	13.763	608.3
27	16.160	534.8	14.980	621.2
28	17.565	538.2	16.182	632.7
29	18.969	540.7	17.369	643.3
30	20.374	542.4	18.543	652.9
31	21.778	543.0	19.703	661.2
32	22.305	542.8		
33	23.182	542.3		
34	24.236	540.5		
35	25.114	537.7		
36	25.991	533.4		
37	26.869	527.4		
38	27.922	518.2		
39	28.800	508.5		
40	29.678	497.1		
41	30.556	483.7		
42	31.609	465.1		
43	32.487	446.9		
44	33.364	426.3		
45	34.418	400.4		
46	35.295	378.6		
47	36.173	357.1		
48	37.051	335.3		
49	38.104	305.6		
50	38.455	293.7		

T1	Engr. Strain (%)	Engr. Stress (MPa)	True Strain (%)	True Stress (MPa)
1	0.000	0.0	0.000	0.0
2	0.004	7.5	0.004	7.5
3	0.017	34.5	0.017	34.5
4	0.035	69.4	0.035	69.5
5	0.052	104.2	0.052	104.3
6	0.069	139.4	0.069	139.4
7	0.086	174.8	0.086	174.9
8	0.104	209.5	0.104	209.7
9	0.121	244.6	0.121	244.9
10	0.138	279.8	0.138	280.2
11	0.155	314.8	0.155	315.3
12	0.173	349.8	0.173	350.4
13	0.190	384.3	0.190	385.1
14	0.196	397.4	0.196	398.1
15	0.370	396.8	0.369	398.2
16	1.238	408.0	1.230	413.0
17	3.495	454.6	3.435	470.5
18	4.883	476.7	4.787	500.0
19	6.272	494.3	6.083	525.3
20	7.661	508.8	7.381	547.7
21	9.050	520.0	8.663	567.1
22	10.439	529.2	9.929	584.4
23	11.827	536.6	11.178	600.1
24	13.216	542.4	12.412	614.1
25	14.605	547.0	13.632	626.9
26	15.994	550.6	14.837	638.7
27	17.383	553.3	16.027	649.5
28	18.771	555.4	17.202	659.6
29	20.160	556.6	18.365	668.8
30	21.549	557.4	19.515	677.5
31	22.417	557.7	20.226	682.7
32	22.938	557.6		
33	23.979	557.0		
34	25.021	556.1		
35	26.063	554.1		
36	27.104	550.4		
37	27.972	545.5		
38	29.014	537.5		
39	30.055	527.0		
40	31.097	514.2		
41	32.139	498.4		
42	33.180	479.6		
43	34.222	458.1		
44	35.263	432.9		
45	36.305	408.8		
46	37.173	385.3		
47	38.215	359.3		
48	39.256	333.1		
49	40.298	300.6		
50	40.819	278.3		

T2	Engr. Strain (%)	Engr. Stress (MPa)	True Strain (%)	True Stress (MPa)
1	0.000	0.0	0.000	0.0
2	0.003	7.0	0.003	7.0
3	0.010	21.1	0.010	21.1
4	0.027	55.9	0.027	55.9
5	0.044	91.1	0.044	91.1
6	0.062	125.9	0.062	126.0
7	0.079	160.8	0.079	161.0
8	0.096	195.5	0.096	195.7
9	0.113	230.5	0.113	230.7
10	0.130	265.3	0.130	265.6
11	0.147	300.1	0.147	300.5
12	0.165	335.4	0.165	335.9
13	0.182	370.3	0.182	371.0
14	0.197	399.7	0.197	400.5
15	0.199	403.9	0.199	404.7
16	0.729	402.5	0.727	405.4
17	2.144	431.2	2.122	440.4
18	3.558	457.6	3.497	473.9
19	4.973	479.1	4.854	502.9
20	6.387	496.2	6.192	527.9
21	7.802	509.9	7.513	549.6
22	9.217	520.8	8.817	568.8
23	10.631	529.4	10.103	585.6
24	12.046	536.2	11.374	600.8
25	13.461	541.5	12.629	614.4
26	14.875	545.7	13.868	626.9
27	16.290	548.8	15.092	638.2
28	17.705	551.2	16.302	648.8
29	19.119	552.9	17.496	658.6
30	20.534	553.9	18.677	667.6
31	21.948	554.4	19.843	676.0
32	22.125	554.4		
33	22.656	554.3		
34	23.540	554.1		
35	24.601	553.4		
36	25.485	552.0		
37	26.546	549.3		
38	27.430	545.1		
39	28.491	537.0		
40	29.375	527.9		
41	30.436	514.3		
42	31.320	500.4		
43	32.204	484.1		
44	33.265	460.9		
45	34.149	439.4		
46	35.210	413.5		
47	36.095	392.0		
48	37.155	365.8		
49	38.040	344.0		
50	39.101	316.2		
51	39.454	304.0		

Table 5. Location 2 Test Results - Top Head (SGV480: Thickness 6 mm)

R3	Engr. Strain (%)	Engr. Stress (MPa)	True Strain (%)	True Stress (MPa)
1	0.000	0.0	0.000	0.0
2	0.002	3.6	0.002	3.6
3	0.014	26.8	0.014	26.8
4	0.021	51.4	0.021	51.4
5	0.018	76.2	0.018	76.2
6	0.032	100.9	0.032	100.9
7	0.040	125.6	0.040	125.7
8	0.056	150.5	0.056	150.6
9	0.063	173.6	0.063	173.7
10	0.075	198.3	0.075	198.4
11	0.089	222.8	0.089	223.0
12	0.098	247.6	0.098	247.9
13	0.110	272.1	0.110	272.4
14	0.117	296.7	0.117	297.0
15	0.126	321.4	0.126	321.8
16	0.131	344.8	0.131	345.3
17	0.157	369.5	0.157	370.1
18	0.201	413.6	0.201	414.7
19	0.340	405.8	0.339	407.2
20	1.158	409.0	1.151	413.6
21	2.460	420.7	2.430	431.1
22	3.203	440.9	3.153	455.0
23	4.068	462.9	3.987	481.7
24	4.953	481.3	4.834	505.2
25	6.174	501.9	5.991	532.9
26	7.591	519.2	7.317	556.6
27	8.850	530.6	8.480	577.6
28	10.271	540.3	9.777	595.8
29	11.512	548.6	10.896	609.6
30	12.795	551.5	12.040	622.1
31	14.507	555.9	13.546	636.6
32	16.008	558.2	14.849	647.6
33	19.813	558.2	18.076	668.8
34	22.852	559.1	20.581	686.6
35	23.009	558.9		
36	24.173	559.0		
37	25.026	558.2		
38	25.907	557.2		
39	27.221	553.8		
40	28.442	548.2		
41	29.560	540.5		
42	30.632	530.6		
43	31.350	522.6		
44	32.546	506.7		
45	33.645	489.3		
46	34.426	474.7		
47	35.091	461.3		
48	35.628	449.8		
49	36.075	438.9		
50	36.659	424.2		
51	37.087	412.9		
52	37.502	401.3		
53	37.911	388.1		

R4	Engr. Strain (%)	Engr. Stress (MPa)	True Strain (%)	True Stress (MPa)
1	0.000	0.0	0.000	0.0
2	0.001	2.7	0.001	2.7
3	0.004	27.0	0.004	27.0
4	0.023	53.2	0.023	53.2
5	0.037	78.0	0.037	78.0
6	0.062	104.4	0.062	104.5
7	0.078	130.6	0.078	130.7
8	0.100	156.8	0.100	156.8
9	0.114	183.1	0.114	183.3
10	0.133	209.4	0.133	209.7
11	0.141	235.6	0.141	235.9
12	0.163	261.6	0.163	262.1
13	0.185	287.9	0.185	288.5
14	0.205	313.5	0.205	314.2
15	0.224	339.5	0.224	340.3
16	0.246	365.9	0.246	366.8
17	0.260	392.3	0.260	393.3
18	0.282	431.7	0.282	432.9
19	0.339	419.7	0.339	421.2
20	1.926	418.3	1.908	426.3
21	3.051	425.1	3.006	438.1
22	3.882	441.2	3.809	458.3
23	5.076	466.6	4.952	490.3
24	6.418	489.3	6.221	520.7
25	7.892	507.6	7.596	547.7
26	9.523	522.6	9.097	572.4
27	11.394	534.8	10.791	595.7
28	13.187	543.2	12.387	614.8
29	15.261	550.1	14.203	634.0
30	17.450	554.5	16.085	651.2
31	18.875	556.2	17.291	661.2
32	20.699	557.4	18.813	672.8
33	21.507	557.7	19.480	677.7
34	25.710	557.6		
35	26.745	557.4		
36	27.562	556.9		
37	27.994	556.3		
38	28.860	555.0		
39	29.632	552.8		
40	30.094	551.0		
41	30.940	547.3		
42	31.422	544.4		
43	32.213	538.7		
44	33.059	531.2		
45	33.867	522.6		
46	34.745	512.2		
47	35.250	505.3		
48	35.839	496.8		
49	36.341	488.9		
50	36.799	481.1		
51	37.255	473.1		
52	37.597	466.6		
53	38.183	454.7		

T3	Engr. Strain (%)	Engr. Stress (MPa)	True Strain (%)	True Stress (MPa)
1	0.000	0.0	0.000	0.0
2	0.002	3.6	0.002	3.6
3	0.008	27.8	0.008	27.8
4	0.023	54.1	0.023	54.1
5	0.050	80.8	0.050	80.8
6	0.068	106.9	0.068	107.0
7	0.092	133.4	0.092	133.5
8	0.119	159.8	0.119	160.0
9	0.143	186.7	0.143	187.0
10	0.173	213.3	0.173	213.7
11	0.185	239.9	0.185	240.3
12	0.218	266.5	0.218	267.1
13	0.242	293.3	0.242	294.0
14	0.260	318.7	0.259	319.5
15	0.284	344.0	0.283	345.0
16	0.307	370.6	0.306	371.7
17	0.316	397.3	0.315	398.5
18	0.352	440.8	0.351	442.4
19	0.547	417.2	0.545	419.5
20	1.146	418.5	1.139	423.2
21	2.500	425.3	2.469	435.9
22	3.830	432.6	3.758	449.1
23	4.842	455.7	4.728	477.8
24	5.968	476.8	5.797	505.3
25	7.570	499.3	7.297	537.1
26	9.583	519.4	9.151	569.1
27	11.464	532.7	10.853	593.8
28	13.609	544.5	12.935	619.7
29	15.974	551.7	14.819	639.9
30	18.083	556.3	16.622	656.9
31	19.913	558.7	18.159	669.9
32	21.762	559.7	19.690	681.5
33	21.910	559.7		
34	22.717	559.2		
35	23.422	558.5		
36	23.985	557.4		
37	24.931	554.9		
38	25.770	551.0		
39	26.363	547.6		
40	27.373	539.5		
41	28.153	531.6		
42	29.187	518.9		
43	29.982	507.5		
44	30.643	496.4		
45	31.040	489.5		
46	31.511	480.6		
47	32.134	467.6		
48	32.629	456.9		
49	32.949	449.2		
50	33.201	441.4		
51	33.560	433.6		
52	34.055	420.3		
53	34.366	411.6		

T4	Engr. Strain (%)	Engr. Stress (MPa)	True Strain (%)	True Stress (MPa)
1	0.000	0.0	0.000	0.0
2	0.002	3.4	0.002	3.4
3	0.035	32.1	0.035	32.1
4	0.070	62.3	0.070	62.3
5	0.097	92.3	0.097	92.4
6	0.127	122.2	0.127	122.3
7	0.151	152.5	0.151	152.7
8	0.175	182.6	0.175	182.9
9	0.207	212.6	0.207	213.0
10	0.225	242.6	0.224	243.2
11	0.255	272.6	0.254	273.3
12	0.273	302.5	0.272	303.4
13	0.297	332.6	0.296	333.6
14	0.318	362.7	0.317	363.8
15	0.356	392.9	0.355	394.3
16	0.371	422.9	0.370	424.4
17	0.389	453.2	0.388	454.9
18	0.410	483.2	0.409	485.2
19	0.431	509.8	0.430	511.9
20	0.764	422.1	0.761	425.3
21	2.056	422.7	2.035	431.4
22	3.851	434.6	3.778	451.4
23	4.703	457.2	4.595	478.7
24	6.132	483.2	5.951	512.6
25	8.005	508.6	7.700	547.4
26	10.309	527.5	9.811	581.9
27	12.164	539.2	11.479	604.8
28	14.540	549.2	13.575	629.0
29	16.159	554.0	14.979	643.5
30	17.990	557.7	16.543	658.0
31	20.381	560.6	18.549	674.8
32	22.169	561.4	20.023	685.9
33	20.055	561.4		
34	23.191	561.0		
35	24.100	560.6		
36	25.000	559.5		
37	25.841	557.0		
38	27.123	552.1		
39	28.200	545.4		
40	29.163	537.0		
41	30.264	528.1		
42	30.474	521.9		
43	31.354	509.7		
44	32.236	495.5		
45	32.727	486.6		
46	33.216	477.4		
47	33.740	466.0		
48	34.406	451.2		
49	34.936	438.2		
50	35.508	423.3		
51	35.895	411.0		
52	36.369	398.0		
53	36.638	389.2		

Table 6. Location 3 Test Results - Upper Conical Shell Between Weld Lines (SGV480: Thickness 7.5 mm)

R5	Engr. Strain (%)	Engr. Stress (MPa)	True Strain (%)	True Stress (MPa)
1	0.000	0.0	0.000	0.0
2	0.004	7.4	0.004	7.4
3	0.012	23.8	0.012	23.8
4	0.030	63.3	0.030	63.3
5	0.048	102.7	0.048	102.7
6	0.066	142.1	0.066	142.2
7	0.084	181.4	0.084	181.6
8	0.103	221.0	0.103	221.3
9	0.121	260.5	0.121	260.8
10	0.139	299.9	0.139	300.3
11	0.157	339.3	0.157	339.8
12	0.175	378.6	0.175	379.3
13	0.193	417.2	0.192	418.0
14	0.613	408.4	0.611	411.0
15	1.871	411.2	1.853	418.9
16	3.129	408.0	3.081	420.7
17	4.388	432.9	4.294	451.9
18	5.646	454.6	5.492	480.3
19	6.905	471.5	6.677	504.1
20	8.163	486.0	7.847	525.7
21	9.421	498.3	9.003	545.2
22	10.680	508.4	10.147	562.7
23	11.938	516.6	11.277	578.5
24	13.197	523.9	12.396	593.0
25	14.455	529.6	13.501	606.1
26	15.713	534.3	14.594	618.2
27	16.972	538.2	15.676	629.5
28	18.230	541.1	16.746	639.8
29	19.489	543.6	17.805	649.8
30	20.747	545.4	18.852	658.6
31	22.005	546.6	19.889	666.9
32	23.264	547.2	20.916	674.5
33	23.683	547.1		
34	24.522	546.7		
35	25.361	545.4		
36	26.200	543.4		
37	27.039	540.2		
38	27.878	535.1		
39	28.717	528.5		
40	29.556	520.2		
41	30.395	510.2		
42	31.233	498.7		
43	32.072	485.1		
44	32.911	469.8		
45	33.750	452.2		
46	34.589	432.1		
47	35.428	409.4		
48	36.267	384.0		
49	37.106	357.8		
50	37.945	331.7		
51	38.364	317.3		

R6	Engr. Strain (%)	Engr. Stress (MPa)	True Strain (%)	True Stress (MPa)
1	0.000	0.0	0.000	0.0
2	0.011	2.8	0.011	2.8
3	0.015	29.2	0.015	29.2
4	0.032	53.9	0.032	54.0
5	0.056	80.1	0.056	80.2
6	0.084	105.6	0.084	106.7
7	0.105	132.8	0.105	132.9
8	0.122	157.0	0.122	157.2
9	0.140	183.6	0.140	183.8
10	0.178	210.1	0.178	210.4
11	0.208	236.6	0.208	237.1
12	0.219	262.9	0.219	263.5
13	0.251	289.4	0.251	290.1
14	0.285	316.3	0.285	317.2
15	0.292	342.6	0.292	343.6
16	0.324	368.9	0.324	370.1
17	0.358	395.3	0.358	396.7
18	0.376	421.7	0.376	423.3
19	0.407	459.4	0.407	461.3
20	0.601	410.9	0.600	413.4
21	1.676	402.4	1.663	409.1
22	2.675	399.5	2.640	410.2
23	3.764	410.4	3.695	425.9
24	5.005	430.5	4.884	452.1
25	6.451	455.0	6.252	484.4
26	7.963	475.4	7.662	513.3
27	9.878	494.8	9.420	543.7
28	12.340	512.6	11.638	575.9
29	14.736	524.5	13.747	601.7
30	17.521	534.1	16.145	627.7
31	20.268	540.2	18.456	649.6
32	22.740	543.3	20.490	666.8
33	23.650	545.3	21.229	674.2
34	24.513	545.0		
35	26.000	543.7		
36	27.232	541.2		
37	28.374	537.3		
38	29.680	530.2		
39	30.911	520.3		
40	32.152	508.1		
41	33.163	495.1		
42	33.946	483.5		
43	34.581	471.5		
44	35.347	458.8		
45	35.921	447.2		
46	36.493	434.7		
47	37.052	421.6		
48	37.635	407.0		
49	38.121	393.8		
50	38.563	381.1		
51	39.042	366.3		
52	39.365	356.1		

T5	Engr. Strain (%)	Engr. Stress (MPa)	True Strain (%)	True Stress (MPa)
1	0.000	0.0	0.000	0.0
2	0.003	6.5	0.003	6.5
3	0.021	43.2	0.021	43.3
4	0.043	87.4	0.043	87.4
5	0.065	131.6	0.065	131.7
6	0.086	175.4	0.086	175.6
7	0.108	219.6	0.108	219.8
8	0.130	263.8	0.130	264.1
9	0.151	307.8	0.151	308.3
10	0.173	352.2	0.173	352.8
11	0.195	396.0	0.195	396.8
12	0.204	413.8	0.204	414.7
13	0.592	414.1	0.590	416.6
14	1.885	412.6	1.868	420.3
15	2.920	410.9	2.878	422.9
16	4.084	407.7	4.003	424.3
17	5.765	452.9	5.605	479.0
18	7.058	473.4	6.820	506.8
19	8.352	489.8	8.022	530.8
20	9.645	503.3	9.208	551.8
21	10.938	514.6	10.380	570.8
22	12.232	523.6	11.540	587.6
23	13.525	531.0	12.685	602.9
24	14.818	536.9	13.818	616.5
25	16.112	541.7	14.939	629.0
26	17.405	545.6	16.046	640.6
27	18.698	548.7	17.141	651.3
28	19.992	550.9	18.226	661.1
29	21.285	552.5	19.297	670.1
30	22.578	553.4	20.358	678.3
31	23.872	553.8	21.408	686.0
32	24.001	553.9	21.512	686.8
33	24.389	553.7		
34	25.294	553.2		
35	26.200	552.2		
36	27.105	550.4		
37	27.881	547.9		
38	28.786	543.7		
39	29.692	537.6		
40	30.597	529.8		
41	31.502	520.1		
42	32.408	508.4		
43	33.184	496.4		
44	34.089	480.4		
45	34.994	461.8		
46	35.900	440.1		
47	36.805	415.1		
48	37.710	386.2		
49	38.486	360.0		
50	39.392	329.2		
51	39.909	310.2		

T6	Engr. Strain (%)	Engr. Stress (MPa)	True Strain (%)	True Stress (MPa)
1	0.000	0.0	0.000	0.0
2	0.004	8.8	0.004	8.8
3	0.024	48.5	0.024	48.6
4	0.043	88.0	0.043	88.0
5	0.062	127.6	0.062	127.7
6	0.082	167.3	0.082	167.4
7	0.102	207.0	0.102	207.2
8	0.121	246.9	0.121	247.2
9	0.141	286.7	0.141	287.2
10	0.160	326.6	0.160	327.1
11	0.180	366.5	0.180	367.1
12	0.200	406.4	0.200	407.2
13	0.206	419.6	0.206	420.5
14	0.613	417.0	0.612	419.5
15	1.832	400.6	1.816	407.9
16	3.322	403.1	3.268	416.4
17	4.271	428.8	4.183	447.2
18	5.490	450.6	5.345	475.4
19	6.709	467.7	6.494	499.1
20	7.928	482.6	7.630	520.6
21	9.148	495.0	8.754	540.3
22	10.367	505.2	9.864	557.6
23	11.586	513.8	10.963	573.3
24	12.805	520.6	12.049	587.3
25	14.025	526.5	13.125	600.4
26	15.244	531.1	14.189	612.1
27	16.463	535.1	15.241	623.1
28	17.682	537.9	16.282	633.0
29	18.902	540.3	17.313	642.4
30	20.121	542.1	18.333	651.2
31	21.340	543.2	19.343	659.1
32	22.559	543.9	20.343	666.6
33	22.830	544.0	20.563	668.2
34	23.237	544.0		
35	24.050	543.7		
36	24.998	543.0		
37	25.811	541.7		
38	26.759	539.1		
39	27.572	535.6		
40	28.520	529.6		
41	29.333	523.2		
42	30.281	513.6		
43	31.094	503.8		
44	31.907	492.2		
45	32.855	476.4		
46	33.668	460.6		
47	34.616	439.6		
48	35.429	418.8		
49	36.378	391.3		
50	37.190	365.2		
51	38.139	334.2		
52	38.545	314.9		

Table 7. Location 4 Test Results - Spherical Shell (SGV480: Thickness 8 mm)

R7	Engr. Strain (%)	Engr. Stress (MPa)	True Strain (%)	True Stress (MPa)
1	0.000	0.0	0.000	0.0
2	0.002	3.7	0.002	3.7
3	0.017	36.9	0.017	36.9
4	0.033	69.8	0.033	69.8
5	0.051	110.4	0.051	110.5
6	0.070	150.8	0.070	150.9
7	0.089	191.4	0.089	191.6
8	0.108	231.5	0.108	231.8
9	0.127	272.3	0.127	272.7
10	0.145	312.7	0.145	313.2
11	0.164	353.1	0.164	353.7
12	0.188	404.8	0.188	405.6
13	1.154	394.4	1.147	399.0
14	2.724	394.3	2.687	405.1
15	3.611	400.7	3.740	416.0
16	5.139	431.7	5.011	453.9
17	6.468	450.2	6.267	479.3
18	7.796	468.4	7.507	504.9
19	9.124	485.3	8.731	529.6
20	10.453	495.3	9.942	547.1
21	11.781	503.9	11.137	563.2
22	13.110	511.4	12.319	578.5
23	14.438	518.7	13.486	593.6
24	15.766	525.1	14.640	607.8
25	17.095	527.4	15.781	617.6
26	18.423	532.1	16.909	630.1
27	19.751	535.4	18.024	641.2
28	21.080	538.5	19.128	652.0
29	22.408	540.3	20.219	661.3
30	23.737	541.6	21.299	670.2
31	25.065	542.5	22.366	678.5
32	26.393	543.0	23.422	686.3
33	27.722	543.3	24.468	693.9
34	27.805	543.3		
35	28.385	543.0		
36	29.048	542.7		
37	29.628	542.1		
38	30.291	541.0		
39	30.871	539.9		
40	31.535	537.1		
41	32.115	534.1		
42	32.778	529.7		
43	33.358	525.4		
44	34.021	515.4		
45	34.601	506.3		
46	35.181	492.0		
47	36.425	461.2		
48	37.668	424.2		
49	38.331	395.2		
50	38.911	369.5		
51	39.574	346.4		
52	40.072	331.7		

R8	Engr. Strain (%)	Engr. Stress (MPa)	True Strain (%)	True Stress (MPa)
1	0.000	0.0	0.000	0.0
2	0.002	3.1	0.002	3.1
3	0.021	43.4	0.021	43.5
4	0.039	84.0	0.039	84.1
5	0.058	124.1	0.058	124.1
6	0.077	164.6	0.077	164.7
7	0.096	204.9	0.096	205.1
8	0.114	245.6	0.114	245.8
9	0.133	285.8	0.132	286.1
10	0.149	320.2	0.148	320.7
11	0.168	360.8	0.167	361.4
12	0.200	430.7	0.199	431.6
13	0.680	415.0	0.677	417.8
14	2.001	394.8	1.981	402.7
15	3.562	396.8	3.500	410.9
16	4.763	400.6	4.653	419.7
17	5.844	430.3	5.679	455.5
18	7.165	449.9	6.920	482.2
19	8.485	470.4	8.144	510.3
20	9.806	481.5	9.354	528.7
21	11.127	493.1	10.550	547.9
22	12.448	502.1	11.732	564.6
23	13.769	510.3	12.900	580.6
24	15.090	515.4	14.054	593.2
25	16.410	520.5	15.194	606.0
26	17.731	525.4	16.323	618.6
27	19.052	528.7	17.439	629.4
28	20.373	531.5	18.542	639.6
29	21.694	533.4	19.634	649.1
30	23.015	534.5	20.713	657.5
31	24.336	535.2	21.781	665.4
32	25.536	535.6	22.742	672.7
33	25.611	535.6		
34	26.135	535.6		
35	26.658	535.2		
36	27.182	534.2		
37	27.705	533.1		
38	28.154	531.4		
39	28.678	528.7		
40	29.201	522.6		
41	29.725	518.4		
42	30.248	507.7		
43	30.772	494.1		
44	31.295	484.8		
45	31.819	470.1		
46	32.342	454.1		
47	32.866	435.7		
48	33.315	418.2		
49	34.362	381.1		
50	34.885	355.6		
51	35.409	330.5		
52	35.858	312.1		

T7	Engr. Strain (%)	Engr. Stress (MPa)	True Strain (%)	True Stress (MPa)
1	0.000	0.0	0.000	0.0
2	0.008	14.7	0.008	14.7
3	0.009	51.4	0.009	51.4
4	0.027	81.9	0.027	81.9
5	0.061	116.4	0.061	116.5
6	0.097	153.1	0.097	153.2
7	0.126	190.0	0.126	190.2
8	0.151	225.9	0.151	226.3
9	0.185	263.0	0.185	263.5
10	0.208	300.2	0.208	300.8
11	0.250	337.0	0.250	337.8
12	0.280	373.7	0.280	374.6
13	0.318	403.0	0.318	404.2
14	0.440	380.5	0.439	382.2
15	1.896	385.7	1.879	393.0
16	2.983	406.6	2.940	416.7
17	3.934	432.4	3.859	449.4
18	4.858	453.2	4.744	475.2
19	5.872	472.2	5.708	499.9
20	6.889	487.2	6.662	520.8
21	7.759	497.8	7.473	536.4
22	8.744	507.6	8.383	552.0
23	9.813	516.8	9.361	567.5
24	10.870	524.1	10.319	581.0
25	11.576	528.0	10.954	589.1
26	12.687	533.4	11.945	601.1
27	13.670	537.0	12.813	610.4
28	14.743	540.9	13.753	620.7
29	15.676	543.2	14.563	628.3
30	16.713	545.0	15.455	638.0
31	17.863	546.9	16.436	644.6
32	18.850	547.8	17.269	651.1
33	19.995	549.0	18.228	658.7
34	20.677	549.1	18.795	662.6
35	20.790	549.0		
36	21.768	549.0		
37	22.598	548.4		
38	23.561	547.6		
39	24.439	546.3		
40	25.341	544.3		
41	25.976	541.9		
42	26.931	537.2		
43	27.679	531.9		
44	28.711	523.2		
45	29.243	517.9		
46	30.008	508.9		
47	30.858	497.5		
48	31.740	483.7		
49	32.447	471.4		
50	33.211	456.9		
51	33.987	440.2		
52	34.892	418.6		
53	35.828	393.2		
54	36.549	371.3		
55	37.150	343.1		

T8	Engr. Strain (%)	Engr. Stress (MPa)	True Strain (%)	True Stress (MPa)
1	0.000	0.0	0.000	0.0
2	0.005	9.7	0.005	9.7
3	0.007	44.9	0.007	44.9
4	0.039	82.8	0.039	82.8
5	0.072	119.8	0.072	119.9
6	0.111	159.7	0.111	159.8
7	0.142	200.0	0.142	200.2
8	0.168	236.9	0.168	237.3
9	0.204	277.1	0.204	277.7
10	0.235	318.3	0.235	319.1
11	0.267	356.1	0.266	357.0
12	0.342	411.6	0.341	413.0
13	0.463	384.7	0.462	386.5
14	1.555	375.6	1.543	381.4
15	2.611	385.4	2.577	395.5
16	3.895	419.5	3.821	435.9
17	5.116	445.5	4.989	468.3
18	6.259	465.5	6.071	494.7
19	7.341	481.3	7.084	516.6
20	8.481	494.2	8.140	536.1
21	9.597	504.6	9.164	553.0
22	10.921	514.5	10.365	570.6
23	12.145	521.9	11.462	585.3
24	13.184	527.1	12.384	596.6
25	14.190	531.0	13.269	606.4
26	15.243	534.2	14.187	615.6
27	16.311	537.5	15.110	625.2
28	17.580	540.3	16.195	635.2
29	18.780	541.5	17.210	643.2
30	19.970	543.4	18.207	651.9
31	20.976	543.9	19.042	658.0
32	22.324	544.6	20.150	666.1
33	22.702	544.8	20.459	668.4
34	22.823	544.5		
35	23.667	544.5		
36	24.354	543.9		
37	25.063	542.9		
38	25.849	541.6		
39	26.548	539.7		
40	27.523	536.4		
41	28.460	531.0		
42	29.227	525.5		
43	30.120	517.7		
44	30.843	510.2		
45	31.826	498.6		
46	32.624	487.8		
47	33.391	475.8		
48	33.954	466.1		
49	34.685	452.3		
50	35.451	436.9		
51	36.272	418.4		
52	37.203	394.2		
53	37.851	375.4		
54	38.434	350.6		

Table 8. Location 5 Test Results - Upper Conical Shell Just Above Middle Stiffener (SGV480: Thickness 8.5 mm)

R9	Engr. Strain (%)	Engr. Stress (MPa)	True Strain (%)	True Stress (MPa)
1	0.000	0.0	0.000	0.0
2	0.002	3.9	0.002	3.9
3	0.003	31.1	0.003	31.1
4	0.005	59.8	0.005	59.8
5	0.008	86.3	0.008	86.3
6	0.009	116.1	0.009	116.1
7	0.028	144.9	0.028	145.0
8	0.052	175.0	0.052	175.0
9	0.078	204.4	0.078	204.5
10	0.104	234.1	0.104	234.3
11	0.119	263.6	0.119	263.9
12	0.142	293.6	0.142	294.0
13	0.185	322.4	0.185	323.0
14	0.199	351.4	0.199	352.1
15	0.226	380.9	0.226	381.6
16	0.247	409.5	0.247	410.5
17	0.312	447.1	0.311	448.5
18	0.647	401.9	0.645	404.5
19	1.006	410.6	1.001	414.7
20	2.433	403.3	2.404	413.1
21	3.031	398.7	2.986	410.8
22	4.257	438.4	4.169	457.0
23	5.627	465.1	5.474	491.3
24	7.361	490.4	7.103	526.5
25	9.135	509.0	8.742	555.5
26	10.841	521.8	10.293	578.4
27	12.432	530.8	11.718	596.8
28	14.273	538.3	13.342	615.1
29	15.871	542.9	14.731	629.1
30	17.708	546.7	16.304	643.5
31	19.544	549.0	17.851	656.3
32	21.218	550.2	19.242	666.9
33	22.369	550.5	20.187	673.6
34	22.488	550.3		
35	23.698	550.0		
36	24.788	549.1		
37	25.911	547.2		
38	26.884	544.3		
39	28.181	537.9		
40	29.202	530.6		
41	30.244	521.1		
42	31.363	508.4		
43	32.350	494.9		
44	33.385	478.4		
45	34.169	464.2		
46	35.096	445.8		
47	35.804	429.9		
48	36.502	413.1		
49	37.063	398.3		
50	37.677	381.3		
51	38.213	364.7		
52	38.767	346.4		
53	39.145	333.2		

R10	Engr. Strain (%)	Engr. Stress (MPa)	True Strain (%)	True Stress (MPa)
1	0.000	0.0	0.000	0.0
2	0.002	3.6	0.002	3.6
3	0.018	37.6	0.018	37.6
4	0.037	78.1	0.037	78.1
5	0.055	118.5	0.055	118.5
6	0.074	158.7	0.074	158.8
7	0.092	198.8	0.092	199.0
8	0.111	238.9	0.111	239.2
9	0.128	275.6	0.128	275.9
10	0.147	315.6	0.147	316.0
11	0.182	392.5	0.182	393.2
12	0.297	390.6	0.296	391.8
13	1.556	397.1	1.544	403.3
14	2.702	399.9	2.666	410.7
15	4.076	419.6	3.995	436.7
16	5.338	442.4	5.198	466.0
17	6.595	460.6	6.386	491.0
18	7.855	476.2	7.562	513.6
19	9.115	491.0	8.723	535.8
20	10.375	501.2	9.871	553.2
21	11.634	511.5	11.005	571.0
22	12.894	518.5	12.128	585.3
23	14.154	524.1	13.238	598.2
24	15.414	529.8	14.335	611.4
25	16.673	534.2	15.420	623.2
26	17.933	537.4	16.494	633.8
27	19.193	540.0	17.557	643.6
28	20.453	542.0	18.609	652.9
29	21.712	543.3	19.649	661.2
30	22.972	544.6	20.678	669.7
31	24.232	545.2	21.698	677.3
32	25.492	545.4	22.707	684.5
33	26.293	545.4		
34	26.395	545.4		
35	27.209	545.3		
36	28.024	544.9		
37	28.838	544.0		
38	29.653	543.1		
39	30.569	540.5		
40	31.384	537.7		
41	32.198	533.9		
42	33.013	530.4		
43	33.827	527.2		
44	34.641	515.4		
45	35.456	502.6		
46	36.270	492.1		
47	37.085	474.4		
48	37.899	456.6		
49	38.816	434.0		
50	39.630	417.2		
51	40.444	394.9		
52	41.259	366.0		
53	42.073	337.0		
54	42.786	317.9		

T9	Engr. Strain (%)	Engr. Stress (MPa)	True Strain (%)	True Stress (MPa)
1	0.000	0.0	0.000	0.0
2	0.003	6.3	0.003	6.3
3	0.013	31.2	0.013	31.2
4	0.023	58.6	0.023	58.7
5	0.033	86.2	0.033	86.2
6	0.054	114.0	0.054	114.0
7	0.070	141.7	0.070	141.8
8	0.102	168.0	0.102	168.2
9	0.114	195.0	0.114	195.2
10	0.146	222.6	0.146	222.9
11	0.162	250.2	0.162	250.6
12	0.178	276.9	0.178	277.4
13	0.192	303.5	0.192	304.1
14	0.225	330.0	0.225	330.7
15	0.234	357.6	0.234	358.4
16	0.266	384.2	0.266	385.2
17	0.310	415.4	0.310	416.7
18	0.409	406.3	0.408	408.0
19	1.658	408.9	1.645	413.6
20	3.031	408.6	2.986	421.0
21	3.864	434.6	3.791	451.6
22	5.041	460.3	4.918	483.5
23	6.430	482.3	6.232	513.3
24	7.981	501.1	7.679	541.1
25	9.647	516.2	9.210	566.0
26	11.011	525.4	10.446	583.3
27	12.599	533.7	11.866	600.9
28	14.288	540.3	13.355	617.4
29	15.579	544.0	14.479	628.7
30	17.035	547.0	15.730	640.2
31	18.452	549.3	16.934	650.6
32	19.823	550.6	18.085	659.8
33	21.586	551.4	19.545	670.5
34	21.702	551.3		
35	22.518	551.4		
36	23.498	551.0		
37	24.421	550.5		
38	25.463	549.1		
39	26.416	546.6		
40	27.346	542.6		
41	28.209	537.9		
42	29.064	531.2		
43	29.640	524.1		
44	30.559	516.0		
45	31.491	503.9		
46	32.424	489.5		
47	33.296	474.7		
48	34.137	456.4		
49	34.795	444.3		
50	35.499	428.1		
51	36.084	413.4		
52	36.688	397.1		
53	37.229	380.6		
54	37.646	365.9		

T10	Engr. Strain (%)	Engr. Stress (MPa)	True Strain (%)	True Stress (MPa)
1	0.000	0.0	0.000	0.0
2	0.003	6.3	0.003	6.3
3	0.013	34.0	0.013	34.0
4	0.031	61.9	0.031	61.9
5	0.052	89.8	0.052	89.9
6	0.064	117.8	0.064	117.9
7	0.088	145.9	0.088	146.1
8	0.109	173.4	0.109	173.6
9	0.130	200.2	0.130	200.4
10	0.156	227.4	0.156	227.8
11	0.180	254.5	0.180	254.9
12	0.208	282.6	0.208	283.2
13	0.222	309.9	0.222	310.6
14	0.272	337.8	0.272	338.8
15	0.276	365.9	0.276	366.9
16	0.302	393.9	0.302	395.1
17	0.338	429.5	0.338	431.0
18	0.474	403.2	0.473	405.1
19	1.450	404.9	1.440	410.8
20	2.376	407.5	2.348	417.2
21	3.582	424.9	3.519	440.1
22	4.666	450.4	4.561	471.4
23	5.932	474.5	5.763	502.7
24	7.690	498.6	7.409	536.9
25	9.257	514.6	8.853	562.2
26	10.795	526.2	10.251	583.0
27	12.320	535.1	11.618	601.0
28	13.903	541.8	13.018	617.2
29	15.475	546.7	14.389	631.3
30	16.903	550.2	15.618	643.1
31	18.432	552.5	16.917	654.3
32	19.676	553.7	17.962	662.6
33	21.553	554.4	19.518	673.9
34	21.676	554.4		
35	22.573	554.4		
36	23.541	553.5		
37	24.323	552.3		
38	25.091	550.8		
39	25.790	548.4		
40	26.755	543.8		
41	27.717	537.4		
42	28.680	529.2		
43	29.503	520.7		
44	30.346	510.5		
45	31.224	498.0		
46	31.916	486.9		
47	32.734	473.1		
48	33.329	461.3		
49	33.891	449.6		
50	34.474	436.5		
51	35.014	417.7		
52	35.492	411.5		
53	35.948	398.3		
54	36.289	387.2		

Table 9. Location 6 Test Results - Upper Member of Lower Stiffeners (SGV480: 9.5 mm)

R11	Engr. Strain (%)	Engr. Stress (MPa)	True Strain (%)	True Stress (MPa)
1	0.000	0.0	0.000	0.0
2	0.002	3.4	0.002	3.4
3	0.017	35.8	0.017	35.8
4	0.039	84.5	0.039	84.6
5	0.062	133.5	0.062	133.6
6	0.085	182.2	0.085	182.4
7	0.107	231.3	0.107	231.6
8	0.130	280.6	0.130	280.9
9	0.153	329.7	0.153	330.2
10	0.175	378.4	0.175	379.1
11	0.197	427.1	0.197	427.9
12	0.202	436.9	0.202	437.8
13	0.614	421.8	0.612	424.4
14	1.987	413.9	1.967	422.2
15	3.359	411.8	3.304	425.6
16	4.732	432.9	4.623	453.3
17	6.105	460.5	5.926	488.6
18	7.478	480.6	7.211	516.6
19	8.850	496.4	8.460	540.3
20	10.223	509.0	9.733	561.0
21	11.596	519.1	10.971	579.3
22	12.969	527.2	12.194	595.6
23	14.341	534.0	13.401	610.6
24	15.714	539.3	14.595	624.0
25	17.087	543.4	15.774	636.2
26	18.460	546.9	16.940	647.9
27	19.832	549.4	18.092	658.3
28	21.205	551.1	19.231	668.0
29	22.578	552.5	20.358	677.3
30	23.951	553.1	21.471	685.6
31	24.637	553.2	22.023	689.5
32	25.049	553.2		
33	25.872	552.9		
34	26.833	551.9		
35	27.657	550.7		
36	28.481	548.8		
37	29.442	544.9		
38	30.265	539.7		
39	31.089	533.0		
40	32.050	522.8		
41	32.873	512.1		
42	33.697	499.4		
43	34.658	481.7		
44	35.482	464.1		
45	36.305	443.6		
46	37.266	415.6		
47	38.090	388.2		
48	38.913	359.3		
49	39.874	325.3		
50	40.286	310.1		

R12	Engr. Strain (%)	Engr. Stress (MPa)	True Strain (%)	True Stress (MPa)
1	0.000	0.0	0.000	0.0
2	0.002	3.4	0.002	3.4
3	0.019	39.9	0.019	39.9
4	0.041	88.8	0.041	88.9
5	0.064	138.0	0.064	138.1
6	0.087	187.4	0.087	187.6
7	0.110	237.1	0.110	237.4
8	0.133	286.7	0.133	287.1
9	0.156	336.1	0.156	336.6
10	0.178	385.8	0.178	386.5
11	0.201	435.0	0.201	435.9
12	0.208	450.0	0.208	451.0
13	0.610	433.4	0.608	436.0
14	1.949	420.2	1.930	428.4
15	3.289	416.4	3.236	430.1
16	4.628	429.7	4.524	449.6
17	5.968	455.6	5.796	482.8
18	7.307	476.8	7.052	511.6
19	8.647	493.4	8.293	536.0
20	9.986	506.6	9.518	557.2
21	11.326	517.3	10.729	575.9
22	12.665	526.1	11.925	592.6
23	14.005	533.1	13.107	607.6
24	15.345	538.9	14.275	621.6
25	16.684	543.4	15.430	634.0
26	18.024	546.9	16.572	645.5
27	19.363	549.9	17.700	656.3
28	20.703	552.1	18.816	666.4
29	22.042	553.6	19.919	675.6
30	23.382	554.6	21.011	684.2
31	24.721	555.1	22.091	692.3
32	24.855	555.2	22.198	693.1
33	25.257	555.1		
34	26.194	554.9		
35	26.998	554.5		
36	27.936	553.6		
37	28.873	551.8		
38	29.677	549.6		
39	30.615	545.5		
40	31.552	539.3		
41	32.356	531.9		
42	33.294	521.3		
43	34.232	507.9		
44	35.035	494.5		
45	35.973	475.7		
46	36.911	453.7		
47	37.714	431.5		
48	38.652	401.4		
49	39.590	367.4		
50	40.393	338.0		
51	40.929	316.7		

T11	Engr. Strain (%)	Engr. Stress (MPa)	True Strain (%)	True Stress (MPa)
1	0.000	0.0	0.000	0.0
2	0.003	6.1	0.003	6.1
3	0.030	32.8	0.030	32.8
4	0.054	64.2	0.054	64.3
5	0.074	95.0	0.074	95.1
6	0.099	126.7	0.099	126.8
7	0.128	156.8	0.128	157.0
8	0.137	188.3	0.137	188.5
9	0.177	218.8	0.177	219.0
10	0.202	250.6	0.202	251.1
11	0.220	282.1	0.220	282.8
12	0.244	313.9	0.244	314.7
13	0.280	343.1	0.280	344.1
14	0.300	374.5	0.300	375.6
15	0.316	406.3	0.316	407.6
16	0.342	438.0	0.341	439.5
17	0.394	488.6	0.393	490.5
18	0.579	431.3	0.577	433.8
19	1.555	405.1	1.543	411.4
20	2.676	406.4	2.641	417.3
21	3.433	413.5	3.375	427.6
22	4.523	444.9	4.424	465.1
23	5.650	467.7	5.496	494.1
24	7.272	491.4	7.020	527.1
25	9.165	511.3	8.787	558.3
26	10.836	523.7	10.288	580.4
27	12.653	533.1	11.914	600.5
28	14.475	540.0	13.519	618.1
29	16.222	544.4	15.033	632.7
30	17.984	547.4	16.538	645.9
31	19.712	549.2	17.992	657.4
32	21.324	550.0	19.329	667.2
33	22.372	550.2	20.190	673.2
34	22.486	550.0		
35	23.342	550.0		
36	24.108	549.7		
37	25.107	548.5		
38	26.038	547.0		
39	27.071	544.2		
40	28.095	540.1		
41	29.143	533.7		
42	30.036	526.4		
43	30.746	519.1		
44	31.677	508.7		
45	32.726	494.4		
46	33.611	479.6		
47	34.226	468.5		
48	35.123	450.6		
49	35.808	435.1		
50	36.554	416.8		
51	37.083	402.2		
52	37.734	383.6		
53	38.109	371.7		
54	38.574	356.0		

T12	Engr. Strain (%)	Engr. Stress (MPa)	True Strain (%)	True Stress (MPa)
1	0.000	0.0	0.000	0.0
2	0.010	8.4	0.010	8.4
3	0.021	35.4	0.021	35.4
4	0.047	62.9	0.047	62.9
5	0.062	88.8	0.062	88.8
6	0.094	116.8	0.094	116.9
7	0.132	144.5	0.132	144.6
8	0.137	173.6	0.137	173.8
9	0.163	200.8	0.163	201.2
10	0.189	227.6	0.189	228.2
11	0.210	254.4	0.210	254.9
12	0.236	281.5	0.236	282.1
13	0.273	309.4	0.273	310.2
14	0.282	338.9	0.282	339.9
15	0.305	366.1	0.305	367.2
16	0.334	393.5	0.334	394.9
17	0.369	436.5	0.369	438.1
18	0.514	413.0	0.513	415.1
19	1.775	403.8	1.760	411.0
20	2.966	404.3	2.923	416.3
21	4.157	419.9	4.073	437.4
22	5.342	441.4	5.204	465.0
23	6.846	465.3	6.622	497.2
24	8.544	486.0	8.199	527.5
25	10.671	505.6	10.139	559.6
26	12.607	518.9	11.874	584.3
27	14.429	528.2	13.479	604.4
28	16.226	535.2	15.037	622.1
29	17.918	540.3	16.482	637.2
30	20.100	545.4	18.316	655.0
31	22.161	548.4	20.017	669.9
32	23.235	550.3	20.892	678.1
33	24.117	551.4	21.606	684.4
34	25.060	551.8	22.379	690.2
35	25.140	551.7		
36	25.736	551.5		
37	26.331	550.6		
38	26.986	549.2		
39	27.582	546.6		
40	28.237	542.1		
41	28.773	535.5		
42	29.428	526.0		
43	30.024	520.5		
44	30.679	509.2		
45	31.274	501.6		
46	31.870	488.3		
47	32.466	475.0		
48	33.121	456.4		
49	33.716	438.1		
50	34.371	419.3		
51	34.907	405.7		
52	35.563	385.7		
53	36.158	367.4		
54	36.813	347.9		
55	37.290	333.0		

Table 10. Location 7 Test Results - Lower Member of Lower Stiffeners (SGV480: Thickness 12.5 mm)

R13	Engr. Strain (%)	Engr. Stress (MPa)	True Strain (%)	True Stress (MPa)
1	0.000	0.0	0.000	0.0
2	0.001	2.3	0.001	2.3
3	0.015	32.6	0.015	32.6
4	0.037	80.6	0.037	80.6
5	0.059	128.6	0.059	128.6
6	0.082	176.7	0.082	176.9
7	0.104	225.0	0.104	225.2
8	0.126	272.7	0.126	273.1
9	0.148	320.8	0.148	321.3
10	0.170	368.7	0.170	369.4
11	0.186	403.7	0.186	404.5
12	0.484	390.5	0.483	392.4
13	1.573	382.3	1.561	388.3
14	2.663	386.3	2.628	396.6
15	3.753	420.2	3.684	436.0
16	4.843	443.9	4.730	465.5
17	5.933	463.6	5.764	491.1
18	7.023	479.4	6.787	513.1
19	8.113	492.6	7.801	532.6
20	9.203	503.3	8.804	549.6
21	10.293	511.8	9.797	564.5
22	11.383	518.9	10.781	577.9
23	12.473	524.6	11.754	590.0
24	13.563	529.1	12.719	600.8
25	14.653	532.7	13.674	610.8
26	15.743	535.6	14.620	620.0
27	16.833	537.9	15.558	628.4
28	17.923	539.8	16.486	636.5
29	19.013	540.9	17.406	643.8
30	20.103	541.8	18.318	650.7
31	21.192	542.1	19.221	657.0
32	22.084	542.4	19.954	662.2
33	22.382	542.3		
34	23.174	542.1		
35	23.868	541.6		
36	24.660	540.9		
37	25.453	539.7		
38	26.246	537.4		
39	26.939	534.5		
40	27.732	529.4		
41	28.525	522.3		
42	29.318	513.0		
43	30.011	503.1		
44	30.804	489.3		
45	31.596	472.7		
46	32.290	455.9		
47	33.083	433.4		
48	33.875	406.7		
49	34.668	375.0		
50	35.362	344.5		
51	35.857	321.0		

R14	Engr. Strain (%)	Engr. Stress (MPa)	True Strain (%)	True Stress (MPa)
1	0.000	0.0	0.000	0.0
2	0.003	5.0	0.003	5.0
3	0.025	52.8	0.024	52.8
4	0.047	100.5	0.046	100.6
5	0.069	148.5	0.068	148.6
6	0.091	196.7	0.090	196.9
7	0.114	245.0	0.113	245.2
8	0.136	293.3	0.135	293.7
9	0.158	341.6	0.157	342.1
10	0.181	389.7	0.180	390.4
11	0.513	379.9	0.511	381.9
12	1.730	388.5	1.715	395.3
13	2.948	382.6	2.905	393.8
14	3.723	403.9	3.655	419.0
15	4.720	441.9	4.612	482.7
16	6.602	477.3	6.393	508.8
17	7.819	490.4	7.528	526.8
18	9.037	500.8	8.651	546.1
19	10.255	509.4	9.762	561.6
20	11.473	516.3	10.861	575.6
21	12.690	521.9	11.947	586.1
22	13.908	526.5	13.022	599.7
23	15.126	530.1	14.085	610.2
24	16.344	533.1	15.138	620.2
25	17.562	535.3	16.179	629.4
26	18.778	537.1	17.209	638.0
27	19.997	538.3	18.229	645.9
28	21.215	539.3	19.239	653.7
29	22.433	539.7	20.239	660.7
30	23.318	539.7		
31	23.649	539.4		
32	24.425	539.0		
33	25.090	538.3		
34	25.865	537.0		
35	26.528	535.0		
36	27.304	531.4		
37	27.968	527.0		
38	28.743	520.0		
39	29.406	512.8		
40	30.182	502.3		
41	30.957	489.8		
42	31.621	477.4		
43	32.396	460.5		
44	33.060	443.9		
45	33.835	422.0		
46	34.500	400.3		
47	35.275	371.4		
48	35.939	345.4		
49	36.382	327.8		

T13	Engr. Strain (%)	Engr. Stress (MPa)	True Strain (%)	True Stress (MPa)
1	0.000	0.0	0.000	0.0
2	0.001	1.9	0.001	1.9
3	0.017	34.3	0.017	34.3
4	0.041	82.6	0.041	82.6
5	0.064	130.7	0.064	130.8
6	0.088	178.6	0.088	178.7
7	0.112	226.5	0.112	226.8
8	0.135	274.4	0.135	274.8
9	0.159	322.5	0.159	323.1
10	0.183	370.5	0.183	371.2
11	0.198	401.1	0.198	401.9
12	1.534	386.8	1.522	392.7
13	2.356	391.4	2.329	400.6
14	3.178	390.7	3.128	403.1
15	3.898	416.9	3.824	433.1
16	5.028	442.3	4.906	464.5
17	6.159	462.0	5.977	490.4
18	7.289	476.2	7.036	513.0
19	8.420	491.1	8.084	532.5
20	9.551	501.9	9.122	549.8
21	10.681	510.5	10.148	565.1
22	11.812	517.6	11.165	578.7
23	12.942	523.2	12.170	590.9
24	14.073	527.9	13.167	602.2
25	15.203	531.6	14.153	612.4
26	16.334	534.7	15.129	622.0
27	17.465	537.0	16.097	630.8
28	18.595	538.6	17.054	638.7
29	19.726	539.8	18.004	646.2
30	20.856	540.7	18.943	653.5
31	21.987	541.1	19.874	660.1
32	23.117	541.4	20.796	666.6
33	23.426	541.4		
34	24.248	541.2		
35	24.967	540.9		
36	25.780	540.3		
37	26.509	539.5		
38	27.331	537.8		
39	28.051	535.4		
40	28.873	531.1		
41	29.592	525.4		
42	30.415	516.8		
43	31.237	505.5		
44	31.956	493.8		
45	32.779	477.6		
46	33.498	460.9		
47	34.320	438.7		
48	35.040	415.7		
49	35.862	384.9		
50	36.581	354.8		
51	37.095	332.9		

T14	Engr. Strain (%)	Engr. Stress (MPa)	True Strain (%)	True Stress (MPa)
1	0.000	0.0	0.000	0.0
2	0.001	2.1	0.001	2.1
3	0.013	27.2	0.013	27.2
4	0.037	75.3	0.037	75.3
5	0.061	123.4	0.061	123.4
6	0.084	171.4	0.084	171.6
7	0.108	219.6	0.108	219.8
8	0.132	267.9	0.132	268.3
9	0.156	316.1	0.156	316.6
10	0.180	364.4	0.180	365.1
11	0.197	399.3	0.197	400.1
12	0.520	386.2	0.519	388.2
13	1.707	386.8	1.693	393.4
14	2.462	390.0	2.432	399.6
15	4.080	420.7	3.999	437.9
16	5.268	444.4	5.132	467.8
17	6.453	463.6	6.253	493.5
18	7.639	479.2	7.361	515.8
19	8.826	492.1	8.458	535.5
20	10.012	502.6	9.542	552.9
21	11.199	511.0	10.615	568.3
22	12.385	518.0	11.676	582.1
23	13.572	523.7	12.727	594.8
24	14.758	528.3	13.766	606.3
25	15.945	531.9	14.795	616.7
26	17.131	534.8	15.812	626.4
27	18.318	537.2	16.821	635.6
28	19.504	538.9	17.818	644.0
29	20.691	540.3	18.806	652.0
30	21.877	541.1	19.784	659.5
31	23.063	541.3	20.753	666.2
32	23.819	541.5	21.365	670.5
33	24.142	541.2		
34	24.897	541.0		
35	25.544	540.3		
36	26.299	539.4		
37	27.054	537.4		
38	27.702	534.7		
39	28.457	530.2		
40	29.212	523.9		
41	29.859	516.8		
42	30.614	507.0		
43	31.369	495.0		
44	32.016	483.2		
45	32.771	467.1		
46	33.526	448.7		
47	34.173	430.3		
48	34.928	406.0		
49	35.683	377.8		
50	36.331	351.7		
51	36.762	329.7		

Table 11. Location 8 Test Results - Middle Stiffener and Upper Stiffener (SGV480: Thickness 19 mm)

R15	Engr. Strain (%)	Engr. Stress (MPa)	True Strain (%)	True Stress (MPa)
1	0.000	0.0	0.000	0.0
2	0.002	3.4	0.002	3.4
3	0.011	27.1	0.011	27.1
4	0.042	50.9	0.042	50.9
5	0.053	76.2	0.053	76.2
6	0.048	101.6	0.048	101.6
7	0.068	127.0	0.068	127.1
8	0.082	152.3	0.082	152.4
9	0.108	176.1	0.108	176.3
10	0.113	201.4	0.113	201.7
11	0.125	226.7	0.125	227.0
12	0.145	250.9	0.145	251.2
13	0.153	276.3	0.153	276.7
14	0.173	301.7	0.173	302.2
15	0.193	326.6	0.193	327.2
16	0.225	351.9	0.224	352.7
17	0.228	377.7	0.227	378.5
18	0.236	401.8	0.235	402.7
19	0.245	430.1	0.244	431.2
20	0.311	383.7	0.310	384.9
21	0.905	377.1	0.901	380.5
22	2.497	376.1	2.466	385.5
23	2.971	401.1	2.927	413.0
24	3.706	425.1	3.639	440.9
25	4.726	449.2	4.617	470.5
26	5.949	470.8	5.778	498.8
27	7.666	491.2	7.386	528.9
28	9.624	506.3	9.188	555.0
29	11.819	516.7	11.171	577.8
30	13.965	522.6	13.072	595.6
31	16.285	526.0	15.087	611.7
32	18.263	527.4	16.774	623.7
33	19.799	527.6	18.064	632.1
34	19.840	527.5		
35	21.221	527.2		
36	22.547	526.5		
37	23.878	525.5		
38	24.883	524.1		
39	26.218	521.4		
40	27.567	517.3		
41	28.786	512.3		
42	29.571	508.7		
43	30.858	499.9		
44	32.237	489.3		
45	33.350	478.7		
46	34.582	465.4		
47	35.805	450.2		
48	36.733	437.9		
49	37.538	425.2		
50	38.173	414.2		
51	38.817	404.0		
52	39.690	387.8		
53	40.328	374.3		
54	40.945	361.1		

R16	Engr. Strain (%)	Engr. Stress (MPa)	True Strain (%)	True Stress (MPa)
1	0.000	0.0	0.000	0.0
2	0.003	5.5	0.003	5.5
3	0.017	31.5	0.017	31.5
4	0.031	56.9	0.031	56.9
5	0.048	81.9	0.048	81.9
6	0.054	106.4	0.054	106.5
7	0.082	131.6	0.082	131.7
8	0.080	156.9	0.080	157.0
9	0.102	181.6	0.102	181.8
10	0.116	206.7	0.116	207.0
11	0.136	231.2	0.136	231.6
12	0.128	255.3	0.128	255.6
13	0.162	280.8	0.162	281.2
14	0.176	306.2	0.176	306.7
15	0.182	331.2	0.182	331.8
16	0.190	356.0	0.190	356.7
17	0.227	381.3	0.226	382.1
18	0.241	416.6	0.240	417.6
19	0.270	384.5	0.269	385.6
20	0.990	378.2	0.985	382.0
21	2.449	372.6	2.419	381.7
22	2.960	403.4	2.917	415.4
23	3.800	428.6	3.729	444.8
24	4.764	451.0	4.654	472.5
25	5.823	470.3	5.660	497.7
26	7.539	491.3	7.268	528.4
27	9.611	507.5	9.177	556.3
28	11.770	517.6	11.127	576.5
29	13.770	523.4	12.901	595.5
30	15.745	526.4	14.622	609.3
31	18.066	528.0	16.607	623.4
32	19.127	528.5	17.502	629.6
33	19.270	528.3		
34	20.350	528.1		
35	21.650	527.5		
36	22.936	526.2		
37	24.367	523.5		
38	25.724	519.1		
39	27.129	512.2		
40	27.670	509.3		
41	28.753	501.2		
42	30.090	489.6		
43	31.379	477.0		
44	32.702	461.1		
45	34.121	441.3		
46	35.139	424.9		
47	35.984	410.2		
48	36.792	395.1		
49	37.640	377.5		
50	38.334	361.4		
51	39.011	344.6		
52	39.517	331.2		

T15	Engr. Strain (%)	Engr. Stress (MPa)	True Strain (%)	True Stress (MPa)
1	0.000	0.0	0.000	0.0
2	0.014	28.9	0.014	28.9
3	0.020	51.6	0.020	51.6
4	0.031	73.7	0.031	73.8
5	0.031	97.5	0.031	97.5
6	0.051	121.5	0.051	121.6
7	0.076	142.9	0.076	143.0
8	0.085	167.3	0.085	167.4
9	0.102	190.2	0.102	190.3
10	0.105	214.1	0.105	214.3
11	0.144	238.1	0.144	238.5
12	0.150	262.0	0.150	262.4
13	0.173	284.5	0.173	285.0
14	0.164	308.3	0.164	308.8
15	0.175	332.2	0.175	332.7
16	0.190	353.1	0.190	353.8
17	0.221	375.9	0.221	376.7
18	0.229	408.0	0.229	408.9
19	0.563	386.4	0.562	388.6
20	1.350	380.4	1.341	385.5
21	2.659	385.6	2.625	395.9
22	2.962	403.2	2.919	415.1
23	3.598	425.4	3.533	440.7
24	4.502	446.6	4.404	468.8
25	5.578	469.3	5.428	495.4
26	6.603	483.6	6.395	515.5
27	7.761	496.1	7.475	534.6
28	9.556	509.7	9.127	558.4
29	11.371	518.7	10.770	577.7
30	13.384	524.6	12.561	594.8
31	15.372	528.3	14.300	609.5
32	17.272	530.1	15.933	621.6
33	19.496	530.6	17.812	634.1
34	19.652	530.5		
35	20.927	530.3		
36	22.074	530.0		
37	23.227	528.9		
38	24.420	527.3		
39	25.608	524.8		
40	26.683	520.5		
41	27.150	519.6		
42	28.680	511.9		
43	30.071	502.4		
44	31.285	492.2		
45	32.447	480.2		
46	33.457	468.8		
47	34.686	453.3		
48	35.583	440.3		
49	36.480	425.7		
50	37.316	410.9		
51	38.089	396.5		
52	38.806	381.8		
53	39.436	368.3		
54	40.014	355.2		

T16	Engr. Strain (%)	Engr. Stress (MPa)	True Strain (%)	True Stress (MPa)
1	0.000	0.0	0.000	0.0
2	0.002	3.1	0.002	3.1
3	0.005	26.7	0.005	26.7
4	0.044	50.3	0.044	50.3
5	0.042	73.8	0.042	73.9
6	0.047	97.9	0.047	97.9
7	0.070	121.6	0.070	121.7
8	0.084	144.9	0.084	145.1
9	0.095	168.9	0.095	169.0
10	0.115	191.6	0.115	191.8
11	0.123	214.6	0.122	214.8
12	0.126	238.4	0.125	238.7
13	0.171	262.2	0.170	262.7
14	0.163	286.2	0.162	286.6
15	0.191	310.0	0.190	310.6
16	0.211	334.0	0.210	334.7
17	0.219	357.8	0.218	358.6
18	0.228	395.4	0.227	396.3
19	0.332	388.0	0.331	389.2
20	1.403	383.5	1.393	388.9
21	2.628	382.1	2.594	392.1
22	2.817	402.1	2.778	413.4
23	3.424	423.7	3.366	438.3
24	4.212	445.1	4.125	463.9
25	5.133	463.7	5.005	487.5
26	6.646	486.3	6.434	518.6
27	8.597	504.8	8.247	548.2
28	10.091	514.2	9.613	566.0
29	11.399	520.1	10.794	579.4
30	13.104	525.1	12.313	594.0
31	14.979	528.9	13.958	608.1
32	16.798	530.5	15.527	619.7
33	18.215	531.0	16.733	627.8
34	19.640	531.3	17.931	635.7
35	19.784	531.3		
36	21.166	530.7		
37	22.540	530.2		
38	24.018	528.8		
39	25.477	526.9		
40	26.859	523.7		
41	28.088	519.1		
42	28.380	517.6		
43	29.544	510.5		
44	31.036	499.7		
45	32.458	486.6		
46	33.733	471.9		
47	34.800	459.1		
48	35.783	444.7		
49	36.913	427.0		
50	37.675	413.8		
51	38.482	398.4		
52	39.224	383.1		
53	39.904	368.0		
54	40.499	353.9		
55	41.059	339.1		

Table 12. Location 9 Test Results - Access Hatch Cover, Equip. Hatch Cover, and Equip. Hatch Sleeve (SGV480: Thickness 20 mm)

R17	Engr. Strain (%)	Engr Stress (MPa)	True Strain (%)	True Stress (MPa)
1	0 000	0 0	0 000	0 0
2	0 002	3 5	0 002	3 5
3	0 041	26 0	0 041	26 0
4	0 038	49 8	0 038	49 8
5	0 047	73 6	0 047	73.7
6	0 061	97 4	0 061	97.4
7	0 089	120 8	0 089	120 9
8	0 117	144 7	0 117	144 9
9	0 123	168 4	0 123	168 6
10	0 134	192 0	0 134	192 3
11	0 151	215 9	0 151	216.3
12	0 153	239 0	0 153	239 4
13	0.162	264 2	0 162	264 6
14	0 187	287.7	0 187	288 3
15	0 198	311 7	0 198	312 3
16	0 193	333 4	0 193	334.1
17	0 207	357.1	0 207	357.8
18	0 223	380 7	0 223	381.5
19	0 243	392 8	0 242	393 7
20	0 411	380.7	0 410	382 3
21	2 287	378.6	2 261	387.3
22	3 172	414 2	3 123	427.4
23	3 921	436 2	3 846	453.3
24	4.781	455 7	4 670	477.5
25	6 029	476 7	5 854	505 4
26	7 349	492 4	7.091	528 6
27	9 387	508 3	8 972	556 0
28	11.217	517.0	10 631	575 0
29	12 768	521 9	12 016	588 5
30	14 629	525 6	13 653	602 5
31	16 594	527 6	15 353	615.1
32	18 508	528 4	16 981	626 2
33	18.939	528 6	17.344	628.7
34	18 984	528 4		
35	20 375	528 3		
36	21.696	527 6		
37	22 973	526 6		
38	24 106	525 4		
39	25 666	523 0		
40	27.189	518 9		
41	27 689	517 5		
42	29 279	509 4		
43	30 486	501 4		
44	31 973	489 2		
45	33.572	472 8		
46	34 803	457 0		
47	35 903	441 4		
48	36 896	425 8		
49	37 662	411 9		
50	38 369	399 1		
51	39.149	383 4		
52	39 951	365 7		
53	40.692	347 8		
54	41.231	331 6		

R18	Engr. Strain (%)	Engr. Stress (MPa)	True Strain (%)	True Stress (MPa)
1	0.000	0.0	0 000	0 0
2	0.002	3 4	0 002	3.4
3	0.008	27.1	0.008	27.1
4	0.013	50.8	0.013	50.8
5	0.024	74.6	0.024	74.6
6	0.047	97.0	0.047	97.0
7	0.058	120.6	0.058	120.7
8	0.077	143.7	0.077	143.8
9	0.077	166.7	0 077	166.8
10	0.116	190.6	0.116	190.9
11	0.116	214.7	0.116	214.9
12	0.130	237.3	0.130	237.6
13	0.136	262.4	0.136	262.8
14	0.161	284.0	0.161	284.5
15	0.158	307.7	0.158	308.2
16	0.177	330.7	0.177	331.3
17	0.186	354.2	0.186	354.9
18	0.194	378.2	0.194	379.0
19	0.211	395.4	0.210	396.2
20	0.311	382.0	0.310	383.2
21	1.532	380.4	1.520	386.2
22	2.589	385.2	2.556	395.2
23	3.271	420.4	3.218	434.2
24	3.991	440.6	3.913	458.2
25	4.929	461.0	4.811	483.7
26	6.100	480.1	5.921	509.4
27	7.889	499.8	7.593	539.3
28	9.906	513.6	9.445	564.5
29	11.773	521.3	11.130	582.7
30	13.706	526.3	12.844	598.5
31	15.334	528.9	14.268	610.0
32	17.095	530.0	15.781	620.5
33	18.845	530.2	17.265	630.2
34	20.084	530.4	18.302	637
35	20.239	530.2		
36	21.407	530.1		
37	22.558	529.3		
38	23.619	528.4		
39	24.814	526.6		
40	26.067	523.9		
41	27.317	520.1		
42	28.646	514.5		
43	29.724	508.4		
44	30.975	499.4		
45	32.213	488.7		
46	33.446	476.8		
47	34.259	467.3		
48	35.112	456.7		
49	35.976	444.8		
50	36.876	431.4		
51	37.697	418.2		
52	38.433	404.8		
53	39.488	384.4		

T17	Engr. Strain (%)	Engr. Stress (MPa)	True Strain (%)	True Stress (MPa)
1	0.000	0.0	0.000	0 0
2	0 002	3 9	0 002	3 9
3	0 022	47.0	0.022	47.0
4	0.042	90.1	0.042	90.2
5	0.062	133.7	0.062	133.7
6	0.082	176.7	0.082	176.9
7	0.102	219.9	0.102	220.1
8	0.122	263.1	0.122	263.4
9	0.142	306.5	0.142	306.9
10	0.162	349.8	0.162	350.4
11	0.179	385.2	0.179	385.9
12	0.508	375.2	0.507	377.1
13	1.716	384.6	1.701	391.2
14	2.925	386.8	2.883	398.1
15	4.133	419.7	4.050	437.1
16	5.341	442.1	5.203	465.7
17	6.549	461.2	6.343	491.4
18	7.758	476.6	7.472	513.6
19	8.966	489.1	8.587	532.9
20	10.174	499.0	9.689	549.7
21	11.382	507.1	10.780	564.8
22	12.590	513.5	11.858	578.1
23	13.799	518.8	12.926	590.4
24	15.007	522.7	13.982	601.1
25	16.215	525.9	15.027	611.2
26	17.423	528.5	16.061	620.6
27	18.631	530.3	17.085	629.2
28	19.840	531.7	18.099	637.2
29	21.048	532.7	19.102	644.8
30	22.256	533.1	20.095	651.7
31	22.915	533.2	20.632	655.4
32	23.245	533.1		
33	24.123	532.9		
34	24.892	532.4		
35	25.771	531.8		
36	26.540	530.7		
37	27.418	529.1		
38	28.187	526.6		
39	29.066	522.5		
40	29.835	517.2		
41	30.713	509.1		
42	31.482	500.0		
43	32.361	487.2		
44	33.130	474.0		
45	34.009	455.8		
46	34.777	437.1		
47	35.656	411.8		
48	36.425	385.9		
49	37.304	354.7		
50	37.743	346.6		

T18	Engr. Strain (%)	Engr. Stress (MPa)	True Strain (%)	True Stress (MPa)
1	0 000	0 0	0 000	0 0
2	0 002	3 9	0 002	3 9
3	0 022	46 5	0 022	46 5
4	0 042	89 2	0 042	89 3
5	0 062	132 5	0 062	132 6
6	0 082	175 6	0 082	175 8
7	0 102	218 7	0 102	218 9
8	0 122	261 8	0 122	262 2
9	0 142	305 3	0 142	305 7
10	0 162	348 4	0 162	349 0
11	0 182	391 7	0 182	392 4
12	0 191	411 2	0 191	412 0
13	0 535	398 5	0 534	400 7
14	1 797	386 7	1 781	393 6
15	3 059	384 6	3 013	396 4
16	4 321	415 4	4 230	433 4
17	5 583	440 2	5 433	464 8
18	6 845	460 0	6 621	491 5
19	8 106	476 1	7 794	514 7
20	9 368	489 0	8 955	534 8
21	10 630	499 4	10 102	552 4
22	11 892	507 7	11 236	568 1
23	13 154	514 3	12 358	581 9
24	14 416	519 7	13 467	594 6
25	15 678	523 9	14 564	606 0
26	16 940	527 2	15 649	616 5
27	18 202	529 9	16 722	626 3
28	19 464	531 8	17 784	635 3
29	20 726	533 1	18 835	643 6
30	21 988	534 0	19 875	651 4
31	23 135	534 6	20 811	658 2
32	23 479	534 6		
33	24 397	534 6		
34	25 429	534 3		
35	26 347	533 8		
36	27 379	533 0		
37	28 297	532 0		
38	29 215	530 4		
39	30 247	527 9		
40	31 165	524 5		
41	32 083	519 2		
42	33 115	510 4		
43	34 033	500 3		
44	35 065	486 0		
45	35 983	470 2		
46	36 901	451 6		
47	37 933	426 3		
48	38 851	399 2		
49	39 884	364 2		
50	40 457	344 3		

Table 13. Location 10 Test Results - Knuckle (SGV480: Thickness 28 mm)

R19	Engr. Strain (%)	Engr. Stress (MPa)	True Strain (%)	True Stress (MPa)	R20	Engr. Strain (%)	Engr. Stress (MPa)	True Strain (%)	True Stress (MPa)	T19	Engr. Strain (%)	Engr. Stress (MPa)	True Strain (%)	True Stress (MPa)	T20	Engr. Strain (%)	Engr. Stress (MPa)	True Strain (%)	True Stress (MPa)
1	0.000	0.0	0.000	0.0	1	0.000	0.0	0.000	0.0	1	0.000	0.0	0.000	0.0	1	0.000	0.0	0.000	0.0
2	0.002	3.2	0.002	3.2	2	0.002	3.3	0.002	3.3	2	0.002	3.3	0.002	3.3	2	0.002	3.2	0.002	3.2
3	0.027	30.5	0.027	30.5	3	0.004	27.6	0.004	27.6	3	0.017	33.0	0.017	33.0	3	0.039	29.7	0.039	29.7
4	0.039	57.8	0.039	57.8	4	0.018	52.9	0.018	52.9	4	0.034	64.9	0.034	64.9	4	0.041	55.5	0.041	55.5
5	0.047	84.7	0.047	84.8	5	0.035	77.1	0.035	77.1	5	0.053	96.5	0.053	96.5	5	0.065	82.7	0.065	82.7
6	0.064	110.7	0.064	110.8	6	0.045	101.6	0.045	101.6	6	0.071	128.5	0.071	128.6	6	0.088	108.8	0.088	108.9
7	0.088	136.3	0.088	136.4	7	0.061	127.2	0.061	127.3	7	0.081	160.1	0.081	160.3	7	0.090	136.5	0.090	136.6
8	0.090	163.7	0.090	163.8	8	0.082	152.4	0.082	152.5	8	0.108	192.8	0.108	193.0	8	0.110	164.3	0.110	164.4
9	0.103	190.9	0.103	191.1	9	0.094	178.4	0.094	178.6	9	0.119	224.1	0.119	224.3	9	0.123	191.7	0.123	192.0
10	0.113	218.5	0.113	218.7	10	0.100	203.4	0.100	203.6	10	0.124	256.6	0.124	257.0	10	0.147	219.2	0.147	219.5
11	0.144	246.0	0.144	246.3	11	0.113	228.5	0.113	228.8	11	0.138	289.6	0.138	290.0	11	0.151	245.6	0.151	245.9
12	0.160	273.8	0.159	274.2	12	0.105	252.8	0.105	253.1	12	0.168	320.2	0.168	320.7	12	0.168	273.1	0.167	273.6
13	0.164	301.9	0.163	302.3	13	0.121	277.1	0.121	277.5	13	0.178	353.1	0.178	353.8	13	0.184	300.7	0.183	301.2
14	0.158	329.0	0.157	329.5	14	0.154	302.0	0.154	302.5	14	0.195	385.8	0.194	386.5	14	0.210	327.8	0.209	328.5
15	0.183	356.2	0.182	356.8	15	0.168	327.5	0.168	328.1	15	0.211	409.9	0.210	410.6	15	0.214	355.6	0.213	356.4
16	0.195	382.1	0.194	382.8	16	0.166	351.9	0.166	352.4	16	0.891	372.2	0.887	375.5	16	0.253	383.0	0.252	383.9
17	0.248	415.5	0.247	416.5	17	0.261	385.5	0.260	386.5	17	1.730	378.3	1.715	384.9	17	0.272	412.4	0.271	413.5
18	0.372	374.6	0.371	376.0	18	0.490	374.3	0.488	376.2	18	2.374	379.5	2.346	388.5	18	0.517	379.1	0.515	381.1
19	1.174	371.0	1.167	375.3	19	1.274	378.4	1.266	381.2	19	3.072	412.4	3.025	425.0	19	1.183	376.7	1.176	381.1
20	2.281	370.0	2.255	378.4	20	2.261	372.1	2.235	380.5	20	3.967	438.1	3.890	455.4	20	2.164	372.0	2.141	380.0
21	2.890	399.2	2.849	410.8	21	2.868	399.1	2.827	410.6	21	4.993	459.6	4.872	482.6	21	2.838	401.0	2.798	412.4
22	3.599	422.3	3.535	437.5	22	3.442	419.9	3.384	434.4	22	6.070	476.9	5.893	505.8	22	3.538	420.7	3.475	435.6
23	4.547	445.5	4.446	465.8	23	4.431	444.6	4.335	464.5	23	7.126	489.6	6.883	524.5	23	4.329	440.8	4.238	459.9
24	5.495	464.7	5.349	490.3	24	5.407	463.0	5.266	488.0	24	8.251	499.7	7.928	541.0	24	5.351	462.1	5.212	486.8
25	6.622	481.1	6.412	513.0	25	6.435	478.6	6.236	509.6	25	9.278	506.7	8.872	553.7	25	6.270	477.0	6.081	506.9
26	7.846	492.8	7.553	531.4	26	7.512	489.9	7.243	526.7	26	10.501	513.1	9.985	567.0	26	7.353	488.7	7.095	524.6
27	9.201	503.7	8.802	550.0	27	8.662	501.0	8.491	545.4	27	11.671	517.5	11.038	577.9	28	8.724	500.8	8.364	544.5
28	10.802	511.6	10.257	566.9	28	10.274	509.2	9.779	561.5	28	12.735	520.2	11.987	586.5	28	10.380	510.6	9.876	563.6
29	12.438	517.4	11.723	581.8	29	11.648	514.5	11.018	574.4	29	13.677	522.6	12.995	595.1	29	11.999	516.7	11.332	578.7
30	13.914	520.7	13.027	593.2	30	13.234	519.3	12.428	588.0	30	15.036	524.0	14.007	602.8	30	13.559	520.9	12.715	591.6
31	15.244	522.7	14.188	602.4	31	14.774	521.6	13.779	598.7	31	16.077	525.1	14.908	609.6	31	15.018	523.2	13.992	601.8
32	16.753	524.3	15.489	612.1	32	16.194	523.6	15.009	608.4	32	17.224	525.6	15.891	616.2	32	16.401	525.0	15.187	611.0
33	17.849	524.9	16.423	618.5	33	17.874	524.3	16.444	618.0	33	18.052	525.7	16.595	620.6	33	18.092	525.7	16.629	620.9
34	17.957	524.5			34	18.109	524.4	16.643	619.3	34	18.069	525.4			34	18.194	525.6		
35	19.140	524.7			35	18.209	524.3			35	18.847	525.4			35	19.398	525.3		
36	20.438	523.9			36	19.597	523.9			36	19.507	524.9			36	20.534	525.1		
37	21.727	523.0			37	20.739	523.6			37	20.229	525.0			37	21.559	524.3		
38	22.641	522.0			38	21.944	522.6			38	20.991	524.2			38	22.760	523.0		
39	23.797	520.1			39	22.824	522.1			39	21.795	523.4			39	23.906	521.0		
40	24.788	517.7			40	24.128	520.1			40	22.545	522.2			40	25.017	518.0		
41	25.995	513.0			41	25.205	518.2			41	23.225	520.9			41	25.528	516.7		
42	27.294	505.9			42	26.398	515.2			42	23.710	519.8			42	26.482	512.0		
43	27.809	502.0			43	27.683	510.2			43	24.785	516.7			43	27.720	504.1		
44	28.854	494.8			44	28.434	506.7			44	25.918	511.9			44	28.674	496.3		
45	29.982	484.5			45	29.765	498.3			45	27.377	504.0			45	29.680	487.5		
46	31.165	471.7			46	30.933	489.2			46	28.758	493.7			46	30.860	474.1		
47	32.381	456.6			47	32.223	477.1			47	30.319	479.3			47	31.648	464.0		
48	33.522	440.2			48	33.338	464.7			48	31.787	462.0			48	32.535	452.7		
49	34.268	427.9			49	34.570	449.0			49	33.018	443.9			49	33.614	436.2		
50	35.242	410.4			50	35.755	431.0			50	33.890	432.2			50	34.497	421.1		
51	36.119	393.0			51	36.895	412.0			51	34.852	414.7			51	35.430	403.2		
52	37.044	373.2			52	37.969	391.7			52	35.908	395.0			52	36.200	387.4		

Table 14. Location 11 Test Results - Lower Cylindrical Shell and Lower Conical Shell (SPV490: Thickness 9 mm)

R21	Engr. Strain (%)	Engr. Stress (MPa)	True Strain (%)	True Stress (MPa)	R22	Engr. Strain (%)	Engr. Stress (MPa)	True Strain (%)	True Stress (MPa)	T21	Engr. Strain (%)	Engr. Stress (MPa)	True Strain (%)	True Stress (MPa)	T22	Engr. Strain (%)	Engr. Stress (MPa)	True Strain (%)	True Stress (MPa)
1	0.000	0.0	0.000	0.0	1	0.000	0.0	0.000	0.0	1	0.000	0.0	0.000	0.0	1	0.000	0.0	0.000	0.0
2	0.002	4.3	0.002	4.3	2	0.002	4.1	0.002	4.1	2	0.005	10.4	0.005	10.4	2	0.005	9.4	0.005	9.4
3	0.007	26.8	0.007	26.8	3	0.005	29.8	0.005	29.8	3	0.010	41.6	0.010	41.6	3	0.049	37.1	0.049	37.1
4	0.035	53.8	0.035	53.9	4	0.013	55.5	0.013	55.5	4	0.031	72.5	0.031	72.5	4	0.074	64.9	0.074	65.0
5	0.070	79.8	0.070	79.9	5	0.035	81.6	0.035	81.6	5	0.060	105.6	0.060	105.7	5	0.108	95.2	0.108	95.3
6	0.078	107.7	0.078	107.8	6	0.046	107.7	0.046	107.7	6	0.088	138.8	0.088	138.9	6	0.141	128.4	0.141	128.6
7	0.111	135.5	0.111	135.7	7	0.071	133.8	0.071	133.9	7	0.124	171.8	0.124	172.0	7	0.167	158.0	0.167	158.2
8	0.144	163.5	0.144	163.7	8	0.093	158.4	0.093	158.5	8	0.145	204.8	0.145	205.1	8	0.201	190.9	0.201	191.3
9	0.155	191.3	0.155	191.6	9	0.115	185.0	0.115	185.2	9	0.182	237.8	0.182	238.2	9	0.219	224.7	0.218	225.2
10	0.182	219.6	0.182	220.0	10	0.137	210.7	0.137	211.0	10	0.197	270.8	0.197	271.3	10	0.239	258.2	0.238	258.8
11	0.201	247.3	0.201	247.8	11	0.170	238.5	0.170	238.9	11	0.236	303.4	0.236	304.1	11	0.278	290.2	0.277	291.0
12	0.234	274.9	0.234	275.5	12	0.173	262.9	0.173	263.4	12	0.246	334.0	0.246	334.8	12	0.314	320.1	0.313	321.1
13	0.253	302.0	0.253	302.8	13	0.220	288.7	0.220	289.3	13	0.278	367.4	0.278	368.4	13	0.337	351.6	0.336	352.8
14	0.283	330.0	0.283	330.9	14	0.223	315.4	0.223	316.1	14	0.301	399.6	0.301	400.8	14	0.358	385.0	0.357	386.4
15	0.302	357.8	0.302	358.9	15	0.239	341.6	0.239	342.4	15	0.330	433.0	0.330	434.4	15	0.381	418.5	0.380	420.0
16	0.311	385.5	0.311	386.7	16	0.264	367.3	0.264	368.2	16	0.363	465.9	0.363	467.6	16	0.417	452.0	0.416	453.9
17	0.346	413.4	0.346	414.8	17	0.289	393.4	0.289	394.6	17	0.394	499.1	0.393	501.0	17	0.443	485.3	0.442	487.5
18	0.373	441.4	0.372	443.0	18	0.314	419.8	0.314	421.1	18	0.420	532.0	0.419	534.2	18	0.466	518.9	0.465	521.3
19	0.390	468.9	0.389	470.7	19	0.330	445.5	0.330	447.0	19	0.454	565.7	0.453	568.2	19	0.502	553.0	0.500	555.8
20	0.431	497.1	0.430	499.2	20	0.349	471.3	0.348	473.0	20	0.472	599.3	0.471	602.1	20	0.525	586.0	0.523	589.1
21	0.458	524.9	0.457	527.3	21	0.374	497.1	0.373	499.0	21	0.496	630.4	0.495	633.5	21	0.553	616.4	0.551	619.8
22	0.474	553.0	0.473	555.6	22	0.402	523.3	0.401	525.4	22	0.607	689.3	0.605	693.5	22	0.592	649.7	0.590	653.5
23	0.494	581.0	0.493	583.9	23	0.407	549.2	0.406	551.4	23	0.802	885.0	0.799	890.5	23	0.749	694.5	0.746	699.7
24	0.504	607.1	0.503	610.2	24	0.435	575.6	0.434	578.1	24	1.952	689.9	1.933	703.4	24	0.880	692.3	0.876	698.3
25	0.554	635.4	0.553	638.9	25	0.457	599.2	0.456	601.9	25	3.011	695.8	2.987	716.7	25	2.381	691.6	2.353	708.0
26	0.604	676.1	0.602	680.2	26	0.484	625.2	0.483	628.2	26	4.032	700.4	3.953	728.6	26	3.418	696.6	3.361	720.4
27	0.926	655.0	0.922	661.1	27	0.515	651.0	0.514	654.3	27	4.927	708.1	4.810	743.0	27	4.545	707.0	4.444	739.1
28	2.244	661.4	2.219	676.2	28	0.601	672.8	0.599	676.9	28	6.059	716.0	5.883	759.4	28	5.500	714.5	5.354	753.8
29	4.096	674.9	4.014	702.5	29	2.296	665.2	2.270	680.5	29	7.220	722.5	6.971	774.6	29	6.679	722.2	6.465	770.4
30	5.808	688.5	5.646	728.5	30	3.776	675.2	3.707	700.7	30	8.025	725.6	7.719	783.8	30	7.845	728.0	7.552	785.1
31	7.758	699.4	7.472	753.7	31	5.486	689.0	5.341	726.8	31	8.814	728.2	8.447	792.4	31	8.803	730.8	8.437	795.1
32	9.355	704.6	8.943	770.5	32	7.441	701.0	7.177	753.1	32	9.993	730.7	9.525	803.7	32	9.755	732.7	9.308	804.1
33	10.836	706.0	10.288	782.5	33	9.153	707.3	8.758	772.0	33	11.115	731.2	10.540	812.5	33	10.515	733.2	9.998	810.3
34	10.979	705.9			34	10.687	709.4	10.154	785.2	34	11.248	731.0			34	10.644	733.2		
35	12.422	703.4			35	10.827	709.2			35	12.113	730.2			35	11.606	731.1		
36	13.971	693.9			36	12.456	706.8			36	13.249	725.9			36	12.661	725.0		
37	15.293	681.0			37	14.068	695.7			37	14.298	717.2			37	13.549	716.1		
38	16.655	664.7			38	16.245	671.2			38	15.381	704.6			38	14.434	704.8		
39	17.379	654.5			39	17.754	650.4			39	16.427	690.2			39	15.257	692.9		
40	18.757	633.9			40	18.961	631.5			40	17.513	673.6			40	16.246	677.3		
41	19.919	614.6			41	20.285	608.2			41	18.446	658.8			41	17.288	659.5		
42	20.890	596.6			42	21.230	590.0			42	19.273	642.4			42	18.230	641.9		
43	22.002	574.8			43	22.345	567.0			43	20.346	621.5			43	18.950	627.2		
44	22.995	552.7			44	23.239	546.5			44	21.307	601.2			44	19.982	604.7		
45	23.835	533.0			45	24.186	522.9			45	21.877	587.7			45	20.875	582.8		
46	24.707	511.1			46	24.798	506.5			46	22.931	562.3			46	21.845	557.4		
47	25.513	489.4			47	25.656	482.7			47	23.604	543.9			47	22.738	531.4		
48	26.203	469.1			48	26.335	462.1			48	24.690	512.6			48	23.499	507.7		
49	26.810	450.5			49	27.072	438.6			49	25.439	489.2			49	24.392	478.2		
50	27.455	429.7			50	27.735	416.5			50	26.000	471.7			50	25.315	444.9		
51	28.115	407.6			51	28.422	393.0			51	26.824	442.5			51	25.981	419.3		
52	28.707	387.1			52	28.995	371.5			52	27.712	409.7			52	26.742	388.7		
53	29.260	366.8			53	29.612	348.3			53	28.350	384.4			53	27.307	364.7		
54	29.788	346.4			54	30.073	329.6			54	28.862	362.7			54	27.862	338.9		

Table 15. Location 12 Test Results - Hatch Reinforcement Plate (SPV490: Thickness 17.5 mm)

R23	Engr. Strain (%)	Engr. Stress (MPa)	True Strain (%)	True Stress (MPa)
1	0.000	0.0	0.000	0.0
2	0.003	6.4	0.003	6.4
3	0.029	33.8	0.029	33.8
4	0.046	62.0	0.046	62.0
5	0.057	91.5	0.057	91.5
6	0.075	119.2	0.075	119.2
7	0.109	147.8	0.109	147.9
8	0.103	172.3	0.103	172.5
9	0.118	201.6	0.118	201.9
10	0.152	231.1	0.152	231.5
11	0.164	259.5	0.164	259.9
12	0.172	289.1	0.172	289.6
13	0.189	319.0	0.189	319.6
14	0.212	347.5	0.212	348.2
15	0.215	373.0	0.215	373.8
16	0.238	400.4	0.238	401.4
17	0.241	428.6	0.241	429.6
18	0.264	458.2	0.264	459.4
19	0.281	488.1	0.281	489.5
20	0.298	516.2	0.298	517.8
21	0.321	545.8	0.321	547.6
22	0.318	573.5	0.318	575.3
23	0.359	609.1	0.359	611.3
24	0.577	599.7	0.578	603.1
25	1.996	615.8	1.977	628.1
26	2.939	630.8	2.897	649.3
27	3.934	644.3	3.859	669.6
28	4.889	654.7	4.773	686.7
29	5.962	662.2	5.791	701.7
30	6.911	666.5	6.683	712.5
31	7.871	668.9	7.577	721.6
32	8.872	669.4	8.500	728.8
33	10.088	669.7	9.611	737.3
34	10.258	669.5		
35	11.270	668.4		
36	12.251	666.1		
37	13.097	662.9		
38	14.251	656.4		
39	16.139	641.4		
40	17.442	629.1		
41	18.340	619.6		
42	19.359	607.5		
43	20.391	594.3		
44	21.461	580.1		
45	22.646	562.3		
46	23.659	545.6		
47	24.754	525.8		
48	25.924	504.3		
49	26.582	490.4		
50	27.486	470.0		
51	28.393	449.5		
52	29.348	425.9		
53	30.003	408.4		

R24	Engr. Strain (%)	Engr. Stress (MPa)	True Strain (%)	True Stress (MPa)
1	0.000	0.0	0.000	0.0
2	0.003	6.7	0.003	6.7
3	0.010	33.3	0.010	33.3
4	0.026	67.0	0.026	67.0
5	0.044	100.3	0.044	100.4
6	0.067	135.4	0.067	135.5
7	0.096	171.0	0.096	171.2
8	0.105	203.8	0.105	204.0
9	0.129	234.5	0.129	234.8
10	0.148	269.2	0.148	269.6
11	0.161	303.5	0.161	304.0
12	0.185	336.8	0.185	337.2
13	0.199	368.8	0.199	369.6
14	0.222	404.8	0.222	405.7
15	0.245	440.5	0.245	441.6
16	0.264	476.0	0.264	477.3
17	0.284	509.5	0.284	510.9
18	0.311	545.2	0.311	546.9
19	0.320	578.3	0.320	580.2
20	0.480	605.2	0.479	608.1
21	1.145	606.9	1.139	613.9
22	1.803	617.5	1.787	628.7
23	2.317	626.2	2.291	640.7
24	2.896	635.9	2.855	654.3
25	3.592	645.6	3.529	668.8
26	4.240	653.7	4.153	681.4
27	4.900	659.8	4.784	692.1
28	5.604	664.8	5.453	702.1
29	6.260	668.3	6.072	710.2
30	6.950	670.7	6.719	717.3
31	7.618	672.1	7.342	723.3
32	8.219	673.2	7.899	728.6
33	9.701	673.6	9.259	739.0
34	9.766	673.3		
35	10.818	673.2		
36	11.789	671.4		
37	12.874	668.9		
38	13.954	663.2		
39	14.920	656.4		
40	15.918	647.3		
41	16.865	637.9		
42	17.857	627.9		
43	18.879	615.9		
44	19.932	602.7		
45	20.995	588.2		
46	22.024	572.8		
47	22.934	558.3		
48	23.966	540.4		
49	25.002	521.0		
50	25.985	500.9		
51	27.015	478.6		
52	28.054	454.1		
53	28.918	432.4		
54	29.946	404.8		

T23	Engr. Strain (%)	Engr. Stress (MPa)	True Strain (%)	True Stress (MPa)
1	0.000	0.0	0.000	0.0
2	0.003	6.4	0.003	6.4
3	0.025	41.5	0.025	41.5
4	0.052	76.9	0.052	76.9
5	0.073	112.9	0.073	113.0
6	0.091	146.2	0.091	146.4
7	0.106	180.1	0.106	180.2
8	0.127	213.6	0.127	213.9
9	0.151	246.1	0.151	246.5
10	0.175	283.4	0.175	283.9
11	0.183	319.0	0.183	319.6
12	0.203	354.4	0.203	355.1
13	0.227	390.1	0.227	391.0
14	0.252	425.5	0.252	426.6
15	0.264	461.1	0.264	462.3
16	0.293	495.8	0.293	497.3
17	0.306	531.1	0.306	532.8
18	0.326	566.6	0.326	568.5
19	0.416	598.9	0.415	601.4
20	0.954	598.5	0.950	604.2
21	1.811	611.7	1.795	622.8
22	2.482	623.4	2.452	638.9
23	3.139	633.8	3.091	653.7
24	3.817	643.1	3.746	667.7
25	4.425	649.8	4.330	678.5
26	5.129	655.7	5.002	689.3
27	5.772	660.3	5.612	698.4
28	6.276	663.2	6.087	704.9
29	6.903	665.0	6.675	710.9
30	7.498	666.8	7.230	716.8
31	8.122	667.7	7.809	722.0
32	8.712	667.7	8.353	725.9
33	8.812	668.0	8.445	726.9
34	8.871	667.8		
35	9.965	666.9		
36	11.078	664.3		
37	12.215	659.7		
38	13.310	652.9		
39	14.334	644.2		
40	15.418	634.7		
41	16.432	623.9		
42	17.558	610.8		
43	18.685	596.2		
44	19.770	580.3		
45	20.761	565.0		
46	21.752	547.5		
47	22.831	527.4		
48	23.929	504.8		
49	24.995	481.3		
50	26.133	453.4		
51	27.225	424.0		
52	28.322	392.2		
53	29.372	359.0		
54	30.403	324.0		

T24	Engr. Strain (%)	Engr. Stress (MPa)	True Strain (%)	True Stress (MPa)
1	0.000	0.0	0.000	0.0
2	0.003	6.0	0.003	6.0
3	0.034	41.0	0.034	41.0
4	0.056	74.9	0.056	75.0
5	0.069	107.6	0.069	107.7
6	0.087	142.9	0.087	143.0
7	0.094	177.1	0.094	177.3
8	0.120	210.7	0.120	211.0
9	0.138	244.1	0.138	244.4
10	0.157	279.8	0.157	280.2
11	0.172	314.1	0.172	314.6
12	0.192	350.0	0.192	350.7
13	0.211	382.6	0.211	383.4
14	0.234	412.0	0.234	412.9
15	0.255	444.7	0.255	445.9
16	0.262	477.0	0.262	478.2
17	0.293	512.5	0.293	514.0
18	0.302	547.9	0.302	549.6
19	0.347	602.9	0.346	605.0
20	0.531	591.4	0.530	594.6
21	1.226	597.9	1.219	605.2
22	1.936	610.2	1.917	622.0
23	2.596	621.9	2.563	638.1
24	3.308	632.6	3.254	653.6
25	3.980	640.8	3.903	666.3
26	4.679	646.4	4.573	678.8
27	5.316	653.3	5.180	688.1
28	5.908	656.9	5.738	695.6
29	6.602	660.0	6.393	703.6
30	7.252	662.3	7.001	710.4
31	7.892	663.2	7.596	715.6
32	8.558	663.8	8.211	720.6
33	8.788	664.0	8.423	722.4
34	8.848	663.4		
35	9.829	662.8		
36	10.970	660.1		
37	11.953	656.3		
38	13.038	650.3		
39	14.197	641.6		
40	15.298	632.1		
41	16.424	621.0		
42	17.441	609.6		
43	18.599	595.5		
44	19.479	581.8		
45	20.574	565.9		
46	21.705	547.4		
47	22.767	528.6		
48	23.883	506.6		
49	25.034	482.2		
50	26.092	457.6		
51	27.256	428.0		
52	28.351	398.0		
53	29.498	363.6		
54	30.603	328.0		

Appendix C

As-Built Features of the Steel Containment Vessel (SCV) Model

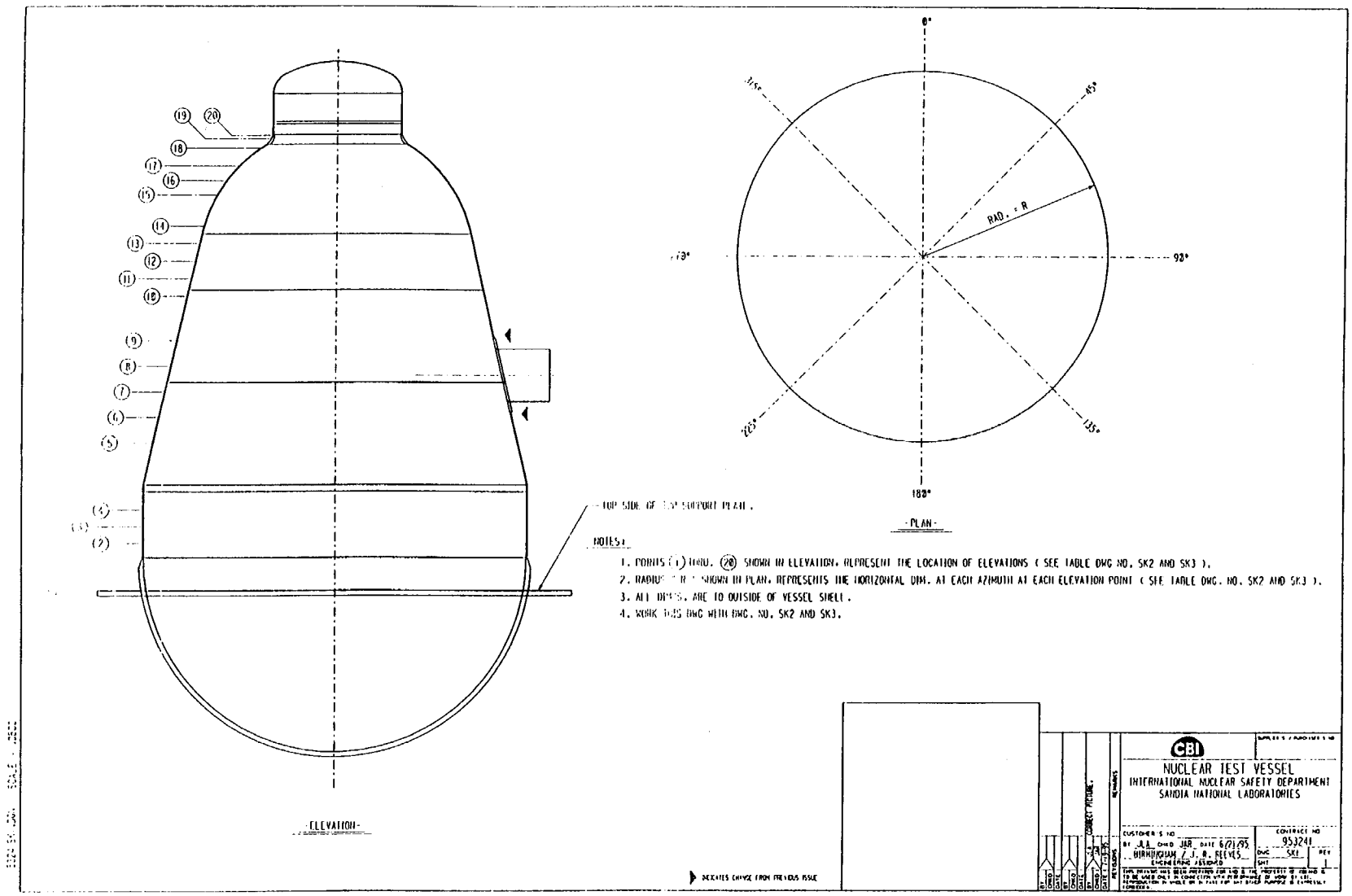

Figure C-1. Steel containment vessel (SCV) model - elevation and plan.

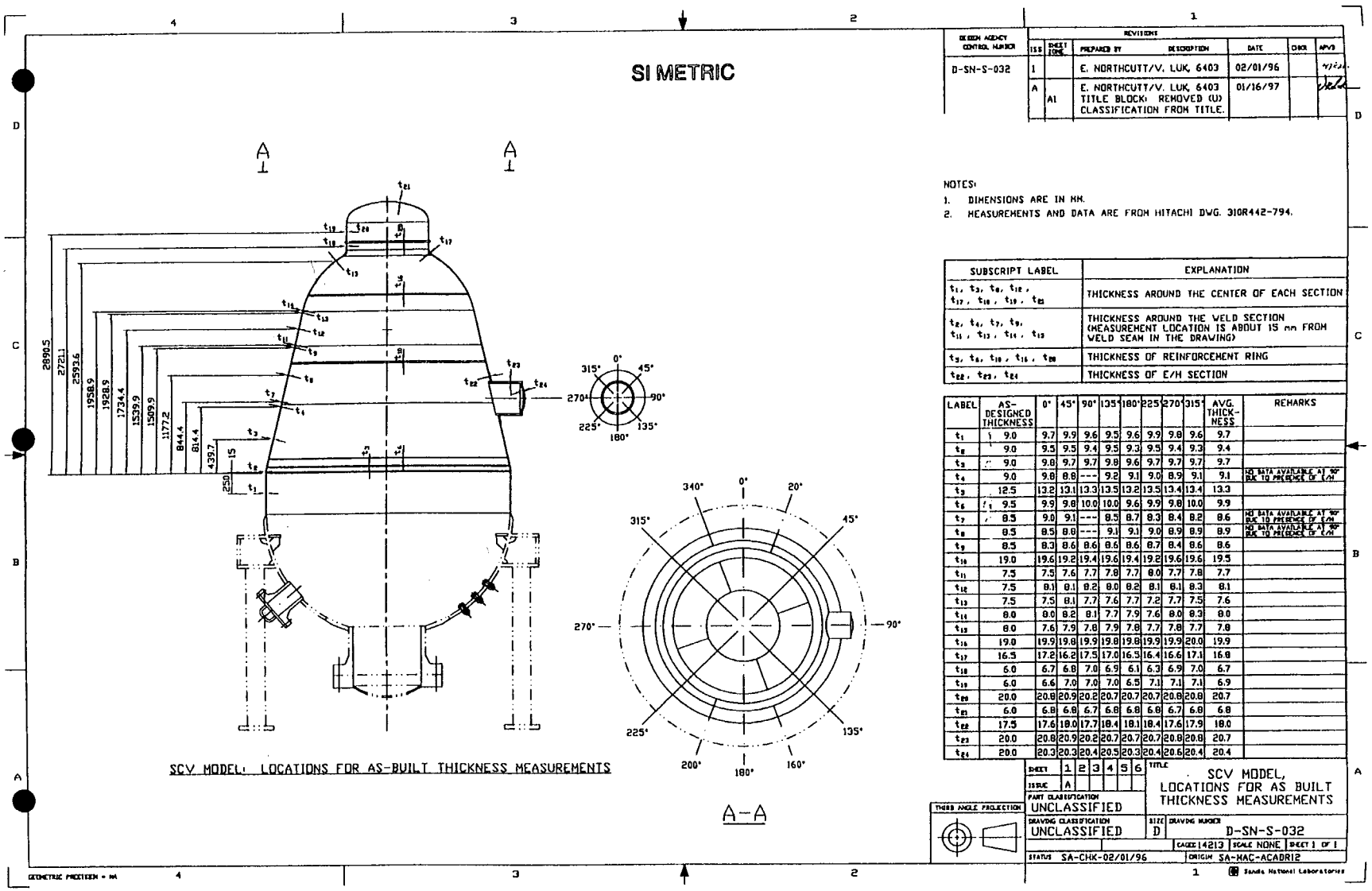

SUBSCRIPT LABEL	EXPLANATION
t_1, t_3, t_6, t_{12}, t_{17}, t_{18}, t_{19}, t_{21}	THICKNESS AROUND THE CENTER OF EACH SECTION
t_2, t_4, t_7, t_9, t_{11}, t_{13}, t_{14}, t_{15}	THICKNESS AROUND THE WELD SECTION (MEASUREMENT LOCATION IS ABOUT 15 mm FROM WELD SEAM IN THE DRAWING)
t_5, t_8, t_{10}, t_{16}, t_{20}	THICKNESS OF REINFORCEMENT RING
t_{22}, t_{23}, t_{24}	THICKNESS OF E/H SECTION

LABEL	AS-DESIGNED THICKNESS	0°	45°	90°	135°	180°	225°	270°	315°	AVG. THICKNESS	REMARKS
t_1	9.0	9.7	9.9	9.6	9.5	9.6	9.9	9.8	9.6	9.7	
t_2	9.0	9.5	9.5	9.4	9.5	9.3	9.5	9.4	9.3	9.4	
t_3	9.0	9.8	9.7	9.7	9.8	9.6	9.7	9.7	9.7	9.7	
t_4	9.0	9.8	8.8	---	9.2	9.1	9.0	8.9	9.1	9.1	NO DATA AVAILABLE AT 90° DUE TO PRESENCE OF E/H
t_5	12.5	13.2	13.1	13.3	13.5	13.2	13.5	13.4	13.4	13.3	
t_6	9.5	9.9	9.8	10.0	10.0	9.6	9.9	9.8	10.0	9.9	
t_7	8.5	9.0	9.1	---	8.5	8.7	8.3	8.4	8.2	8.6	NO DATA AVAILABLE AT 90° DUE TO PRESENCE OF E/H
t_8	8.5	8.5	8.8	---	9.1	9.1	9.0	8.9	8.9	8.9	NO DATA AVAILABLE AT 90° DUE TO PRESENCE OF E/H
t_9	8.5	8.3	8.6	8.6	8.6	8.6	8.7	8.4	8.6	8.6	
t_{10}	19.0	19.6	19.2	19.4	19.6	19.4	19.2	19.6	19.6	19.5	
t_{11}	7.5	7.5	7.6	7.7	7.8	7.7	8.0	7.7	7.8	7.7	
t_{12}	7.5	8.1	8.1	8.2	8.0	8.2	8.1	8.1	8.3	8.1	
t_{13}	7.5	7.5	8.1	7.7	7.6	7.7	7.2	7.7	7.5	7.6	
t_{14}	8.0	8.0	8.2	8.1	7.7	7.9	7.6	8.0	8.3	8.0	
t_{15}	8.0	7.6	7.9	7.8	7.9	7.8	7.7	7.8	7.7	7.8	
t_{16}	19.0	19.9	19.8	19.9	19.8	19.8	19.9	19.9	20.0	19.9	
t_{17}	16.5	17.2	16.2	17.5	17.0	16.5	16.4	16.6	17.1	16.8	
t_{18}	6.0	6.7	6.8	7.0	6.9	6.1	6.3	6.9	7.0	6.7	
t_{19}	6.0	6.6	7.0	7.0	7.0	6.5	7.1	7.1	7.1	6.9	
t_{20}	20.0	20.8	20.9	20.2	20.7	20.7	20.7	20.8	20.8	20.7	
t_{21}	6.0	6.8	6.8	6.7	6.8	6.8	6.8	6.7	6.8	6.8	
t_{22}	17.5	17.6	18.0	17.7	18.4	18.1	18.4	17.6	17.9	18.0	
t_{23}	20.0	20.8	20.9	20.2	20.7	20.7	20.7	20.9	20.8	20.7	
t_{24}	20.0	20.3	20.3	20.4	20.5	20.3	20.4	20.6	20.4	20.4	

Figure C-2. SCV model - locations for as-built thickness measurements.

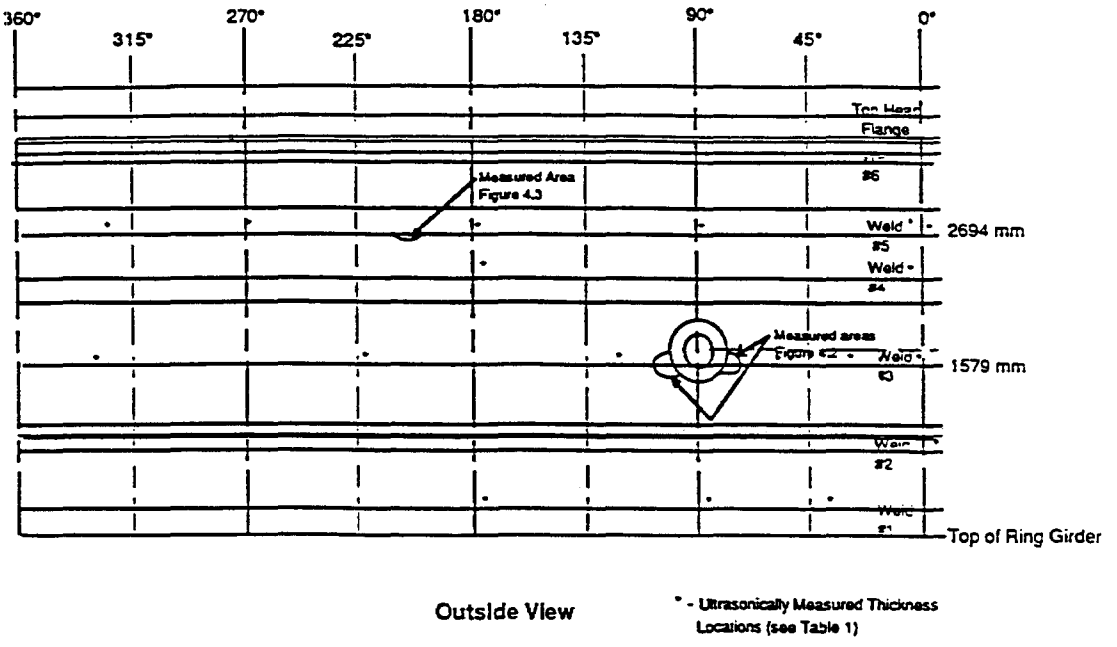

Figure C-3. Stretched layout view of the SCV model, indicating locations of as-built thickness measurements.

Weld	Azimuth	Thickness (mm)
1	40°	9.3
1	90°	9.1
1	180°	8.8
2	0°	9.4
3	3°	9.2
3	17°	8.9
3	56°	9.0
3	117°	9.2
3	227°	8.9
3	324°	8.9
4	0°	8.3
4	180°	7.3
5	0°	7.1
5	7°	8.1
5	90°	7.6
5	180°	7.3
5	270°	7.2
5	318°	7.9

Figure C-4. Tabulation of SCV model as-built thickness measurements shown in Figure C-3 (above).

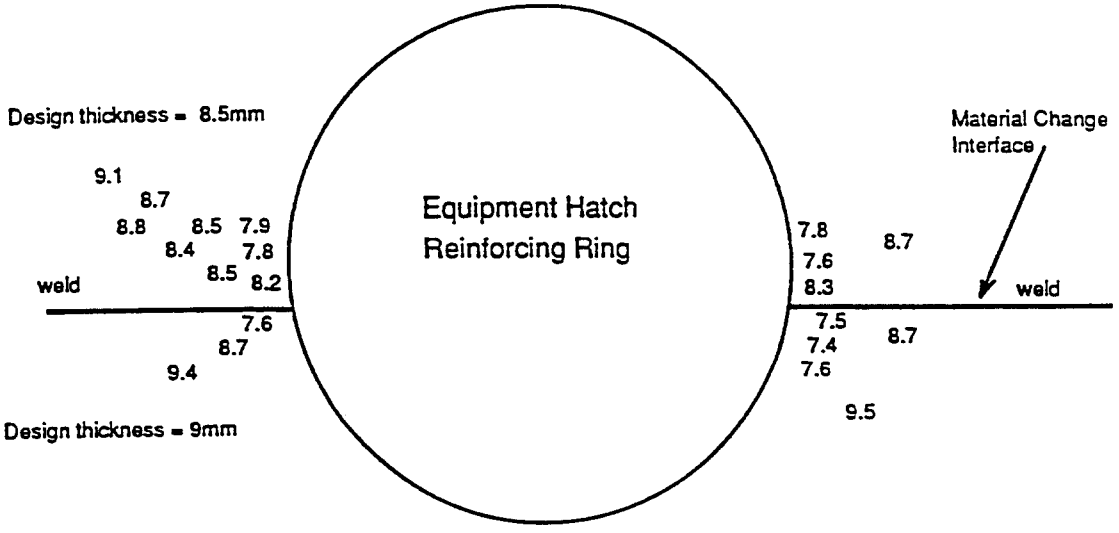

Note:
1. all thickness measurements are from an ultrasonic thickness measuring device.
2. all thickness measurements in mm.
3. values for thickness measurements indicate approximate locations only.

Figure C-5. Thickness measurements at SCV equipment hatch.

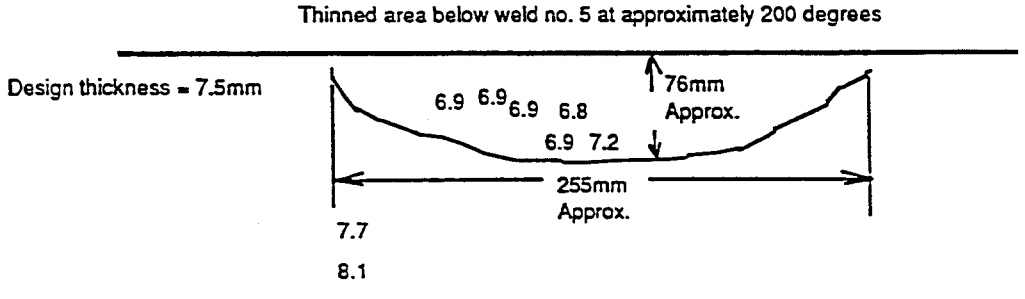

Note: all thickness measurements are from an ultrasonic thickness measuring device.
all thickness measurements in mm.

Figure C-6. Thickness measurements of SCV at weld #5, azimuth 200°.

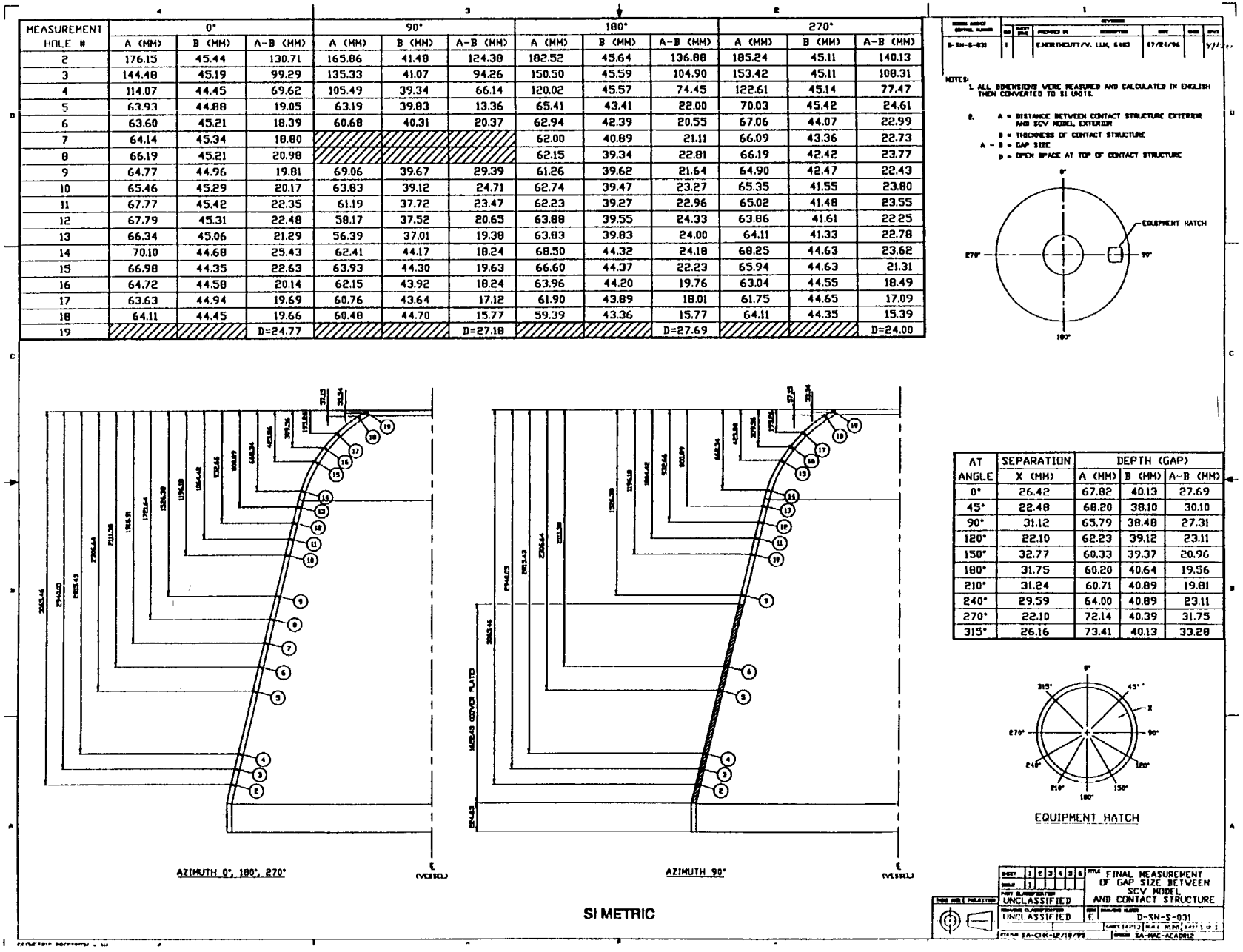

MEASUREMENT HOLE #	0° A (MM)	0° B (MM)	0° A-B (MM)	90° A (MM)	90° B (MM)	90° A-B (MM)	180° A (MM)	180° B (MM)	180° A-B (MM)	270° A (MM)	270° B (MM)	270° A-B (MM)
2	176.15	45.44	130.71	165.86	41.48	124.38	182.52	45.64	136.88	185.24	45.11	140.13
3	144.48	45.19	99.29	135.33	41.07	94.26	150.50	45.59	104.90	153.42	45.11	108.31
4	114.07	44.45	69.62	105.49	39.34	66.14	120.02	45.57	74.45	122.61	45.14	77.47
5	63.93	44.88	19.05	63.19	39.83	13.36	65.41	43.41	22.00	70.03	45.42	24.61
6	63.60	45.21	18.39	60.68	40.31	20.37	62.94	42.39	20.55	67.06	44.07	22.99
7	64.14	45.34	18.80				62.00	40.89	21.11	66.09	43.36	22.73
8	66.19	45.21	20.98				62.15	39.34	22.81	66.19	42.42	23.77
9	64.77	44.96	19.81	69.06	39.67	29.39	61.26	39.62	21.64	64.90	42.47	22.43
10	65.46	45.29	20.17	63.83	39.12	24.71	62.74	39.47	23.27	65.35	41.55	23.80
11	67.77	45.42	22.35	61.19	37.72	23.47	62.23	39.27	22.96	65.02	41.48	23.55
12	67.79	45.31	22.48	58.17	37.52	20.65	63.88	39.55	24.33	63.86	41.61	22.25
13	66.34	45.06	21.29	56.39	37.01	19.38	63.83	39.83	24.00	64.11	41.33	22.78
14	70.10	44.68	25.43	62.41	44.17	18.24	68.50	44.32	24.18	68.25	44.63	23.62
15	66.98	44.35	22.63	63.93	44.30	19.63	66.60	44.37	22.23	65.94	44.63	21.31
16	64.72	44.58	20.14	62.15	43.92	18.24	63.96	44.20	19.76	63.04	44.55	18.49
17	63.63	44.94	19.69	60.76	43.64	17.12	61.90	43.89	18.01	61.75	44.65	17.09
18	64.11	44.45	19.66	60.48	44.70	15.77	59.39	43.36	15.77	64.11	44.35	15.39
19			D=24.77			D=27.18			D=27.69			D=24.00

AT ANGLE	SEPARATION X (MM)	DEPTH (GAP) A (MM)	B (MM)	A-B (MM)
0°	26.42	67.82	40.13	27.69
45°	22.48	68.20	38.10	30.10
90°	31.12	65.79	38.48	27.31
120°	22.10	62.23	39.12	23.11
150°	32.77	60.33	39.37	20.96
180°	31.75	60.20	40.64	19.56
210°	31.24	60.71	40.89	19.81
240°	29.59	64.00	40.89	23.11
270°	22.10	72.14	40.39	31.75
315°	26.16	73.41	40.13	33.28

Figure C-7. Final measurement of gap size between SCV model and contact structure.

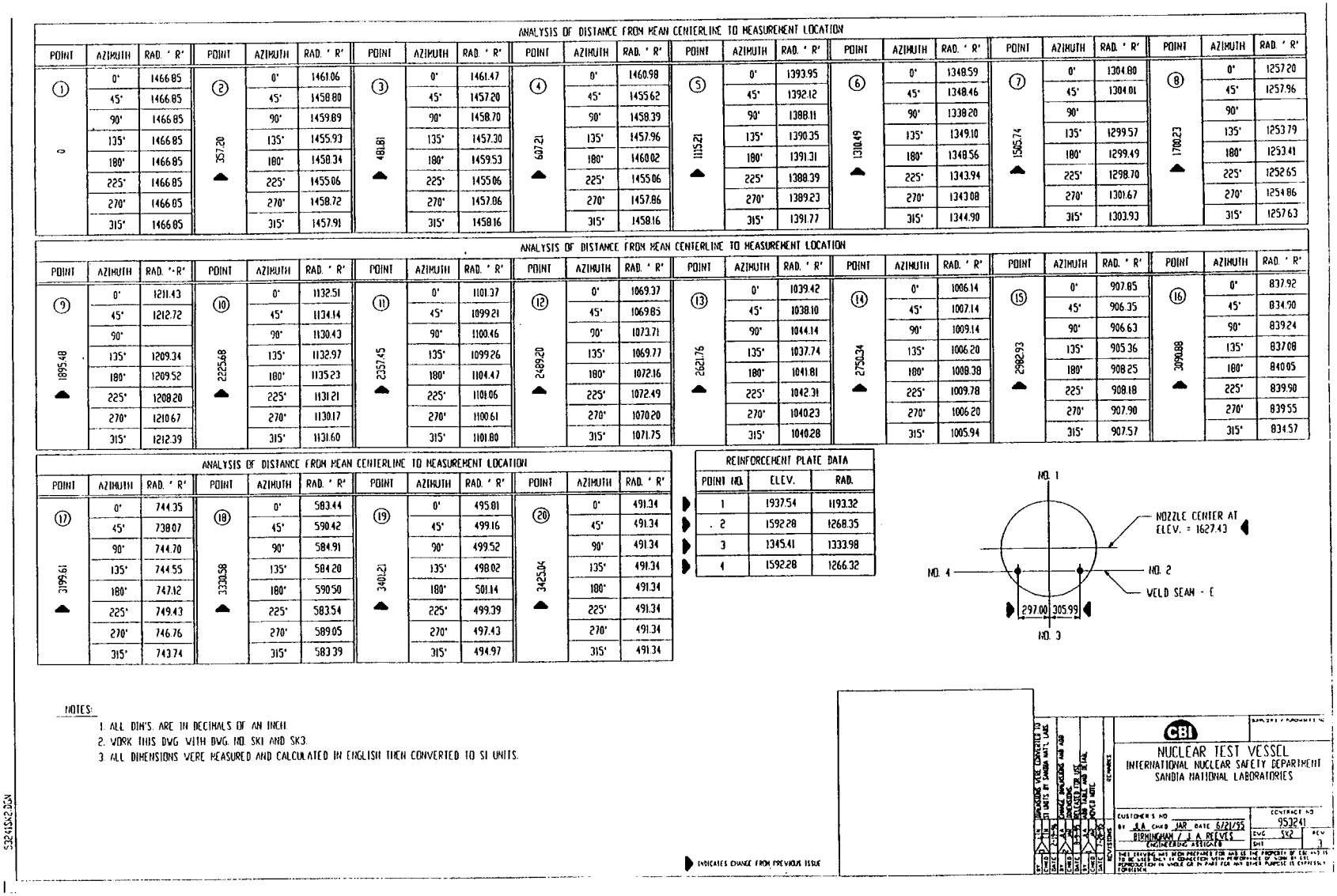

ANALYSIS OF DISTANCE FROM MEAN CENTERLINE TO MEASUREMENT LOCATION

POINT	AZIMUTH	RAD. 'R'	POINT	AZIMUTH	RAD. 'R'	POINT	AZIMUTH	RAD. 'R'	POINT	AZIMUTH	RAD. 'R'	POINT	AZIMUTH	RAD. 'R'	POINT	AZIMUTH	RAD. 'R'	POINT	AZIMUTH	RAD. 'R'	POINT	AZIMUTH	RAD. 'R'
①	0°	1466.85	②	0°	1461.06	③	0°	1461.47	④	0°	1460.98	⑤	0°	1393.95	⑥	0°	1348.59	⑦	0°	1304.80	⑧	0°	1257.20
	45°	1466.85		45°	1458.80		45°	1457.20		45°	1455.62		45°	1392.12		45°	1348.46		45°	1304.01		45°	1257.96
	90°	1466.85		90°	1459.89		90°	1458.70		90°	1458.39		90°	1388.11		90°	1338.20		90°			90°	
	135°	1466.85		135°	1455.93		135°	1457.30		135°	1457.96		135°	1390.35		135°	1349.10		135°	1299.57		135°	1253.79
0	180°	1466.85	257.20	180°	1458.34	481.81	180°	1459.53	607.21	180°	1460.02	1115.21	180°	1391.31	1318.49	180°	1348.56	1565.74	180°	1299.49	1780.23	180°	1253.41
	225°	1466.85	▲	225°	1455.06	▲	225°	1455.06	▲	225°	1455.06	▲	225°	1388.39	▲	225°	1343.94	▲	225°	1298.70	▲	225°	1252.65
	270°	1466.85		270°	1458.72		270°	1457.06		270°	1457.86		270°	1389.23		270°	1343.08		270°	1301.67		270°	1254.86
	315°	1466.85		315°	1457.91		315°	1458.16		315°	1458.16		315°	1391.77		315°	1344.90		315°	1303.93		315°	1257.63

ANALYSIS OF DISTANCE FROM MEAN CENTERLINE TO MEASUREMENT LOCATION

POINT	AZIMUTH	RAD. 'R'	POINT	AZIMUTH	RAD. 'R'	POINT	AZIMUTH	RAD. 'R'	POINT	AZIMUTH	RAD. 'R'	POINT	AZIMUTH	RAD. 'R'	POINT	AZIMUTH	RAD. 'R'	POINT	AZIMUTH	RAD. 'R'	POINT	AZIMUTH	RAD. 'R'
⑨	0°	1211.43	⑩	0°	1132.51	⑪	0°	1101.37	⑫	0°	1069.37	⑬	0°	1039.42	⑭	0°	1006.14	⑮	0°	907.85	⑯	0°	837.92
	45°	1212.72		45°	1134.14		45°	1099.21		45°	1069.85		45°	1038.10		45°	1007.14		45°	906.35		45°	834.90
	90°			90°	1130.43		90°	1100.46		90°	1073.71		90°	1044.14		90°	1009.14		90°	906.63		90°	839.24
	135°	1209.34		135°	1132.97		135°	1099.26		135°	1069.77		135°	1037.74		135°	1006.20		135°	905.36		135°	837.08
1895.48	180°	1209.52	2225.68	180°	1135.23	2357.45	180°	1104.47	2489.20	180°	1072.16	2621.76	180°	1041.81	2750.34	180°	1008.38	2982.93	180°	908.25	3090.88	180°	840.05
▲	225°	1208.20	▲	225°	1131.21	▲	225°	1101.06	▲	225°	1072.49	▲	225°	1042.31	▲	225°	1009.78	▲	225°	908.18	▲	225°	839.90
	270°	1210.67		270°	1130.17		270°	1100.61		270°	1070.20		270°	1040.23		270°	1006.20		270°	907.90		270°	839.55
	315°	1212.39		315°	1131.60		315°	1101.80		315°	1071.75		315°	1040.28		315°	1005.94		315°	907.57		315°	834.57

ANALYSIS OF DISTANCE FROM MEAN CENTERLINE TO MEASUREMENT LOCATION

POINT	AZIMUTH	RAD. 'R'	POINT	AZIMUTH	RAD. 'R'	POINT	AZIMUTH	RAD. 'R'	POINT	AZIMUTH	RAD. 'R'
⑰	0°	744.35	⑱	0°	583.44	⑲	0°	495.81	⑳	0°	491.34
	45°	738.07		45°	590.42		45°	499.16		45°	491.34
	90°	744.70		90°	584.91		90°	499.52		90°	491.34
	135°	744.55		135°	584.20		135°	498.02		135°	491.34
3199.61	180°	747.12	3330.58	180°	590.50	3401.21	180°	501.14	3425.04	180°	491.34
▲	225°	749.43	▲	225°	583.54	▲	225°	499.39	▲	225°	491.34
	270°	746.76		270°	589.05		270°	497.43		270°	491.34
	315°	743.74		315°	583.39		315°	494.97		315°	491.34

REINFORCEMENT PLATE DATA

POINT NO.	ELEV.	RAD.
1	1937.54	1193.32
2	1592.28	1268.35
3	1345.41	1333.98
4	1592.28	1266.32

NO. 1
NOZZLE CENTER AT ELEV. = 1627.43
NO. 4
NO. 2
WELD SEAM - E
297.00 305.99
NO. 3

NOTES:
1. ALL DIM'S. ARE IN DECIMALS OF AN INCH.
2. WORK THIS DWG WITH DWG. NO. SK1 AND SK3.
3. ALL DIMENSIONS WERE MEASURED AND CALCULATED IN ENGLISH THEN CONVERTED TO SI UNITS.

▶ INDICATES CHANGE FROM PREVIOUS ISSUE

CBI
NUCLEAR TEST VESSEL
INTERNATIONAL NUCLEAR SAFETY DEPARTMENT
SANDIA NATIONAL LABORATORIES

CUSTOMER'S NO
BY S.A. CHKD JAR DATE 6/21/95
BIRMINGHAM / J.A. REEVES
ENGINEERING ASSIGNED

CONTRACT NO 953241
DWG SK2 REV 3
SHT

532415K2.DGN

Figure C-8. Tabulation of radius from the mean centerline to measurement location for the SCV model.

NRC FORM 335 (2-89) NRCM 1102, 3201, 3202

U.S. NUCLEAR REGULATORY COMMISSION

BIBLIOGRAPHIC DATA SHEET

(See instructions on the reverse)

1. REPORT NUMBER (Assigned by NRC, Add Vol., Supp., Rev., and Addendum Numbers, if any.)

NUREG/CR-6516
SAND96-2877

2. TITLE AND SUBTITLE

Pretest Analyses of the Steel Containment Vessel Model

3. DATE REPORT PUBLISHED

MONTH	YEAR
January	1999

4. FIN OR GRANT NUMBER

L1299, A1401

5. AUTHOR(S)

V.L. Porter, P.A. Carter, S.W. Key

6. TYPE OF REPORT

Technical

7. PERIOD COVERED *(Inclusive Dates)*

June 1993-November 1996

8. PERFORMING ORGANIZATION - NAME AND ADDRESS *(If NRC, provide Division, Office or Region, U.S. Nuclear Regulatory Commission, and mailing address; if contractor, provide name and mailing address.)*

Sandia National Laboratories
Albuquerque, NM 87185-0443

9. SPONSORING ORGANIZATION - NAME AND ADDRESS *(If NRC, type "Same as above"; if contractor, provide NRC Division, Office or Region, U.S. Nuclear Regulatory Commission, and mailing address.)*

Division of Engineering Technology
Office of Nuclear Regulatory Research
U.S. Nuclear Regulatory Commission
Washington, DC 20555-0001

10. SUPPLEMENTARY NOTES

J.F. Costello, NRC Project Manager

11. ABSTRACT *(200 words or less)*

As part of the containment integrity program jointly sponsored by the Nuclear Power Engineering Corporation (NUPEC) of Japan and the United States Nuclear Regulatory Commission (NRC), Sandia National Laboratories (SNL) conducted a high pressure test of a steel containment vessel (SCV) model, nominally based on a Japanese Improved MK-II boiling water reactor containment. The test included an external contact structure (CS), a steel shell that covered most of the SCV model with a gap between the two structures. One of the program objectives is to validate analytical methods used to predict the response of containment buildings subjected to severe accident pressures. This report describes the finite element analyses conducted by Sandia in support of the test program and for pretest prediction of model behavior. Preliminary calculations were performed to support model design, such as the effects of mixed scaling and the effects of including a contact structure in the test. Global response of the SCV model was predicted using both axisymmetric and three-dimensional shell models. An axisymmetric continuum analysis of the top head and a three-dimensional shell analysis of the equipment hatch region were developed to provide detailed mappings of local model responses.

12. KEY WORDS/DESCRIPTORS *(List words or phrases that will assist researchers in locating the report.)*

Finite element analysis
Reactor containments
Steel containment vessel
Severe accident
Structural response
Model validation

13. AVAILABILITY STATEMENT

unlimited

14. SECURITY CLASSIFICATION

(This Page) unclassified

(This Report) unclassified

15. NUMBER OF PAGES

16. PRICE